Atomistic Simulations of Iron Oxides

DANIEL MEILAK

DOCTOR OF PHILOSOPHY

The University of York
PHYSICS

APRIL 2021

Abstract

Iron oxides such as magnetite, maghemite and cobalt ferrite are of huge importance to biomedical applications where they are used in cancer treatments and drug delivery. The ability to fine tune their magnetic properties for these applications has seen great interest in recent years. While they have been studied for centuries in bulk form, their properties at the nanoscale have only seen a surface level of understanding. In this thesis, I present a state-of-the-art investigation into the strength and scaling of these materials using an atomistic model to simulate them on a scale comparable to realistic applications. By forming an accurate model of the materials, outlining their structure, exchange interactions and anisotropy, each material is simulated with unprecedented detail, showing the changes in the overall system as the individual atomic spins move. This study shows how finite size effects lower the magnetic properties, such as the Curie temperature and magnetisation scaling of the system depending on the size and shape of the particle. As they are modelled at the atomic scale, the sublattices of each material have been investigated, showing that the overall properties are a symptom of multiple interacting components which can behave differently to each other and scale differently with temperature. In addition to simulating each material on its own, core-shell particles consisting of combinations of each material have also been investigated to better understand the behaviour of each system when the relative sizes of the core and shell are changed, as well as the overall properties of the particle which can be fine tuned for different applications.

Acknowledgments

I would like to thank my supervisor, Richard Evans, for steering me throughout the PhD. Without your help, knowledge and enthusiasm, as well as the many conversations and similar interests we shared, I would not have been able to do this work. The computational magnetism group was a wonderful environment to be in. I'll never forget the outings and hiking adventures, as well as the many lunches we enjoyed together. Thank you, Roy, Mara, Sergiu, Andrea, Sarah, Luke, Andrew, Tim and everyone else I met in the group, it would not have been half as fun without you.

I must extend a huge thanks to my parents, who have pushed me along the whole way, offering help and guidance at every step. A 'thank you' in a hundred languages would not be nearly enough to start with.

Finally, I owe both my sanity and happiness to the many friends I made at my time in university. Noodles and Scot, I treasure every minute I've been around you, sorry for riling you both so much! Charlie, Patrick, Joshua, Drezzak, Kieran, Nolly, Ciaran, Chris, Shane, Mitty, Jay, Fluro, Conor, Dhillan, Simon, Ben, Jacob, Tommy, Toby, Ali and everyone else I haven't named here, you are all the best and I love you all dearly.

AUTHOR'S DECLARATION

I declare that the work in this thesis was carried out in accordance with the requirements of the University's Regulations and Code of Practice for Research Degree Programmes and that it has not been submitted for any other academic award. Except where indicated by specific reference in the text, the work is the candidate's own work. Work done in collaboration with, or with the assistance of, others, is indicated as such. Any views expressed in the thesis are those of the author.

SIGNED: ..... DATE: .....

List of Publications

1. SD Oberdick, A Abdelgawad, C Moya, S Mesbahi-Vasey, D Kepaptsoglou, VK Lazarov, RFL Evans, D Meilak, E Skoropata, J van Lierop, et al. Spin canting across core/shell $Fe_3O_4/Mn_xFe_{3-x}O_4$ nanoparticles. *Scientific reports*, 8(1):1–12, 2018

2. D Meilak, S Jenkins, R Pond, and RFL Evans. Massively parallel atomistic simulation of ultrafast thermal spin dynamics of a permalloy vortex. *arXiv preprint arXiv:1908.08885*, 2019

3. R Moreno, S Poyser, D Meilak, A Meo, S Jenkins, VK Lazarov, G Vallejo-Fernandez, S Majetich, and RFL Evans. The role of faceting and elongation on the magnetic anisotropy of magnetite Fe_3O_4 nanocrystals. *Scientific reports*, 10(1):1–14, 2020

CONTENTS

List of Tables

Table **Page**

List of Figures

Figure **Page**

CHAPTER 1

INTRODUCTION

1.1 Origins of Magnetism

While in modern times magnets play an important role in almost all parts of our life, being integral to electronics of all forms, their history stretches to the first great scientists and mathematicians who studied the world around them. The first magnetic materials were found across the globe in iron rich areas, where lodestones affected by the strong fields in lighting became weakly attracted to the Earth's magnetic field. Centuries would pass before these magnetised rocks would be studied closely to better understand their origins and properties, with one of the first truly scientific studies being done by William Gilbert who published "*De Magnete*" in 1600 [4]. Moving ahead several centuries further, magnets of all forms are being used in electronics for data storage, with a rapid need for faster, and more dense media fuelling further research into the properties of magnetic materials.

The origin of magnetism within these materials is from the electrons bound to every atom in the system. The electrons possess both orbital and spin magnetic moments, the former relating to the movement of the electronic charge about the nucleus, while the latter comes from an intrinsic property of the elementary particle, its spin. The orbital moment of electrons is typically small due to the strong electrostatic interaction with the crystal field however the spin moment of the electrons can be a significant contribution depending on the atomic species. Typically, the moments of each electron bound by an atom align such that they form pairs of opposite magnetic moments, with parallel orientations of the same

energy state disallowed by the Pauli exclusion principle. This is the case for most materials which exhibit diamagnetism. In the presence of a magnetic field, a purely diamagnetic material opposes the field.

Other forms of magnetism are possible due to unpaired electrons, which leave the atoms with a net angular momentum. This results in several different behaviours depending on how the magnetic moments align.

1.1.1 Types of Magnetism

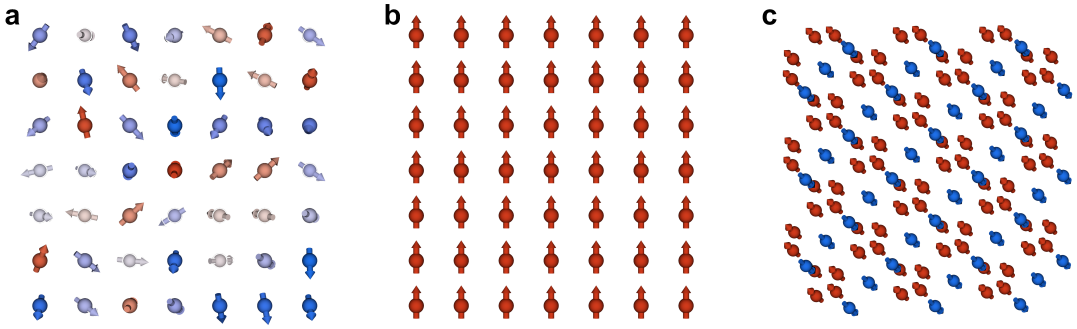

Figure 1.1: **Types of magnetism.** In the absence of a magnetic field, spins in a paramagnet, (a), are randomly oriented. In a ferromagnet, (b), the spins tend to align in parallel, causing a net magnetic field. In an antiferromagnet, (c), neighbouring spins prefer to align antiparallel causing the material to have zero net magnetisation. Ferrimagnets behave similarly to antiferromagnets (c) however the neighbouring spins have unequal moments, leaving a net overall magnetic field.

While diamagnets oppose an applied field, paramagnets are weakly attracted to them. The unpaired electrons in paramagnetic materials will tend to align along the direction of the magnetic field, forming a net magnetic moment. In the absence of a field, or when the field is moved away from the paramagnetic material, the electrons do not stay aligned as the interaction is weak and thermal energy is able to move the spins into random orientations (Figure 1.1a).

When two atoms close to each other have unpaired electrons, there is a probability that an electron will jump from one atom to another, known as Heisenberg exchange [5]. This interaction couples the two neighbouring atoms and can cause the spin moments to align without the influence of an external magnetic field. With certain materials, notably the transition metals such as nickel, iron and cobalt, spin moments are large and align in parallel (Figure 1.1b). These materials are called ferromagnets and have a net spontaneous magnetic moment. Similarly, in antiferromagnetic materials, neighbouring spins take part in another form

of coupling where the spins are aligned antiparallel to each other. The material is made up of two competing sublattices with equal moments which cause the overall material to have a zero net magnetic moment and therefore no field.

One further state of ordered magnetism is called ferrimagnetism, which shares some of the properties of ferro and antiferromagnets. In a ferrimagnet, two competing sublattices exist where neighbouring spins align antiparallel, however the moments on the electrons in each sublattice are unequal leading to a dominant spin orientation in the material. Due to the dominant orientation, the material exhibits a net magnetic moment. Ferrimagnetism was one of the last forms of magnetic ordering to be discovered after research by Louis Néel in 1948[6]. From this research we now know that the first magnetic material found in lodestones, an iron oxide called magnetite, was a ferrimagnet.

1.2 Motivation for Research

The magnetic properties of small particles have become hugely important in the last 50 years due to their intrinsic properties that make them ideal for various applications. Nanoparticles can be made to relatively specific sizes, close to the sizes of cells, proteins and genes, allowing them to interact with every level of cellular biology. Depending on the material, these nanoparticles can be biocompatible, such as magnetite which is readily detected in the brain [7], or in the case of cobalt ferrite, where studies are still being performed to determine the level of cytotoxicity [8], these nanoparticles can also be coated in biocompatible non-magnetic materials.

Due to their magnetic properties, these particles can be manipulated by an external magnetic field opening up a host of biomedical applications. Drug delivery is a promising field due to the current problems caused by the usage of non-specific chemicals which are administered in high dosages, causing significant side effects [10–12]. The aim of magnetic carriers is to target specific sites and reduce the amount of systemic distribution of the cytotoxic drug, reducing side effects. This also leads to a reduction in dosage which further reduces adverse effects.

Varying magnetic fields can also be used, transferring energy from the exciting field to the nanoparticle. Due to Néel relaxation, the particles then output energy in the form of heat, which affects the surrounding area. The field of hyperthermia, a form of cancer treatment, has seen groups around the world studying different materials to find an ideal method of delivering toxic amounts of thermal energy

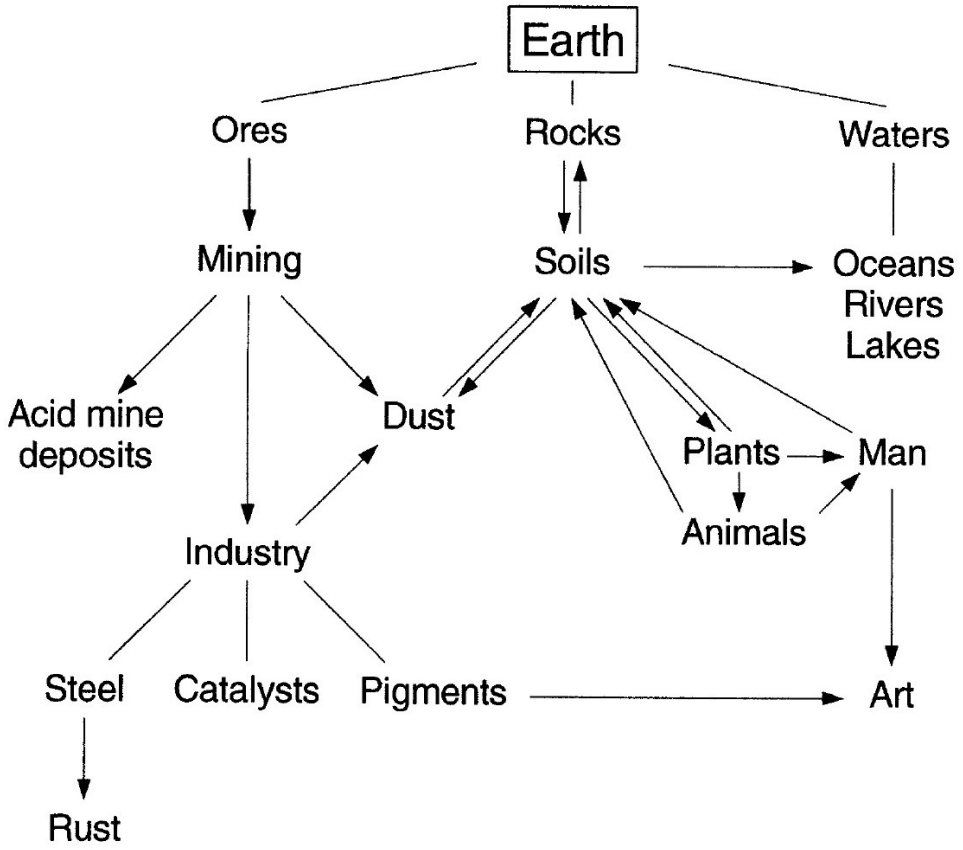

Figure 1.2: **Iron oxides in the global system.** Iron oxides are widespread in nature and present in almost all compartments of the global system. Their frequency in nature makes them cheap and relatively easy to process for many different applications. Figure from reference [9].

to targeted bodies such as tumours [13, 14]. Experimental investigations of the applications of magnetic materials for hyperthermia date back to 1957 when Gilchrist *et al.* [15] heated various tissue samples with 20-100 nm size particles of maghemite exposed to a 1.2MHz magnetic field. Ideally these nanoparticles would be used to heat targeted regions while leaving nearby healthy tissues intact.

In addition to biomedical applications, iron oxide nanoparticles of magnetite and maghemite have been used to remove heavy metals from contaminated water such as industrial wastewater produced by electroplating [16]. The magnetic nanoparticles possess large surface areas, high numbers of surface active sites and ideal magnetic properties leading to high adsorption efficiency and removal rate of contaminants. Using an external magnetic field, the particles can also be separated from the contaminants and reused. Since they do not suffer from reduced performance after successive usage, the particles can then be removed post treatment.

Iron oxide nanoparticles have hugely benefited from recent research, and it is now possible to consistently reproduce particles with a desired surface structure [17]. Their surfaces frequently reconstruct, and the resulting surfaces can exhibit markedly different electronic and magnetic structures to the bulk compound. Interface engineering offers an interesting opportunity to improve performance and apply the particles to newer fields of research such as spintronics where studies into magnetite had recently stagnated due to the presence of a magnetic dead layer at the interface [18]. It may now be possible to reconstruct the surface of iron oxide nanoparticles to avoid this issue [17].

While years of research have gone into studying the formation of nanoparticles, their surfaces and structure, far fewer studies have laid out an in-depth analysis of the magnetic properties of the particles specific to their size and mineral content. Surface effects drastically alter the properties of the particles away from that of bulk, leading to more research being required to fully understand the materials. Here, an opportunity for different methods of study arises. Most of the applications mentioned here make use of iron oxide nanoparticles less than 30 nm in diameter, particularly in biomedical applications as above this size particles will quickly be endocytosed by macrophages and removed from the body [19]. At this scale it becomes more difficult to synthesise consistent nanoparticle shapes and sizes however a different approach, such as theoretical modelling and simulation, allows for studying these materials with relative ease and can help to study more complex materials made up of different elements.

Micromagnetic modelling is a commonly used technique which helps to study large uniform magnetic systems by treating continuous regions of similar spins as single units and simulating the system by evaluating the magnetic properties at each unit. For nanoparticles around 30 nm in size, a more detailed approach is possible and, in many cases, necessary. In nanoparticles of this size, the number of atoms is typically around 100 thousand to 1 million, making fine grain atomistic simulations, which treat each atomic moment individually, possible on modest hardware. This can lead to more detailed analysis of the systems under question, revealing the properties of the system as well as any sublattices which exist in more complex materials. In many systems, the spin configuration is also complex, and cannot be grouped well into similar domains, leading to atomistic modelling being the easiest way to accurately represent their structure.

This general approach to studying iron oxides is not new [20, 21], however it is still nascent, with the current state of research requiring large scale approx-

imations to modelling and the current output being low in resolution, dealing with only the smallest scale nanoparticles around 6 nm in size, and few other published data sets for particle shapes and sizes. In addition, not all materials currently have the information available to be modelled accurately. In studies which use the popular 3D Heisenberg model to simulate iron oxides, the largest contribution to the magnetic properties of the system comes from the exchange interaction of the neighbouring spins. These interactions can be defined by a set of constants which are unique to each material. While for the most well studied materials, such as magnetite, these values have been well studied, most other iron oxides are simulated using borrowed sets of exchange from differing materials, or use exchange values calculated from mean field models with significant approximations, which have not been tested appropriately in multiple works and show some disagreement with past studies.

This work attempts to bridge together the current available information on three materials, the well-studied magnetite and its close neighbours maghemite and cobalt ferrite. This is done by creating a complete set of atomistic models, which agree well with current experimental data. In particular we study their temperature scaling properties, as well as the finite size effects which affect all systems at the nanometre scale. The VAMPIRE software package has been used to create high quality data for these magnetic properties, as well as other areas of interest such as spin switching, and core-shell nanoparticles made up of combinations of these materials.

1.3 Thesis Outline

To start we shall cover the various methods used throughout the thesis in Chapter 2, with an in depth look at the 3D Heisenberg Hamiltonian and the methods used to solve it as well as visualisation methods to better understand our results. Chapter 3 then introduces the core elements of this thesis concerning magnetite, its history, current state of understanding and finally simulations of the material in bulk form, with Chapter 4 focusing on nanoparticles of magnetite and their finite size effects. Chapters 5 and 6 cover similar materials in maghemite and cobalt ferrite respectively, going over the differences of these materials and magnetite and performing similar simulations and analysis. Chapter 7 puts together some of the information from previous chapters to look at mixed iron oxide core-shell nanoparticles and how they behave depending on their constitution. Finally, Chapter 8 concludes this thesis, covering the main points of the thesis as well as

outlining future work.

CHAPTER 2

MODELLING METHODS

2.1 Introduction

Modelling of magnetic materials has become a necessity for assessing and predicting the usability of different materials for specific purposes. Without it, it would be difficult for magnet based appliances to reach their current level of speed, reliability and efficiency. Early models, such as that developed by Ernst Ising [22], were used to understand phase changes in magnetic materials by modelling the system as a lattice of spin-up or spin-down magnetic dipole moments. This simplified system would be affected by heat but tend to equilibrium over time, creating magnetic phases.

Most modern day magnetic materials modelling is done using micromagnetics [23, 24] which predicts the behaviour of systems of sub-micrometer length scales. While this approach is more complex that the Ising model it must still make significant approximations; rather than account for every atomic spin, dipoles are grouped forming a continuous vector field. Here it is assumed that due to exchange interactions, the atomic dipoles within a small volume are mostly aligned and their averaged behaviour is a good approximation to that of individual spins. One of the downsides of this method is that it struggles to correctly model systems where short range spin fluctuations are large or can deviate from nearby spins quickly. In addition, non-uniform systems made up of multiple materials pose a significant hurdle to micromagnetics as complex crystal structures often involve short range interactions between divergent spins. To remedy this a different approach is required, which gives up some of the benefits of micromagnetics in

being able to model very large uniform systems but instead allows for a much higher resolution and detailed understanding of nanometre scale magnetism.

Atomistic modelling is now one of the most promising tools available in understanding magnetic materials. Atomistic spin models are based on the principle that each atom possesses a local magnetic moment located on the lattice site. This assumes that all the electrons are localised around the atom which could be at odds with metals containing 3D outer electrons such as iron where the electrons are loosely bound, however *ab-initio* calculations of the electron density show that even in 3D ferromagnetic materials the spin polarisation is well localised to the lattice site [25]. These localised moments are known as magnetic moments and their magnitudes depend on the atomic species.

2.2 Heisenberg Hamiltonian

The Heisenberg spin model encapsulates the essential physical components of a magnetic material at the atomic level. Its aim is to describe the interactions of each atomic spin moment, μ_s, and its neighbouring moments within the system and possible external magnetic field. The energy contributions of each interaction are summed together to make up the overall energy of the system. Thus, the spin Hamiltonian, $\mathscr{H}$, can be written in the following form:

$$\mathscr{H} = \mathscr{H}_{\text{exchange}} + \mathscr{H}_{\text{anisotropy}} + \mathscr{H}_{\text{applied}} \tag{2.1}$$

This describes the energy contributions of the exchange interaction, the magnetic anisotropy and any externally applied magnetic field. The exchange and anisotropy energies are intrinsic to the material however the applied field, $\mathscr{H}_{\text{applied}}$, is usually the result of an external system, such as a nearby magnetic material or an effective field from an electric current. The energy of the applied field is given by:

$$\mathscr{H}_{\text{applied}} = -\sum_i \mu_s \mathbf{S}_i \mathbf{B}_{applied} \tag{2.2}$$

where μ_s is the spin magnetic moment and $\mathbf{S}_i$ the spin vector at site i. The lowest energy configuration corresponds to the spins aligning along the applied field, $\mathbf{B}$.

2.2.1 Exchange Interaction

The dominant contribution of the spin Hamiltonian in ferromagnetic materials is the exchange field, which arises due to the symmetry of the electron wavefunction and the Pauli exclusion principle which affects the orientation of spins in overlapping electron orbitals [26]. To understand how this interaction arises, we can examine the simple case of the helium atom. Consider an electron in a state $\psi_a(\mathbf{r}_1)$ at $\mathbf{r}_1$ and another at state $\psi_b(\mathbf{r}_2)$ at $\mathbf{r}_2$, the combined wavefunction of the system, $\Psi(\mathbf{r}_1,\mathbf{r}_2)$, can be defined as a linear combination of the individual election wavefunctions which must be a solution to the Schrödinger equation:

$$\Psi(\mathbf{r}_1,\mathbf{r}_2) = \psi_a(\mathbf{r}_1)\psi_b(\mathbf{r}_2) \tag{2.3}$$

$$\left[-\frac{\hbar^2}{2m}\nabla_1^2 - \frac{\hbar^2}{2m}\nabla_2^2 - \frac{2e^2}{\mathbf{r}_1} - \frac{2e^2}{\mathbf{r}_2} + \frac{e^2}{\mathbf{r}_{12}}\right]\Psi(\mathbf{r}_1,\mathbf{r}_2) = E\Psi(\mathbf{r}_1,\mathbf{r}_2) \tag{2.4}$$

Here E is the energy of the system and is equal to $E_a + E_b$, the energy of electrons a and b. r_{12} is the separation between the two electrons and corresponds to the interaction between them. The electrons are indistinguishable therefore $\psi_a(\mathbf{r}_2)\psi_b(\mathbf{r}_1)$ is also a solution to the Schrödinger equation, hence the following must be true:

$$|\Psi(\mathbf{r}_1,\mathbf{r}_2)|^2 d\mathbf{r}_1 d\mathbf{r}_2 = |\Psi(\mathbf{r}_2,\mathbf{r}_1)|^2 d\mathbf{r}_1 d\mathbf{r}_2 \tag{2.5}$$

There are two possibilities from this equation: Ψ_{sym}, the wavefunction is symmetric as $\Psi(\mathbf{r}_1,\mathbf{r}_2) = \Psi(\mathbf{r}_2,\mathbf{r}_1)$ or the wavefunction is anti-symmetric, Ψ_{anti}, as $-\Psi(\mathbf{r}_1,\mathbf{r}_2) = \Psi(\mathbf{r}_2,\mathbf{r}_1)$. We can form a general solution to the wavefunction using either state:

$$\Psi_{\text{sym}}(\mathbf{r}_1,\mathbf{r}_2) = \frac{1}{\sqrt{2}}\left[\psi_a(\mathbf{r}_1)\psi_b(\mathbf{r}_2) + \psi_a(\mathbf{r}_2)\psi_b(\mathbf{r}_1)\right] \tag{2.6}$$

$$\Psi_{\text{anti}}(\mathbf{r}_1,\mathbf{r}_2) = \frac{1}{\sqrt{2}}\left[\psi_a(\mathbf{r}_1)\psi_b(\mathbf{r}_2) - \psi_a(\mathbf{r}_2)\psi_b(\mathbf{r}_1)\right] \tag{2.7}$$

As electrons are bound by the Pauli exclusion principle, and two identical electrons cannot occupy the same quantum state, the overall wavefunction must

be anti-symmetric. So far we have not included the spin component of the wavefunction, with α = spin up, β = spin down, which also come in symmetric and anti-symmetric forms. There are eight possible configurations of the two electron spin states [26]:

$$\begin{array}{ll} \psi_a(\mathbf{r}_1)\alpha_a\psi_b(\mathbf{r}_2)\alpha_b & \psi_b(\mathbf{r}_1)\alpha_a\psi_a(\mathbf{r}_2)\alpha_b \\ \psi_a(\mathbf{r}_1)\alpha_a\psi_b(\mathbf{r}_2)\beta_b & \psi_b(\mathbf{r}_1)\beta_a\psi_a(\mathbf{r}_2)\alpha_b \\ \psi_a(\mathbf{r}_1)\beta_a\psi_b(\mathbf{r}_2)\alpha_b & \psi_b(\mathbf{r}_1)\alpha_a\psi_a(\mathbf{r}_2)\beta_b \\ \psi_a(\mathbf{r}_1)\beta_a\psi_b(\mathbf{r}_2)\beta_b & \psi_b(\mathbf{r}_1)\beta_a\psi_a(\mathbf{r}_2)\beta_b \end{array} \tag{2.8}$$

The anti-symmetric wavefunctions for the system can be constructed by taking appropriate linear combinations of the products in 2.8. If the total wavefunction is to be anti-symmetric, either the spin-dependent part must be anti-symmetric and the spatial part symmetric, or vice versa. Doing this we end up with four functions:

$$\begin{aligned} \Psi(\mathbf{r}_1,\mathbf{r}_2) &= \frac{1}{\sqrt{2}}\left[\psi_a(\mathbf{r}_1)\psi_b(\mathbf{r}_2) - \psi_a(\mathbf{r}_2)\psi_b(\mathbf{r}_1)\right]\alpha_a\alpha_b \\ \Psi(\mathbf{r}_1,\mathbf{r}_2) &= \frac{1}{\sqrt{2}}\left[\psi_a(\mathbf{r}_1)\psi_b(\mathbf{r}_2) - \psi_a(\mathbf{r}_2)\psi_b(\mathbf{r}_1)\right]\beta_a\beta_b \\ \Psi(\mathbf{r}_1,\mathbf{r}_2) &= \frac{1}{\sqrt{2}}\left[\psi_a(\mathbf{r}_1)\psi_b(\mathbf{r}_2) - \psi_a(\mathbf{r}_2)\psi_b(\mathbf{r}_1)\right]\frac{1}{\sqrt{2}}\left[\alpha_a\beta_b + \alpha_b\beta_a\right] \\ \Psi(\mathbf{r}_1,\mathbf{r}_2) &= \frac{1}{\sqrt{2}}\left[\psi_a(\mathbf{r}_1)\psi_b(\mathbf{r}_2) + \psi_a(\mathbf{r}_2)\psi_b(\mathbf{r}_1)\right]\frac{1}{\sqrt{2}}\left[\alpha_a\beta_b - \alpha_b\beta_a\right] \end{aligned} \tag{2.9}$$

The spin components are eigenfunctions of the operators representing the total spin, S, of the two particles and of their total z-component. In the first three states the electron spins are aligned in parallel, while in the fourth they are antiparallel. The first three functions have their total spin quantum number $S = 1$, and the quantum numbers associated with the z-component equal to 1, -1 and 0 respectively. Collectively, these states are known as a triplet Ψ_T, with energy E_T. The fourth function has zero spin, $S = 0$, and is know as a singlet Ψ_S with energy E_S. Hence we can condense the four states into two possible wavefunctions:

$$\begin{aligned} \Psi_T &= \frac{1}{\sqrt{2}}\left[\psi_a(\mathbf{r}_1)\psi_b(\mathbf{r}_2) - \psi_a(\mathbf{r}_2)\psi_b(\mathbf{r}_1)\right]\chi_T \\ \Psi_S &= \frac{1}{\sqrt{2}}\left[\psi_a(\mathbf{r}_1)\psi_b(\mathbf{r}_2) + \psi_a(\mathbf{r}_2)\psi_b(\mathbf{r}_1)\right]\chi_S \end{aligned} \tag{2.10}$$

with energies:

$$\begin{aligned} E_T &= \int\int \Psi_T^* \mathscr{H} \Psi_T d\mathbf{r}_1 d\mathbf{r}_2 \\ E_S &= \int\int \Psi_S^* \mathscr{H} \Psi_S d\mathbf{r}_1 d\mathbf{r}_2 \end{aligned} \tag{2.11}$$

with the assumption that the spin parts of the wave function χ_T and χ_S are normalised, the difference between the two energies is:

$$E_S - E_T = 2\int\int \psi_a^*(\mathbf{r}_1)\psi_b^*(\mathbf{r}_2)\mathscr{H}\psi_a(\mathbf{r}_2)\psi_b(\mathbf{r}_1)d\mathbf{r}_1 d\mathbf{r}_2 \tag{2.12}$$

If we consider two spin half particles coupled by an exchange interaction, the joint operator $\mathbf{S}_{tot} = \mathbf{S}_1 \cdot \mathbf{S}_2$, so $\mathbf{S}_{tot}^2 = \mathbf{S}_1^2 + \mathbf{S}_2^2 + 2\mathbf{S}_1 \cdot \mathbf{S}_2$. Therefore, the difference between single and triplet states can be parameterized by $A\mathbf{S}_1 \cdot \mathbf{S}_2$. Combining these two particles results in a joint entity with spin quantum number $S = 0$ (singlet) or $S = 1$ (triplet) depending on the relative orientation of the two spins. The eigenvalues of $\mathbf{S}_{tot}^2$ are $\mathbf{S}(\mathbf{S}+1)$ so for the singlet case $\mathbf{S}_1 \cdot \mathbf{S}_2 = -3/4$ whereas for the triplet case $\mathbf{S}_1 \cdot \mathbf{S}_2 = 1/4$ [27].

Hence the Hamiltonian can be written in the form:

$$\mathscr{H} = \frac{1}{4}(E_S + 3E_T) - (E_S - E_T)\mathbf{S}_1 \cdot \mathbf{S}_2 \tag{2.13}$$

This Hamiltonian can be split into two terms, a radial component $\mathscr{H}_{rad}$ and a spin component $\mathscr{H}_{spin} = (E_S - E_T)\mathbf{S}_1 \cdot \mathbf{S}_2$. From this we define an exchange constant, J_{ex}:

$$J_{ex} = \frac{1}{2}(E_S - E_T) \tag{2.14}$$

or more simply the spin Hamiltonian is:

$$\mathscr{H}_{\text{spin}} = -2J_{ex}\mathbf{S}_1 \cdot \mathbf{S}_2 \tag{2.15}$$

When J_{ex} is negative, an anti-ferromagnetic arrangement is more favourable ($E_S < E_T$), while if J_{ex} is positive, a ferromagnetic arrangement is more favourable

($E_T < E_S$). This is a simple example for the interactions of two identical electrons however it forms the basis for more complex systems with higher numbers of electrons. In the extended Heisenberg model, an approximation to the exchange treats all spins in the systems as pairs of electrons leading to the overall exchange Hamiltonian:

$$\mathscr{H}_{\text{exchange}} = -\sum_{i<j} J_{ij}\mathbf{S}_i \cdot \mathbf{S}_j \tag{2.16}$$

where $\mathbf{S}_i$ and $\mathbf{S}_j$ are spins of atoms i and j. The form of J_{ij} depends on the form of the interaction. In the simple case this interaction is isotropic, depending on the relative orientation of the spins not their particular directions. In more complex materials it forms a tensor with components:

$$\overline{\overline{J}}_{ij} = \begin{pmatrix} J_{xx} & J_{xy} & J_{xz} \\ J_{yx} & J_{yy} & J_{yz} \\ J_{zx} & J_{zy} & J_{zz} \end{pmatrix} \tag{2.17}$$

In practice, the values of J_{ij} can be calculated (typically approximated) using *ab-initio* methods or by fitting experimental results [28, 29]. The energies of exchange are around 1-2eV which is usually much larger than the next largest contribution and gives rise to magnetic ordering temperatures around 300-1300K[30]. While equation 2.16 takes into account all spins in the system, the exchange energy is dependent on the distance between each spin. The energy contributions from spins further than second or third nearest neighbours is often small, hence it is often approximated to be only nearest neighbour exchange.

2.2.2 Magnetocrystalline Anisotropy

While the exchange energy affects the interatomic spin interactions, the anisotropy energy determines the preferred directions of the atomic moments. Anisotropy can be caused by several different mechanisms, such as overall system structure in the case of elongated particles, which causes an overall shape anisotropy as the demagnetising field will not be equal for all directions causing spins to align along the axis of elongation. The most common form of anisotropy is magnetocrystalline anisotropy which is a result of the crystal symmetries interacting with the spin-orbit coupling of the electron. Magnetocrystalline anisotropy can form in different flavours, the simplest being uniaxial anisotropy, where the spins prefer to align along a single axis, called the easy axis. This form of anisotropy usually

exists when there is a distortion along a single axis of the material, such as in hexagonal systems. The uniaxial single-ion anisotropy single energy is given by the expression:

$$\mathscr{H}_{\text{uniaxial}} = -k_{\text{u}} \sum_i (\mathbf{S}_i \cdot \mathbf{e})^2 \tag{2.18}$$

where k_{u} is the uniaxial anisotropy energy per atom and $\mathbf{e}$ is the easy axis vector. In cubic systems a different form of magnetocrystalline anisotropy usually occurs: cubic anisotropy. Materials such as iron and nickel have multiple preferred anisotropy directions which are separated in energy level leading to one direction being preferred. This type of anisotropy is usually much weaker than uniaxial anisotropy. The axes are typically called the easy, medium and hard axes, in order of increasing energy. Cubic anisotropy can be described by the following equation:

$$\mathscr{H}_{\text{cubic}} = \frac{+k_{\text{c}}}{2} \sum_i (\mathbf{S}_x^4 + \mathbf{S}_y^4 + \mathbf{S}_z^4) \tag{2.19}$$

where k_{c} is the cubic anisotropy energy per atom and S_x, S_y and S_z are the components of the spin moment $\mathbf{S}$.

2.3 Integration Methods

The Heisenberg Hamiltonian provides a robust method of finding the energy of the system however methods for calculating time evolution or thermal fluctuations is still required. In addition, it is important to show the temperature dependence of the system as well as its ground state, therefore methods for relaxing the system are also needed. There are several possible models that can find the ground state of the system. Some require a time-dependent simulation of the system while others are time-independent and relax to the ground state. Two such methods are presented here: the stochastic Landau-Lifshitz-Gilbert equation for calculating spin dynamics, and the Monte Carlo method for calculating static properties.

2.3.1 Spin Dynamics

Landau and Lifshitz [31] first described the time-dependent behaviour of a magnetic materials (specifically ferromagnets) by using equation 2.20, named after its authors, created from looking at magnetic resonance experiments.

$$\frac{\partial \mathbf{m}}{\partial t} = -\gamma[\mathbf{m} \times \mathbf{B} + \alpha \mathbf{m} \times (\mathbf{m} \times \mathbf{B})] \tag{2.20}$$

Here, $\mathbf{m}$ is a unit vector describing the direction of the sample magnetisation, $\mathbf{B}$ is the effective field acting on the system, γ called the gyromagnetic ratio is the ratio of its magnetic moment to its angular momentum, and α, a phenomenological damping constant which is dependent on the material. The physical origin of the Landau-Lifshitz equation can be explained by splitting equation 2.20 into two terms. The first refers to the quantum mechanical precession of spins around an applied field. The second term containing the damping constant α accounts for energy dissipation from the system. Energy transfer occurs due to the coupling of the atomic moments to a heat bath. The strength of the coupling is linked to the value of the damping constant, which determines how quickly the atomic moments align to the applied field.

Gilbert would later show that this method yields incorrect dynamics for materials with high damping [32] and adjusted the damping parameter to have a maximum value, called critical damping, when $\alpha = 1$. The altered equation is known as the Landau-Lifshitz-Gilbert equation, or LLG, and was originally used to describe macroscopic magnetisation of a sample, however in principle the equation applies equally well to micromagnetics and is often used in this field [33].

The LLG can be formulated for atomistic simulations by excluding extrinsic spin interactions, such as from demagnetising fields or surface defects. Here, only intrinsic damping contributions from the spin-lattice and spin-electron interactions are considered. To distinguish the macroscopic damping parameter α, which includes all damping contributions, from the microscopic, we use a different parameter, λ. The LLG equation can be described by:

$$\frac{\partial \mathbf{S}_i}{\partial t} = -\frac{\gamma}{(1+\lambda^2)}[\mathbf{S}_i \times \mathbf{B}^i_{\text{eff}} + \lambda \mathbf{S}_i \times (\mathbf{S}_i \times \mathbf{B}^i_{\text{eff}})] \tag{2.21}$$

where $\mathbf{S}_i$ is a unit vector representing the direction of the magnetic spin moment of site i and $\mathbf{B}^i_{\text{eff}}$ is the net magnetic field on each spin. The atomistic LLG describes the interaction of an atomic spin moment with an effective magnetic field. The effective field at the site i can be calculated as:

$$\mathbf{B}^i_{\text{eff}} = -\frac{1}{\mu_s}\frac{\partial \mathscr{H}}{\partial \mathbf{S}_i} \tag{2.22}$$

where μ_s is the local spin moment.

2.3.2 Langevin dynamics

So far we have described the time-dependent behaviour of a system using the LLG however equations 2.21 and 2.22 are independent of temperature and only apply at zero Kelvin. At high temperatures, the magnetic properties of the system can change completely as the energy of the temperature fluctuations becomes higher than that of the exchange and the system transitions to a paramagnetic state. To take this behaviour into account, Brown developed a new approach by using Langevin Dynamics [34]. The thermal effects are modelled as a Gaussian white noise term affecting each atomic site where increasing the temperature increases the width of the Gaussian distribution. This in turn represents stronger thermal fluctuations. The Gaussian distribution is three dimensional with a mean of zero and the instantaneous thermal field on each spin is given by:

$$\mathbf{B}^i_{\text{thermal}} = \Gamma(t)\sqrt{\frac{2\lambda k_B T}{\gamma \mu_s \Delta t}} \tag{2.23}$$

where $k_B = 1.38064852 \times 10^{-23}$ J is the Boltzmann constant, T the simulation temperature, λ the Gilbert damping parameter, γ the gyromagnetic ratio, μ_s the magnitude of the magnetic moment and Δt the integration time step. Hence combining equations 2.22 and 2.23 the modified effective field at site i is:

$$\mathbf{B}^i_{\text{eff}} = -\frac{1}{\mu_s}\frac{\partial \mathscr{H}}{\partial \mathbf{S}_i} + \mathbf{B}^i_{\text{thermal}} \tag{2.24}$$

2.3.3 Time Integration of the LLG

An integration scheme is required to solve the LLG to determine the time evolution of a system of spins. Due to the physical nature of the problem, there are limitations on the solvers we can use. The principal requirement for a solver [35] is that the magnitudes of the spins are conserved. The most simple but robust solver that satisfies this requirement is the Euler method which assumes a linear change in spin direction in a single time step. Nowadays the Euler method is seldom used due to the popularity of improved Euler methods [36] such as the Runge-Kutta family of methods, which are more stable and reduce the number of steps required to calculate the next spin position.

A popular second order, two stage, Runge-Kutta method is known as the Heun method [37] which employs a predictor-corrector algorithm allowing for larger time steps and a possible large speed up in calculation time. The Heun scheme does not conserve energy and must be continually renormalized to predict correct dynamics. Despite other schemes existing which would intrinsically preserve energy, there is often a computational cost incurred in their usage that outweighs the possible benefits. Hence the simplicity and ease of application of the Heun method makes it a popular choice in magnetics simulations[30, 37].

The predictor-corrector algorithm functions as follows: first the predictor step calculates a spin direction $\mathbf{S}_i^{'}$ by performing one Euler integration step:

$$\mathbf{S}_i' = \mathbf{S}_i + \Delta\mathbf{S}\Delta t \tag{2.25}$$

where

$$\Delta\mathbf{S} = -\frac{\gamma}{(1+\lambda^2)}[\mathbf{S}_i \times \mathbf{B}_{\text{eff}}^i + \lambda\mathbf{S}_i \times (\mathbf{S}_i \times \mathbf{B}_{\text{eff}}^i)] \tag{2.26}$$

The effective field is then recalculated with the predicted spin positions and this step is repeated for every spin in the system. The corrector step then performs another Euler integration step and uses the predicted spin positions and revised field to calculate the final configuration by averaging the results. The completed integration step is given by:

$$\mathbf{S}_i^{t+\Delta t} = \mathbf{S}_i + \frac{1}{2}[\Delta\mathbf{S} + \Delta\mathbf{S}']\Delta t \tag{2.27}$$

where

$$\Delta\mathbf{S}' = -\frac{\gamma}{(1+\lambda^2)}[\mathbf{S}_i' \times \mathbf{B}_{\text{eff}}^{i'} + \lambda\mathbf{S}_i' \times (\mathbf{S}_i' \times \mathbf{B}_{\text{eff}}^{i'})] \tag{2.28}$$

The corrector step is also performed for every spin in the system and the overall process is repeated many times to determine the time-dependent properties.

The speed of the algorithm is dependant on the size of the time step, Δt. Ideally one would like to use the largest time step possible to simulate systems quickly or for a long time. In micromagnetics, the minimum time step is a well

defined quantity since the largest field (typically the exchange term) defines the precession frequency. For atomistic simulations using Langevin dynamics, the effective field becomes temperature dependant. Hence for atomistic models, the most difficult region to integrate is in the immediate vicinity of the Curie point. This leads to a straight forward method for testing the parameter: a time step size is chosen appropriately if the mean magnetisation varies smoothly around the Curie temperature of the system. If the chosen time step is low enough, the Heun scheme and LLG will be able to simulate realistic time-dependent dynamics for magnetic systems.

2.3.4 Monte Carlo Methods

By using the LLG, an investigation of the time-dependent dynamics will reveal realistic physical dynamics from the starting point of the simulation through to the equilibrium point where the system is fully relaxed. In some cases, these dynamics are not required and only the eventual equilibrium point is needed. The Monte Carlo Metropolis algorithm is a simple but robust method that offers a more optimal method to determine equilibrium properties when intermediate dynamics are not necessary [38].

Applied to a classical spin system, the Monte Carlo Metropolis algorithm works by choosing a random spin i, and changing its direction, $\mathbf{S}_i$, to a new trial position $\mathbf{S}_i'$. The difference in energy $\Delta E = E(\mathbf{S}_i') - E(\mathbf{S}_i)$ between the initial and final position is calculated and the trial move is accepted or rejected according to a probability, P, such that:

$$P = \exp\left(-\frac{\Delta E}{k_{\mathrm{B}}T}\right) \tag{2.29}$$

If ΔE is negative, the final state is lower in energy and the trial move is accepted ($P > 1$). If the probability is less than 1, and ΔE is positive, the value is compared to a random number between 0-1 and the move is accepted if the probability value is higher, allowing for thermal fluctuations to cause a small increase in energy trial move. This process is repeated for every spin in the system and after each move is accepted or rejected, the result is a single Monte Carlo step.

The typical requirements for a Monte Carlo algorithm are ergodicity and reversibility, i.e. all spin movements must be possible and the probability of a move from position $\mathbf{S}_i$ to $\mathbf{S}_i'$ must be the same as the probability of a move from $\mathbf{S}_i'$

to $\mathbf{S}_i$. The latter follows from equation 2.29 as the probability is only dependent on the initial and final energies. The former, ergodicity, is also true as any spin trial move is possible however their probabilities can be drastically different. At high temperatures, most moves are roughly equally probable, however at low temperatures, large spin deviations are very unlikely, leading to most trial moves being rejected. For an efficient algorithm, an acceptance rate of around 50% is desired.

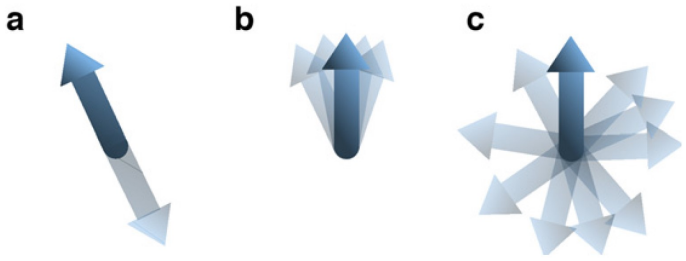

Figure 2.1: **Monte Carlo trial moves.** The three possible trial moves proposed by Hinzke and Nowak for the Monte Carlo Metropolis algorithm: (a) spin flip; (b) Gaussian perturbation; and (c) random movement. Figure from Ref. [30]

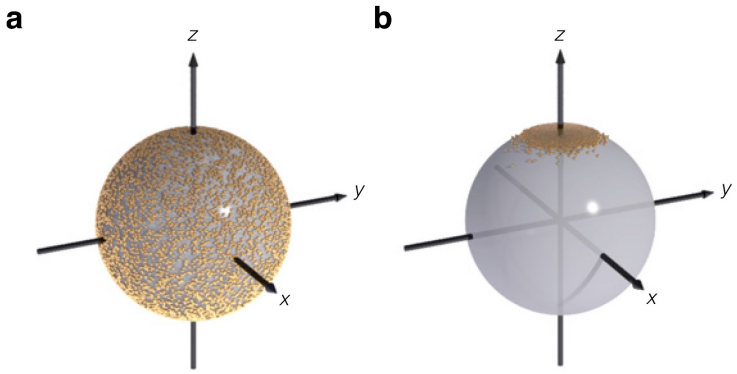

Figure 2.2: **Monte Carlo sampling.** Trial moves using the random sampling (a) and Gaussian perturbation (b) methods. The random sampling shows good coverage of the unit cell with no bias, while the Gaussian move shows trial moves centred around the initial spin position along the positive z-axis. Figure from Ref. [30]

Hinzke and Nowak [39] developed an efficient algorithm which uses three different trial moves: a spin flip, a Gaussian perturbation and a random move, illustrated in Figure 2.1. While each method alone does not necessarily satisfy ergodicity, a combination of the methods creates a non-zero probability for every possible spin movement. The spin flip moves a spin to an antiparallel position, $\mathbf{S}_i = -\mathbf{S}_i'$, much like an Ising model spin movement. The Gaussian trial move takes a spin and moves it by a small amount according to the following expression:

$$\mathbf{S}_i' = \frac{\mathbf{S}_i + \sigma_g \mathbf{\Gamma}}{|\mathbf{S}_i + \sigma_g \mathbf{\Gamma}|} \tag{2.30}$$

where σ_g is the width of a cone around the initial spin and $\mathbf{\Gamma}$ is a Gaussian distributed random number. The size of the cone depends on temperature and is usually of the form

$$\sigma_g = \frac{2}{25}\left(\frac{k_B T}{\mu_B}\right)^{1/5} \tag{2.31}$$

At low to medium temperatures, small spin movements are more likely, and the Gaussian trial move is favoured. Finally, the random spin movement chooses a position on the unit sphere according to

$$\mathbf{S}_i' = \frac{\mathbf{\Gamma}}{|\mathbf{\Gamma}|} \tag{2.32}$$

ensuring ergodicity for the complete algorithm. The three possible move are performed one at a time, chosen randomly, for each spin in the system per Monte Carlo step.

2.4 Temperature Rescaling

The Heisenberg model we have introduced can be used to effectively model magnetic materials of all forms, using *ab initio* or experimental input parameters to produce well defined output. On comparison with experimental results however, many properties such as temperature scaling behaviour of magnetisation or specific heat have been shown to depart from those expected from experiment. The major contributing factor to this effect is the classical nature of the model, where spins are defined as localised classical atomic spins $\mathbf{s}_i = \mu \mathbf{S}_i$ on the surface of the unit sphere, $|\mathbf{s}_i| = 1$. At the lowest level, magnetic materials, and in particular spins, behave according to quantum mechanical effects and are constrained to particular eigenvalues. While at the macroscopic level, a quantum mechanical system and a classical one is able to take on all possible values of overall spin direction due to an averaging out of individual spins, this does not yield the same thermodynamic effects.

To remedy the disparity between quantum and classical models, a temperature rescaling mechanism has been developed by Evans *et al.* [40]. To derive an

appropriate scaling method, we compare the magnetisation and temperature relationship for each approach. First we consider the total magnetisation $M(T) = \langle \mathbf{S} \rangle$ and the normalised magnetisation $m(T) = M(T)/M(0K)$. In the low temperature limit, m can be calculated as:

$$m = 1 - \frac{1}{N} \sum_k n_k \tag{2.33}$$

where N is the number of spins and the sum is over the spin-wave occupation number of wave vector k. Classically, the occupation number of a spin wave of energy ϵ_k corresponds to the high-temperature limit of the Boltzmann law in reciprocal space:

$$n_k = k_B T/\epsilon_k \tag{2.34}$$

however quantum mechanically they are bosonic modes of the spin lattice and therefore follow the Bose-Einstein distribution:

$$n_k = 1/[\exp(\epsilon_k/k_B T) - 1] \tag{2.35}$$

The spin wave energy should be the same irrespective of the model used, hence the difference in the magnetisation predicted by quantum and classical models is due to their different statistical behaviours. We now examine the behaviour of both models in a low and high temperature phase. At low temperatures equation 2.33 has a well-known result [41]:

$$m_{\text{classical}}(T) \approx 1 - \frac{1}{3} \frac{T}{T_{\text{C}}} \tag{2.36}$$

where T_{C} is the Curie temperature which has the same value for both classical and quantum systems. Similarly in the quantum Heisenberg case:

$$m_{\text{quantum}}(T) \approx 1 - \frac{1}{3} s \left(\frac{T}{T_{\text{C}}} \right)^{3/2} \tag{2.37}$$

we obtain the Bloch law [26]. Here s is a slope factor which is a function of the spin quantum number, the Watson integral and the Riemann ζ function. Equating equations 2.36 and 2.37 we find:

$$\frac{T_{\text{classical}}}{T_{\text{C}}} = s\left(\frac{T_{\text{quantum}}}{T_{\text{C}}}\right)^{3/2} \tag{2.38}$$

which relates the low temperature quantum magnetisation to a rescaled classical magnetisation. In the high temperature phase close to T_{C}, the spin-wave energy is high and $\epsilon/k_B T \rightarrow 0$. Hence $1/[\exp(\epsilon_k/k_B T) - 1] \approx \epsilon_k/k_B T$. Spin quantisation is therefore not a factor in the high temperature phase. At high temperatures the magnetisation should scale according to a power law, $m(\tau) = (1-\tau)^{\beta}$, where $\tau = T/T_{\text{C}}$ and β is a critical exponent often cited as 1/3 for the Heisenberg model [42].

The low temperature behaviour of classical and quantum systems can be related using a relatively simple equation and the high temperature behaviour for both cases tends to equality. Evans [40] suggests that a good relation between both regimes for all temperatures can be modelled using the Curie-Bloch equation:

$$M(\tau) = \left(1 - \tau^{\alpha}\right)^{\beta} \tag{2.39}$$

This equation is a direct extrapolation of low temperature behaviour according to Bloch's law and high temperature behaviour near the critical exponent. α is the only fitting parameter required to relate the classical and quantum scaling at all temperatures. With the assumption that β is the same for both classical and quantum systems, we can fit experimental data using equation 2.39 to find the appropriate value of α for our system. We are then able to rescale the temperatures of simulated results according to:

$$\frac{T_{\text{sim}}}{T_{\text{C}}} = \left(\frac{T_{\text{exp}}}{T_{\text{C}}}\right)^{\alpha} \tag{2.40}$$

which should yield results much closer to experiment with a better qualitative magnetisation scaling. This technique has already been applied to elemental ferromagnets and shows very good agreement with the experimentally measured magnetisations for all studied materials [40].

2.5 VAMPIRE Software Package

The modelling methods explained in this chapter have been implemented into VAMPIRE, an open-source atomistic spin dynamics software package developed

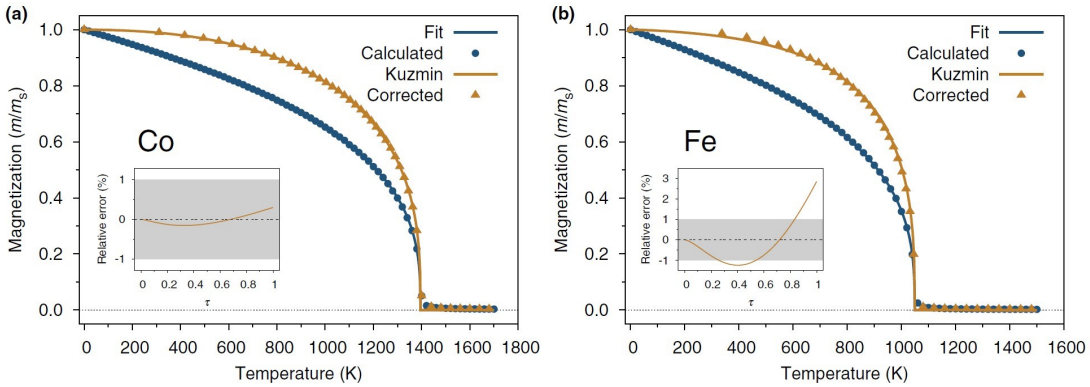

Figure 2.3: **Rescaling applied to Fe and Co.** Blue points show the simulated data points using a Monte Carlo approach. These are fit using the Curie-Bloch equation and shown with blue curves. The gold curves show the experimentally measured temperature-dependent magnetisation, Ref. [43] for cobalt, (a), and Ref. [44] for iron, (b). The gold points are the simulated data points, rescaled using equation 2.40. Both sets of data show excellent agreement with experimental results. Insets are plots of relative error of the rescaled magnetisation compared to the experimental data. Figure from Ref. [40].

at the University of York [30]. This package is authored by Richard Evans and the computational magnetism group at the University of York and is available for personal research according to the rules of the GNU General Public License or GPL. The code base is written in C++ and can run on most hardware, in either serial, parallel or GPU modes. Most results in this thesis are calculated using the VAMPIRE software package which handles simulation as well as data output. In addition, this work made extensive use of the Viking Cluster, a high performance compute facility provided by the University of York, which was used to run VAMPIRE.

2.6 Visualisation

The VAMPIRE software package outputs data such as temperature or magnetisation values in plain text. Most of the plots using the data presented in the thesis are made using Gnuplot [45], a portable command-line driven graphing utility. In addition to raw data, VAMPIRE is able to output spin coordinate data such as positions and spin directions for output using external programs. Atomic positions can be displayed using chemical structure visualisation software such as Jmol [46] or Rasmol [47].

A component of the work done for this thesis was rewriting the spin's direction visualisation output in VAMPIRE. Alongside common simulation output such as

magnetisation or field strength which are easily accessible from the data output, system visualisation forms a crucial component of data analysis as it provides a more easily readable form of visual output, as well as allowing for much easier system set up and testing. As ferro, ferri and anti-ferromagnetic systems have significantly different spin structures, spin visualisation is a relatively quick and easy method for parameter verification before starting simulations. Visualisation of the initial system state can save hours of wasted simulation time by catching simple errors in system set-up. In addition, spin visualisation can complement plots of output data as together they form a more complete picture of the magnetic properties being investigated. To render this data, external programs such as POV-Ray [48] are used.

The reliability of spin visualisation is therefore of crucial importance both to the user and to any desired recipients of the final data. A significant issue with spin visualisation is the type of colour map and its parent colour space used to colour individual elements. A colour map can be thought of as a line or curve drawn through a three dimensional colour space, or an organisation of colours collected arbitrarily or by using mathematical rigour (for example Adobe RGB or sRGB [49]). An effective colour map presents a list of colours which can be structured and allows the communication of metric information. The latter has become a common issue in widely used vendor colour maps due to a few different factors separate to those related to the representation when displayed digitally due to viewing angle or display calibration. Colours can be represented as a tuple of values between 0-255(RGB) or 0-1(HSL) and while it is possible to create a colour map consisting of equally spaced positions between these values, the relationship between the distance of the colours from each other is non-linear with human perception of colour difference. It is therefore common for colour maps to contain perceptually uniform or flat regions of colour which may vary significantly in RGB value but be very difficult to distinguish using only human perception. Put differently, human perception can cause distinct groups of colours to become essentially indistinguishable from each other leading to a loss or corruption in conveyed information. While not directly related, colour maps used to address colour blindness can also be adjusted. In addition to colour, lightness can pose another barrier due to high brightness or saturation causing perceived colour blending [50]. Most studies looking at colour perception in scientific data analysis have been restricted to cartographic applications [51, 52] however inspired by the work done by Peter Kovesi [53] this theory has been applied to the visualisation output of VAMPIRE.

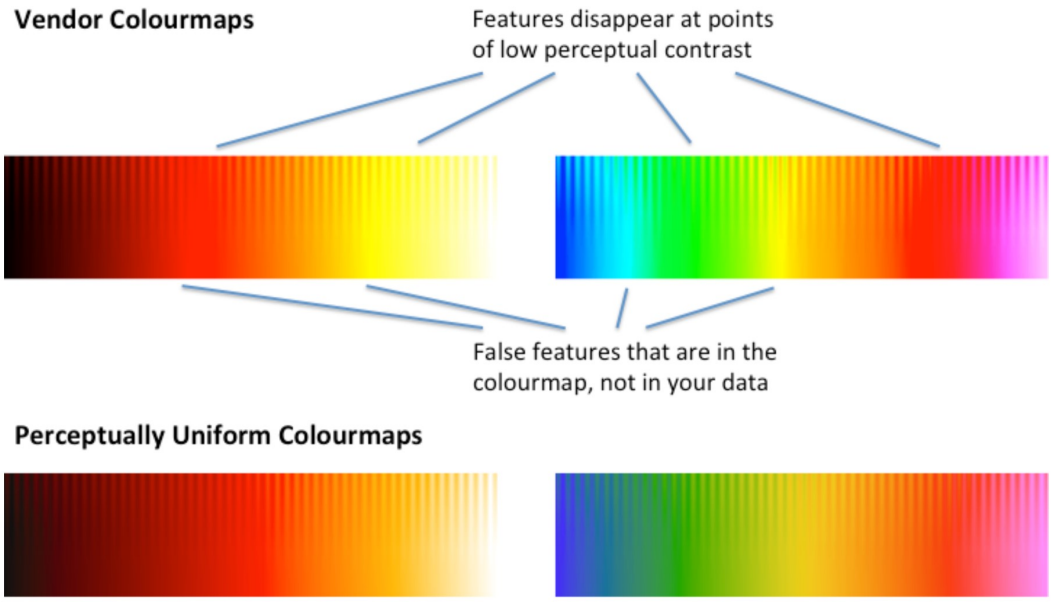

Figure 2.4: **Comparison of commonly used colour maps and perceptually uniform colour maps designed by Kovesi [53].** To show their differences they are shown on top of a sine wave gradient superimposed on a ramp function which provides a set of constant magnitude features presented at different offsets. High saturation regions such as red or green are blurred in the base colour maps but can be adjusted to have reduced intensity and higher perceptual uniformity in the modified maps. Image from Ref. [54]

This change is particularly relevant to spin direction visualisation as the data varies over a continuous range, leading to high likelihoods of similarly oriented groups of spins positioned closely to each other. As an example, consider a system in a low temperature regime being modelled using the Monte Carlo method explained earlier. Due to the low temperature, the most likely Monte Carlo trial move is the Gaussian move as spin flips and random movements occur when the system is higher in energy and are more likely to be rejected. This would lead to small spin deviations centred around the initial positions of the spins. Depending on the colour map used, deviations from the initial spin direction by as much as 10% can appear as the same colour as the initial direction leading to a simple misunderstanding of the generated results. Vortex configuration systems, such as permalloy [55], pose a significant issue as they are usually represented by a colour wheel which uses a high saturation continuous colour spectrum, susceptible to reduced colour perception.

To remedy this issue, where possible, any spin visualisation shown in this thesis is made using a perceptually uniform colour map which makes as clear as possible the difference in similar value spin orientations while making little

sacrifice in colour fidelity and visual appeal. A comparison of colour maps used in this work and common maps supplied by different vendors is shown in Figures 2.4 and 2.5.

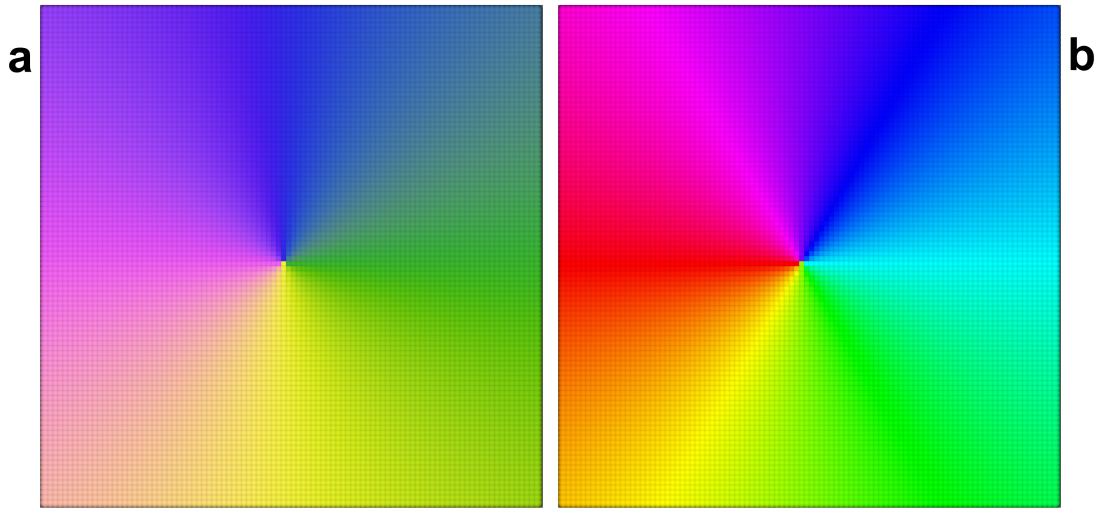

Figure 2.5: **Comparison of two cyclic colour maps.** (a) is a perceptually uniform colour map and (b) is the "HSV" colour map commonly used in Matlab [56]. (b) suffers from radial artefacts around the bright saturated areas while (a) has an almost uniformly smooth colour gradient except for small irregularities around blue.

Figure 2.5 was made in VAMPIRE. To create this, a synthetic system of 2D spins in a grid was created with all spins oriented perfectly along a circumference around the centre. To help with readability, the spins are represented as coloured spheres as opposed to arrows to fill in all white space. Figure 2.5(a) has a perceptually uniform colour map applied to the spin colour and shows a smooth gradient throughout the image with small artefacts on the edges of the blue area. 2.5(b) has a different cyclic colour map taken from the "HSV" map used in Matlab [56], which is made up of a linear increase of values in the RGB colour space, with no additional factoring in of human perception. In 2.5(b), radial artefacts extend from the centre of the image outwards in the pink, yellow and cyan areas which is mainly due to the high saturation in these areas which blurs the grid lines made by the spheres. The possible issues caused by the usage of non perceptually uniform colour maps is therefore twofold, being able to cause a loss of visual data by blurring high saturation areas, as well as causing visual artefact, which might at first appear as physical phenomena inside the studied material.

In addition to colour accuracy, several options have been added to VAMPIRE to help with image creation for both this work and future users of the software. Large systems pose a significant problem in visualisation due to the large amount

of memory and rendering time required for hundreds of millions of spins. To help with this, it is possible to ignore spins behind the outer layer of atoms, which are required for the simulation but can be effectively removed for visualisation purposes. In addition, sometimes it is only the spins on a cross section or within the block of simulated material that is of particular interest. With the latest changes, it is possible to cut a cross section of the system to reveal a plane of spins across any axis. Finally, the last option added to VAMPIRE POV-Ray visualisation is suited to ferri or antiferromagnetic materials as it can flip the colour of antiparallel spins. In antiferromagnetic materials, two competing sublattices show up in visualisation as antiparallel arrows in different colours. Due to the change in colour, the overall image exhibits a blurry quality as the two opposite colours are on adjacent spins. To remedy this, the usual arrow shape of the spins are conserved, making it obvious that the material is still antiferromagnetic, however the colours of one sublattice are swapped to match those opposing. This makes the overall direction of the spins more obvious, hence domains of spins oriented in slightly different directions can be more easily identified.

Almost all these additions have been used in creating visualisation for this thesis and are now implemented in the latest available versions of the VAMPIRE software package.

2.7 Conclusion

In this chapter we have discussed the fundamentals of atomistic spin models, simulation methods for finding both time-dependant and time-independent states of magnetic systems, and visualisation methods for better understanding our results. In the next chapter we shall apply these methods to magnetite, a well-known magnetic material, to better understand its magnetic properties in both bulk and nanoparticle form.

CHAPTER 3

MAGNETITE

3.1 Introduction

Magnetite is the oldest known magnetic substance, found in lodestones, it was the first major discovery of magnetism by ancient peoples. It is also the most magnetic of all the naturally occurring minerals on Earth. On its own, it does not ordinarily retain a permanent magnetisation, however with the inclusion of minerals such as ions of titanium and manganese, its coercivity rises enough to be a permanent magnet [57]. Pieces of magnetite were used in China as early as 300BC as compasses, and references to lodestones can be found in Greek texts such as "Theogony" by Hesiod, where the Titan Cronus was given a lump of magnetite instead of his son Zeus. In addition, the mineral was also broken down as a source for iron, which gave the first glimpse into the crystal structure of the material.

Magnetite is an iron oxide known as a ferrite, initially thought to be ferromagnetic such as plain iron. In a paper published in 1948, L. Néel showed that this was not the case and that there existed several distinct forms of magnetism, magnetite itself being ferrimagnetic [6]. Ferrimagnets were found to behave somewhat similarly to ferromagnets, both carrying a spontaneous magnetisation which disappears above a critical point, Figure 3.1. The magnetic properties of ferrites are a result of their complex crystal structures.

Ferrites can be divided into two major groups, also shown in Figure 3.2:

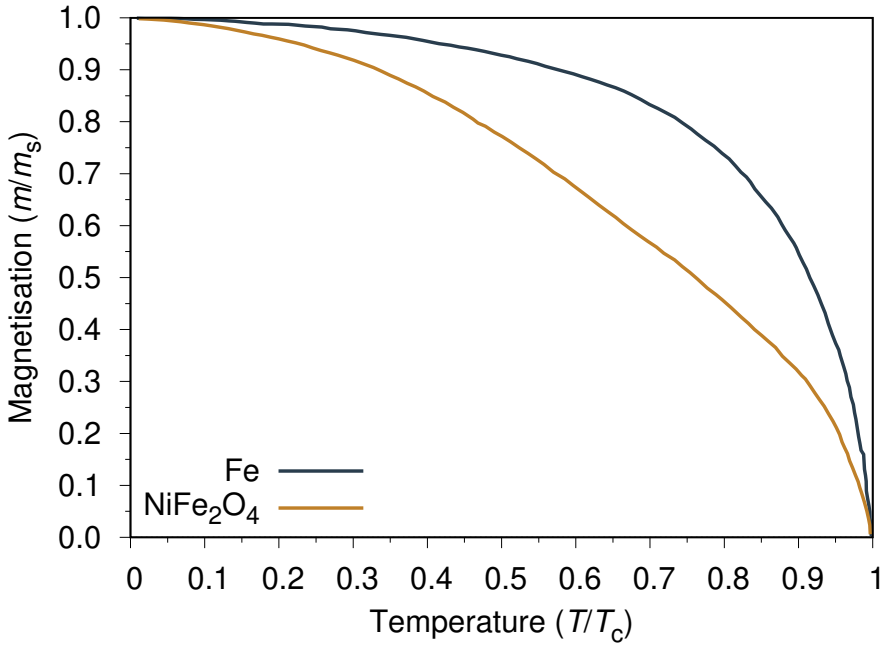

Figure 3.1: **Temperature dependence of magnetic properties of a typical ferrimagnet, $NiO{\cdot}Fe_2O_3$ [58].** The fractional magnetisation σ_0/σ_s decreases more quickly with higher temperature than that of iron.

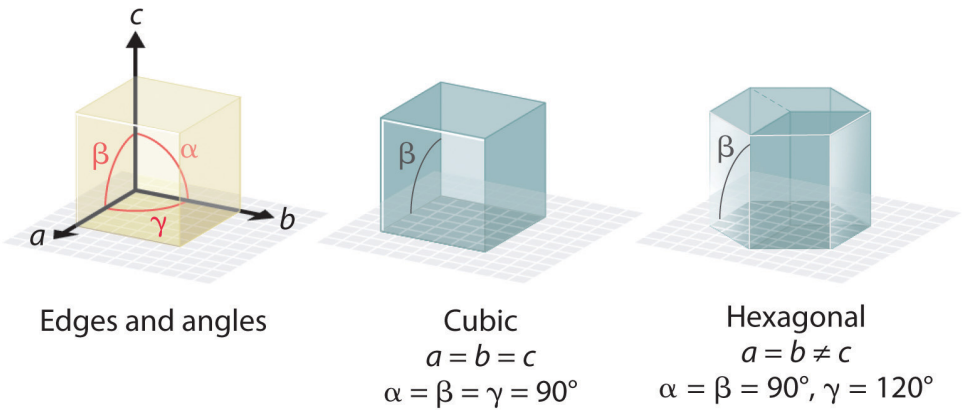

Figure 3.2: **The crystal lattices of ferrites.** Cubic lattices have sides of equal length with 90° angles between each side, while hexagonal lattices have a side of unequal length and angles $\alpha = \beta = 90°$, $\gamma = 120°$

1. Cubic ferrites have the general formula $MO{\cdot}Fe_2O_3$ where M is a divalent metal ion, like Co, Ni, Cu, Mn, Ti. These ferrites have high magnetic susceptibility and lower coercivity, and are classified as soft magnetic materials, often used as RF transformers due to their easily reversible magnetisation and low energy dissipation. A notable exception to this is Cobalt ferrite, often dubbed a semi-hard magnet due to its higher relative susceptibility

and magnetostriction.

2. Hexagonal ferrites are permanent magnets which do not demagnetise easily. The most common hard ferrites are strontium and barium ferrite which have seen use in recording media and general permanent magnet applications.

While the minerals found in these ferrites were often distinguishable, knowledge of the ionic and spin configuration was required to understand their magnetic properties. Oxygen O^{2-} ions are non-magnetic and the spin configuration of the metal ions can be understood using *Hund's rule*. This states that spins in a partially filled shell are arranged to produce the maximum spin unbalance consistent with the Pauli exclusion principle [59]. Applied to elements in the first transition series; the outermost shell is $3d$ and can contain 10 electrons, 5 spin up and 5 spin down. The first five will be of the same orientation, say spin up, while the sixth must be spin down due to the Pauli exclusion principle. Hence, an Fe^{2+} ion with 6 outer electrons will have a magnetic moment of $5-1=4\ \mu_B$. More magnetic moments can be found in Table 3.1.

Ions										Number of 3d Electrons	Spin-Only Moment in μ_B
Sc^{3+}	Ti^{4+}									0	0
	Ti^{3+}	V^{4+}								1	1
	Ti^{2+}	V^{3+}	Cr^{4+}							2	2
		V^{2+}	Cr^{3+}	Mn^{4+}						3	3
			Cr^{2+}	Mn^{3+}	Fe^{4+}					4	4
				Mn^{2+}	Fe^{3+}	Co^{4+}				5	5
					Fe^{2+}	Co^{3+}	Ni^{4+}			6	4
						Co^{2+}	Ni^{3+}			7	3
							Ni^{2+}			8	2
								Cu^{2+}		9	1
								Cu^{+}	Zn^{2+}	10	0

Table 3.1: **Spin-only moments of ions of first transition series**

Applying this to nickel ferrite, $NiO{\cdot}Fe_2O_3$, which contains one divalent nickel ion and two trivalent iron ions, with magnetic moments of 2 μ_B and 5 μ_B respectively. A parallel alignment of the spins as expected in a ferromagnetic arrangement would require a positive exchange force between the ions and results in a total of 12 μ_B per formula unit, however the measured saturation magnetisation σ_0 at 0 K is 56 Am^2/kg, which corresponds to 2.3 μ_B per formula unit. Hence the magnetic moments cannot be aligned parallel in this material.

This was noticed by Néel who assumed that distinct A and B sites in the material shared a negative exchange force, as in antiferromagnetic materials. The

A sites would be spontaneously magnetised in one direction, while those on the B sites would be opposite. The magnitudes of these spontaneous magnetisations would not be equal however, leading to a net magnetisation for the material.

3.2 Modelling Magnetite

3.2.1 Structure

The A and B sites postulated by Néel are a result of the structure of magnetite which we shall expand on here. Magnetite can be split into eight formula units, or $8 \times 7 = 56$ ions per unit cell. Large oxygen ions make up most of the unit cell and form a face-centred cubic arrangement. The metal ions occupy spaces in between the oxygen and form two distinct sites. A sites, or tetrahedral sites, are at the centre of a tetrahedron whose corners are made up of oxygen ions. Similarly, the B sites, or octahedral sites, are at the centre of an octahedral crystal symmetry site.

Multiplicity	Wyckoff Letter	Site Symmetry	Coordinates	
8	a	-43m	1/8,1/8,1/8)	(7/8,3/8,3/8)
8	b	-43m	(3/8,3/8,3/8)	(1/8,5/8,1/8)
16	c	.-3m	(0,0,0) (1/4,1/2,3/4)	(3/4,1/4,1/2) (1/2,3/4,1/4)
16	d	.-3m	(1/2,1/2,1/2) (3/4,0,1/4)	(1/4,3/4,0) (0,1/4,3/4)
32	e	.3	(x,x,x) (-x+1/4,x+1/2,-x+3/4) (x+3/4,x+1/4,-x+1/2) (x+1/4,-x+1/2,x+3/4)	(-x+3/4,-x+1/4,x+1/2) (x+1/2,-x+3/4,-x+1/4) (-x,-x,-x) (-x+1/2,x+3/4,x+1/4)
48	f	2.m m	(x,1/8,1/8) (1/8,x,1/8) (1/8,1/8,x) (7/8,x+1/4,3/8) (x+3/4,3/8,3/8) (7/8,3/8,-x+1/2)	(-x+3/4,1/8,5/8) (5/8,-x+3/4,1/8) (1/8,5/8,-x+3/4) (7/8,-x,7/8) (-x+1/2,7/8,3/8) (3/8,3/8,x+3/4)

Table 3.2: **Wyckoff positions for Fd-3m crystal structures**

Due to the complexity of the unit cell, we can divide it into eight octants. Four corners, shown in grey in 3.3c, contain the 16 octahedral sites 3.3b, while those shown in blue contain the 8 tetrahedral sites 3.3a. Figure 3.3d shows how these octants join together.

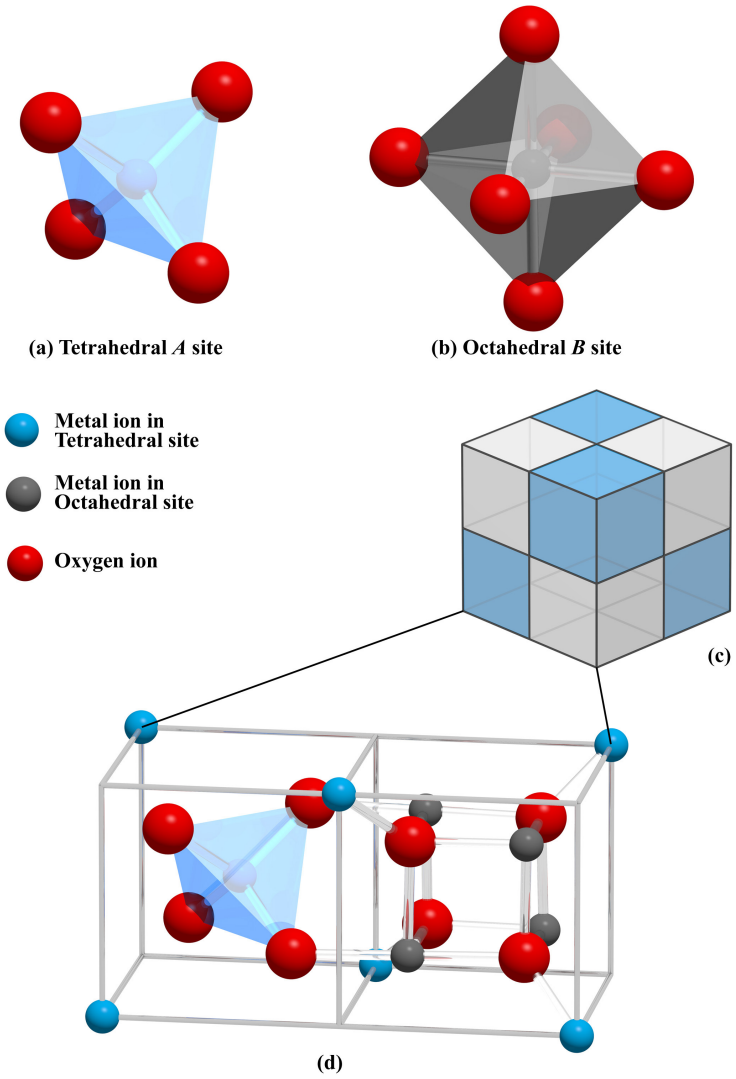

Figure 3.3: **Crystal Structure of cubic ferrites**. Atomic radii drawn roughly to scale, both iron ions are around half the radius of the oxygen ions.

Studies on various materials with similar crystal structures have shown that these sites are not unique and belong to cubic crystal structures of the family Fd-3m, known as spinels. Atomic sites are constrained to specific positions in these crystal groups and can be reconstructed using Wyckoff positions shown in Table 3.2. The Fd-3m group contains many positions, most of which are left unoccupied by the cubic ferrites, however through various studies over the 20th century and the usage of experimental techniques such as X-ray crystallography, we know that the 8a, 16d and 32e sites are occupied [60–62].

The Wyckoff positions can be used as fractional coordinates for atomic positions in a cubic ferrite unit cell. Here, the 8a sites refer to the eight tetrahedral positions, the 16d sites the octahedral positions and the 32e sites the oxygen ions. The 32e

sites are not given simply with coordinates but involve an additional parameter, x in Table 3.2. In oxide spinels, this is known as the oxygen positional parameter and is represented by the symbol u, rather than the more general x. u typically has a value close to 0.25 and varies between about 0.24 and 0.275 depending on the specific spinel being studied and its purity. At a value of 0.25, the anions form a perfect tetrahedral coordination about the 8a site and regular octahedra around the 16d sites. An increase in u reflects a displacement of oxygen ions in the [111] direction, causing the tetrahedral site to enlarge at the expense of the octahedral site. The bond lengths within these sites should remain the same. As the parameter u is tied to the bond lengths of the A and B sites or, put differently, to the ionic radii of the cations, we can work out a value for the parameter using the following formulas, where a is the lattice constant:

$$R_{\mathrm{Tet}} = a\sqrt{3\left(u - \frac{1}{8}\right)} \tag{3.1}$$

$$R_{\mathrm{Oct}} = a\sqrt{3u^2 - 2u + \frac{3}{8}} \tag{3.2}$$

	R_{Tet}	R_{Oct}
Fe^{2+}	0.615	0.74
Fe^{3+}	0.485	0.645
O^{2-}	1.38	1.38

Table 3.3: **Ionic radii (in Å) of divalent and trivalent iron as well as oxygen in spinels.** Data adapted from Ref. [63]

The ionic radii in spinel oxides have been studied by Shannon and Prewitt [64, 65] and revised by O'Neill and Navrotsky [63] to calculate the value of the oxygen positional parameters. The values relevant to magnetite are shown in Table 3.3. From this, the accepted value of u in magnetite is 0.2548.

The complete 56 atom unit cell of magnetite, including extra tetrahedral ions around the cell border, is shown in Figure 3.4. The tetrahedral and octahedral block are packed very closely together within the unit cell, with Figure 3.4 only showing the completed symmetries within the primitive unit cell. The lattice constant of magnetite above the Verwey transition is reported as 8.396 Å [9].

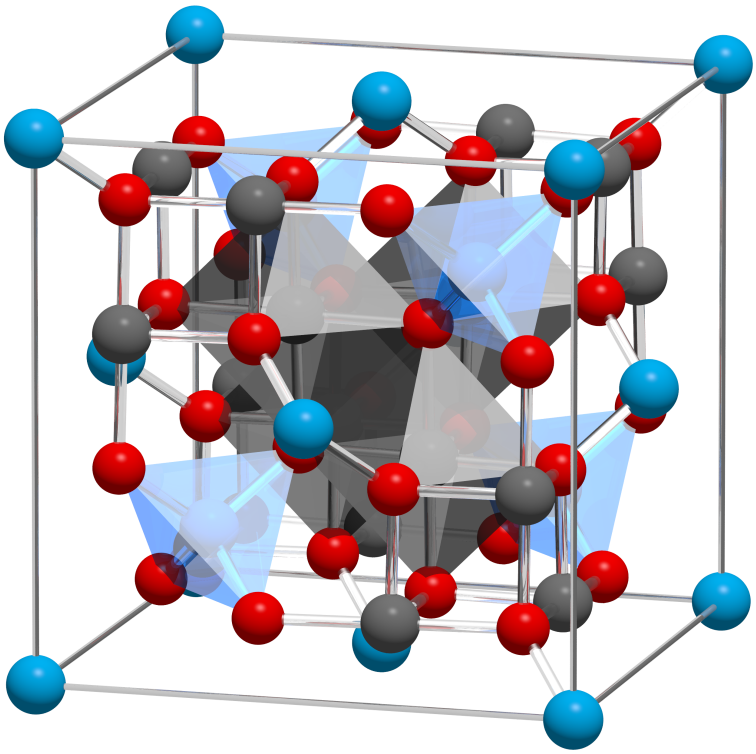

Figure 3.4: **Full unit cell of magnetite.** Tetrahedral iron ions are shown in blue, octahedral ions in grey and oxygen in red. Atomic radii not shown to scale. The glass bonds show the nearest neighbour interactions, and the tetrahedral and octahedral blocks are also shown to demonstrate their symmetry within the unit cell.

3.2.2 Cation Occupancy

The cations which take up the tetrahedral and octahedral sites vary for each spinel material. In the mineral spinel $MgAl_2O_4$ the Mg^{2+} ions are in the A sites while the Al^{3+} ions are all in the B sites. This is called the normal spinel with other examples of normal spinels being zinc and cadmium ferrite. Many other ferrites have the inverse spinel structure where the divalent atoms are on B sites and the trivalent ions are equally divided between A and B sites. Using parentheses and closed brackets to distinguish between the two sites, they can be generalised as $(B)[AB]O_4$. Magnetite, as well as other iron, cobalt and nickel ferrites are inverse spinels.

The two spinel types explained here should be regarded as extreme cases as many other spinel materials exist in between these two states, a random assortment of divalent and trivalent ion distributions can also occur. As the cation occupancy will affect the bond lengths of the A and B sites, the degree of inversion,

or the fraction of tetrahedral sites which are occupied by trivalent atoms also has a large effect on the oxygen positional parameter mentioned previously.

3.2.3 Phase Changes

Néel's paper [6] on ferrites prompted further studies into the magnetic properties of these materials however years earlier it was a paper written by Evert Verwey which began a still ongoing study into the electronic structure of magnetite [66]. In it he started with some of the assumptions we have so far covered concerning the mixed B site occupation of Fe^{2+} and Fe^{3+} ions;

"Fe_3O_4 has a very remarkable crystal structure involving a probably statistical distribution of both Fe^{2+} and Fe^{3+} ions at equivalent lattice points."

In this paper, Verwey examined a transition in the properties of magnetite around 120 K. He cited changes in the magnetic properties, specific heat and lattice constant of the material. This anomaly would come to be recognised as a first-order phase transition later named after Verwey. At 124 Kelvin, magnetite undergoes a structural change becoming monoclinic, the lattice parameters a, b, c are no longer equal and the angles are no longer all 90°. The exact causes for this transition are still heavily debated today [67], however they are related to the B site iron atoms. Initially, a purely ionic picture was assumed, postulating that conductivity occurred via the hopping of electrons on the octahedral sublattice ($Fe^{2+} - e^- \rightleftharpoons Fe^{3+}$). Below the Verwey transition, this electron exchange would be frozen out and with a long-range charge order established between the cations.

For the next 40-50 years since Verwey's paper, many studies were done on the transition to find whether it occurred over a single or multiple stages, as this was suggested by the existence of multiple peaks in the specific heat and could be a possible reason for the large changes in conductivity before and after the transition. Some of these issues would be resolved after a meeting in 1979 arranged by Sir Nevill Mott in Cambridge focusing on the transition. Studies done on magnetite after the meeting benefited hugely from some of the insight it gave on sample preparation. Researchers learned that only by carefully preparing high-quality single crystals could these questions be addressed. The Verwey transition is highly dependent on the quality of the system being studied and defects such as oxygen vacancies, or the existence of small quantities of maghemite, hematite or other impurities, as well as system shape and size, can affect the temperature or even existence of the transition. An excellent paper on the history of studies on the Verwey transition as well as developments up to 2002 was written by Walz

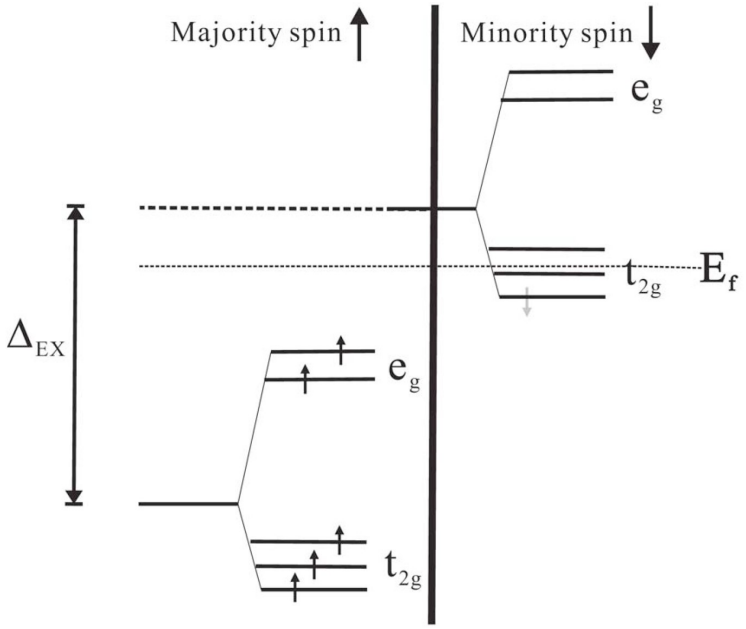

Figure 3.5: **Energy levels of the Fe_{oct} ions of magnetite.** The majority up spin band and minority down spin band are split by an exchange energy Δ_{EX}. For both Fe^{2+} and Fe^{3+} ions five electrons occupy the majority t_{2g} and e_g levels. The extra electron of the Fe^{2+} ion occupies the minority t_{2g} band, which is the only band located at E_f, giving rise to half-metallic behaviour. The high room temperature conductivity of magnetite is attributed to the hopping of this down electron between Fe_{oct} sites. Figure from Ref. [68]

[67].

Several theories have been proposed to explain the electrical properties of magnetite above the Verwey transition. One theory focuses on band conduction, where two octahedral iron atoms distribute their eleven d-electrons across two distinct bands, with ten spin-down electrons occupying a lower energy band and one electron in a higher energy band that crosses the Fermi level and is responsible for the metallic conduction (see Figure 3.5). This model does not suggest an increase in conductivity up to room temperature which is inconsistent with experimental data. Other models focus on small-polaron hopping i.e. slow moving electrons which distort the local lattice (small implying that the distortion is smaller than or equal to the lattice constant). Ihle and Lorenz [69, 70] have proposed that conductivity arises from a superposition of small-polaron band and small-polaron hopping mechanisms, which agrees better with experimental data.

In more recent years, researchers have turned to a Density functional theory (DFT) approach to study the electronic conductivity of magnetite. This is a computational quantum mechanical approach that is often used to investigate

the ground state of materials by taking advantage of the periodicity of the unit cell to simulate bulk properties. The computational cost of simulating a system of many interacting electrons is reduced by simulating an energetically equivalent system of non-interacting electrons in an external effective potential, such as the local-density approximation (LDA), which is based upon the exchange and correlation energy density in a uniform gas. Computational cost can be further reduced by dividing the total number of electrons, with which computational time scales, into inner electrons and valence electrons. Inner core electrons are strongly bound and do not play a significant role in chemical binding of atoms. Particularly in metals and semiconductors, these inner electrons screen the nucleus from the valence electrons and can therefore be approximated by using a pseudopotential which replaces the potential felt by the valence electrons.

Early DFT calculations, performed as early as 1984 [71], were used to calculate the band structure of magnetite however these calculations were not yet completely reliable due to the relative crudeness of approximations which had to be used at the time due to the lack of computational power [72]. The LDA is another problem for materials such as magnetite which have more strongly correlated electrons and is often remedied with the usage of a Hubbard-like term (which helps to approximate interacting particles). This approach is known as DFT+U. A summary of this method and its usage on magnetite is provided in Ref. [73].

The exact distinction between divalent and trivalent iron ions in the octahedral lattice remains a contentious issue however it is generally agreed that the high temperature phase of magnetite does not distinguish between them [74]. The oxidation states below the Verwey transition are often reported to vary between 2.4+ and 2.9+ [75].

3.2.4 Anisotropy

So far we have a clear understanding of the structure of magnetite, its unit cell atom positions and their occupation at various temperatures. Next, we shall cover the main forces which affect its magnetic properties. The anisotropy, here referring to the magnetocrystalline anisotropy, is intrinsic to the crystal and describes the magnetic properties of a material according to the direction its spins are aligned. In cubic crystals, there are three principal directions along which the spins can align, shown in Figure 3.6: the ⟨100⟩, ⟨110⟩ and ⟨111⟩ directions.

Different materials can be aligned along any of these directions however the

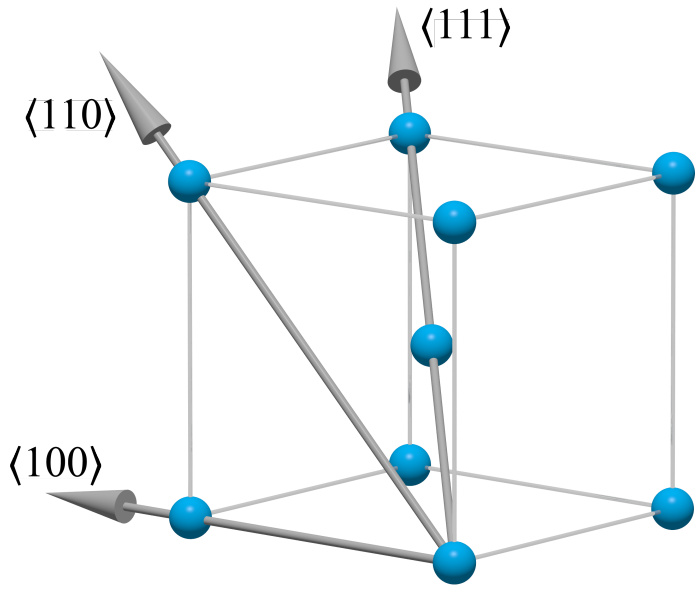

Figure 3.6: **Principal anisotropy directions in a body centred cubic crystal.** The bracket notation denotes a family of orientations along the symmetry of the system.

energy, or field, required to do this is different for each orientation and specific to each material. The directions are therefore referred to as easy, medium and hard axes depending on the field required to fully magnetise a material in that direction, from lowest energy required to highest, respectively. As an example, Figure 3.7 shows the field strength (in Oersteds) required to magnetise iron along each of the directions. Iron has an easy axis along the ⟨100⟩ direction, and only requires a few tens of Oersteds to be fully magnetised in this direction. This requirement is significantly increased to align iron along ⟨110⟩ or ⟨111⟩. In fact, the easy axis of a material describes the spin configuration in a demagnetised sample. The notation for ⟨100⟩ describes not only a spin orientation along the positive x-axis, but also along directions of the same symmetry i.e. [100], [010], [001], $[\bar{1}00]$, $[0\bar{1}0]$ and $[00\bar{1}]$. Hence in a demagnetised state, an iron disk cut along (001) will be made up of many small domains aligned in approximately equal proportion to the following four axes: [100], [010], $[\bar{1}00]$, $[0\bar{1}0]$.

Spins aligned along the easy axis require energy to move to a different axis, this is the energy barrier that must be overcome to move large domains of spins. Hence a crystal aligned along a hard axis is at a local minimum in energy, higher than the lowest, easy axis state. This energy is called the crystal anisotropy energy E and in 1929, a Russian physicist Akulov showed that it can be expressed in terms of a series expansion of the direction of cosines of M_s. Taking a, b, c as

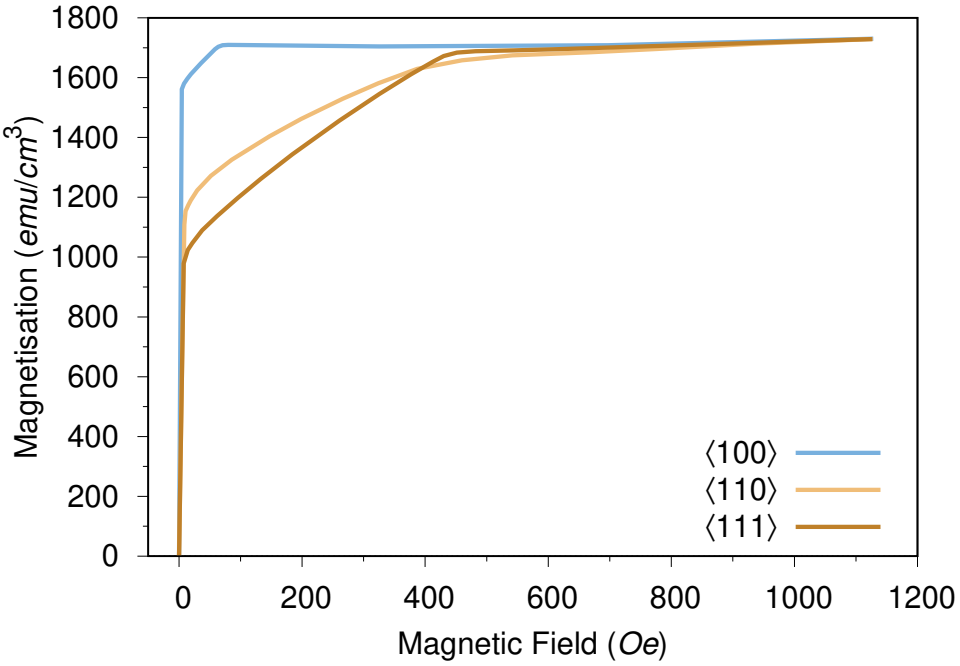

Figure 3.7: **Magnetisation curves for iron.** Iron requires only a few tens of Oersteds to reach the saturation magnetisation in the ⟨100⟩ direction, its easy axis, while hundreds of Oersteds are required to fully magnetise it along ⟨110⟩ or ⟨111⟩. Figure adapted from Ref. [58].

the angles M_s makes with the crystal axes and α, β, γ the cosines of these angles, called direction cosines. The energy is then:

$$E = K_0 + K_1(\alpha_1^2\alpha_2^2 + \alpha_2^2\alpha_3^2 + \alpha_3^2\alpha_1^2) + K_2(\alpha_1^2\alpha_2^2\alpha_3^2) + \ldots \tag{3.3}$$

where K_0, K_1, K_2 are constants for different materials and dependent on temperature. K_0 is independent of angle and often ignored as we are usually interested in changes in energy due to an M_s rotation. K_2 is also sometimes ignored as it is often much smaller than K_1.

In magnetite, the low temperature phase present a problem due to having different anisotropy constants K_1 and K_2. From Figure 3.8, we can see that as we approach the Verwey transition from room temperature, the constants begin to change in their behaviour and trend upwards to positive values. This does not fit well into Equation 3.3 which does not account for such a phase change. Thanks to the work done by Abe *et al.* however, we do have an indication of the anisotropy scaling at very low temperatures, which should correspond to magnetite in the room temperature spinel structure. Below the transition the anisotropy is strongly

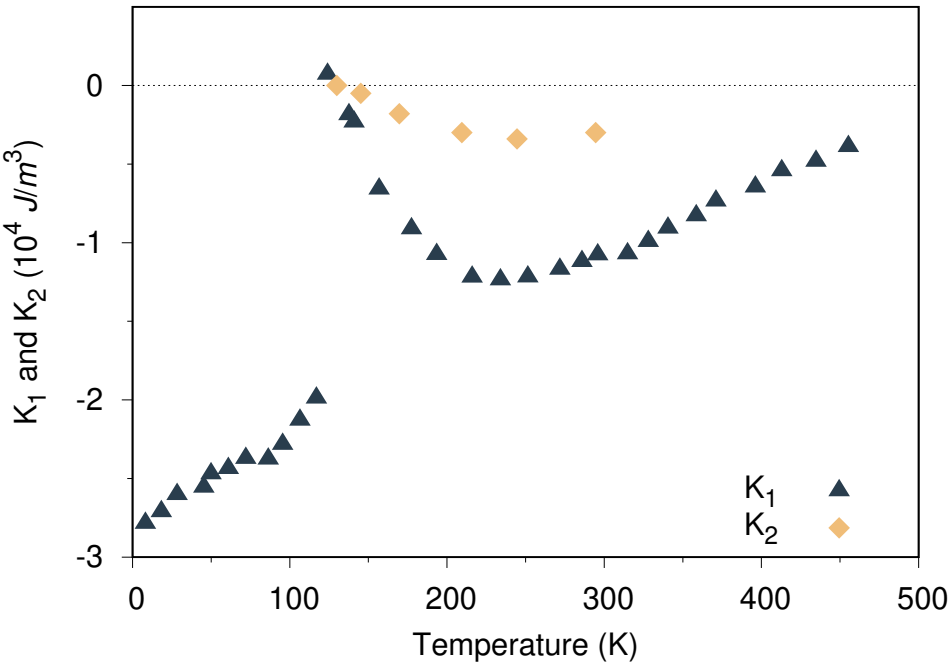

Figure 3.8: **Magnetite anisotropy constants variation with temperature.** These values change significantly below the Verwey temperature. K_1 data from Abe *et al.* [76], K_2 data from Kakol *et al.* [77].

negative [76], starting at around -2.8×10^4J/atom and, putting aside the phase transition, tends linearly upwards to 0 around 500 K.

To use the bulk cubic anisotropy values from Ref. [77], we need to convert them to atomistic magnetocrystalline anisotropies, k_u, according to the following Equation [30]:

$$k_u = \frac{K_u a^3}{n_{at}} \tag{3.4}$$

where K_u is the macroscopic anisotropy constant, a is the lattice constant and n_{at} is the number of magnetic atoms in the unit cell. For our simulations it would also be ideal to have a value for the anisotropy of each lattice. Due to the difference in ionic species and symmetry of the ions within the unit cell, the two lattices likely do not have the same anisotropy. Here we are therefore making an approximation by using the measured bulk anisotropy as an average of the contributions of the A and B sites.

3.2.5 Exchange

While the magnetocrystalline anisotropy has a significant effect on the overall spin directions of a material, its energy is much lower in magnitude to the exchange energies which interact between the individual spins of the system. Heisenberg described the quantum mechanical interaction by the Hamiltonian[1]:

$$\mathscr{H}_{\text{exc}} = -\sum_{i \neq j} J \hat{S}_i \cdot \hat{S}_j \tag{3.5}$$

where S_i and S_j are operators describing the localised spins on two adjacent atoms. J is an exchange constant, which has dimensions of energy (though often expressed in Kelvins by dividing it by the Boltzmann constant, k_B). An exchange constant $J > 0$ indicates a ferromagnetic interaction where spins tend to align parallel, while $J < 0$ indicates antiferromagnetic exchange where the spins align antiparallel.

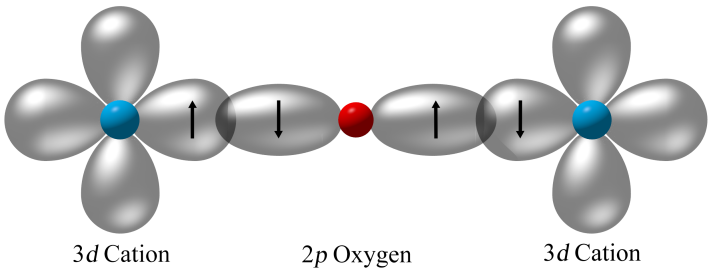

Figure 3.9: **Oxygen mediated superexchange.** Cations such as iron or manganese can undergo superexchange where the oxygen allows a spin up and spin down electron to be shared between the cations. This happens due to the hybridisation of the cation 3*d* shells and the oxygen 2*p* shells.

Exchange does not only occur between neighbours but can be mediated. This is the case in magnetite where the exchange is carried over the oxygen atoms between the cations. This is called superexchange and occurs due to the hybridisation of the 3*d* iron orbitals and the 2*p* oxygen orbitals. Figure 3.9 shows the overlap of the orbitals. The superexchange interaction J involves simultaneous virtual transfer of two electrons with the instantaneous formation of an excited state. The size of J depends on the interatomic distances and the bond angle. The Goodenough-Kanamori rules, reformulated by P. W. Anderson, provide a simple way to understand the classes of superexchange [78]:

[1] depending on convention, a constant of 2 is sometimes included in the equation, here it is factored into the exchange constant

1. When two cations have lobes of singly occupied $3d$ orbitals which point towards each other giving large overlap and hopping integrals, the exchange is strong and antiferromagnetic. This is the usual case, for 120-180° $M-O-M$ bonds.

2. When two cations have an overlap integral between singly occupied $3d$ orbitals which is zero by symmetry, the exchange is ferromagnetic and relatively weak. This is the case for about 90° $M-O-M$ bonds.

3. When two cations have an overlap between singly occupied $3d$ orbitals and empty or doubly occupied orbitals of the same type, the exchange is also ferromagnetic, and relatively weak.

In Figures 3.3 and 3.4, we can see the three different types of interactions in magnetite: Fe^{tet} - Fe^{tet} (Fe^{AA}), Fe^{oct} - Fe^{oct} (Fe^{BB}) and Fe^{tet} - Fe^{oct} (Fe^{AB}). These interactions have different bond lengths and angles however we can make some assumptions on their relative sizes and sign. The Fe^{AB} bonds correspond well to the first category presented by Anderson, they are between 120-180° degrees and expected to be antiferromagnetic, with negative exchange values. The Fe^{BB} bonds fall into the second category of bond types, they are weak ferromagnetic 90° bonds with positive exchange. Finally, the Fe^{AA} exchange is difficult to evaluate as the angles between the ions can vary depending on which ions are chosen. The bond length is larger than that of Fe^{AB} and Fe^{BB}, hence the strength of exchange should be relatively weak. The sign of exchange is also ambiguous however this interaction is likely antiferromagnetic (due to relative positions) and negative.

	J^{AA}	J^{BB}	J^{AB}
Uhl and Siberchicot [28]	-0.11	+0.63	-2.92
Néel [79]	-1.50	+0.04	-2.00
Glasser and Milford [80]	0	+0.24	-2.40
Möglestue [81]	-1.52	+0.31	-2.42

Table 3.4: **Calculated and experimental values of nearest-neighbour exchange constants in Fe_3O_4.** All values in units of meV. Adapted from Ref. [28]

A first-principles study of exchange integrals in magnetite was carried out by Uhl and Siberchicot [28]. In this paper they find the exchange integrals using spin-spiral configurations to calculate the spin-wave spectrum. Table 3.4 shows their results, as well as other theoretical and experimental values from previous papers. We can see some similarities between the values: the Fe^{AB} interactions are antiferromagnetic and the largest, as expected from Anderson's description.

The Fe^{BB} interactions are much smaller, with most values given being an order of magnitude lower than the Fe^{AB} interactions. The Fe^{AA} interactions present the largest variance as the results of Néel and Möglestue suggest they are close to the Fe^{AB} interactions in magnitude. The results presented by Uhl and Siberchicot are most commonly found in the literature and generally regarded as accurate, hence we shall be using these values as a starting point for our calculations.

3.3 Simulating Magnetite

Magnetite is the first material we consider in this thesis. The aim is to understand the data produced, keeping in mind our initial assumptions and the properties discussed in the previous chapter. As this work is being done using the VAMPIRE simulation package, we have unprecedented access to single spin level data which is still rare to see in current research papers. At the same time, we shall still be able to compare micromagnetic level behaviour to similar theoretical works which studied this material [20, 21, 82] as well as the experimental data for the overall system properties such as the Curie temperature.

3.3.1 First Simulation

We can simulate a small system with periodic boundary conditions (PBCs) to approach bulk properties. To recap some of the system parameters we have discussed in this chapter:

- The system is cubic with a lattice constant of $a = 8.397$Å
- There are three unique materials:
  - Tetrahedral site iron 3+ ions with spin moment 5 μ_B
  - Octahedral iron ions in a mixed 2.5+ state with spin moment 4.5 μ_B
  - Non-magnetic oxygen 2- ions
- The anisotropy direction is $\langle \bar{1}\bar{1}\bar{1} \rangle$, with a negative anisotropy constant.
- The exchange interaction values (in meV) are $J^{AA} = -0.11$, $J^{BB} = 0.63$ and $J^{AB} = -2.92$.

As a first simulation we can find the equilibrated magnetisation of a PBC particle. To keep simulation time low, we shall use a system of around 8 nm width

or 10 times the lattice constant. As we are creating an initial fixed system with spins perfectly oriented in the ⟨111⟩ direction, we expect to see small change in the magnetisation over the equilibration, however to make sure the system is in a relaxed state, the value must converge over a significant number of time steps. We first look at the normalised values for the spin x, y and z component.

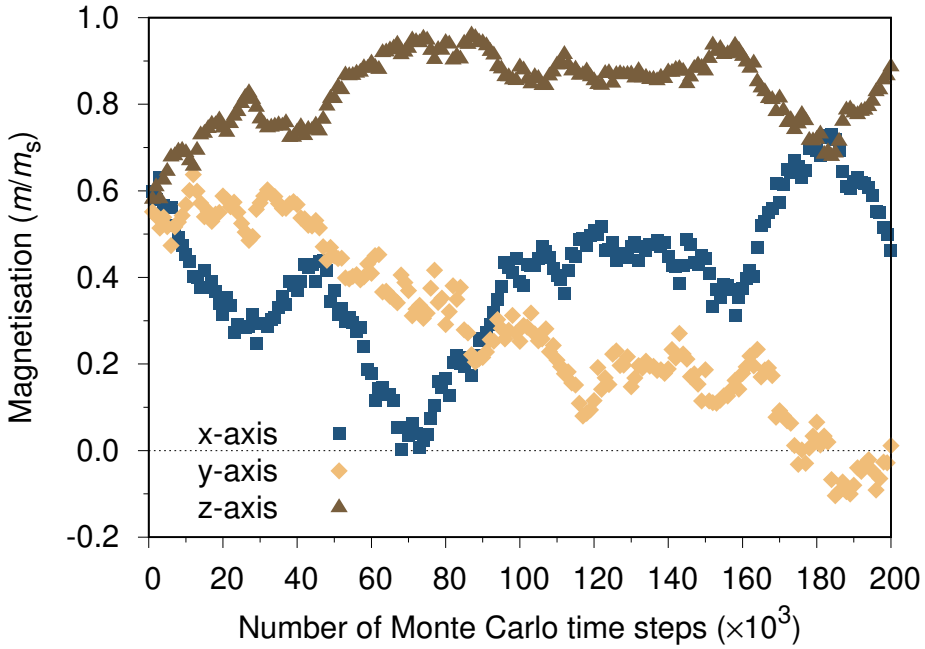

Figure 3.10: **Unit vector magnetisation for a periodic boundary condition magnetite particle.** It is difficult to tell the overall spin orientation of the system or the overall magnetisation.

In Figure 3.10, the x, y and z components of each spin is averaged out resulting in continuous but erratic behaviour. There are several possible reasons for this: the spins could have enough energy to rotate relatively freely and are not bound by the material anisotropy; the spins have enough energy to move out of the easy axis and access the medium and hard axes; or the spins have low energy and move only between the 8 easy axis directions [111], [$\bar{1}$11], [1$\bar{1}$1], [11$\bar{1}$], [$\bar{1}\bar{1}$1], [$\bar{1}$1$\bar{1}$], [1$\bar{1}\bar{1}$], [$\bar{1}\bar{1}\bar{1}$] will still be common. We can output the spin configuration from VAMPIRE at the end of the simulation to analyse the spin components in more detail.

By looking at each spin direction, we can tally the number of spins aligned with the ⟨111⟩, ⟨110⟩ and ⟨100⟩ directions. To allow for small movements due to thermal effects, we say that all spins lying within 15° of an axis are aligned with it. As the number of directions for each axis are different (for example, there are only 6 ⟨100⟩ directions compared to 12 ⟨110⟩) we also divide by the relative area. Figure 3.11 shows this data against system temperature. At 0K, the spins

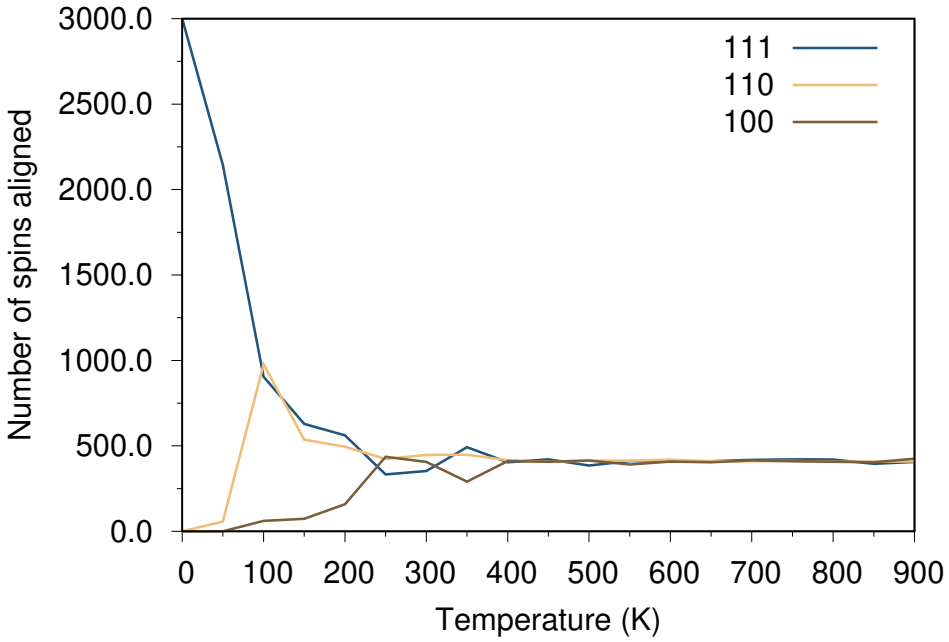

Figure 3.11: **Fe_3O_4 spin orientation vs temperature.** Spins within 15° of the anisotropy axes against system temperature. Above around 200 K the anisotropy energy is overcome completely and the spins are no longer bound to these axes.

are fully aligned along the ⟨111⟩ axis, $\frac{2}{3}$ along [111] and $\frac{1}{3}$ along $[\bar{1}\bar{1}\bar{1}]$. Below 50 K there isn't enough energy to move a significant number of spins off the easy axis. Here the spins only transition between ⟨111⟩ directions. As the temperature increases, the spins start to explore higher energy directions and very quickly, by around 300K, are no longer bound by the system anisotropy. This is expected as the exchange dominates the magnetic properties of magnetite which has a relatively low anisotropy.

Hence the room temperature system has more than enough energy to allow spins to move relatively freely. The system should however still be magnetised, or have an overall non-zero magnetisation, as it is far below the Curie temperature of magnetite. To see this we need to look at the normalised magnetisation:

$$|m| = \frac{|\sum_i \mu_i S_i|}{\sum \mu_i} \tag{3.6}$$

These are calculated as the normalised sum of the components multiplied by their moments, with units $m = M/M_s$. The overall system magnetisation will give a better idea of how strongly the system is magnetised at higher temperatures.

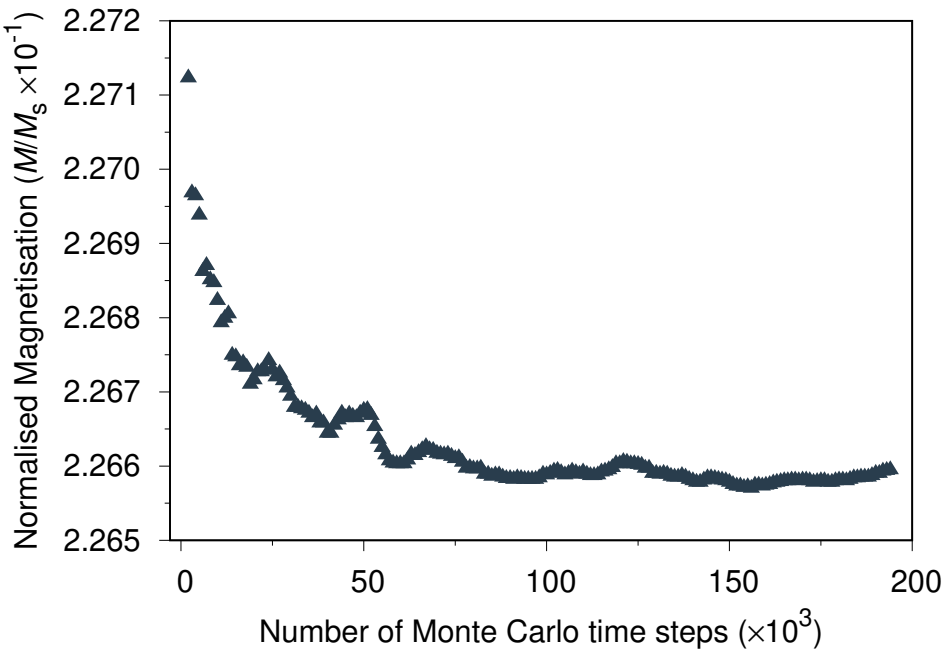

Figure 3.12: **Convergence of magnetisation for a periodic boundary condition magnetite particle.** After 10^5 steps, the magnetisation is already close to convergence at around $0.2266m$.

Figure 3.12 shows the normalised magnetisation against Monte Carlo time steps. As explained in Chapter 2, at each time step, a single spin is moved; either a spin flip, a random direction or a Gaussian perturbation. For output clarity and I/O performance, the magnetisation value is recorded every 1000 time steps and for the first recorded data point (not shown in Figure 3.12) the magnetisation is slightly higher at $0.2279m$. This quickly lowers over 50×10^3 steps to around $0.2266m$ where the magnetisation is close to converged. Hence in spite of the large changes in average x,y and z components of the spins, the overall magnetisation of the system after reaching equilibrium has only changed by 0.1% from its initial configuration.

It is important to note that Figures 3.12 and 3.10 do not show a realistic physical relaxation over a fixed time as they do not involve time-dependent dynamics. Rather, they are calculated from a statistical Monte Carlo simulation over a number of time steps. In practice, to make sure the magnetisation is converged, a simulation is normally run for around a million time steps in total. For this example, the end magnetisation hovered around 0.22618 to $0.22621m$.

The number of steps required for convergence is important for several reasons: first the system can reach a local energy minimum which is higher than the

global i.e. the spin configuration is not completely relaxed. This can occur if the system is first heated enough to allow spins to explore non ⟨111⟩ directions with a higher probability, and then cooled slowly to allow it to relax along a medium or hard anisotropy axis such as ⟨100⟩. The second reason is for computational efficiency. An 8 nm system equilibrium simulation with PBCs is small enough to require only 2 hours of simulation however larger simulations will require more time to compute and possibly more time to converge and will therefore take exponentially longer times for increasing system sizes. It is important to minimise wasted simulation time to not take up excess computational resources.

While the number of steps to convergence for the last simulation is verified, it cannot be assumed to be the same for other temperatures. The Monte Carlo method requires spin moves to be accepted and rejected based on current temperature, hence low temperature simulations close to 0 K will have a significantly larger number of rejected moves while high temperature simulations around the Curie temperature will have a larger number of accepted moves and will take longer to converge to constant magnetisation. Figure 3.13 shows the comparison between a system relaxing at 10 K versus a system at 850 K. At 10 K, the magnetisation value changes by very small amounts (around $10^{-5}m$) while at 850 K the magnetisation relaxes from $5.6m$ to $4.4m$.

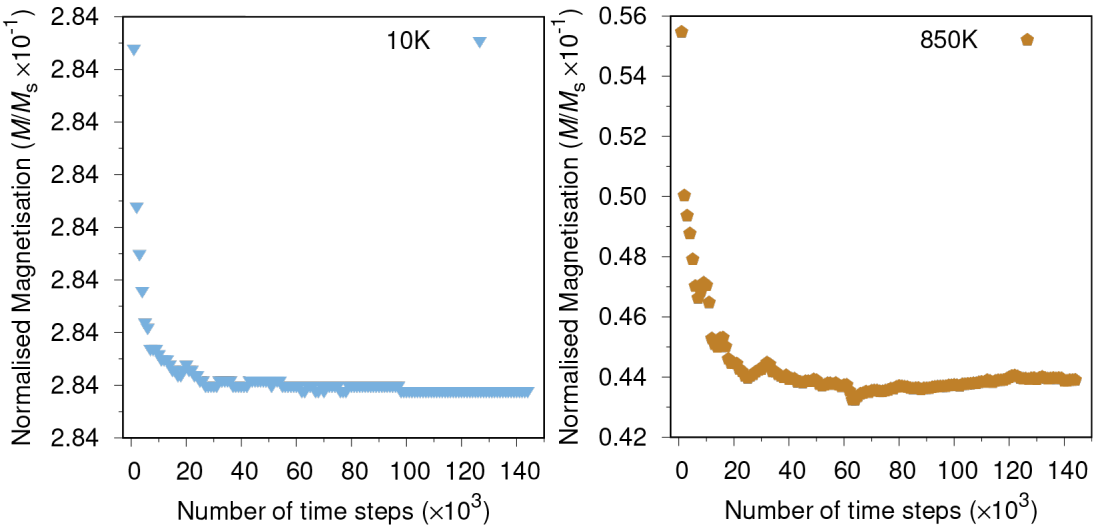

Figure 3.13: **Fe_3O_4 magnetisation at 10 and 850K.** Low temperature equilibration simulations relax quickly to constant values of magnetisation as most spin movements are rejected. At very high temperatures, the magnetisation does not converge as quickly and fluctuates due to constant spin reorientation.

We conclude that around 200k time steps will achieve a reasonable level of magnetisation convergence for all temperatures. Where possible, such as for

system sizes lower than 12 nm, a minimum of 1 million time steps can be used for high quality data with relatively minimal time loss.

3.4 Magnetisation Curves

One of the best ways to verify the validity of our simulation is to study the Curie temperature predicted. We have shown that we are able to relax a magnetite system to a stable state using a Monte Carlo method. Next, we can perform multiple of these simulations to find the relaxed magnetisation values at different temperatures, in particular around the Curie point of magnetite, at 858 K [58]. There are several ways to go about this; one would be to simulate magnetite starting at 0 K and increasing the temperature slowly to make sure the system has relaxed after each temperature increment. In this case, the start and end point of each temperature change is a realistic relaxed state and linked to the next as the simulation is continuous. It is also possible to extract the same data by running many separate simulations starting at a high energy state with a fixed temperature and allowing the system to relax at that temperature. While the simulation starting points will likely be relatively unphysical, given enough Monte Carlo spin movements, the final relaxed state should be the same. There are various reasons to use each method however as we are only interested in the end points of each temperature step, each method is valid. If the Monte Carlo method employed can only be run single threaded (most Monte Carlo methods run in serial as it can be difficult to validate parallel methods), then it is usually faster to use the latter method as each temperature can be run as a separate simulation and therefore the workload can be parallelized over many computational cores.

Figure 3.14 shows the magnetisation curve for a 6 nm magnetite system with periodic boundary conditions. The data for this plot is made up of magnetisation points at 10 K intervals. While each data point came from a separate simulation, the plot appears perfectly continuous due to being fully relaxed. At zero Kelvin we expect the system to be fully magnetised, and this is indeed the case even though the initial magnetisation is around $0.3m$. Magnetite is made up of two antiparallel sublattices initialised in the [111] and $[\bar{1}\bar{1}\bar{1}]$ directions. It does not start at exactly $3.33m$ as these sublattices are made of different cations with slightly different moments. Due to the way we calculate the normalised magnetisation (Equation 3.5) these moments are used to calculate the overall magnetisation.

Between 0-800 K the system increases in energy but maintains a magnetised state. The spins are able to explore most directions as they are not bound by

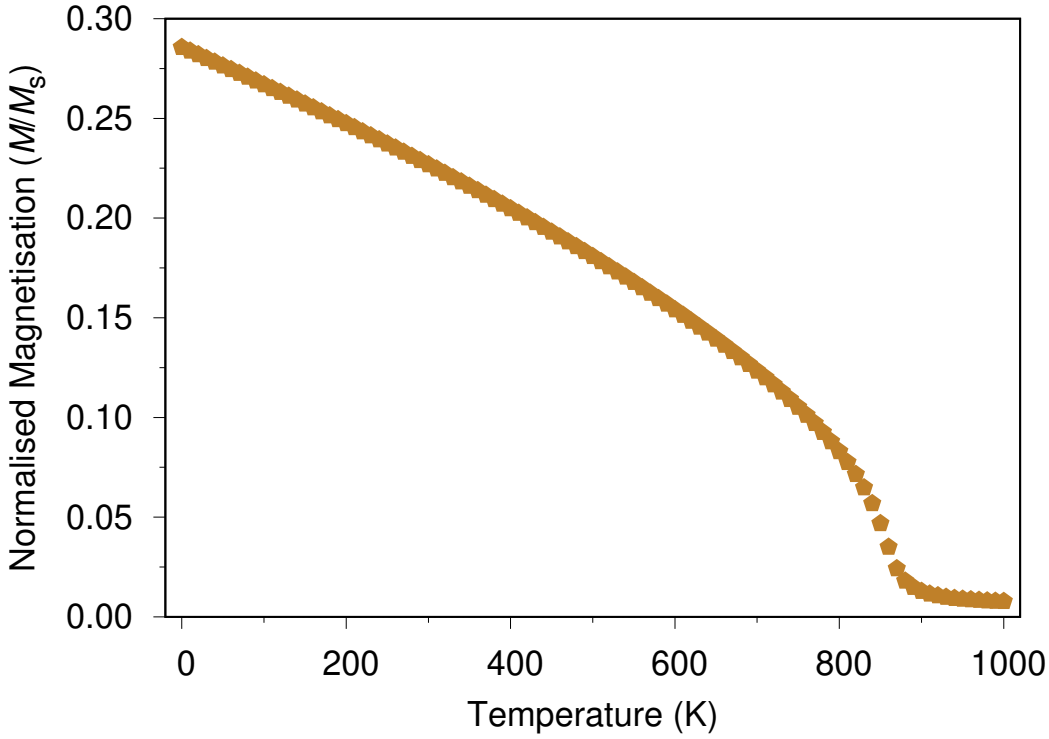

Figure 3.14: **Magnetisation vs temperature for a 6 nm PBC system.** At 0 K the system is fully magnetised and lowers in magnetisation as the temperature increases until the Curie point is reached around 860 K. Here the magnetisation is close to zero and the system is in a paramagnetic state.

the material anisotropy above around 200 K however they maintain an overall direction. As the energy increases this becomes less likely as the spins are more likely to make larger orientation changes until the system reaches the Curie point. Here the system should be fully demagnetised however according to Figure 3.14 it never reaches exactly 0 magnetisation. This is most likely linked to the periodic boundary conditions: in a periodic system the spins repeat over a regular distance, in this case 6 nm or around 7 unit cell lengths, hence there is increased correlation in the spins. If the boundary distance is small, the correlation increases as the spins affect each other more easily, while if the boundary distance is large this effect should be minimal. Due to a statistical effect proportional to the number of atoms in the system, we also expect the magnetisation to never reach exactly 0 K as the spins must be oriented perfectly randomly or conversely in a highly ordered and antiparallel manner to exactly cancel each other out. At all times it is likely that there is a small remnant magnetisation ($\leq 0.05m$) for systems less than 50 nm diameter. This value disappears slowly as the system tends to a bulk state.

While preliminary theoretical investigations of the saturation magnetisation scaling with temperature suggested that a discontinuity occurs at the Curie temperature [58], it is now known that the transition from ferro/ferrimagnetic to paramagnetic occurs gradually. This gives rise to two possible Curie points, T_C and T_p, shown in Figure 3.15. T_p is usually defined as the point where the magnetisation reaches zero however as this does not occur for small systems, it can instead be defined as the point where the magnetisation reaches a constant (or near constant) value. T_C is instead found by extrapolating the magnetisation below the critical point and finding its intersection with the x-axis. This value also coincides with the point at which the experimentally attained susceptibility goes to infinity, or where $1/\chi_{exp} = 0$. This Curie point is what we shall refer to as the Curie temperature going forwards. The gradual transition to a paramagnetic state is attributed to spin clusters, small groups of atoms, which retain parallel spins over a small temperature range above T_C. These small domains exist within the overall disordered spin structure and gradually disappear as the temperature is increased. This contrasts with the long-range spin ordering which exists below T_C and is measured as the spontaneous magnetisation.

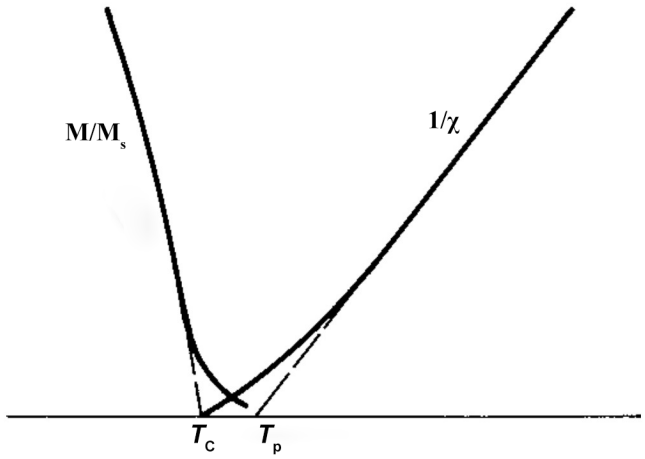

Figure 3.15: **T_C and T_p points.** The two types of Curie points are usually 10-30 K apart, with T_C being extrapolated from the magnetisation before the phase change and T_p usually being the point where the magnetisation equals zero. Figure adapted from Ref. [58]

The magnetisation scaling data can be used to test the modelling methods we have used so far. Here we have so far employed the Monte Carlo method to find the equilibrium state of the system at all temperatures. We can also use the LLG to test the same end point. The LLG (as it is implemented in VAMPIRE using the Heun integration scheme and Langevin dynamics) should simulate the time-dependent relaxation of the system and while we are not yet interested in

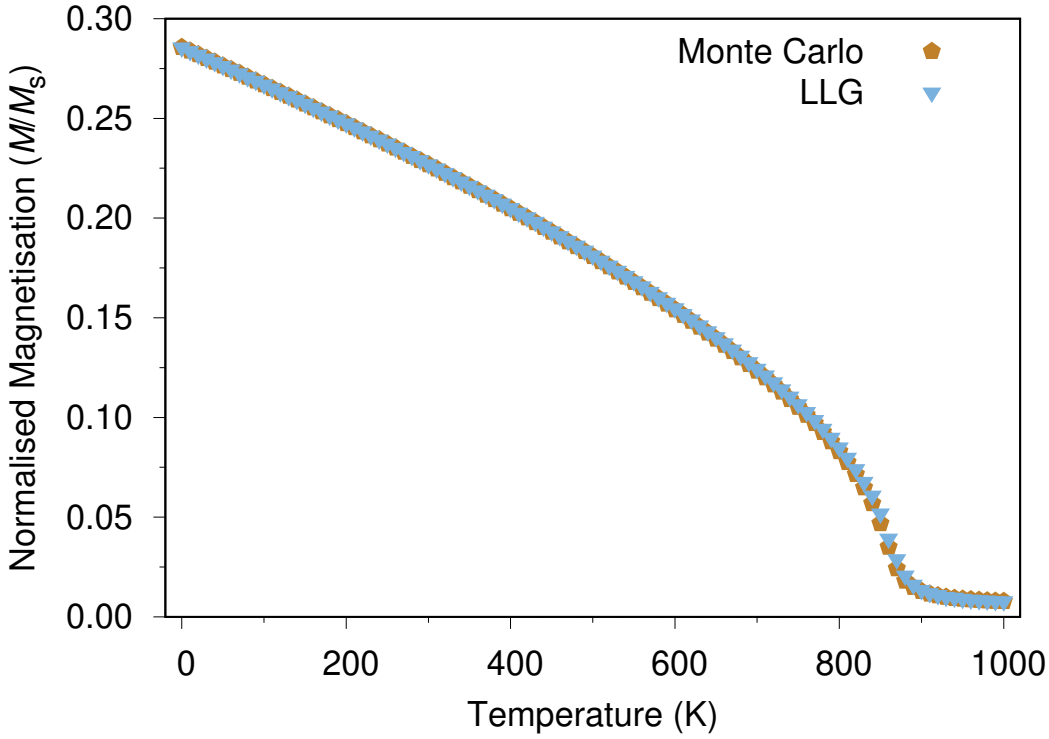

Figure 3.16: **Magnetisation vs temperature for a 6 nm PBC system done using a Monte Carlo method and LLG integration.** Both sets of data agree well and are fully converged. The LLG method requires more time steps to fully relax around the system Curie temperature.

the dynamics as the material cools, the end point should be very close to the data we achieved with the MC method.

The LLG method employed by VAMPIRE uses Langevin dynamics to simulate materials at non-zero temperatures. Thermal fluctuations are modelled as a Gaussian noise function proportional to the system temperature. Because of this data around the Curie point of the system is prone to errors and must be given extra time to converge. Figure 3.16 shows the previous data compared with one done using the LLG. We can see that the two data sets agree well with each other with minimal differences in the low temperature range where $T << T_C$ and in the high temperature range where $T >> T_C$. Around the Curie temperature the two plots diverge very slightly due to the small errors around the Curie temperature using the LLG. The data points around the Curie temperature were allowed to converge for ten times longer than the points outside this range and the percentage difference between the Monte Carlo data and the LLG reduced significantly however this can still be further improved. Nonetheless we are satisfied with the accuracy of both methods using the current chosen parameters

and they already agree well with each other.

3.4.1 Spin visualisation

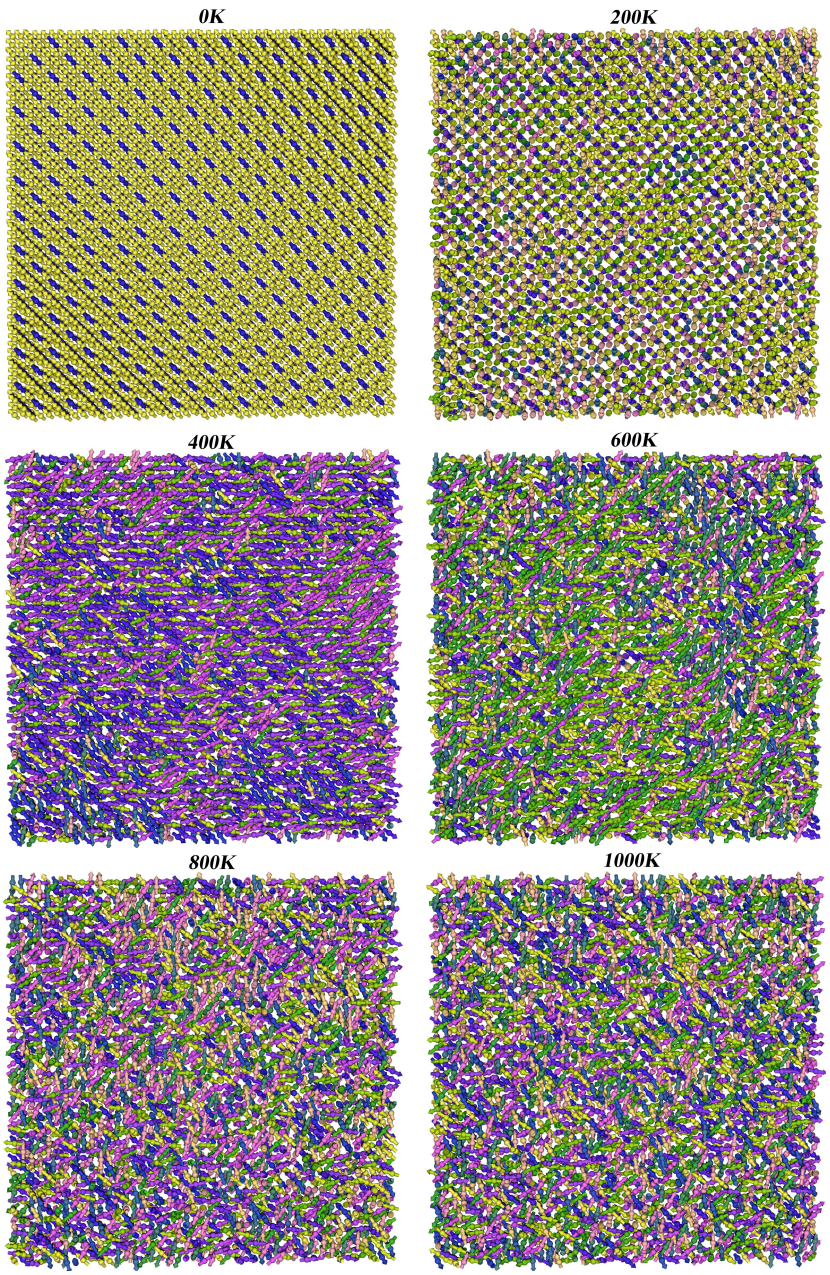

Figure 3.17: **Visualisation of the spin behaviour with increasing temperature.** The spins transition from fully to partially ordered as temperature increased towards T_C. After the critical point the system is paramagnetic, and the spins are randomly oriented.

Figure 3.17 shows a graphical representation of the spins in an 8 nm PBC system of magnetite. The non-magnetic oxygen atoms have been removed leaving only the iron ions. In addition, the system is pruned to show only a thin slice

of the fully simulated material for visual clarity. These images were the result of Monte Carlo simulations used to find the equilibrated state of magnetite at various temperatures.

Starting at 0K, the system starts fully magnetised with each sublattice oriented along the easy axis. Here, yellow spins point along the positive axis, while blue spins are negative. The bright green and magenta coloured spins are oriented perpendicular to these and transitional colours are used in between.

Due to the lack of thermal energy, spins are essentially locked into the easy axis orientation for temperatures close to 0 K. With a significant increase to thermal energy, at 200 K, the spins start to move out of their initial orientation, which can be seen from the new spin colours which deviate from the 0 K yellow and blue.

In spite of the new spin orientations in the system, a long-range ordering occurs over the whole system as it is still magnetised below its Curie temperature. The 400 and 600 K images show that many spins reorient into the ⟨100⟩ axis and there is still a clear distinction between spins on the tetrahedral and octahedral axes which remain mostly antiparallel. At 600 K this is slightly less clear as small, localised, clusters of spins become oriented randomly.

At 800 K it is difficult to visually discern a long range ordering of the spins. The system is only 50 K below the Curie temperature and the transition to a paramagnetic state has begun. Somewhat opposite to the 400 K image, it is possible to spot clusters of aligned spins indicating that the system remains slightly magnetised. Finally at 1000 K the system has passed T_{C} and is fully demagnetised. The distribution of colours in the visualisation is roughly equal as there is no overall spin direction and any spin orientation is allowed.

3.4.2 Sublattice Magnetisation

Earlier in the chapter we looked at the spin direction values of the system on a single spin level. Another method we can use to more closely examine the physical properties of our system is to look at the individual sublattices of magnetite. VAMPIRE is able to output material based properties of the system, such as the material magnetisation, and since these materials are distinct, not just in number but also spin moment and exchange, it is worth looking at differences in their magnetic properties. The overall magnetic properties of the system are a symptom of these smaller scale properties and while most experimental data

is only able to study the overall scaling, we can instead extract data for the individual sublattices.

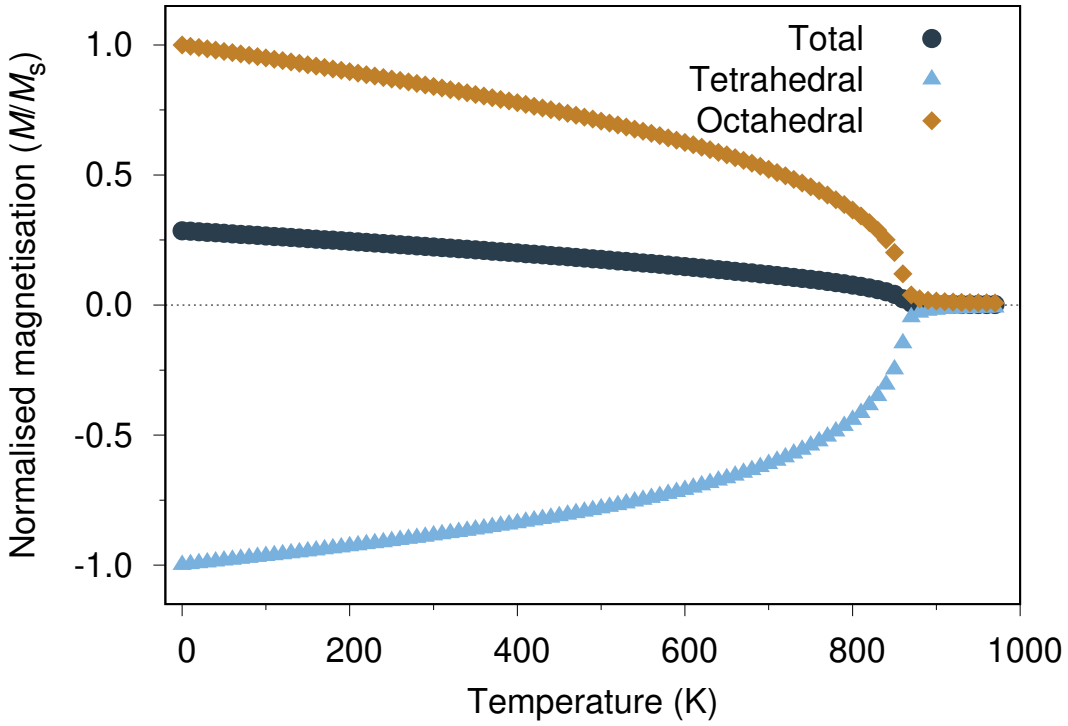

Figure 3.18: **Fe_3O_4 sublattice magnetisation.** Magnetisation vs temperature for a PBC system showing the overall magnetisation as well as the individual sublattice magnetisations, normalised independently. The sublattices start fully magnetised in their respective directions. The overall magnetisation is a result of the $\frac{2}{3}$ octahedral and $\frac{1}{3}$ tetrahedral contributions.

The octahedral sublattice of magnetite, composed of a mixed valence state of $Fe^{2.5+}$ ions makes up two thirds of the total magnetic atoms in the system and is initialised in the [111] direction, while the tetrahedral sublattice, containing only Fe^{3+} atoms makes up the remaining third and is initialised in the opposite $[\bar{1}\bar{1}\bar{1}]$ direction.

As we look at magnetisation values for each sublattice individually, they start at 0 K fully magnetised in their respective directions, shown in Figure 3.18. This shows more clearly the difference in magnetisation of the sublattices to the much weaker overall system. With increasing temperature the system demagnetises at seemingly the same rate for all components until the Curie temperature. Here it is difficult to assess exactly where each material reaches T_C, whether this is the same for the overall system and the sublattices, as the values cannot easily be discerned by eye. A fitting method is required to check the Curie temperatures

of the various components as it is a non-trivial question whether the T_C point should be the same.

3.5 Calculating the Curie Temperature

The Curie point of magnetite has already been mentioned several times as the temperature region around 850 K. Figure 3.18 clearly shows the system tending to a demagnetised state in this region and we have already suggested a reason for the magnetisation never reaching exactly 0 K. The value of T_C is mainly dictated by the exchange interaction values of magnetite however it can deviate from the bulk value for various reasons including material imperfections, surface defects and system shape. In ideal conditions bulk magnetite has a Curie temperature of 858 K [58] however our current model employs PBC and will not necessarily produce the same value. We need to find an appropriate method for extracting the Curie temperature of our system to better understand how parameter changes such as system size and shape will affect the system.

The temperature dependence of magnetisation at low temperatures can be approximated using Bloch's law [83]:

$$M(T) = M(0)\left(1 - \tau^{\frac{3}{2}}\right) \tag{3.7}$$

Here $M(0)$ is the spontaneous magnetisation at 0 K and $\tau = T/T_C$. Alone this equation does not approximate well the magnetisation around the critical point [84] where:

$$M(T) \propto (T_C - T)^{\beta} \tag{3.8}$$

Hence we use an interpolation of equations 3.7 and 3.8 to form the Curie-Bloch equation:

$$M(\tau) = \left(1 - \tau^{\alpha}\right)^{\beta} \tag{3.9}$$

where α is an empirical constant, here equal to 1 as we are modelling classical physics. The parameter β is a critical exponent related to the Curie temperature of the system [85] and often linked to a universality class which suggests that the value of the exponent changes only with the model used (such as Heisenberg

or Ising) [42, 86] and macroscopic parameters such as system dimensions. While this fitting method is very commonly used for the temperature dependence of the magnetisation, other fitting models are also used such as one developed by Kuz'min [87]:

$$M(\tau) = \left(1 - s\tau^{\frac{3}{2}} - (1-s)\tau^{p}\right)^{\beta} \tag{3.10}$$

Here s and p are used as fitting parameters, $p > 3/2$ and $s > 0$. Notice that if the system is treated as a pure Bloch ferromagnet, i.e. $s = 1$, $p = 3/2$ and $\alpha = p$, equations 2.39 and 3.10 are identical, demonstrating the same physical origin of these equations. We now can fit the overall magnetisation of the 6 nm PBC system we have simulated however it is necessary to make small adjustments to both equations to resolve the initial and final values of the plots. Both equations expect a ferromagnetic MvsT, starting at $1m$ at 0 K and finishing at $0m$ at the Curie point. To resolve this we use two parameters, A and B, which are set to the initial and final (in temperature) magnetisation values of our simulation.

$$A = M(0)$$
$$B = M(1000)$$
$$M(\tau) = A\left(1 - \tau^{\alpha}\right)^{\beta} + B \tag{3.11}$$
$$M(\tau) = A\left(1 - s\tau^{\frac{3}{2}} - (1-s)\tau^{p}\right)^{\beta} + B \tag{3.12}$$

Using this modification, both fitting equations can handle ferrimagnetic systems which do not reach a magnetisation value of $0m$ at high temperature. Figure 3.19 shows the fitting, done using Gnuplot [45], which employs the nonlinear least-squares (NLLS) Marquardt-Levenberg algorithm. Using both methods, the Curie temperature was calculated to be 878.4 K with a standard error < 0.5 K while β was calculated to be 0.563 ($\pm$0.0023) using the Curie-Bloch equation and 0.0565 ($\pm$0.0074) using the Kuz'min equation. This shows excellent agreement using both fitting methods, however the s and p parameters used in Equation 3.10 showed a high sensitivity to change and relatively higher standard error. Due to the relative simplicity of the Curie-Bloch equation, we shall use it by default when fitting magnetisation plots in the future.

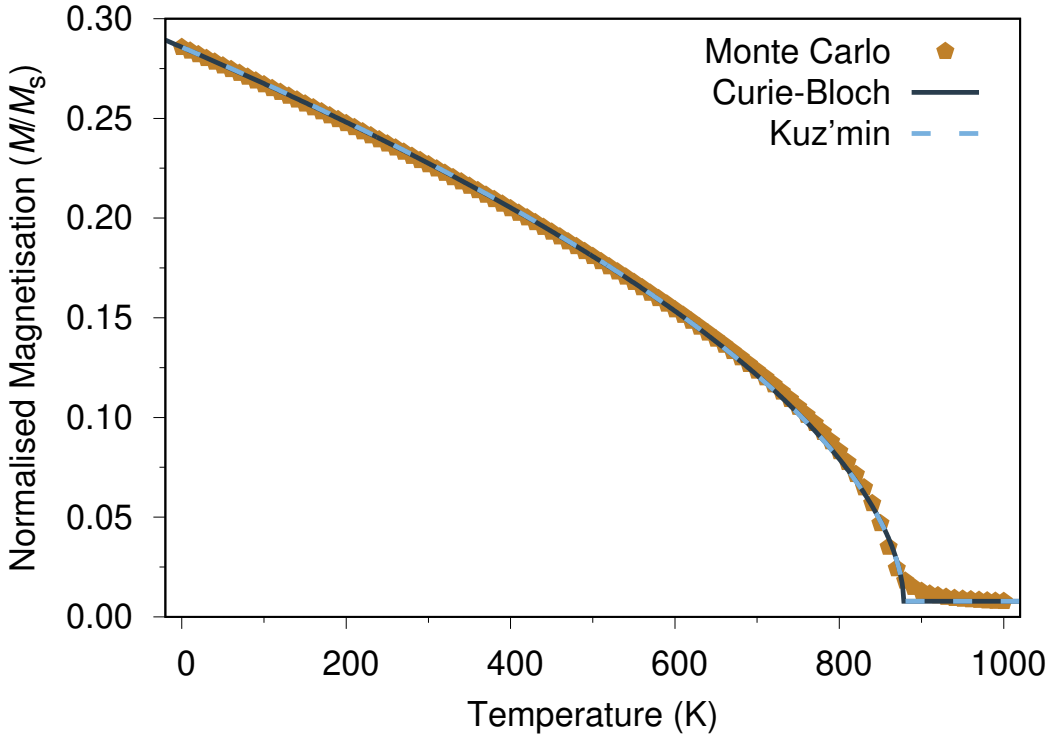

Figure 3.19: **Fitting the MvsT curve of a 6 nm PBC particle using the Curie-Bloch and Kuz'min equations.** The two fitting methods agree very well with each other and overlap. Predicted T_C is 878.4 K and $\beta \approx 0.564$.

We now have a calculated value for the Curie temperature of our 6 nm PBC system, at 878.4K, which is somewhat higher than the cited 858 K for an ideal bulk system. These values are different enough to warrant questioning the methods we have used to calculate our value. There are various possible reasons for our calculated value to be different:

- Physical model
- Material parameters
- System properties
- Fitting method

For now we shall assume that the physical model used, i.e. the Heisenberg Hamiltonian, and the Monte Carlo method used as the base for this simulation, is accurate. Moving from this, the material parameters most likely to affect the Curie temperature of the system are the exchange interaction values, which correlate directly to the Curie temperature of the system. A percentage increase or

reduction of the exchange interaction magnitudes will cause a similar percentage increase or reduction in the Curie temperature, hence the values currently used may be slightly higher than required. Next, the system properties could also be affecting the Curie temperature. For example, we have chosen a block particle as a base with periodic boundary conditions. The periodic nature of our system could easily increase the overall spin correlation if it is in effect over a short enough distance. With an overall system size of only 6 nm, less than 10 times the lattice constant, it is very likely this is having a non-negligible effect. Finally, the fitting method may also be at fault. While the equations suggested seem physically sound, there are enough degrees of freedom to allow for statistical errors. If we take a closer look at the fitting and evaluate it by eye, the low temperature region shows much better fitting than the area around the critical point. Due to the asymptotic decrease in magnetisation around T_{C}, both models struggle to follow the data points well.

It is very likely that each of these factors is affecting the calculated Curie temperature. An easy fix to this issue would be to change the exchange parameters by a factor, to achieve the same calculated T_{C} as the ideal, however this would be a very lazy approach and would not reflect on the accuracy of our model or methods used. The physical properties of the system, its shape, size and surface properties will be explored in later chapters as, while they may be having lesser effects here, changes will be much more apparent when we are no longer trying to approximate bulk conditions. To improve our fitting methods, we can look to reduce the degrees of freedom used in our equations, either by constraining β or T_{C}, or attempt to calculate the system Curie temperature from other data.

3.5.1 Fitting Sublattice Magnetisation

In addition to fitting the overall material magnetisation, we can also use the Curie-Bloch equation to fit the sublattice magnetisation which will not necessarily predict the same Curie temperature or β values. Each sublattice experiences different values for the exchange and can therefore have a subtly different critical point. We use the Curie-Bloch equation to fit the sublattice magnetisation in Figure 3.20.

While the sublattice appear to have very similar shapes, we can first compare the fitted values of β: 0.297 and 0.399 for the tetrahedral and octahedral sublattices respectively, with an asymptotic standard error less than 1.6%. These values are very distinct from each other and the overall system which had a fitted

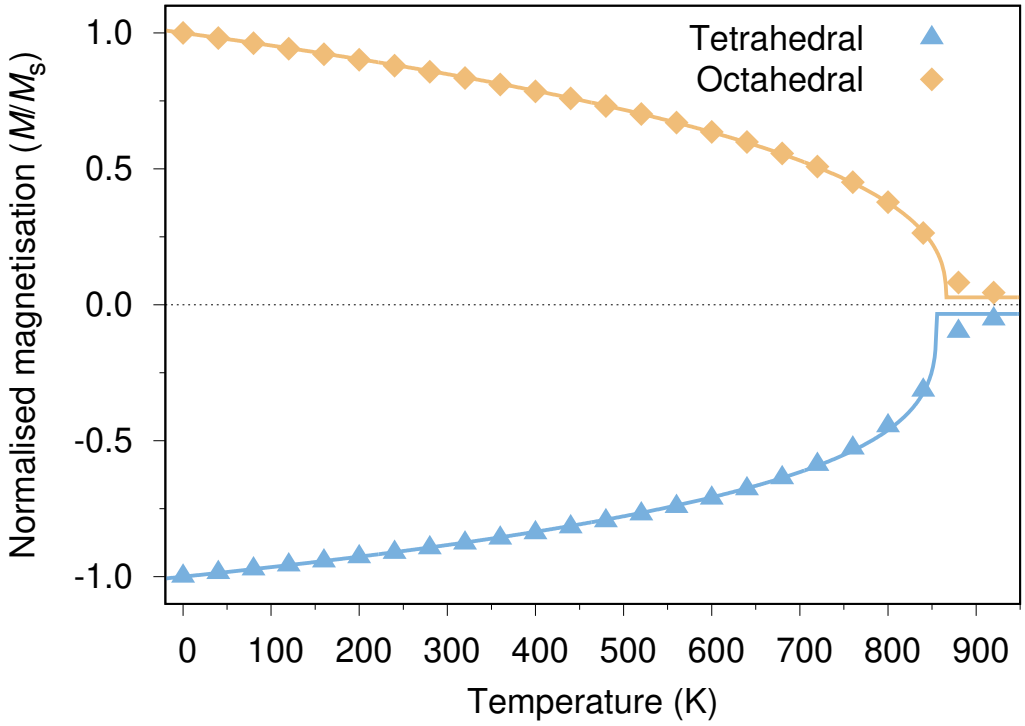

Figure 3.20: **Fitting the sublattice magnetisation of a 6 nm PBC system using the Curie-Bloch equation (2.39).** The tetrahedral sublattice has a fitted T_C of 854 K while the octahedral sublattice has a fitted T_C of 866 K.

$\beta = 0.564$. The shape of the curves is therefore quite different for all components of the system. The predicted T_C fall much more closely together at 854 K and 866 K again for the tetrahedral and octahedral sublattices respectively with an error less than 0.25% using a nonlinear least-squares fitting algorithm. It is still quite difficult to determine the exact reason for the variation in these parameters, whether it is truly a symptom of the underlying physics or a fitting error however the fact that the overall fitted Curie temperature does not lie between those predicted for the sublattices might suggest that the fitting method must be refined further as explained in the previous section.

3.6 Specific Heat

In thermodynamics the specific heat is often used as a measure to determine the amount of energy required for one unit of mass of a material to cause an increase of one unit in temperature. This value is not necessarily constant with temperature as more energy can be required to heat a material from 100 K than from 0 K. Phase transitions also have a large effect on the specific heat, for example the specific heat of water at 20°C is $4182 J/K \cdot kg$, while for ice just

below $0°C$ it is only $2093 J/K \cdot kg$. If we consider a material being heated through a phase transition, such as melting ice or boiling water, and assume that the phase transition occurs spontaneously, then we expect three values for the specific heat between the phase transitions, assuming that the value is constant with temperature between these points. A plot of temperature against enthalpy change is shown in Figure 3.21.

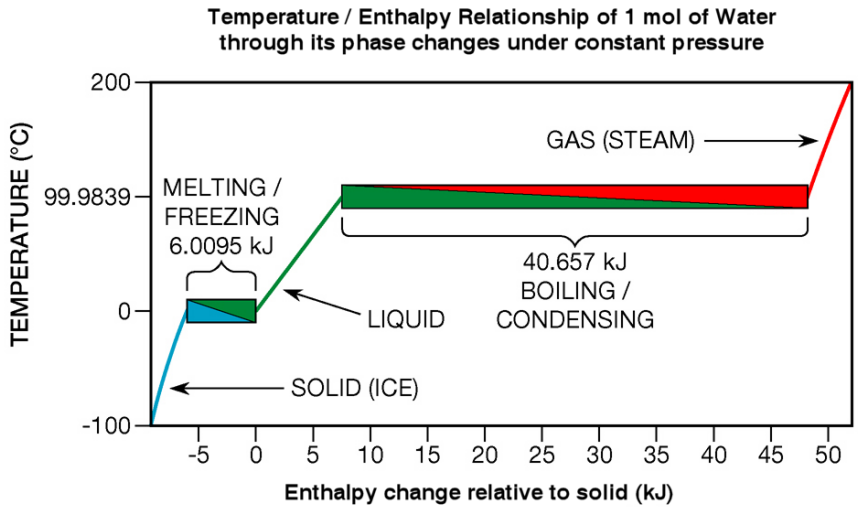

Figure 3.21: **Temperature enthaply relationship of 1 mol of water through its phase changes under constant pressure.** This graph shows that the temperature of a water sample does not change during phase transitions as heat flows in or out of it due to latent heat. Figure adapted from Wikipedia [88]

The enthalpy of water is related to the specific heat by the following equation:

$$Q = mc\Delta T \tag{3.13}$$

Where Q is the heat gained or lost, m the mass of the object multiplied by its specific heat c and ΔT is the change in temperature. From this, the specific heat of water can be calculated using the gradient of the plot. We can see that the plot does not curve between the phase changes hence the specific heat of water is constant during its solid, liquid and gas phase. During the phase transition the plot is flat, suggesting that the specific heat is undefined during the phase transition. To explain this, we must look at the specific heat differently. Outside of a phase transition, energy is being used to agitate the material and increase its temperature. During a solid phase the atoms are confined and have a reduced degree of freedom. When the melting point is reached, the energy is no longer

raising the temperature of the material but instead being used to fuel the transition from solid to liquid. As the atoms of water are more free to move around, they have a higher degree of freedom, and their heat capacity is increased. The phase change is therefore observed as a discontinuity in the specific heat of a material.

While we have used the solid to liquid and liquid to gas phase changes of water to illustrate the behaviour of specific heat, it is not only relevant to these types of phase changes. Magnetite undergoes a structural phase change at the Verwey transition and will therefore have a discontinuity in its specific heat at this point. However, we are not modelling this phase change (atomic positions are being modelled as constant) and therefore cannot probe this behaviour. Instead we model a different type of phase change at the Curie point. Here the material transitions from being ferrimagnetic with an overall ordered spin orientation which reacts more strongly to an external applied field, to a paramagnetic state where the spins are randomly oriented and only weakly respond to an external magnetic field.

The specific heat of a magnet can be defined in several ways however the general idea is always to reflect the number of spins deviating from a fully magnetised state per degree temperature increase. As we are dealing with a magnetic material, there are two possible types of specific heat that we encounter: an electronic specific heat, which tracks the energy input into the lattice, the thermal vibrations and kinetic energy of the valence electrons; and a magnetic specific heat where energy goes into disordering the spins. If the two components were separated, the electronic specific heat would be linear in temperature while the magnetic component is related to the gradient of the M vs T curve and should therefore show a peak at T_{C}.

In VAMPIRE, the specific heat of the system is defined as:

$$C_v = \frac{\left(\langle U^2 \rangle - \langle U \rangle^2\right)}{k_B T^2} \tag{3.14}$$

Where U is the internal energy of the system. From the equation we can see that we are studying the standard deviation of the internal energy. This is expected to be low when the system is at low temperatures, with well aligned spins and minimal deviations. When the system is high in energy, spin directions are distributed randomly and there is high variance, the standard deviation is high. It will therefore reach a maximum at the Curie temperature where this

system is in a highly disordered state, and then decrease as the temperature is further increased, according to Equation 3.14. It is worth noting that as we do not model lattice dynamics, we are only focused on the magnetic specific heat, hence this data will deviate from experimentally calculated specific heat which contains both electronic and magnetic components.

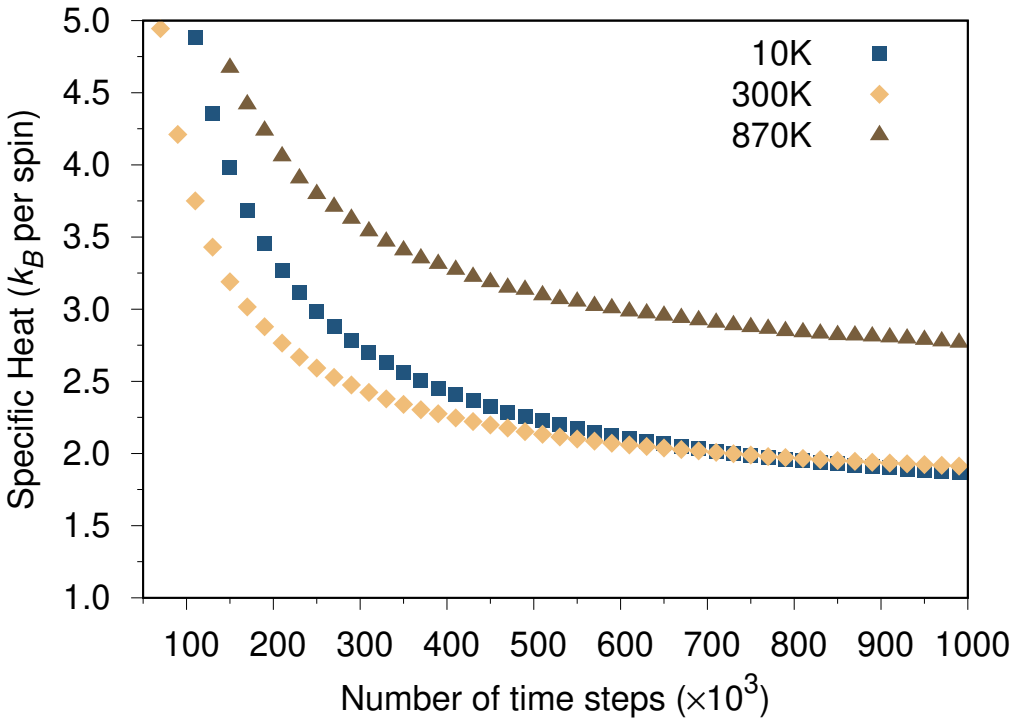

Figure 3.22: **Convergence of specific heat for different temperatures of a 6 nm PBC magnetite particle.** The convergence is relatively slow and similar for all temperatures. Around room temperature it reaches a converged value faster than the simulations at very low temperature or at the Curie point.

To achieve well converged data for the specific heat it is necessary to visualise its convergence with the number of Monte Carlo time steps. This is shown in Figure 3.22. The magnitude of the specific heat at a converged state is relatively similar for low and high temperatures however it is slightly faster around room temperature. The number of times steps required for convergence is noticeably higher than what was needed for converging the magnetisation as here we are using millions of time steps while for the magnetisation only hundreds of thousands were needed, hence for good data we need to run the simulation for longer.

Looking at the specific heat as a function of temperature we see that there is indeed a peak at the Curie point however the specific heat does not tend to zero at low temperatures or immediately after T_C as we see in the magnetisation. Above

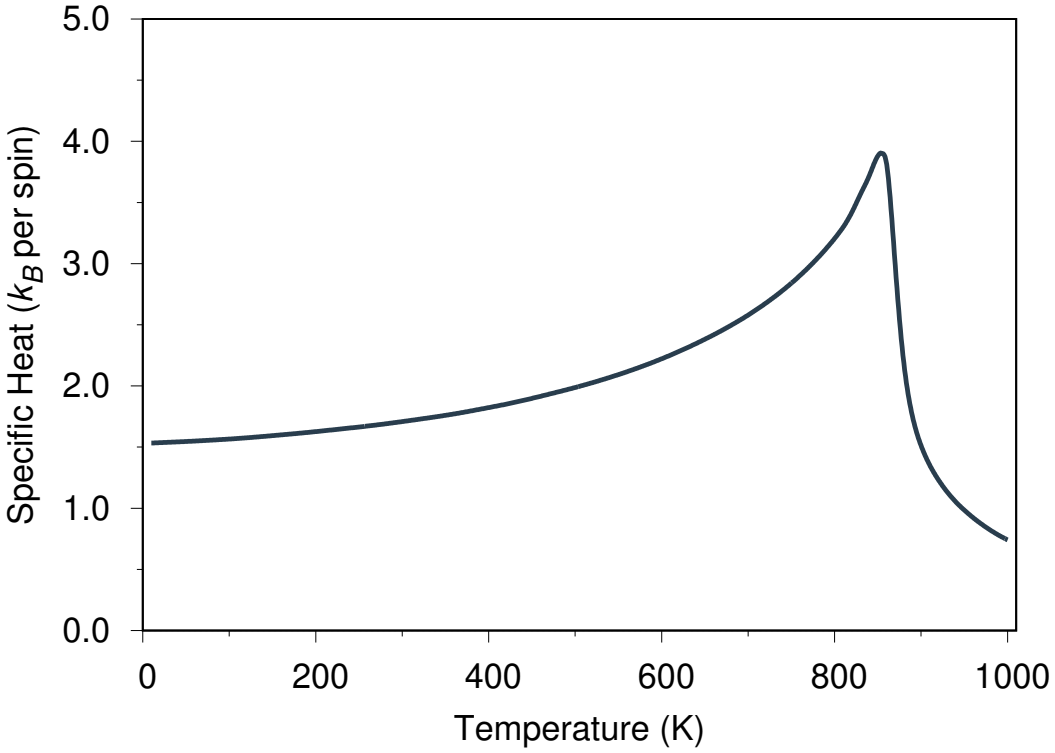

Figure 3.23: **Specific heat scaling of a 6 nm PBC magnetite particle.** The peak denotes the position of the Curie point.

the Curie temperature excess heat goes towards increasing the temperature of the system, requiring less energy as the temperature increases further. The shape of the plot follows $1/T^2$ behaviour as expected from Equation 3.14. If we were also modelling structural phase changes, it would reach another peak around 1600 K as this is the melting point of magnetite. Below the Curie temperature we see a steady increase in the specific heat as more energy is required to agitate the system just below the phase transition. At low temperatures, the specific heat is approximately constant, around $1.8k_B$ per spin, before increasing towards T_{C}. This is mostly a symptom of the model used. Close to zero Kelvin, the input energy should not be able to move the spins as they are quantum systems constrained to particular eigenvalues. As the model used is the Classical Heisenberg Hamiltonian, this is not the case here and spins are allowed to move anywhere along the unit sphere, hence for $T > 0$, thermal fluctuations give rise to a non-zero specific heat.

By doing simple fitting on this data, with the help of an increased resolution of 1 K around the critical point, we can extract the predicted Curie temperature from the peak by looking at the intersection of two lines fitted to either side of the peak. This comes out to be around 857K, noticeably lower than the value given by

fitting the magnetisation using Equation 2.39. This could indicate that the specific heat peaks at a value of T_C consistently lower than the magnetisation however for now we have only one sample to indicate this and would need to repeat the simulation, possibly with different parameters to compare the two methods. A possible approach could also be to assume the value from the specific heat as more correct and use it as a constant in fitting the magnetisation. From this we will get an altered value of β, the critical exponent, and a slightly different shape to the overall fitted curve.

3.7 Susceptibility

Another magnetic property we can look at is the magnetic susceptibility traditionally used to assess the behaviour of a magnetic material with an external field. In the absence of an external field, the susceptibility measures the difficulty in changing the spin orientation of a material. At low temperatures far below the critical point of a magnetic material, the spin orientations are strongly ordered, such as in ferro, ferri and antiferromagnetism. While highly correlated, the material has a very low susceptibility due to a very large amount of energy required to separate the spins. At higher temperatures the materials do not necessarily have all their spins aligned in the same directions however domains can form which preserve the spin orientations within local clusters. Size becomes an important factor in these scenarios as the domains cannot form if the number of spins is to small or the system is finite in size and below a critical length.

The susceptibility is calculated using the following formula [30]:

$$\chi_\alpha = \frac{\sum_i \mu_i}{k_B T} \left(\langle m_\alpha^2 \rangle - \langle m_\alpha \rangle^2 \right) \tag{3.15}$$

where χ_α is the magnetic susceptibility and $\alpha = x, y, z, m$ giving the directional components of the susceptibility as well as the longitudinal susceptibility χ_m. Hence it is proportional to the standard deviation of the magnetisation. From this we expect the susceptibility of a material to be low far below and above the Curie temperature as a low standard deviation indicates that values tend to be close to the mean. In the low temperature region magnetisation fluctuation is low, spins are well ordered and strongly aligned in one direction, hence small spin deviations should be close to the mean as there isn't enough energy for the spins to explore exited states. Around the critical point the average spin direction is random, and the system exhibits high fluctuations in the magnetisation, causing a peak in

the susceptibility. Above T_C, all spin directions are treated similarly and the susceptibility decreases as T is increased. This formulation of the susceptibility is quite different to the experimentally measured values of χ or $1/\chi$, which are less commonly used when discussing nanoparticles as its measurement becomes difficult and artificial. As such the formulation of susceptibility in Equation 3.15 is best used for investigating the Curie temperature of the system.

To achieve well converged data for the susceptibility, many millions of Monte Carlo time steps must be used. Compared to the magnetisation, at least ten times the number of steps is used to have a relatively smoothly varying susceptibility versus temperature plot. The convergence also scales with temperature as values for susceptibility around the critical point take noticeably longer to converge than data points further away. Even for relatively small systems around 10 nm diameter, susceptibility data is the most time consuming to calculate however it should give a very good indication of the Curie temperature as this should be indicated by a simple peak. It is difficult to fit the susceptibility due to its discontinuity at T_C and therefore the sample rate around this point is increased. While the susceptibility behaviour is smooth away from the critical point, we perform one equilibration simulation per 10 K temperature step however around T_C, this is increased to one simulation per 1 K temperature step to fully capture the peak of the susceptibility as well as any sharp increases or decreases in its value. For a PBC system of around 6 nm size, each simulation can take around twelve hours to complete on a single core of a modern Intel Xeon processor (released around 2017).

The susceptibility for a 6 nm PBC particle is shown in Fig. 3.24. At low temperatures the spins are aligned close together and there isn't enough energy for the spins to diverge from each other significantly. As the temperature increases the standard deviation increases as it is more likely for spins to follow random directions, as seen in Figure 3.11. At the Curie point, the system transitions to a disordered state as it is now paramagnetic and the susceptibility peaks. As the system is heated further, the average spin orientation is random and the standard deviation lowers again due to the overall properties becoming uniform.

To extract a value for T_C, we can fit two curves on each side of the susceptibility and find their intersection. This shows that the predicted Curie temperature for this system is around 862 K which lies somewhere in between the values predicted by the magnetisation and the specific heat. Before making a comparison of these values, we can also study the sublattice susceptibility of the system to check

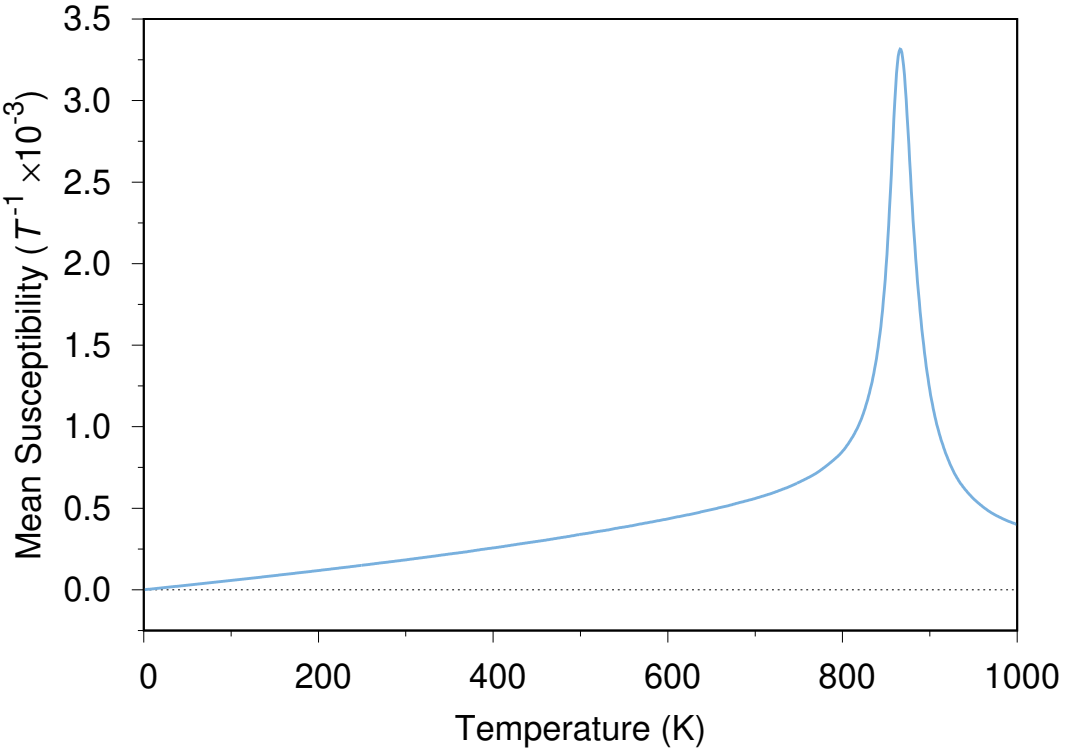

Figure 3.24: **Susceptibility vs temperature curve of a 6 nm PBC magnetite particle.** The susceptibility is very low below the Curie temperature as the average spin directions are still ordered and the standard deviation of the spins is small. At the Curie temperature there is a sharp discontinuity as the spins transition from an ordered to disordered (paramagnetic) state.

whether these are predicted to be different, as shown with the magnetisation, or if they lie closer together.

Figure 3.25 compares the sublattice susceptibilities to the overall susceptibility of the system which is an order of magnitude lower in size. To understand why this is the case we must consider the sublattices individually as on their own they are mostly made up of spins oriented in similar directions, as least during the low temperature phase, which are still strongly correlated to each other. When we add up the contributions of both sublattices, we are now comparing spins which have much larger difference in their directions as the two sublattices are antiparallel at low temperatures. This creates a distinction between the intra-sublattice susceptibility, that of the sublattices individually, and the inter-sublattice susceptibility which is the result of the overall contributions and represented by the "Total" line on Figure 3.25. An illustration of these two modes is shown in Figure 3.26.

The overall behaviour for the plots remains the same irrespective of the magnitudes of the components. We can now extract the Curie temperatures

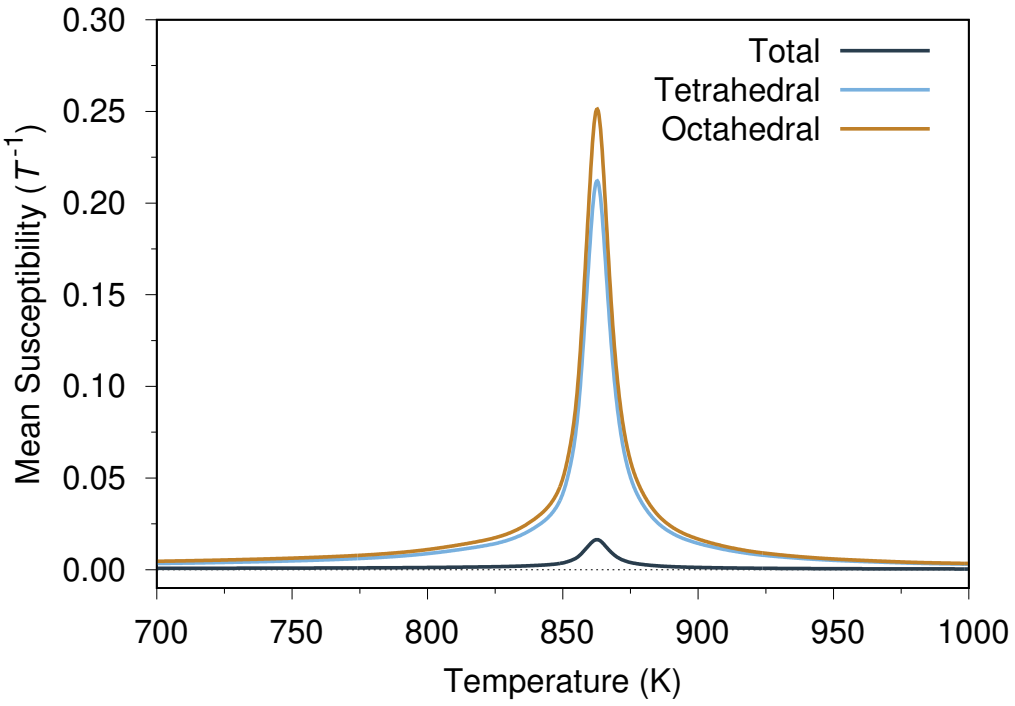

Figure 3.25: **Susceptibility vs temperature curves for the overall and sublattice susceptibilities of a 6 nm PBC system.** The magnitude of the overall susceptibility is much lower than that of the individual sublattices. This shows the difference between the changes in susceptibility for an individual lattice where most spins point in the same overall direction as opposed to the spins on different sublattices which are antiparallel.

predicted by the susceptibility for the sublattices by a simple fit, or in this case due to the relatively simple peak, we can use a rough estimate at the peak of each plot. Looking closely at the data, its possible to see that each peak lies at the same point along the x-axis, at a temperature of 862 K. This is a surprising result relative to that seen from the magnetisation as we now have the same Curie point predicted by all components of the system. It is possible that the clarity of the susceptibility data, which takes the longest time to converge to well relaxed values, makes it easier to extract correct values for the Curie temperature if we assume that they should be the same for all components of the system however for now we do not have enough information to make a good decision on which method is the most reliable for calculating the overall Curie temperature. The three methods presented so far, the magnetisation, specific heat and susceptibility, give T_{C} values which lie relatively close to each other; however we need more data to make a final decision, hence we shall continue to use at least the magnetisation and susceptibility to analyse the predicted T_{C} with future simulations.

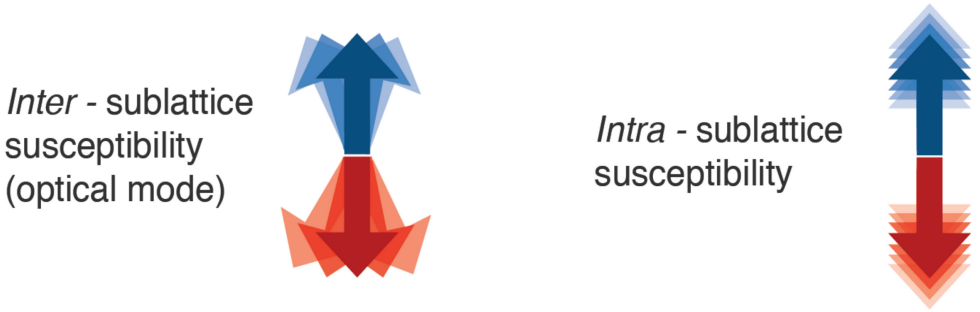

Figure 3.26: **Visualisation of the difference between inter and intra-sublattice spin modes.** The inter-sublattice spins lead to high susceptibilities for the individual sublattices, while intra-sublattice spins compete which results in much lower susceptibilities when sampling the system as a whole.

3.8 Rescaling

High temperature effects such as the Curie temperature can be studied closely using our current methods and compared to values found in experiment, however at low temperatures the Classical Heisenberg Hamiltonian fails to correctly replicate the quantum mechanical behaviour of spins. This leads to more obvious issues such as the high specific heat values at low temperatures shown in Figure 3.23, as well as more nuanced issues in the magnetisation scaling. If we make a comparison of our current data set with experimentally obtained saturation magnetisation plots (figure 3.27), we can see a significant deviation from experiment to theory, down to the same quantum mechanical effects the classical theory fails to model. At all points below T_C the magnetisation is underestimated using the classical model. In experiment the magnetisation is maintained above 90% of the fully saturated value below room temperature and falls much more steeply as it approaches the critical point. It is therefore difficult to make justified statements about the magnetisation drop-off at mid to high temperatures using only a classical model. To remedy this, we make use of a rescaling method explained in section 2.4 developed by Evans *et al.*

According to this method, a temperature rescaling can be applied to the classical model by using one additional scaling parameter, α, as shown in Equation 2.40 below:

$$\frac{T_{\text{sim}}}{T_C} = \left(\frac{T_{\text{exp}}}{T_C}\right)^{\alpha} \tag{2.40}$$

We assume that the Curie temperature remains the same for both the classical

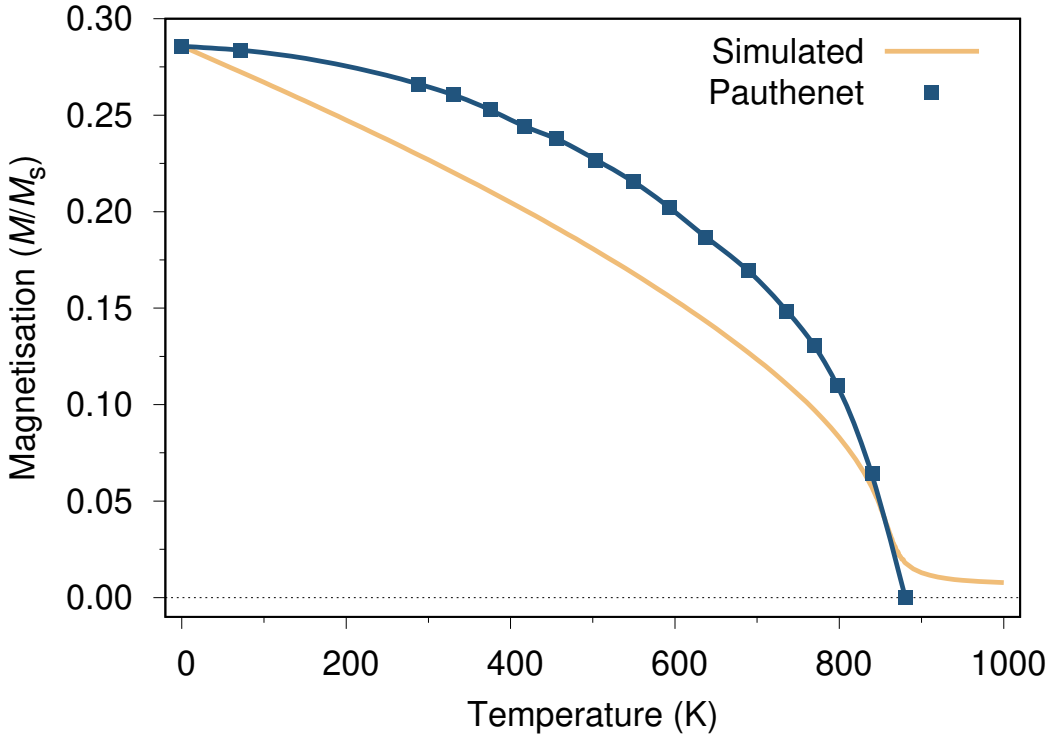

Figure 3.27: **Comparison of simulated and experimental magnetisation scaling.** The gold curve shows magnetite for a simulated system using the Classical Heisenberg Hamiltonian while the blue points are experimental data from Pauthenet *et al.* [82] (data points are shown with a cubic spline interpolation). Both plots are scaled to have the same T_C as this is expected to remain the same and the experimental data comes from a sample of bulk magnetite hence it reaches zero at T_C. At all points below T_C, the magnetisation is higher than the calculated value by varying amounts along the temperature range.

and the quantum model, a modest assumption as quantum effects decrease drastically at higher temperatures and are expected to vanish at and above T_C. To find alpha we can fit experimental data according to the Curie-Bloch equation:

$$M(\tau) = \left(1 - \tau^{\alpha}\right)^{\beta} \tag{2.39}$$

As we are dealing with experiment, α is no longer one as in Equation 3.9. Here, β is expected to have the same value irrespective of model due to the nature of universality classes [42]. The material parameters have not changed; hence we are able to fit our current data for α. We have so far simulated relatively small periodic boundary conditions systems of magnetite of 6 nm size. The value of β can change depending on the size of system used hence it is better to use as large as possible an initial system size to lower the change of increased spin correlation

due to PBCs. Using a system of 16 nm diameter or 20 lattice lengths of magnetite in each direction, we find the value of $\beta = 0.55$. Next we need to fit experimental plots of the saturation magnetisation of magnetite to the Curie-Bloch equation, constraining both $\beta = 0.55$ and $T_C = 862$ K and fitting for α.

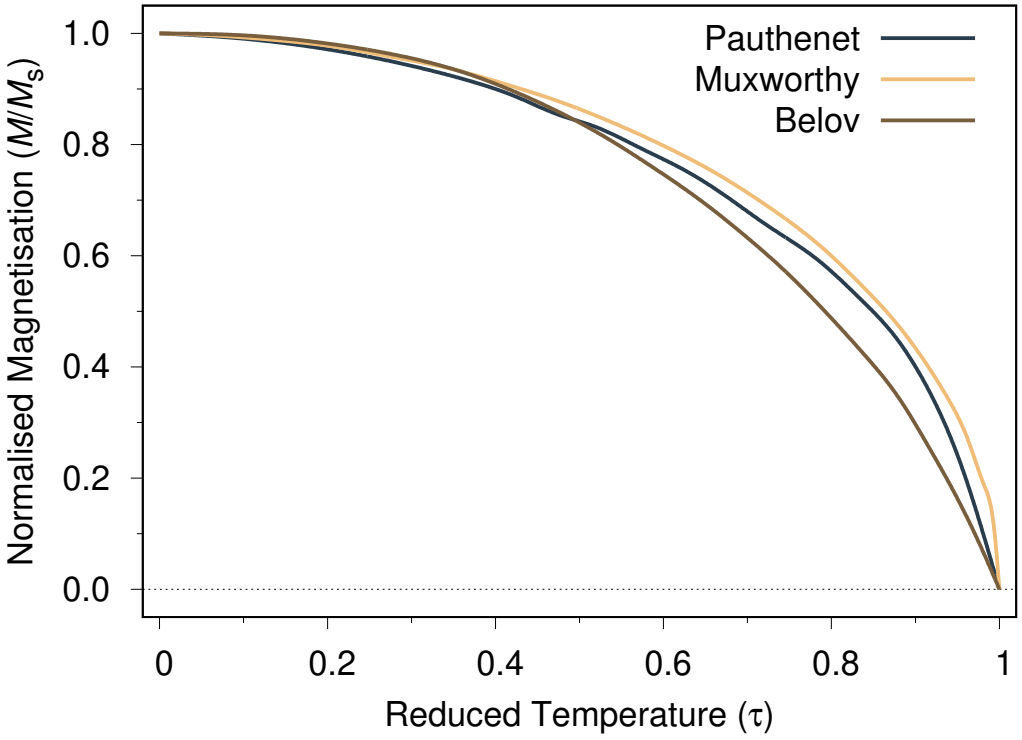

Figure 3.28: **Experimental saturation magnetisation scaling of Fe_3O_4.** Different experimental curves for the bulk magnetisation scaling of magnetite can be found from Pauthenet *et al.* [82] (blue), Muxworthy *et al.* [89] (gold) and Belov *et al.* [90] (brown). Results from Muxworthy and Pauthenet are similar with approximately equal scaling, while the sample used in Belov may have not been a bulk system or one with impurities due to the drastically different scaling displayed.

This step proves to be difficult due to the lack of magnetisation scaling data available. Much like the exchange constants, magnetisation scaling data can be hard to find from recent studies, and often much older papers must be relied upon. This brings to question the validity of the data as, depending on the material, it becomes difficult to assess the quality of the material and the conditions it has been studied in. So far we have shown data from Pauthenet *et al.* [82] however several other examples of Fe_3O_4 magnetisation scaling with temperature have been found [89, 90]. They are shown in Figure 3.28. The data from Pauthenet is often cited in more recent theoretical papers on magnetite, in spite of the low number of experimental data points used to make the plot, while the data from Muxworthy and Belov is smoother however both papers fail to describe

exactly how the data is fit. Comparing the plots, the scaling from Muxworthy and Pauthenet is very similar, with relatively small changes in magnetisation for all values of temperature. The data from Belov suggests that the system studied was not bulk as the magnetisation lowers less steeply towards the magnetisation, suggesting very high values of β. The scaling of the MvsT plot from Belov also appears to be different as the magnetisation is higher at low temperatures. It is difficult to make a judgement on which data set is truer to bulk magnetite however it is more likely that the data sets of Pauthenet and Muxworthy are appropriate.

To fit the data well we shall constrain the Curie temperature to the value we have fit previously, 862 K, but allow the value of β to change. This gives room for our proposed value of β to be optimised but also acts as a fail-safe if our initial value is in error. Using Equation 2.39 and a fitting program such as Gnuplot [45], which uses a nonlinear least-squares fitting algorithm, we can find a value for α. The fitting is shown in Figure 3.29 and the proposed values of α and β in Table 3.5.

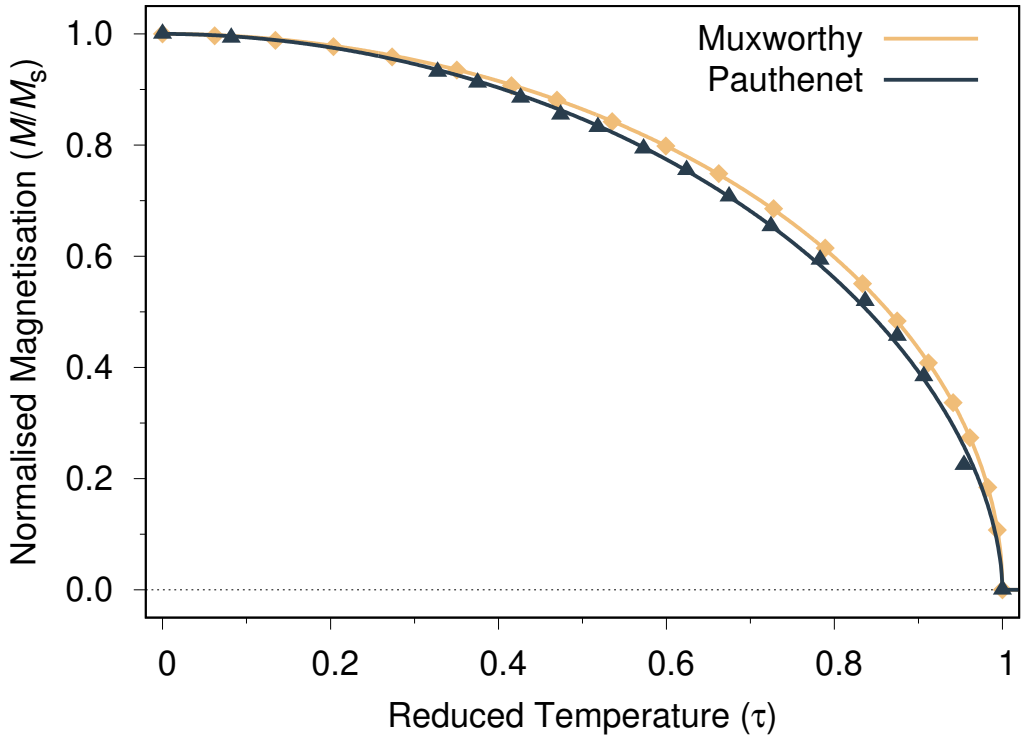

Figure 3.29: **Fitting the experimental magnetisation scaling from Pauthenet [82] and Muxworthy [89].** While the proposed fit for Muxworthy follows the data points more clearly, this is likely due to the data already being produced from a fit in the original paper, while the data points from Pauthenet are explicitly stated as experimentally produced data points.

	α	β
Pauthenet	1.951	0.5557
Muxworthy	1.985	0.5004
Belov	2.399	0.8231

Table 3.5: **Calculated values for α and β for experimentally produced magnetisation scaling with temperature.** Values from Belov [90] deviate significantly from those expected ($\beta \approx 0.55$). Data from Pauthenet [82] and Muxworthy [89] is likely more reliable and produce values more in line with current results.

Assuming our proposed value of β is correct, we see that the proposed magnetisation scaling from Belov is likely incorrect for bulk magnetite. $\beta = 0.8231$ is significantly different to any other proposed value and likely due to significant errors in experimental methods or samples with high impurity content. The proposed values for β from Muxworthy and Pauthenet lie much more closely to those found in our simulations and produce similar values for α. As explained earlier, it is difficult to assess the methods used to extract the magnetisation data in the original paper from Muxworthy, as experimental data points are not shown and the curve is of seemingly high quality suggesting it is a fit. The data from Pauthenet, despite being the oldest, clearly shows the original data points, which have been used here. As the proposed value of $\beta = 0.5557$ is inline with the value we have already calculated, we shall also make use of the fit value of $\alpha = 1.951$.

It is worth expanding on the value of $\beta \approx 0.55$ we have suggested so far as we have now fit a value for it from external data which seems to agree with the current assumptions. β, originally from the critical point scaling as shown by Chikazumi [84], is a critical exponent related to the magnetisation of the system around the ferro/ferrimagnetic to paramagnetic phase transition. Further, these exponents are described as being independent of the details of the system (such as the materials involved) but proportional to general properties such as theoretical model, system size and interaction length. As such, they are linked to Universality classes which aim to calculate upper limits for the exponents which depend on the model (Heisenberg, Ising etc.) [42]. The general idea for the Universality classes is that systems which do not exhibit finite scale properties have critical exponents whose values tend to a limit. For the 3D Heisenberg model, β is approximately 1/3. This seems to agree with previous work done using the Heisenberg model, which found that elemental ferromagnets had a value of $\beta \approx 0.34$.

When initially fitting the value of β to magnetite, the value 0.55 was a worrying sign due to the large discrepancy between its value for magnetite, the suggested

	Co	Fe	Ni	Gd
T_C (K)	1395	1049	635	294
β	0.340	0.339	0.341	0.339

Table 3.6: **Fitted values of β for elemental ferromagnets.** Calculated using a classical spin model simulation and the Curie-Bloch equation with $\alpha = 1$. Table adapted from Ref. [40].

limit for the Heisenberg model and previous data from Evans *et al.* [40]. With external data suggesting this value is correct, the next logical question is to ask why the value is so different. Earlier, in sections 3.4.2 and 3.5.1 we showed the magnetisation scaling of the tetrahedral and octahedral sublattices of magnetite, and provided values for their β of 0.297 and 0.399 respectively. These values are also distinctly different to the overall value of β however they are much closer to the reference value of around 1/3. As the magnetic properties of magnetite are a result of the competing properties of the two sublattices, perhaps the new value of β for magnetite originates from the sublattices. To make a fair comparison, these values are fit from a 6 nm PBC system, which is only around 9 unit cell lengths of magnetite. As the value of β should reach a limit for more bulk like systems, we should first fit the sublattice β for a 16 nm system as we have done for the overall value.

Figure 3.30 shows that the values of β do not change significantly in periodic boundary condition systems. The tetrahedral and octahedral fits show $\beta \approx 0.3$ and 0.4 respectively. While it would be easy to point out that the average of these values lies clearly within the expected range of β for its universality class values, this still does not explain why the overall value of β for magnetite is 0.55. In addition, the sublattices should not be considered wholly separate as they do of course interact due to exchange and influence the magnetisation scaling of each other. The exact reason why magnetite displays such different values of β is uncertain however this may be a wider symptom of ferrimagnetic materials with competing sublattices as a whole.

We can now use the rescaling parameter $\alpha = 1.951$ to adjust our magnetisation scaling and compare this to the original data from Pauthenet. To do this we apply Equation 2.40 to the temperature points of our data set for a 16 nm system under periodic boundary conditions, to best approximate bulk. In addition, as the data from Pauthenet *et al.* is normalised to a value of 1 for both magnetisation and temperature, we have done the same for our simulated data for comparison.

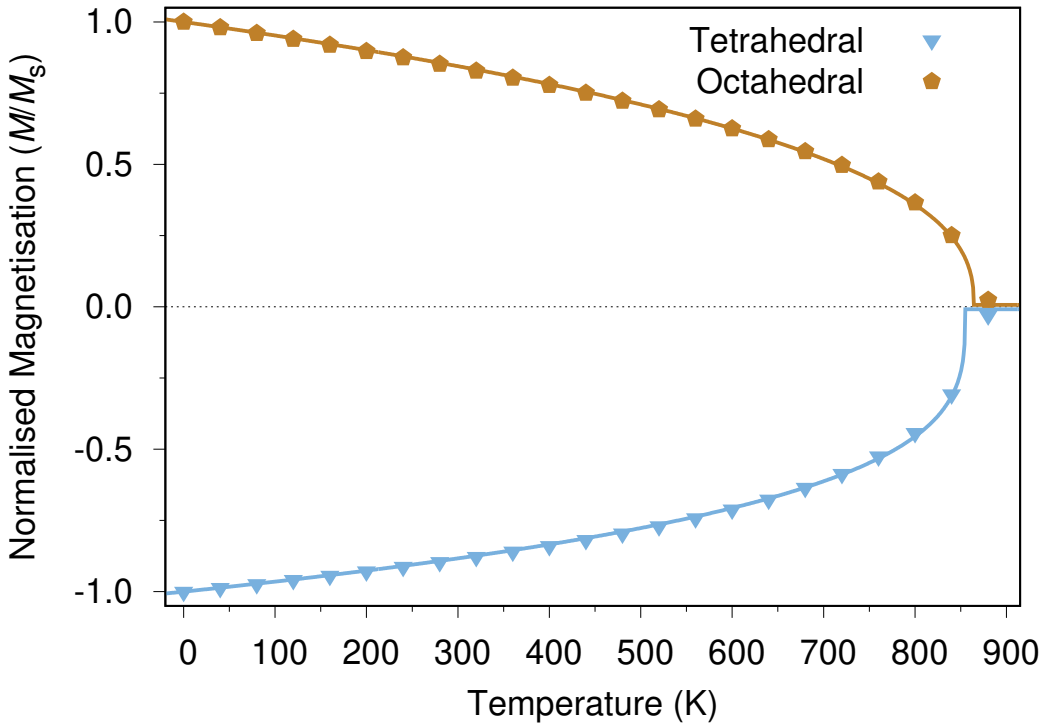

Figure 3.30: **The tetrahedral and octahedral sublattices of a 15.96 nm PBC magnetite system.** Fit according to the classical Curie-Bloch equation, with no rescaling, the tetrahedral lattice has a slightly lower $T_C = 855$ K and $\beta = 0.301$, while the octahedral lattice has a fit $T_C = 864$ K and $\beta = 0.399$.

Figure 3.31 shows that our data agrees very well with the experimental points for Pauthenet which we have used to correct the low temperature scaling of the system. Below $\tau = 0.8$ or roughly 700K, the data sets are almost overlapping. This is in large part due to the α rescaling parameter which more heavily affects the low temperature region; however it is also an indication that the majority of the parameters, constants and models used so far to simulate magnetite are at least close to those found in experiment. Above this temperature, the data sets do not agree perfectly however they remain close. Here the dominant fitting parameter is β, which is in fact slightly different for both curves. In the experimental case, β is around 0.56, while for our data β is fit to 0.53. Lower values of β result in steeper approaches to the Curie point which is what we can see in Figure 3.31. Above the critical point the plots cannot match as the bulk experimental data stops at the Curie temperature where the magnetisation reaches zero, whereas for our simulation with a finite number of spins, even with PBCs, there is a small remnant magnetisation.

We also revisit the specific heat of magnetite using this new rescaling method

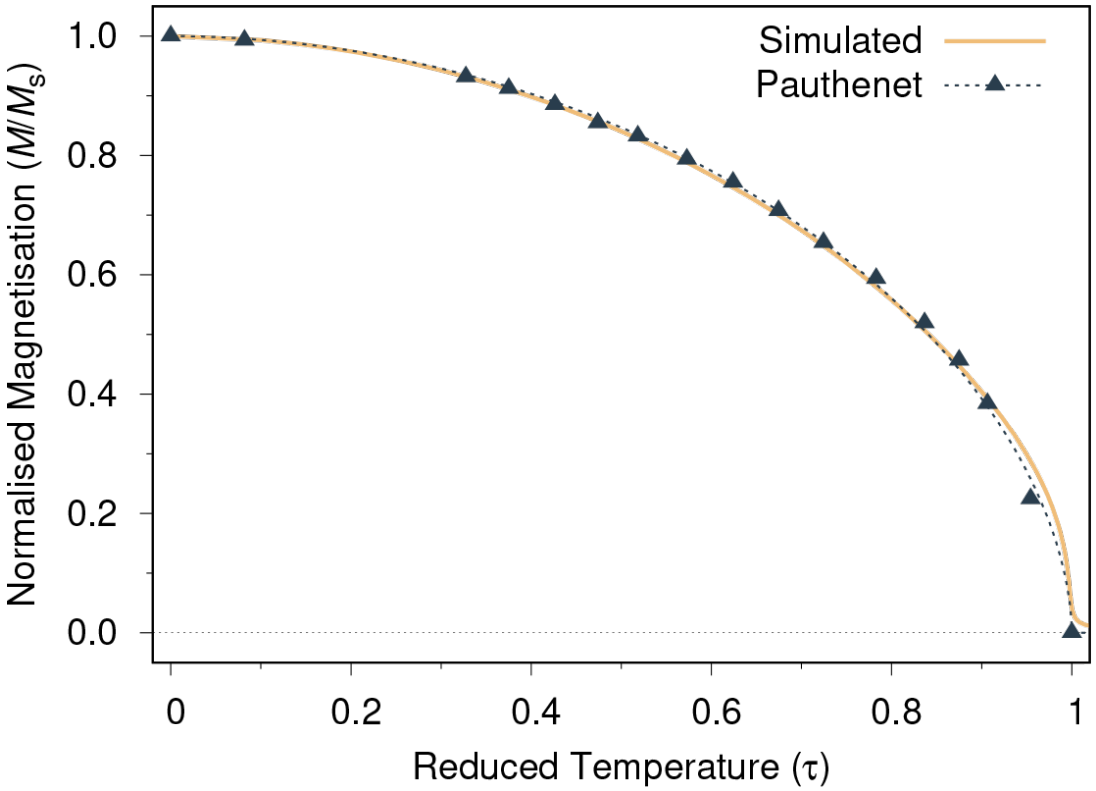

Figure 3.31: **Comparison of simulated magnetisation scaling using a rescaling parameter.** With $\alpha = 1.951$ the data agrees very well with experimental data from Pauthenet *et al.* as the low temperature scaling of the magnetisation correctly models the required quantum mechanical effects.

to fix the low temperature scaling. In a quantum model, the specific heat is expected to start from zero and rise slowly as there is not enough energy for spins to explore higher direction eigenvalues. The rescaled specific heat corrects the low temperature behaviour by using the rescaled temperature calculated in Equation 2.40 and substituting into Equation 3.14. With this, the specific heat correctly starts at $0k_B$ per spin at zero Kelvin and maintains a low value until the critical point.

$$T_{\text{resc}} = T_{\text{C}} \left(\frac{T_{\text{exp}}}{T_{\text{C}}} \right)^{\alpha} \tag{3.16}$$

$$C_v = \frac{\left(\langle U^2 \rangle - \langle U \rangle^2 \right)}{k_B T_{\text{resc}}^2} \tag{3.17}$$

Assuming the value of α is correct, it is almost always worth using the rescaling method however there are a few downsides to using it unilaterally. For the magnetisation scaling with temperature, it is very important to use the rescaling

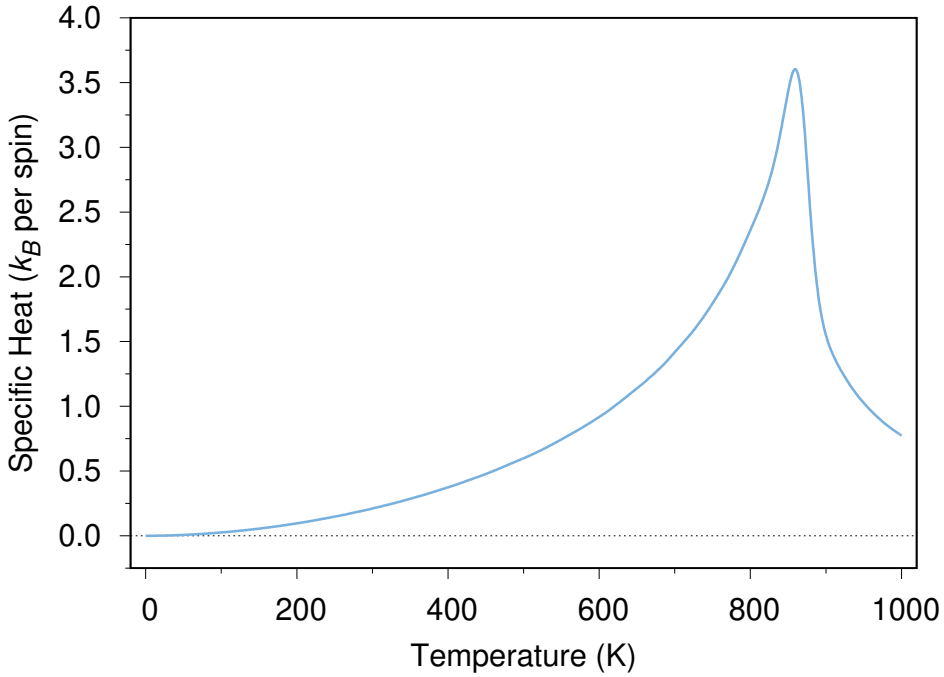

Figure 3.32: **Rescaled specific heat of 6 nm magnetite with PBC.** By applying the quantum rescaling method, we can correct the specific heat scaling at low temperature which used to start at a finite value near 0 K. The rescaled plot accurately models the low magnetic specific heat due to the constrained spin directions.

to achieve the correct indication of magnetisation drop off. The magnetisation curve supplies important data for the whole temperature range. In the case of specific heat and susceptibility, these plots provide data which is less relevant further away from the critical point. The susceptibility in particular bears less resemblance to experimentally measured susceptibilities and is mostly used here to accurately measure the Curie point. Hence, quantum rescaling becomes an unnecessary venture as the vast majority of change it causes in the results occurs away from the critical point where quantum effects are minimal. In addition, to apply the rescaling method, it is required to know the position of T_{C} beforehand, which in some cases required running the same simulation twice. Because of this, the rescaling will mostly be used to achieve correct magnetisation scaling, a relatively low computational cost data output, while it will be used less for calculating the susceptibility or specific heat, which can take an order of magnitude (or higher) longer computational time to achieve.

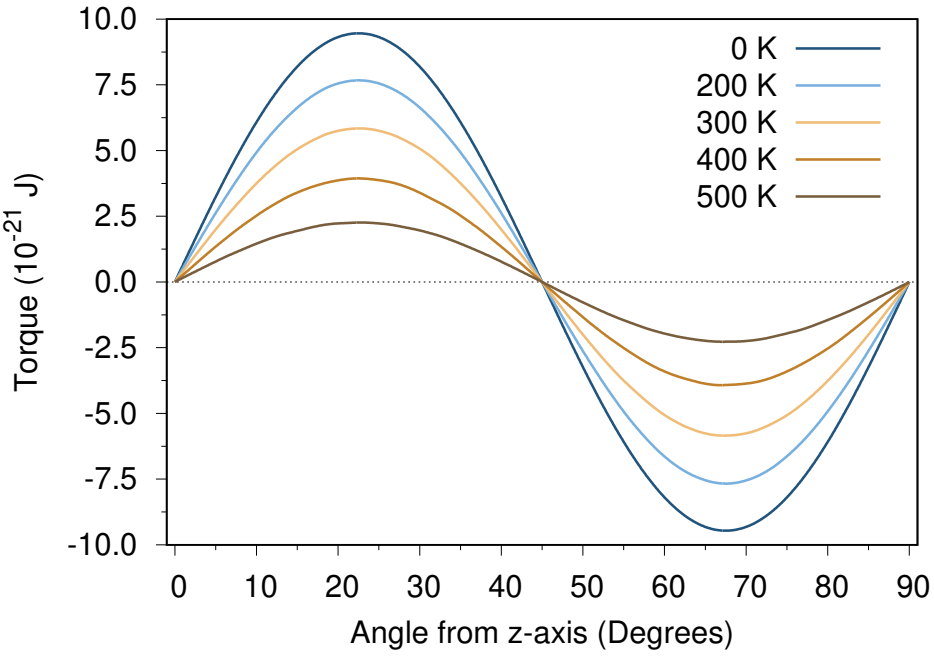

Figure 3.33: **Plot of the restoring torque for different temperatures as a function of angle from the z-axis.** The maximum of the torque occurs at 22.5° and is independent of temperature.

3.9 Anisotropy

While we have been looking more closely at the temperature effects which occur at the Curie temperature of the system, some effects, such as those dominated by the magnetocrystalline anisotropy, are only visible at low temperatures. In Section 3.2.4 we considered the anisotropy constant K_1 of magnetite which defines the strength of the cubic anisotropy in magnetite, however we do not get a clear picture of the temperature scaling of this constant in our simulations. To do this we can employ a constrained Monte Carlo algorithm [91].

For our magnetisation curves we have allowed the system to reach an equilibration state at each temperature point. All spins in the system are allowed to rotate freely and reach their lowest energy configuration. For this simulation we shall instead constrain spins in one of the sublattices to a fixed orientation and allow all other spins to rotate freely, being simulated using the traditional Monte Carlo method. Figure 3.33 shows the restoring torque as a function of the angle from the z-axis.

The torque is calculated as the integral of the anisotropy energy and has the form of $0.5 \sin 4\theta$ as a result of this. In fact, the 0 K torque and anisotropy

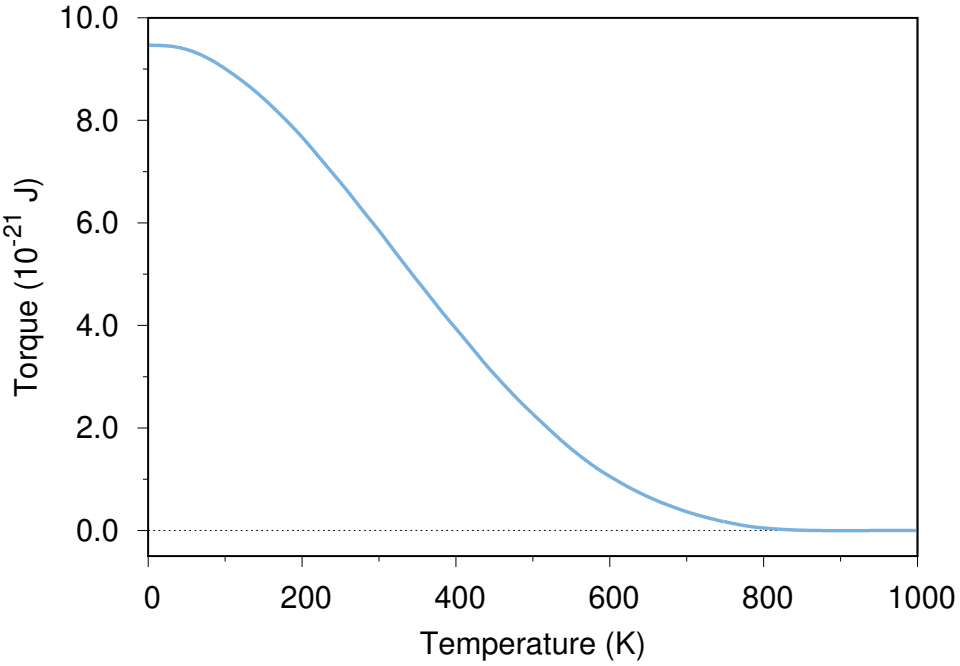

Figure 3.34: **Plot of the restoring torque as a function of temperature.** The torque (and anisotropy energy) does not disappear completely until the system reaches the Curie temperature however the increased thermal energy of the system makes it difficult to observe anisotropic effects above room temperature.

for a given particle can be found by plotting this equation multiplied by the 0 K anisotropy constant and the number of atoms in the system. The shape is independent of temperature, however an increase in temperature causes a reduction in the amplitude of the curve, also indicating the reduction in the effective anisotropy energy. We can also plot the maximum of the torque with respect to temperature, shown in Figure 3.34. Compared to the magnetisation, the torque, and by association the anisotropy, lowers much more quickly with increasing temperature, maintaining a peak value for only a few Kelvin before decreasing linearly between 100 K to 600 K. Near and above the Curie temperature the torque is zero while the anisotropy maintains a constant low value.

We can also study the relationship between the magnetocrystalline anisotropy and the magnetisation. From the studies done by Akulov [92] and refined by Callen and Callen [93], cubic anisotropy scales with the magnetisation according to an M^{10} law. Figure 3.35 shows that our simulated anisotropy scaling follows the M^{10} law for high values of magnetisation, where the temperature is low. As the magnetisation lowers, the discrepancy between the calculated data and theory could come from the fact that the theory assumed a mean-field approach, where the exchange interactions are equal and long ranged. In the simulations exchange

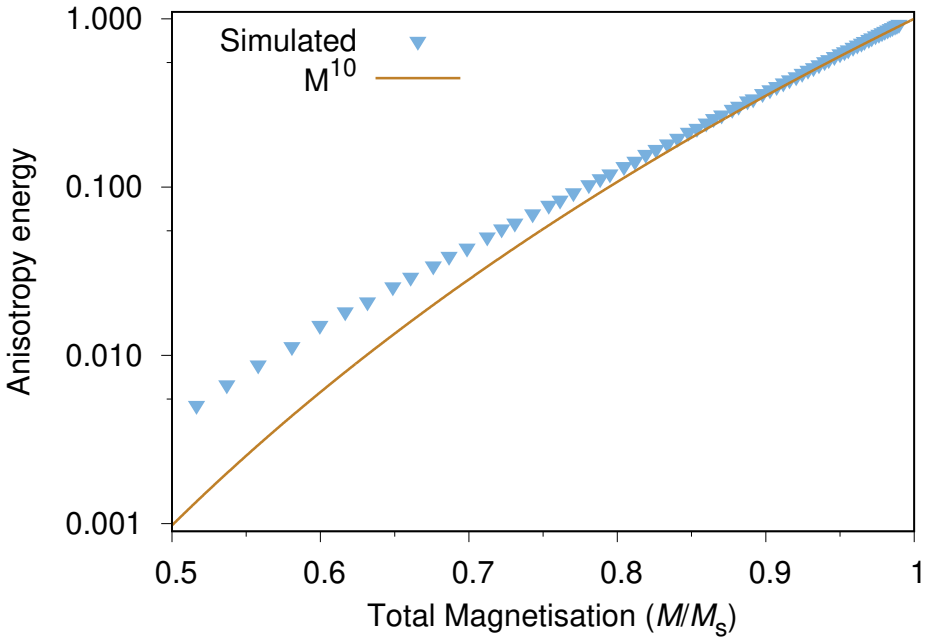

Figure 3.35: **Plot of the anisotropy scaling with magnetisation.** The anisotropy follows the M^{10} law at high magnetisation, when the system is fully magnetised and at low temperatures

interactions were limited to nearest neighbours only.

3.10 Conclusion

As magnetite is a well-studied material we are able to form a high quality model of atomistic spin dynamics. The structure of the unit cell of magnetite and related ferrites has been used to form a Hamiltonian made up of two components, the tetrahedral and octahedral sublattices of magnetite, which together form the overall magnetic properties of the system. This required a good understanding of the exchange constants and anisotropy energy of magnetite.

From our simulations we have also compared various methods for calculating precise values of physical parameters such as the Curie temperature and critical exponents of the system. The temperature scaling of magnetite has been explored for PBC systems which approximate bulk conditions, allowing us to compare our data with the experimental work done previously. With the help of a rescaling parameter, we were also able to correct the temperature dependent scaling to accurately reflect the quantum mechanical effects which take place in real world magnetic materials.

Next we shall explore how the properties of magnetite vary when it is in nanoparticle form and subject to topological effects.

CHAPTER 4

FINITE SIZE SCALING AND PARTICLE ELONGATION

4.1 Introduction

At small sizes where the number of atoms in a magnetic particle are in the order of 10^3 to 10^5, statistical effects occur due to the finite number of spins. These effects are described as finite size effects, with early studies into magnetic applications by D. P. Landau and K. Binder [94, 95] who used Ising models and Monte Carlo methods to predict how this affects more simple systems. This area of study has remained popular with other groups focusing on specific materials such as the recent work done by Jun Wang [96] looking at barium hexaferrite platelets. The finite size scaling (FSS) occurs irrespective of the dimensionality of the system, either in 3D nanoparticles, or 2D thin films [20, 97]. While this analysis has already been applied to magnetite [20, 98] using both experimental and computational approaches, much of the studies performed relied on simplifications such as particularly small systems sizes with low sampling at these scales, or model approximations such as the Ising model which fails to accurately model magnetite due to its constrained spin directions. This makes it difficult to model the intra and inter sublattice effects shown in chapter 3.4.2. Experimental studies have additional complexity due to the possibility of imperfect samples, particularly when dealing with less stable materials. It can also be very difficult to study nanoparticles with constrained sizes and more often a range of particle sizes is observed. The purity of the samples is also not easy to control as magnetite nanoparticles can exhibit rust, the formation of maghemite or hematite as well as other impurities depending on the materials and methods used to create the

sample.

Here, we try to model finite size systems using the 3D Heisenberg model and study both the overall magnetic properties, as well as any differences that occur at the sublattice level, to form a complete data set of finite size scaling from small particles of the order of one unit cell, to a system which approaches, at least asymptotically, a bulk magnetite system.

So far we have covered various magnetic properties we can use to assess the system. Periodic boundary condition systems give a good benchmark for bulk system properties, and we can now compare this with finite size systems which have broken exchange interactions at the surface. There are various types of finite size systems that we can explore, which highlight different properties. Here these shall be divided into spherical and faceted systems. Spherical nanoparticles can be formed, depending on experimental methods used, for various iron oxide nanoparticles [17] however these are often less stable. For this work, they have the benefit of maintaining the ratio of each sublattice despite their size. As the surface is terminated at the same radius over the whole particle, no sublattice or surface termination is preferred or dominant over another. Faceted particles suffer from exactly this issue. Many different types of faceted iron oxide particles have been seen in experiment [9, 99], their structures depending on the surface orientation and termination. In addition to finite size effects, these particles are usually dominated by the sublattice which terminates their composition. Of course, the separation between these types of particles is not always obvious as a highly faceted particle may be approximately spherical however we shall only deal with perfectly spherical nanoparticles and faceted particles with only two or three different surface orientations.

4.1.1 Spherical Nanoparticles

First we can look at spherical particles as they simplify two aspects of the finite size scaling that we will examine: the shape and surface. Roughly spherical particles can be formed in experiment and are often coated in silicon, for biomedical applications [100]. Their surfaces are usually not perfectly spherical however for now we shall approximate this and assume an ideal sphere.

To start we can look at the finite size scaling properties of spherical particles of diameters ranging between 2 and 16 nm diameter, or up to 20 unit cell widths. At this size range, we are dealing with fine nanoparticles containing up to roughly 100,000 magnetic atoms. Figure 4.2 shows the finite size scaling of these nanopar-

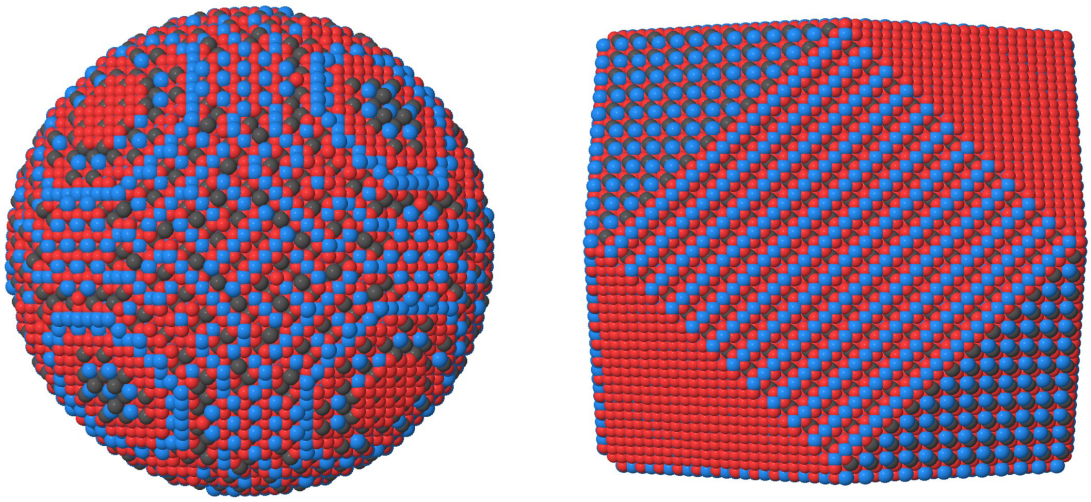

Figure 4.1: **Comparison of the surface of spherical and faceted nanoparticles.** While the spherical particle has a smooth transition between the layers of the sublattices at the surface, the faceted particle is dominated by an outer (red) oxygen and (blue) tetrahedral iron layer.

ticles. The exact diameters chosen are multiples of the lattice constant to maintain an ordered increase in particle size. As a side effect of recording susceptibility data at the same time, this magnetisation data is highly converged for each system, with the smallest requiring only minutes to calculate on modern hardware while for the largest it can take a full day to achieve high quality results.

For now, the magnetisation data is shown with no rescaling applied to first compare this data with the initial MvsT data. At 0 K the particles start at roughly the same magnetisation, and do not follow any order. This is down to the exact proportions of ions in the system but is roughly the same. From this point, the magnetisation lowers for each size however there is a noticeable spread in the magnetisation of the smallest system and the largest, increasing until just before the phase change at T_{C}. This change in magnetisation is around 10-15% lower for the 2 nm system over the low temperature range. In practice this becomes important for nanoparticle usage as the range of particle diameters produced in practice will therefore have a significant effect on the overall saturation magnetisation of the sample.

At the other end of the data, we see that smaller particles exaggerate the statistical effects seen above T_{C}. The 2 nm particle in particular comes to rest in a paramagnetic state with $0.05m$. At the lowest diameter, this particle is somewhat of an anomaly as it does not exactly follow the same scaling behaviour as all other particles. Looking at a visualisation of the particle, it becomes clear

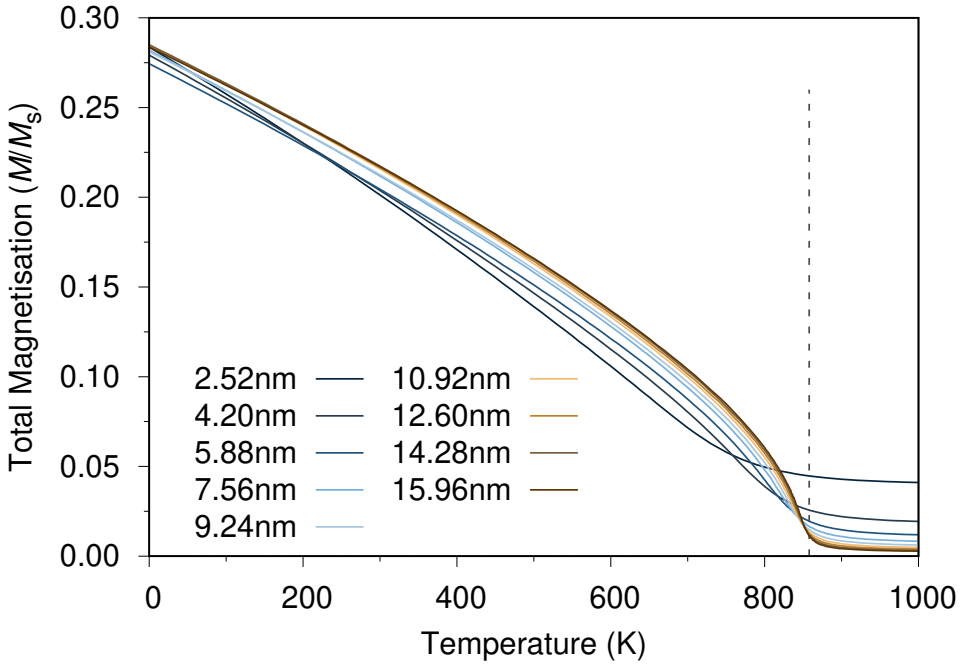

Figure 4.2: **Finite size scaling of spherical magnetite nanoparticles between 2 and 16 nm diameter.** While not bulk, the particles with increased size tend towards the largest, 16 nm system.

why this is the case. Containing under a thousand atoms, only a few hundred of which are magnetic, at this size the particle cannot be perfectly spherical, it is only 3 unit cells of magnetite in diameter. The facets of the underlying unit cell become apparent, creating flat surfaces and missing corners. Above this size, the particles follow a more ordered scaling as each particle succeeding particle is indeed approximately spherical.

At the Curie point, denoted by the dashed red line, we observe a new behaviour. The phase change occurs at lower temperatures for smaller particles and is sharper as the size increases. This is an early indication that fitting for the exact exponent, β, and Curie temperature using the magnetisation alone will be a difficult process and can be aided significantly with susceptibility data. Starting from the 4 nm particle, as we have explained that the 2 nm case can be somewhat of an anomaly, we can see that the magnetisation levels off earlier by around 20-30 K. The high temperature behaviour for nanoparticles is therefore highly dependent on the particle size.

When we apply rescaling, using the values of β and T_C calculated from the susceptibility, to correct the classical low temperature behaviour, the magnetisation scaling changes significantly below T_C. Below room temperature, there

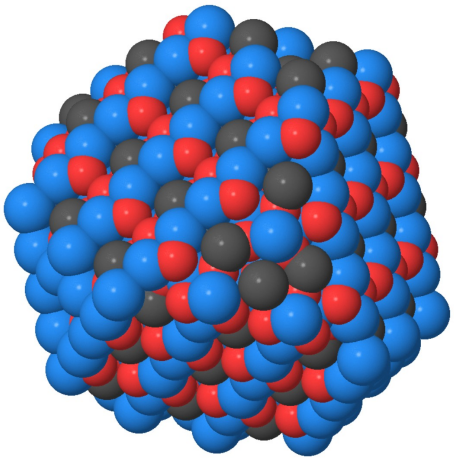

Figure 4.3: **2 nm particle of magnetite.** At 2 nm, the system is barely large enough to be cut in a roughly spherical shape due to the underlying unit cell structure.

is barely any change in the magnetisation which lowers by around 10% for all sizes. As the temperature rescaling does not affect the Curie temperature point of any system, we still see clearly that the Curie point occurs earlier for smaller nanoparticles.

The differences between rescaled and non-rescaled data is most apparent when looking at the magnetisation scaling. The low temperature magnetisation should deviate slowly from its value at 0 K and decrease more quickly towards T_C. This is not the case in the classical data as the magnetisation decreases in an almost linear fashion. The overall susceptibility is difficult to distinguish and therefore we shall only show the rescaled susceptibility here. In general, the susceptibility shows thinner peaks at all sizes when rescaled and maintains near zero susceptibility for the whole of the low temperature region. Figure 4.5 shows the susceptibility scaling for these nanoparticles.

The susceptibility peaks can be used to accurately find the Curie temperature of each system however we can see that the peaks not only differ in temperature but also magnitude. At lower particle sizes, the susceptibility peaks are both broader and lower. This is possibly due to the increased ability in larger particles for small pockets of spin domains to align more closely to each other, leading to increased spin correlation and hence an increase in the magnitude of the susceptibility. The susceptibility data also makes it much easier to see by how much the critical point decreases in temperature for smaller particles. Here, the 2 nm system peaks around 100 K lower than the largest system. This decrease in the Curie temperature is relatively minor for systems above 8 nm but becomes

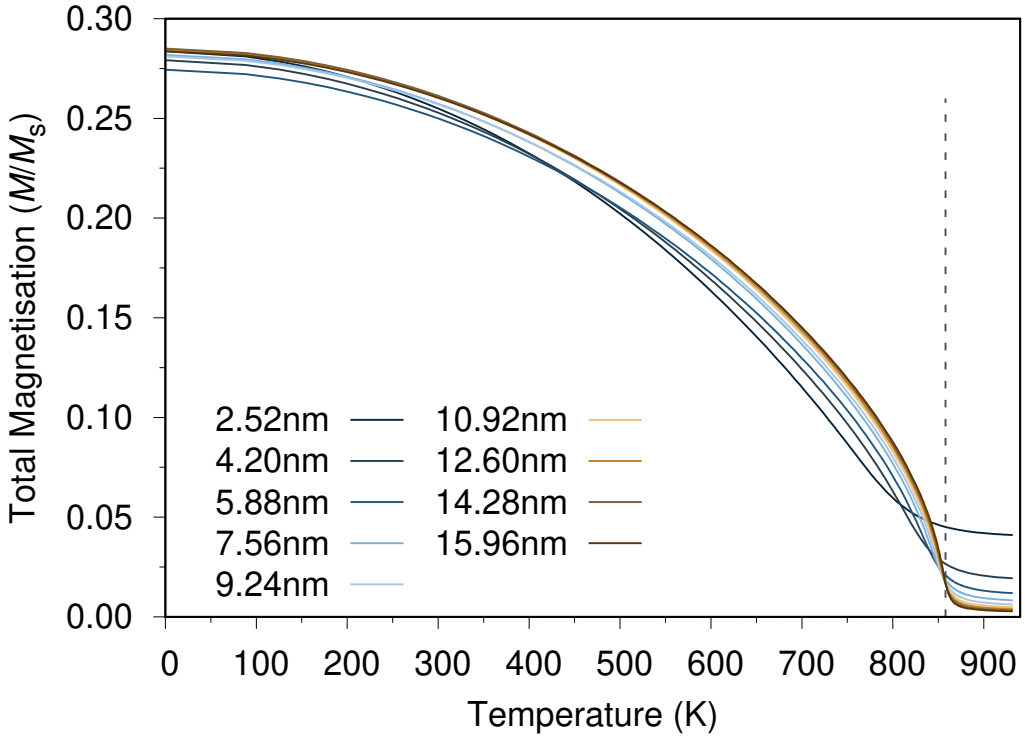

Figure 4.4: **Rescaled magnetisation scaling for spherical nanoparticles.** The lowering of the magnetisation is much more gradual, and each curve reaches T_C more steeply.

much larger below this threshold. The exact values of the Curie temperature and β extracted from the magnetisation and susceptibility plots are shown in Table 4.1 and plots of this data, as well as sublattice scaling data is shown in Figure 4.6.

Particle Diameter (nm)	Curie Temperature (K)	β
2.52	680	0.670
4.20	780	0.679
5.88	809	0.635
7.56	829	0.620
9.24	835	0.601
10.92	843	0.603
12.60	844	0.587
14.28	847	0.582
15.96	850	0.579

Table 4.1: **Fit β and T_C for spherical magnetite nanoparticles.** The Curie temperature increases toward bulk values with increased particle size while the exponent lowers slowly.

For all components of the nanoparticle the Curie temperature decreases with particle size however the overall Curie temperature is predicted to be lower than that from the sublattices. This might be due to the individual lattices individually maintaining some level of magnetisation close to T_C. At higher temperatures,

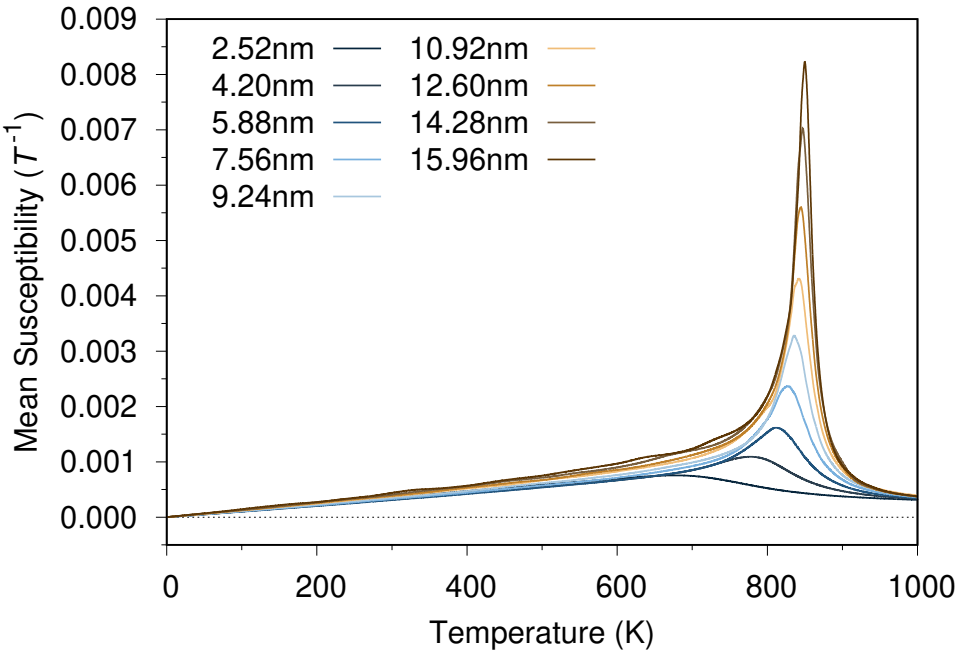

Figure 4.5: **Rescaled susceptibility scaling for spherical nanoparticles.** The magnitude of susceptibility increases with size and is possibly related to domain formation in larger particles.

the data points lie exactly on top of each other due to the 1 K temperature resolution. What is somewhat surprising from this data is the near levelling off of the Curie temperature at the largest particle sizes. 16 nm diameter particles are still considered to be fine and should be far from bulk properties however within the parameters set out for this study, the Curie temperature is close to reaching a bulk state. Compared to some of the periodic boundary condition systems looked at earlier, the largest T_C fitted here is around 850K, 8 K lower than experimental bulk T_C and around the same value of T_C extracted from our 16 nm PBC system. Hence, it is the contributions from the structural strain at the surface of the nanoparticle, and the formation of antiphase boundaries which cause the different magnetic properties to bulk.

The β scaling is quite different however as it does not seem to be fully converged for the 16 nm particle. The individual sublattices are relatively flat, with noticeably difference values for β at all sizes. Due to the sublattices having different values of β to the overall system, it is difficult to use rescaling on the sublattice data as they require different values of α. Ideally a value of alpha is found by fitting the Curie-Bloch equation to experimental sublattice data, however no such data currently exists. The overall α exponent can be used as a substitute however it is likely to be inaccurate for the sublattices.

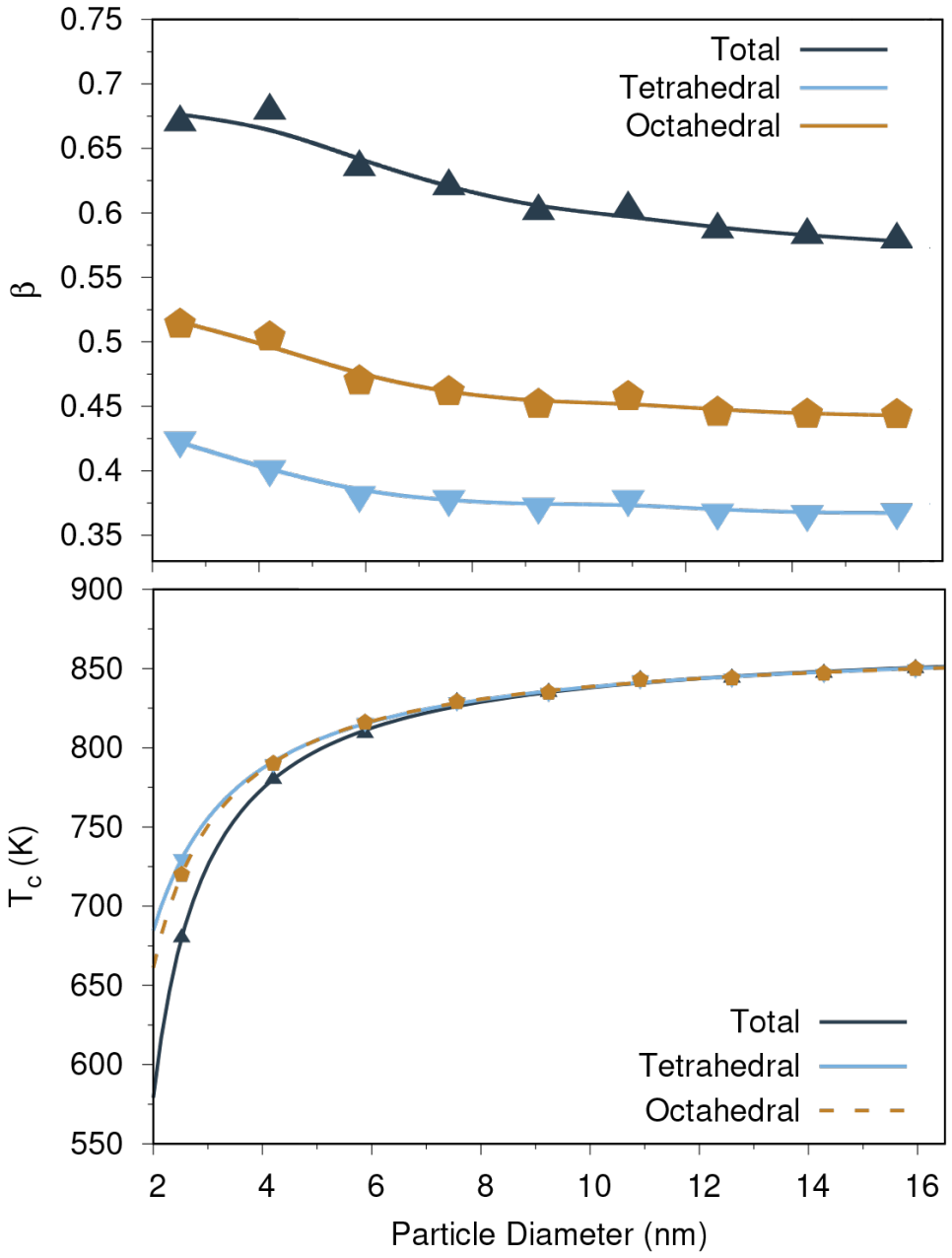

Figure 4.6: **Curie temperature and β scaling with size for the overall and sublattice components of spherical nanoparticles of magnetite.** The Curie temperature tends to bulk with increasing size while the value of β has not converged fully.

4.1.2 Faceted Nanoparticles

The method used to generate arbitrarily faceted nanocrystals is shown in Figure 4.8. We first create a large single crystal of magnetite of size $4r$ along each spatial direction where $2r$ is the intended particle size. We then define fractional radii along the different crystal directions r_{100}, r_{110} and r_{111} defining the extent of truncating planes along the respective crystal directions in the positive quadrant

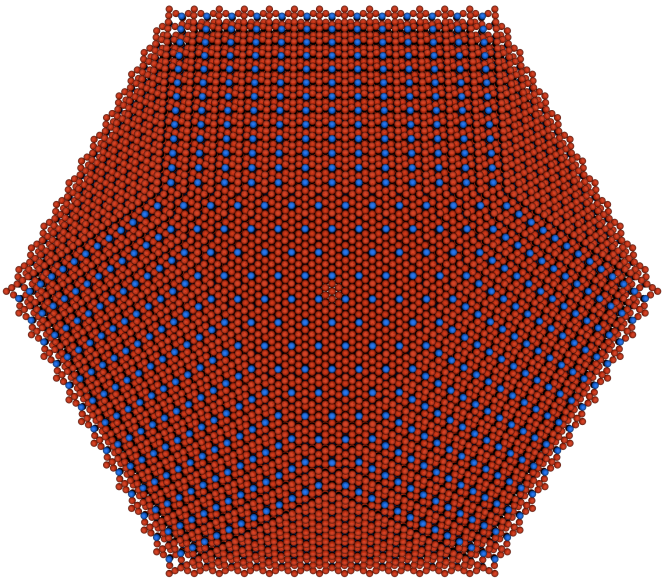

Figure 4.7: **Head on look at the surface of a faceted nanoparticle.** Red spins show tetrahedral atoms while blue spins are octahedral. Due to the nature of faceting, one ionic species dominates the surface of the nanoparticle.

$(|x|, |y|, |z|)$. Atoms between these planes and the origin are retained within the particle and the rest are deleted, leaving a faceted nanoparticle. The choice of relative radii therefore selects the shape of the particle, for example if $r_{100} = 2r$, $r_{110} = 2r$ and $r_{111} = r\sqrt{3}$ this will construct a regular octahedron particle with diagonal diameter $2r$.

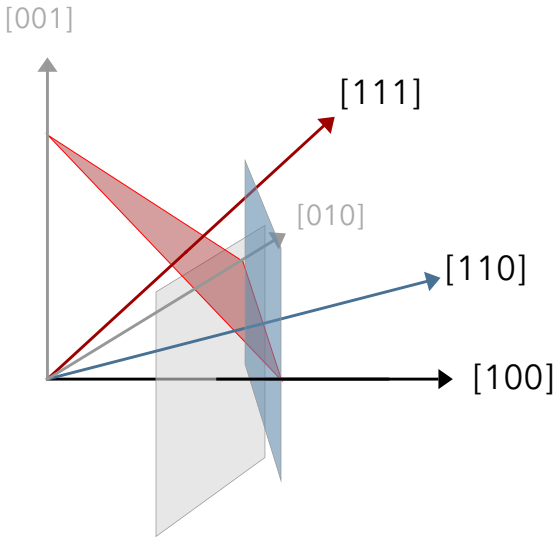

Figure 4.8: **Schematic illustration of how faceted nanoparticles are constructed.** The particles are cut from a single crystal of magnetite. Planes perpendicular to the [100], [010], [001], [110] and [111] crystal directions define the limits of the particle along each direction as a function of particle size r. Atoms between the origin and all defined planes are kept within the particle.

Faceted nanoparticles require extra care when analysing magnetisation data as the system tends to be dominated by one of the sublattices which can deviate the system from an overall magnetisation of around a third. In addition, when changing the size of the nanoparticle to study finite size scaling data, it is difficult to maintain the same surface type for each system as there are several layers of tetrahedral and octahedral iron atoms with different densities and the faceted particle generation does not distinguish between the ionic species. This can lead to magnetisation data as shown in Figure 4.9 where a spread of magnetisation values at 0 K leads misleading magnetisation curves for the given data set. The intersection point of the curves is not a physical phenomenon but arises due to the statistics of the data. It is therefore required to normalise the data set as rescaling cannot be applied properly without the curves starting from the same (or very close) starting point.

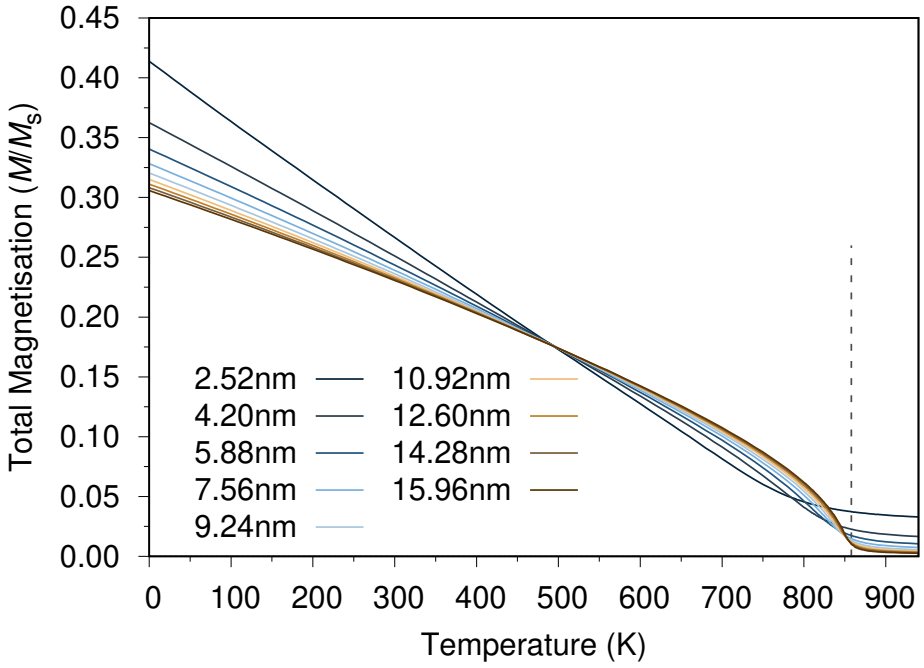

Figure 4.9: **Non-normalised MvsT of faceted Fe_3O_4.** Faceted particles of varying size cause a spread of magnetisation curves due to the different overall densities of each sublattice between the particles. The intersection point arises due to the statistical properties of the size distribution.

Once the data is normalised, the magnetisation curves are very similar to those seen in the spherical nanoparticles. The plots for the smallest, 2 nm, system is better behaved as the system can be cut more easily into a faceted particle and contains more atoms overall than a spherical particle of equivalent diameter.

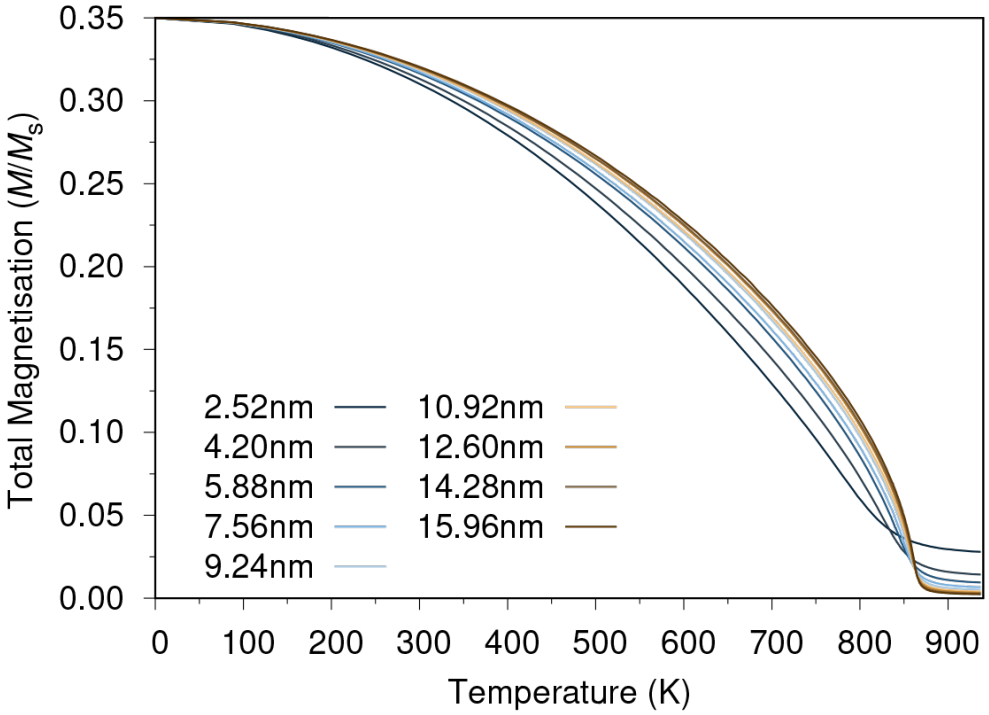

Figure 4.10: **Normalised MvsT of faceted Fe_3O_4.** After normalisation, the magnetisation versus temperature curves of faceted particles such as cubeoctahedra are similar to those produced by spherical nanoparticles. Faceted particles generally contain more atoms than cubeoctahedra, due to how their diameter is measured, leading to a more ordered set of FSS data.

4.1.3 Periodic Systems

From looking at both spherical nanoparticles and different faceted nanoparticles, we can see that the general tendencies of finite size scaling are the same with some small changes depending on the surface to volume ratio of the particle, with spheres having the lowest, and the included complexity of faceted particles being dominated by a particular surface leading to a spread of initial magnetisation values at low temperature. There is however one further case of finite size scaling that we can analyse which gives a key insight into the cause of the FSS effects. Periodic boundary condition systems have so far been used to replicate bulk properties by using a large cell of the material which is repeated using boundary conditions on each axis. This method provides an easy way to simulate much larger blocks of the material without needing to calculate the extra exchange interaction associated with the larger system. The size of the initial block has a large impact on the physics of the simulation however as small blocks down to the size of the unit cell are not appropriate for all simulations. When the unit cell can be used for hysteresis calculations where strong fields bound the spin orientation and the external field becomes the largest component of the system Hamiltonian,

in Curie temperature simulations, the spins must be able to relax naturally hence the most significant component in the Hamiltonian is the exchange. In a PBC system, spins on either end of the unit cell are repeated in the neighbouring block and therefore influence the spins in adjacent blocks. With a small initial unit cell, where the same spin can influence its replica in a neighbouring cell significantly, this leads to an effective increase in the exchange strengths of the system. Hence, depending on the initial system size, the Curie temperature as well as other magnetic properties of the system can change depending on the system size (the size of the original cell).

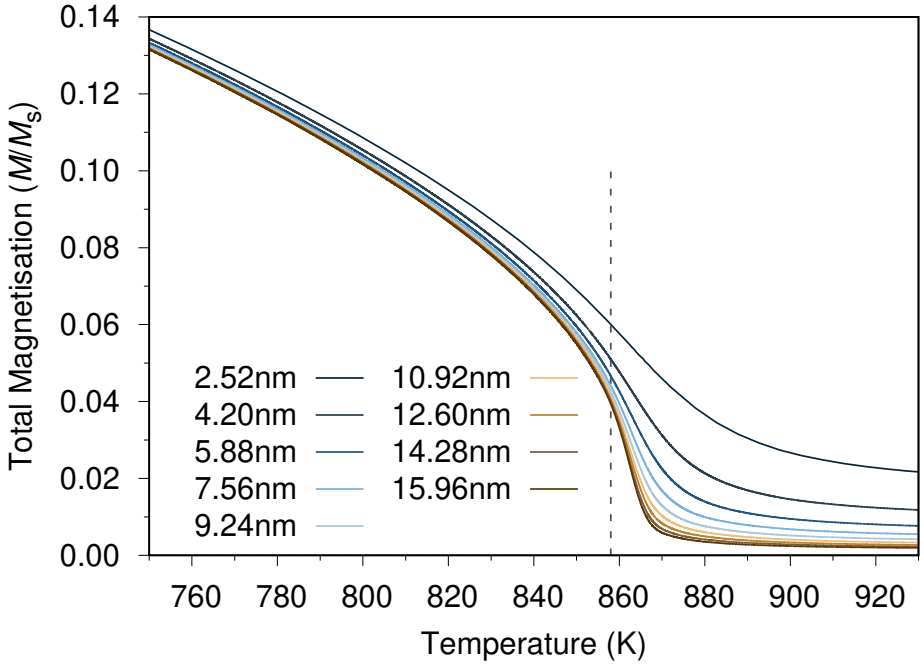

Figure 4.11: **Finite size scaling effects in PBC systems of magnetite with core sizes between 2 and 16 nm.** For all sizes, the Curie temperature is overestimated due to the higher effective exchange in the system.

For comparison with the nanoparticles seen earlier, we simulate PBC systems of magnetite with a core cell size between 2-16 nm. We find that for all core sizes, the Curie temperature is now overestimated, with the largest systems size, 16 nm, tending towards bulk. The deviation of the Curie temperatures from the values found in experiment for bulk, 858K, is much lower than that found in the nanoparticles where the smallest particles had a fit T_C around 100 K lower than bulk.

The main difference in system properties between the nanoparticles and PBC systems is the lack of a surface on the periodic systems. There are no missing exchange bonds as the system is continuous, therefore the surface is the main

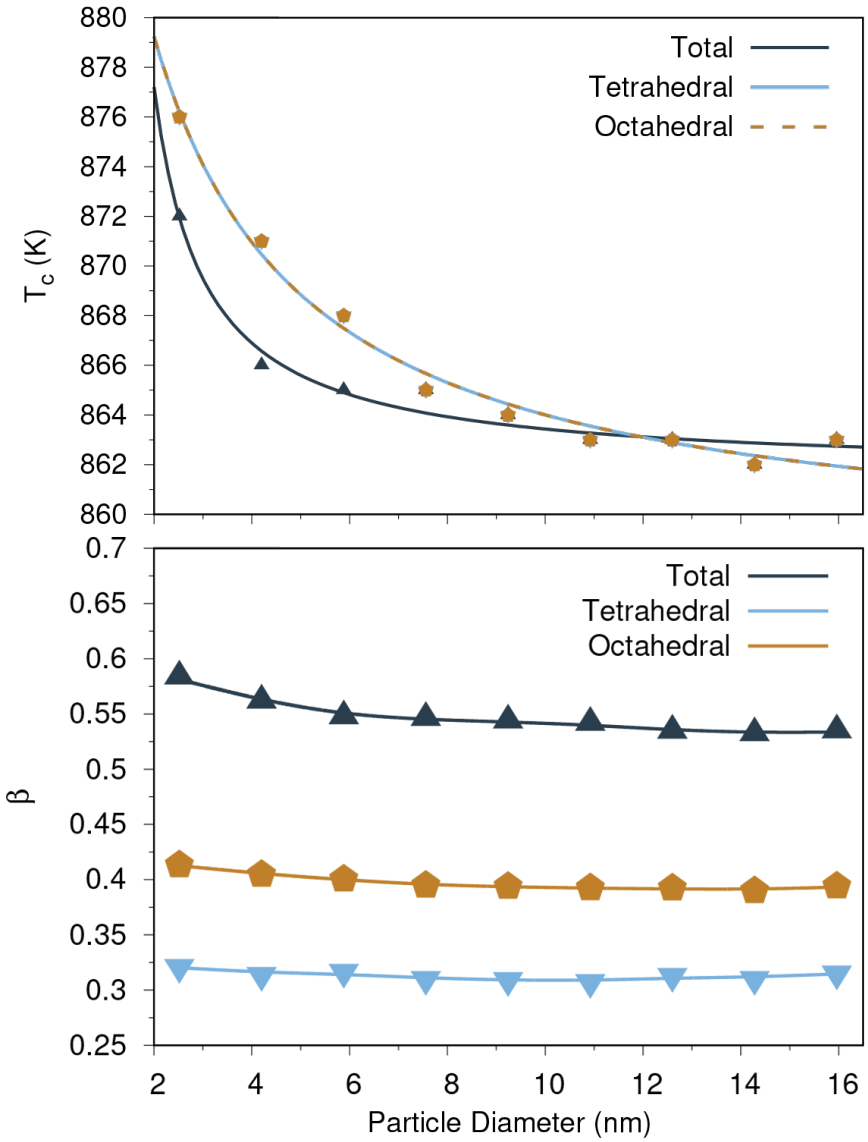

Figure 4.12: **Curie temperature and β scaling of PBC systems of magnetite.** The sublattices have a noticeably different T_C scaling to the overall system for low sizes. Unlike in nanoparticles, β quickly converges to a near constant value for all components of the system, with lower values overall.

cause of the finite size effects we have seen so far in this chapter. This surface effect is also separate from those derived from any tension found in synthesised or natural nanoparticles as well as and shift of the surface structure as described earlier in the chapter. Without being able to model these effects we have still found significant reduction in the Curie temperature of the system as well as of the saturation magnetisation at all temperatures.

For these systems, the critical exponent β, shown in Figure 4.12, also scales slightly differently. From even the smallest periodic systems, β maintains a near

constant value for all components of the system, unlike the nanoparticles where the values for the overall system had not fully converged. The values for β are still lowered across the board with the tetrahedral and octahedral sublattices at 0.313 and 0.392 respectively and the overall system at 0.541.

4.2 Particle Elongation

Particle size effects are not constrained to uniform size changes, some effects are only observed when a single axis of the particle is increased. The magnetocrystalline anisotropy can be affected by particle elongation, changing the magnetic properties of the system from superparamagnetic to a blocked ferrimagnetic state. So far, we have covered intrinsic contributions to the anisotropy such as uniaxial or cubic. Magnetite itself is subject to cubic anisotropy [101] however this is not necessarily the largest contribution to the effective anisotropy, K_{eff}. Cubic anisotropy itself is much smaller than would be expected from the usual anisotropy constants K_1 and K_2 due to the nature of the energy surface. The effective anisotropy is $K_{\text{eff}} = K_1/4$ for $\langle 100 \rangle$ easy and $K_{\text{eff}} = K_1/12$ for $\langle 111 \rangle$ easy axis systems, the latter being the case for most ferrites including magnetite. Surface anisotropy can also have significant effects on the structural [102] and magnetic properties [103], and is difficult to model due to its dependence on the surface termination of the nanoparticles. While some surfaces such as the [100] termination are found to have a large surface anisotropy contribution [104], these surfaces are also likely to be unstable due to their polar nature at the interface. As we cannot model structural changes at the surface of nanoparticles, and the strength of the surface anisotropy is highly variable, we cannot correctly factor it into our low temperature calculations. Shape anisotropy, or the anisotropy contributions due to changes in the elongation of the system, are more easily modelled and may also dominate the effective anisotropy [105].

Shape anisotropy is related to the demagnetising field, which opposes and is caused by the magnetisation of the particle. The energy of the field is given by

$$\mathscr{H}_{\text{demag}} = \frac{1}{2}\mu_0 \mathbf{M} \cdot (\bar{\bar{N}}\mathbf{M}) \tag{4.1}$$

where $\mu_0 = 4\pi \times 10^{-7}$ is the permeability of free space, $\mathbf{M}$ is the vector magnetisation and $\bar{\bar{N}}$ is the demagnetisation tensor, which depends on the shape and geometry of the system. For simple elongated systems which we shall use here,

the off-diagonal components of the demagnetisation tensor are small and $\bar{\bar{N}}$ can be approximated by a diagonal matrix:

$$\bar{\bar{N}} \approx \begin{pmatrix} N_{xx} & 0 & 0 \\ 0 & N_{yy} & 0 \\ 0 & 0 & N_{zz} \end{pmatrix} \tag{4.2}$$

Hence Equation 4.1 expands to:

$$\mathscr{H}_{\text{demag}} = \frac{\mu_0}{2} \begin{pmatrix} M_x & M_y & M_z \end{pmatrix} \begin{pmatrix} N_{xx} & 0 & 0 \\ 0 & N_{yy} & 0 \\ 0 & 0 & N_{zz} \end{pmatrix} \begin{pmatrix} M_x \\ M_y \\ M_z \end{pmatrix} \tag{4.3}$$

$$\mathscr{H}_{\text{demag}} = \frac{\mu_0}{2}(N_{xx}M_x^2 + N_{yy}M_y^2 + N_{zz}M_z^2) \tag{4.4}$$

For a uniformly magnetised particle elongated along the z-axis the perpendicular components of the demagnetising energy are the same. Considering the change in energy for a rotation of the magnetisation in the x-z plane the z and x components of the magnetisation are related by $M_x^2 = (1 - M_z^2)$. Applying the substitution $M_z = m_z M_s$, where M_s is the saturation magnetisation, yields an effective shape anisotropy of

$$\mathscr{H}_{\text{shape}} = \frac{\mu_0 M_s^2}{2}(N_{xx} - N_{zz})m_z^2 \tag{4.5}$$

Combining the shape and cubic anisotropy contributions, we get

$$\mathscr{H}_{\text{eff}}(\mathbf{m}) = +\frac{K_c}{2}(m_x^4 + m_y^4 + m_z^4) + \frac{\mu_0 M_s^2}{2}(N_{xx} - N_{zz})m_z^2 \tag{4.6}$$

where $\mathbf{m}$ is a unit vector with components m_x, m_y, m_z describing the magnetisation of the particle and K_c is the effective cubic anisotropy.

Nanoparticle elongation is not uncommon in experimental samples, with different elongation lengths in the range 0-20% [106]. While larger elongations will have a stronger effect on the anisotropy, it is worth simulating the effect of elongations within this range as they are more likely to occur. Figure 4.13 shows the orientation dependence in spherical polar coordinates of the effective anisotropy

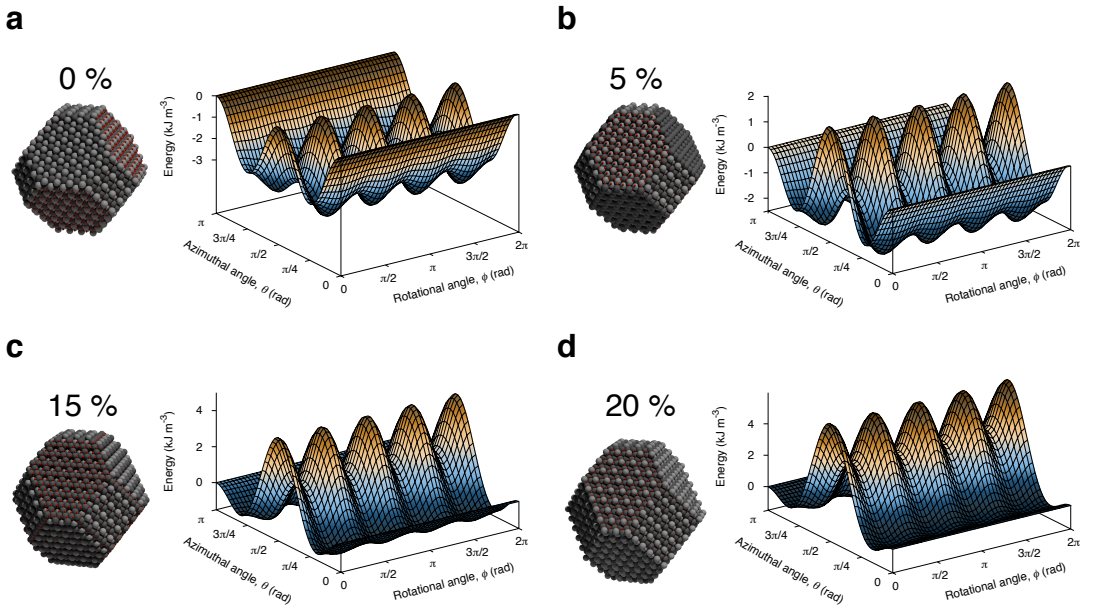

Figure 4.13: **Plots of the effective anisotropic energy surface for elongated truncated octahedron nanoparticles.** All particles have a lateral size of 6 nm along the x, y directions but different elongations: 0% (a), 5% (b), 15% (c), and 20% (d). The data shows that the cubic anisotropy makes a significant contribution to the effective anisotropy for all elongations with rotational energy barriers existing up to 15% elongation. Figure from Ref. [3].

energy for a 6 nm (in x and y) particle size for different z elongations. When the particle is perfectly uniform, Fig. 4.13(a), the energy surface is completely cubic, with 8 energy minima corresponding to the ⟨111⟩ crystal directions. When the particle is elongated, the shape contributions to the anisotropy increase maxima around the x,y-plane. This is effectively an increase in the energy barrier between the stable energy minima of the easy axis directions. While the shape anisotropy contributions grow to around five times larger than those of the cubic anisotropy, at 20% elongation, the energy surface retains a cubic shape.

We can simulate elongated nanoparticles and their time-dependant behaviour using the stochastic Landau-Lifshits-Gilbert equations described in Chapter 2.3.1. To show the effects of elongation on the particle anisotropy, the particle size and temperature must be tuned as the cubic anisotropy energy maintains a superparamagnetic state during the low temperature (<250 K) regime. In addition, particle elongations increase the magnetic volume of the particle by a significant amount for large elongations, further strengthening the intrinsic particle anisotropy. For our simulations, a temperature of 300 K with 12nm nanoparticles was found to be a turning point at which the shape anisotropy showed noticeable effects on the magnetisation dynamics of the system.

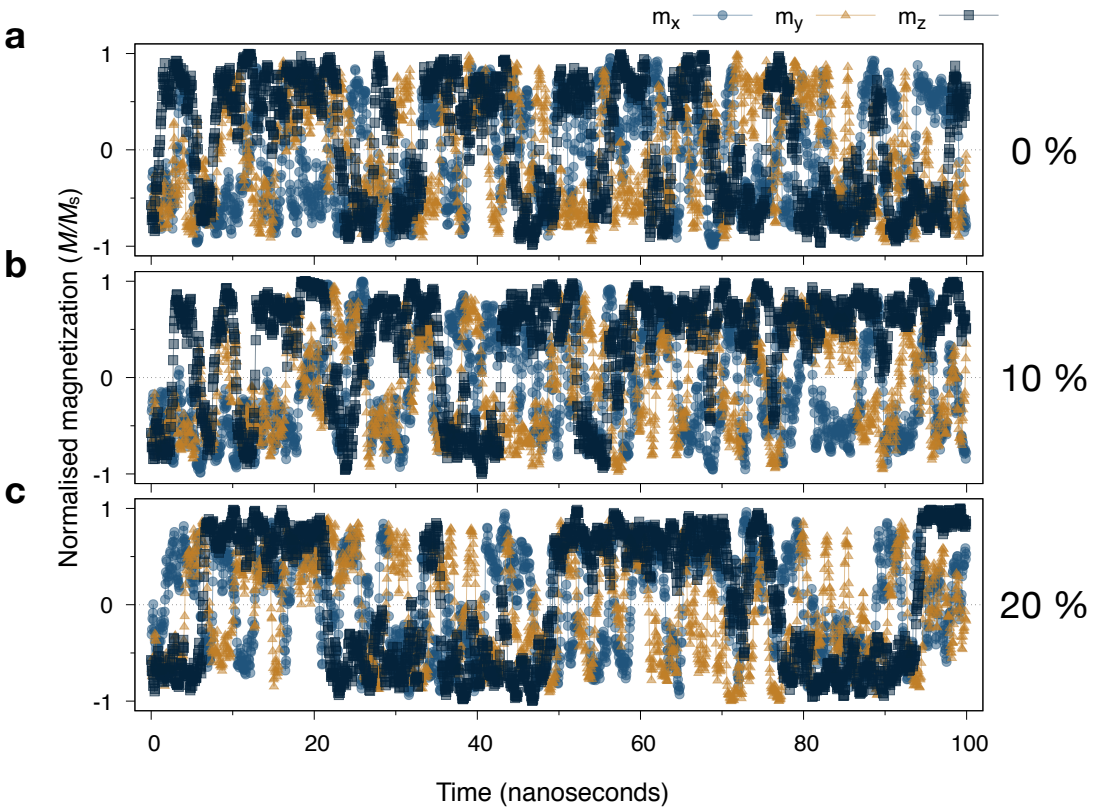

Figure 4.14: **Magnetisation components of elongated magnetite nanoparticles.** Plot of the time dependence of the magnetisation components for a 12 nm diameter octahedral nanoparticle for (a) 0%, (b) 10% and (c) 20% elongation at $T = 300$ K. The z-component data shows a transition from a fully superparamagnetic regime for the isotropic particle to a partially blocked regime for a particle with 20% elongation. The rotational components (transitions in x,y) are superparamagnetic in all cases.

The magnetic relaxation of superparamagnetic nanoparticles is determined by the energy barrier ΔE between stable minima, and is governed by the Arrhenius-Néel law

$$\tau = \frac{1}{f_0} \exp\left(\frac{\Delta E}{k_B T}\right) \tag{4.7}$$

where τ is the relaxation time, $f_0 \sim 10^9$ is the attempt frequency, $k_B = 1.380649 \times 10^{-23}$ J/K is the Boltzmann constant and T is the temperature. The energy barrier, ΔE, is determined from Equation 4.6. Figure 4.14 shows the switching dynamics of a 12 nm diameter nanoparticle simulated over 100 ns for different particle elongations. Uniform particles, Fig. 4.14(a), show superparamagnetic behaviour in x, y and z orientations. The thermal energy of the system is enough to overcome the energy barrier and the system spends time

equally in the 8 easy axis directions. A large time scale is required to see the effects of particle elongation as even at 0% elongation, the system is metastable along the different orientations, spending around 2-5 ns in each before switching. At 10% elongation, Fig. 4.14(b), the spin switching has slowed and there are fewer transitions along the $\pm z$-axis due to the increased shape anisotropy. This effect is not drastic however and despite the significant change in particle shape, the increased number of magnetic volumes simultaneously increases the cubic anisotropy which maintains a similar regime. At 20% elongation, Fig. 4.14(c), the shape anisotropy and increased energy barrier has stopped more transitions occurring. The system now spends around $\tau \approx 15$ ns in each orientation. This is still much shorter than the blocking times found in experimental measurements of individual nanoparticles which are in the microsecond timescale [107], likely indicating that surface anisotropy, which we are unable to show here, has a more significant effect on small particles with elongations around 20%.

4.3 Conclusion

The temperature scaling properties of magnetite are heavily affected by finite size effects. The magnetisation of nanoparticles can be reduced by more than 10% at room temperature which is significant for applications which require a fine understanding of the overall magnetic properties of a sample. In addition, the shape of the nanoparticles may have more nuanced effects on the temperature scaling due to the dominance of a sublattice at the surface of the particle. When comparing PBC systems to nanoparticles, we find that most of these effects are dependent on the surface to volume ratio of particle, with larger ratios causing exponentially higher deviations of the magnetic properties from bulk. By using methods from the previous chapter, we were able to accurately model the changes to the Curie temperature and β parameter of the system when nanoparticles were small, leading to longer phase transitions and difficult to fit magnetisation curves.

We have also modelled non-uniform changes to the particle size, which can change the low temperature magnetic properties of the particle from a fully superparamagnetic state to a partially blocked state, depending on the elongation of the system along a particular axis. While this does not fully capture the experimental anisotropy of the nanoparticles, which are found to be fully blocked for a longer time scale, we have developed a more sophisticated model of the anisotropy which is important for the future development of magnetic hyperthermia where nanoparticle properties should have reproducible heating properties

with a narrow distribution of size and magnetic properties.

Next, we shall look at a closely related material, maghemite, which shares many traits with magnetite but is less stable and, because of this, less well reviewed in the literature.

CHAPTER 5

MAGHEMITE

5.1 Introduction

Maghemite, not to be confused with magnetite, is another well-known magnetic iron oxide that has been studied for more than a century. In nature it occurs near iron oxyhydroxide rich minerals as a brown or yellow pigment in terrestrial sediments and soils. Synthesis of impure maghemite has been documented since the 19th century, according to the 1837 textbook of Schubarth [108]. The alchemist Kunckel had already synthesised maghemite by heating metallic iron in air until red-hot. Initially, likely due to impurities, the samples of maghemite were thought to be paramagnetic and its use was restricted to pigments or as an abrasive material. Through oxidation of magnetite, a method still used today, Baudisch and Welo [109] explored the magnetic properties of maghemite but were not able to distinguish these properties as being intrinsic to maghemite rather than a remnant from magnetite or other iron oxide impurities.

Maghemite and its structure was characterised in the early 20th century, noting the distinction between hematite, another iron oxide with a closely related chemical structure, and magnetite, which is structurally the closest. While hematite, an antiferromagnetic material then thought of as paramagnetic (this was before Néel developed the concept of antiferromagnetism [6]), was noted to be stable, maghemite was found to be unstable even at room temperature [110], with an inverse spinel defect structure. Much like magnetite, it was not immediately realised that maghemite was not ferromagnetic, as in elemental iron,

but ferrimagnetic due to its more complicated structure.

One of the first uses of maghemite had to do with one of the early technological advances in the 1930-40s, the magnetic tape. Initially made using carbonyl iron, these were later improved through the usage of magnetite and then maghemite with the development of acicular (needle shaped) magnetic particles [111]. More recently, they have been used along with other iron oxides for biomedical applications due to their biocompatibility and relative ease of synthesis. Paired with a surface coating of various possible materials such as silica, PVA or dextran, it has seen use as a magnetic drug carrier, able to carry cytotoxic drugs, or target antibodies [112]. Another important field of study is magnetic hyperthermia involving the catabolism of tumours by magnetic heating of the nanoparticles. These studies date back to 1957 when Glichrist *et al.* heated various tissue samples with 20-100 nm size particles of maghemite exposed to a 1.2MHz magnetic field [15]. Finally, maghemite nanoparticles are a promising material for adsorption of heavy metals from industrial wastewater due to their adsorption efficiency and reusability and recoverability, making them distinct from similar iron based materials which are more difficult to recover and become a secondary waste product [16, 113].

5.2 Structure

The simple chemical formula of maghemite is Fe_2O_3 however there are several other minerals that share the same formula. In the 1987 edition of his book, Wells mentions four different Fe_2O_3 phases [114] which had been studied: the thermodynamically stable, almost non-magnetic, hematite phase α-Fe_2O_3 which has a trigonal corundum structure [115]; two less stable phases known as β-Fe_2O_3, a body-centred cubic oxide which converts to hematite at high temperatures, and ϵ-Fe_2O_3, a rhombic phase which is difficult to prepare without impurities [116]; and a probably cubic phase which would be known as γ-Fe_2O_3, due to a proposal of Haber as γ-Fe_2O_3 can be made from dehydrating needle-shaped γ-FeOOH crystals.

The exact structure of maghemite was uncovered through the oxidation of magnetite. When Fe_3O_4 is oxidised directly, Fe^{2+} is converted to Fe^{3+} within the spinel structure and compensating iron vacancies appear in the octahedral sublattice. The defective spinel structure is remarkably robust and can accommodate the full range of stoichiometry between Fe_3O_4 and Fe_2O_3. In the extreme case, all Fe is oxidised to Fe^{3+}, and maghemite is formed. γ-Fe_2O_3 is metastable against transformation to α-Fe_2O_3 but exists partly because the conversion from

the spinel to corundum structure requires the O^{2-} lattice to be converted from face centred cubic (fcc) to hexagonal closest packed (hcp). In contrast, switching between γ-Fe_2O_3, Fe_3O_4 and $Fe_{1-x}O$ is remarkably fluid because this only requires a rearrangement of the cations within the fcc oxygen lattice. Impurities can make this process more difficult. When oxidising magnetite it is important to have no traces of hematite as these act as nucleation sites for the formation of more α-Fe_2O_3.

Hence maghemite holds a similar structure to magnetite, but with iron vacancies appearing in the octahedral sublattices. The exact nature of these vacancies has also taken some time to understand. There are three different variations of maghemite which can form depending on the size of the crystals and preparation conditions [117], which have different orders for the vacancies:

- A cubic structure with random distributions of the vacancies (Fd-3m) [118]
- Vacancies distributed as the Li cations in $LiFe_5O_8$ ($P4_332$) [119]
- An ordered distribution of the vacancies with tetragonal symmetry and a three-fold doubling along the c-axis ($P4_12_12$) [120]

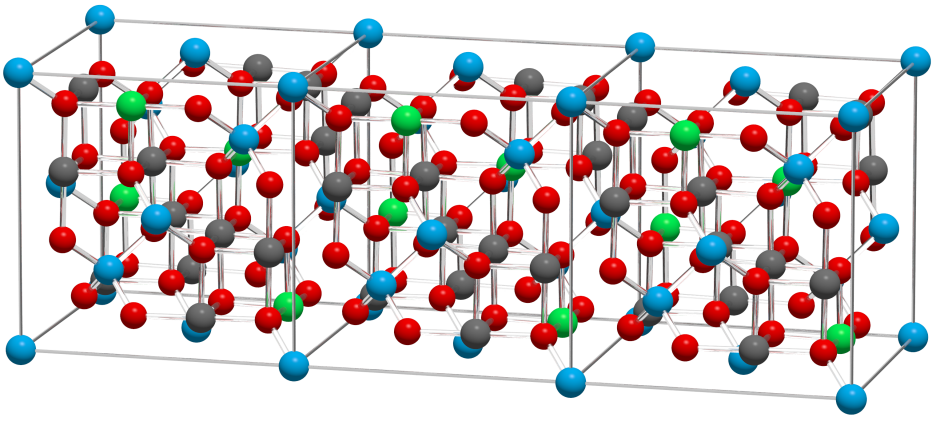

Figure 5.1: **Maghemite unit cell vacancies.** Octahedral lattice iron vacancies (green) occur in the $P4_332$ crystal group structure. As this structure still involves a measure of disorder, only 2/3 of these sites are actually vacant with a random distribution of Fe^{3+} filling the rest.

The first studies that indicated a departure from the Fd-3m symmetry were reported by Haul and Schoon [121], who noticed extra reflections in the powder diffraction pattern of maghemite prepared by oxidising magnetite. In the space

group $P4_332$ of lithium ferrite, there are two types of octahedral sites, one with multiplicity 12 in the unit cell, and one with multiplicity 4, which is the one occupied by Li. In maghemite, the same symmetry exists if the Fe vacancies are constrained to these Wyckoff 4b sites, instead of being distributed over all the 16 octahedral sites. This configuration still has a level of disorder as the 4b sites have fractional iron occupancies. A more ordered vacancy distribution involves a tetragonal distortion where the primitive unit cell is a superstructure with lattice constants $c/a \approx 3$. This ordered maghemite structure has the tetragonal space group $P4_12_12$. The exact positions of these vacancies have been refined by Jorgensen *et al.* based on synchrotron x-ray powder diffraction data [120]. The fractional positions are shown in Table 5.1.

	Coordinates		
Position label	x	y	z
L1	7/8	3/8	1/24
L2	1/8	7/8	3/24
L3	5/8	5/8	5/24
L4	3/8	1/8	7/24
L5	7/8	3/8	9/24
L6	1/8	7/8	11/24
L7	5/8	5/8	13/24
L8	3/8	1/8	15/24
L9	7/8	3/8	17/24
L10	1/8	7/8	19/24
L11	5/8	5/8	21/24
L12	3/8	1/8	23/24

Table 5.1: **Coordinates of the 12 possible vacancy sites in the maghemite supercell.** These positions correspond to the Wyckoff 4b sites of cubic space group $P4_332$, expanded to a $1 \times 1 \times 3$ supercell. Table adapted from Ref. [118]

To determine which of these very similar structures is lower in energy, studies have been done using DFT (explained in 3.2.3); Grau-Crespo *et al.* modelled both systems to determine this and examine more closely the band structure of the lower energy system [118]. The supercell for maghemite in the disordered phase is shown in Figure 5.1. Each unit cell is isostructural with the magnetite unit cell shown in Chapter 3, however the possible vacancy sites are highlighted in green. These sites have a 1/3 Fe^{3+} occupation randomly distributed throughout. Figure 5.2 shows the $P4_12_12$ phase of maghemite with thirty six missing bonds compared to Figure 5.1, and eight missing Fe^{3+}. This supercell exhibits no disorder and is consistent throughout the material. This distribution of vacancies is distinctive as it creates the maximum possible homogeneity of iron cations and vacancies over

the possible sites. In this configuration, vacancies never occupy three consecutive layers.

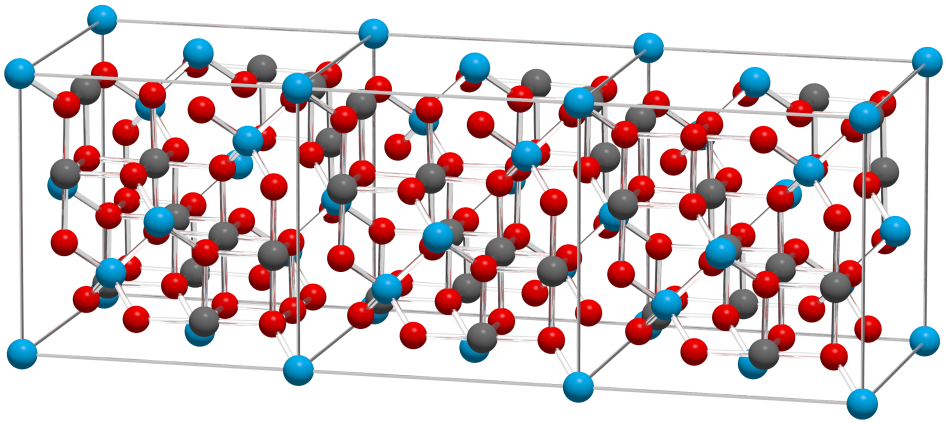

Figure 5.2: **Maghemite supercell in the $P4_12_12$ phase.** Eight Fe^{3+} ionic positions are vacant compared to Figure 5.1, and these vacancies are consistent throughout the material.

The conclusion of Grau-Crespo *et al.* was that the $P4_12_12$ crystal structure was able to relax to the lowest energy and would therefore be the most likely candidate structure under most conditions. They also showed that for almost all temperature values up to the Curie point, this configuration was the most likely to occur by at least 98% probability. There is still however one final caveat to the investigation of cation vacancies noted by the same paper and past studies. Maghemite nanoparticles have been shown to lack vacancy ordering when below a certain size [122]. Haneda *et al.* studied samples of maghemite particles between 9 and 30 nm with low magnetite or hematite content [123]. They found that vacancies occurred only in the B-sites in a disordered state for particles below 20 nm diameter. The occurrence of the vacancies was higher in the surface layers of the nanoparticles and was reduced with increasing particle size, making it difficult to establish the cause as a size or surface effect. This would mean that they follow the Fd-3m magnetite symmetry with a distribution of vacancies within the octahedral sublattice when in ultrafine nanoparticle form.

For this work we have chosen to use the Fd-3m cubic symmetry for two main reasons: as we are mainly investigating the magnetic properties of particles below 20 nm in diameter, this is well within the suggested range for disorder of the vacancies. In addition, Grau-Crespo suggests that it is surface effects that may be contributing the most to the lack of ordered vacancies and below 20 nm, the surface to volume ratio is very high making it possible for surface effects

to dominate. For the second reason, as we shall see in later chapters, we shall be investigating core-shell particles with magnetite cores and maghemite shells where it is very likely that, in practice, the unit cell structure for both materials will relax to accommodate both materials and therefore maghemite will be bound more strongly to an Fd-3m crystal symmetry.

5.3 Parameters

Due to the uncertainty in the structure of maghemite due to its different phases as well as possibilities of mixing with similar ferrites, it is often difficult to find consistently used parameters for the material. The lattice constant of maghemite is sometimes reported to be around 8.347 Å[17] however this value changes slightly from paper to paper. In some experiments where maghemite was prepared by oxidation of magnetite particles, lattice parameters between 8.347Å and 8.397Å have been shown, suggesting a mixing of structures between maghemite and magnetite [124]. In a DFT study, which determined the regular vacancy distribution in bulk maghemite, a relaxed lattice constant of 8.359Å was suggested [118], however this is specific to the tetragonal structure of maghemite. For this study, we shall use the most commonly reported value of 8.347Å, which seems to be used in conjunction with cubic symmetry maghemite.

Another important parameter for maghemite is its Curie temperature which has been used to identify the material, in particular due to its chemical composition being very similar to magnetite and hematite. There is much debate on the exact value of this parameter for several reasons. Similar to the determination of the lattice parameter, it can be difficult to test the purity of the sample being studied leading to averaged out values of Curie temperature somewhere between magnetite and maghemite. Also, due to the metastability of maghemite, it is difficult to study the temperature dependent properties of the material if it is decomposing during the process. The actual temperature of conversion from maghemite to hematite is also disputed with some papers suggesting very low values close to room temperatures [125], while others record much higher temperatures around 900 K [126]. This is likely due to sample contamination where small hematite impurities act as nucleation sites, causing the material to decompose more quickly. Initially it was assumed to be impossible to determine the Curie temperature of maghemite for this reason. While some natural samples of maghemite would convert completely to hematite before reaching T_{C}, this is not true for all geological variations of maghemite as others have reported thermal

stability of around 870 K [127, 128], with a possible reason being the inclusion of metallic impurities which help to stabilise the system. More recently, theoretical studies of maghemite which can remove the possibility of metallic or other iron oxide impurities have been done to determine the exact value of T_{C}.

A recent study by Liu *et al.* in 2010 [125] looked at the magnetisation versus temperature properties of various grain sizes of maghemite to determine their Curie point. What they found was a strong dependence of the critical point on the shape of the grains, in particular their spin orientation being in either a multi-domain (MD) state with multiple different spin orientation regions, or a single-domain (SD) state where most of the spins where magnetised in the same direction. Larger particles can form multi-domain structures more easily as they are heated as different spin domains are able to grow naturally when they are far away enough from surface boundaries which would constrain spin direction and domain growth. In small particles this is much more difficult as the spins do not have enough space to form multi-domain structures and are influenced more heavily by their nearby spin neighbours. At the same time, both particle types were subject to the same rapid heating process to convert them from magnetite to maghemite and after analysis of the particles by Mössbauer spectroscopy, only the small single-domain particles were fully converted, while the larger particles still showed high levels of magnetite.

The saturation magnetisation curves from Liu *et al.* [125] are shown in Figure 5.3, which has two plots, one for the MD particles, and one for the SD particles. We can see without fitting the plots that the Curie temperature is lower for the MD particles. The exact method for extracting the Curie temperature is not specified however the Curie temperatures for the MD particles is around 850 K and for the SD particles 910K, suggesting that the Curie temperature of maghemite is higher than that of magnetite. This difference is important when we apply it to the nanoparticles we are simulating as they are always within the small particle single-domain phase, hence we expect a Curie temperature above 900 K. Aside from the Curie temperature we note that the scaling behaviour of the magnetisation for these particles is also very different. The multi-domain particles maintain a higher magnetisation, and therefore spin correlation, for higher temperatures, while the single-domain particles see a steady decrease to the Curie point. At room temperature there is a 20% difference in the magnetisation of the particles which would need to be considered when using them for biomedical heating applications. This temperature scaling demonstrates some of the differences between magnetite and maghemite particles and is a strong reason for their usage in individual appli-

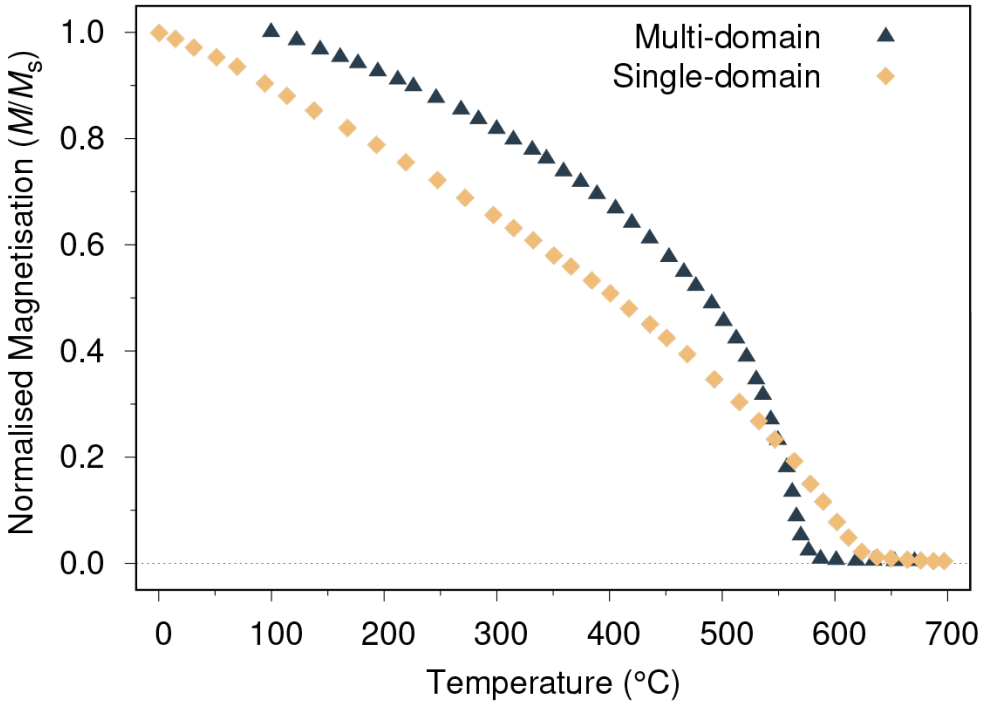

Figure 5.3: **Experimental saturation magnetisation plots for maghemite grains of different sizes.** The multi-domain particles have a predicted Curie temperature of around 850K, while the smaller single-domain particles have a Curie temperature of 910 K. Data adapted from Ref. [125].

cations. At lower temperatures, for example, the magnetite particles will remain more strongly magnetised than those made of maghemite. This of course does not take into account the magnitude of their magnetisation, as maghemite is reported to have a higher overall saturation magnetisation [126]. Hence there is likely a balance between the materials according to what temperature the material is required for.

According to Liu, the grains used in the study were around 70% pure maghemite, leaving 30% as other iron oxide impurities, most likely magnetite left over from the original sample, and hematite formed during the heating process. As the Curie temperature has risen, it is very likely that maghemite in a pure bulk system would have a higher T_C than magnetite. Hence for this work we shall expect a bulk Curie temperature of maghemite of 950 K as this is often referenced in the literature [9, 17]. There is an argument to be made that this value should be lower, however for the purposes of this work, the absolute value of the bulk Curie temperature expected is not as important as any deviations we shall see from it due to shape or size changes. The bulk temperature is important as it is used as a benchmark for when a simulation suggests a lowering or increasing of

the critical point. The values of exchange used in our simulations are the largest contributors to the system Curie temperature however if we change all exchange values by the same factor, the system Curie point will change by a similar amount. Hence, if in reality the Curie temperature of maghemite is 800K, we can divide all exchange values by a constant to simulate a lower T_{C} while preserving the ratio of the exchanges which is much more important. These ratios, such as the ratio of FeA-FeA (tetrahedral to tetrahedral exchange) compared to FeB-FeB (octahedral to octahedral exchange) help to evaluate the overall magnetic properties of the system as they define the temperature scaling.

5.3.1 Anisotropy

Following on from the uncertainty in macroscopic properties of maghemite, we find that current research is no clearer on theoretical modelling parameters such as the magnetocrystalline cubic anisotropy constant K, or the exchange interaction values. The nature of the anisotropy in maghemite is cubic, with an easy axis direction of [111] and is likely to be very weak, lower than the anisotropy of magnetite which is well known for having a relatively low bulk anisotropy. In the literature it is possible to find a value of $4.7 \times 10^4 \mathrm{erg/cm}^3$, cited from Krupička *et al.* [129], however we do not have an idea of the temperature scaling of the anisotropy, nor do we have any higher order anisotropy values. In addition, the original source is no longer available and therefore further research into the origin of this value is impossible. In spite of this, several theoretical modelling papers [130, 131] use the same value and therefore it is currently the best choice available. Using equation 3.3, the bulk cubic anisotropy can be converted to an atomistic anisotropy, $k_u = -5.12 \times 10^{-26}$J/atom.

5.3.2 Exchange

The exchange interaction values for magnetite we use are from Uhl and Siberchicot [28] who calculated them from first principles. This type of analysis does not exist for maghemite, and the exchange values found in the literature come from different sources. Two sets of exchange parameters for maghemite are listed in Table 5.2, which come from proposed exchange values of different materials. They are shown in units of Kelvin, as in the original paper where these values are expressed as temperatures, and in units of energy (meV) which is more commonly used today. These values are related by the simple equation $E = k_B T$.

The first set of values should look familiar as they are from the same paper by

Uhl and Siberchicot that discusses magnetite [28]. These values have been used in recent work [130] to look at surface anisotropy in maghemite nanoparticles. While this might look like a crude approximation, there are several compelling reasons to use these values. Magnetite and maghemite are isostructural materials with exchange occurring in similar ways, through oxygen mediated paths, and with interaction distances being approximately equal. The tetrahedral interactions, Fe^{AA}, could be very similar in maghemite as the ions are the same however the interactions involving Fe^{2+} ions, Fe^{AB} and Fe^{BB} may see larger differences due to the lack of Fe^{2+} in maghemite. Another set of values, used in several other papers concerning atomic scale modelling of maghemite [131, 132] instead use interaction values based on nickel ferrite, $NiFe_2O_4$. This is another good approximation for maghemite as it is also isostructural, since $NiFe_2O_4$ is an inverse spinel, with similar lattice parameters. $NiFe_2O_4$ has 6 pairs of exchange interactions as it includes Fe^{3+}, Fe^{2+} and Ni^{2+} ions and the exchange values used in maghemite correspond only to Fe^{3+} interactions from these. This could be a big improvement from the interaction values of magnetite as the ionic species is always the same.

		J^{AA}	J^{AB}	J^{BB}
From Fe_3O_4	meV	-0.11	-2.92	0.63
	K	-1.3	-33.9	+7.3
From $NiFe_2O_4$	meV	-1.81	-2.42	-0.74
	K	-21.0	-28.1	-8.6

Table 5.2: **Proposed exchange interaction values for maghemite in units of Kelvin and meV.** These values are not specific to maghemite but adapted from similar materials with isometric structures to maghemite and exchange between Fe^{3+} ions.

The exchange parameters coming from $NiFe_2O_4$ are slightly more commonly used in the literature on computational investigations of maghemite however on analysing the values proposed there are a few possible issues. Both sets of exchange values agree on the J^{AB} interaction; it is the largest of the three and antiferromagnetic. The J^{BB} interaction value from $NiFe_2O_4$ is suggested to be antiferromagnetic, rather than ferromagnetic as in magnetite, however its relative strength is still small. This is at odds with our previous analysis of Fe^{BB} in magnetite as the superexchange interaction occurs over a 90° angle (this can be seen very clearly by looking at the unit cell, Figure 3.4) and should therefore be a weak ferromagnetic interaction. Despite the relatively weak magnitude, the sign difference should have a significant impact on the overall exchange. Finally, the J^{AA} interaction is suggested to be antiferromagnetic, as we assume in magnetite. In this case the sign of the exchange is ambiguous as the exchange

occurs infrequently in the unit cell and over large distances. It is because of this that the relatively high magnitude of the J^{AA} interaction taken from $NiFe_2O_4$ does not apply well to maghemite. The strength of an Fe^{3+}-O^{2-}-Fe^{3+} interaction is likely related to the number of such interactions within the unit cell and their interaction ranges [133]. Here this interaction is both infrequent and over a long range therefore it is much more likely to be the smallest interaction as in magnetite. It is also worth pointing out that this interaction occurs in exactly the same way, and between exactly the same species in magnetite, and should therefore be the most transferable value between systems.

In Chapter 3.3, we have shown that the original exchange interaction values suggested by Uhl and Siberchicot replicate the magnetic properties of magnetite well, the predicted Curie temperature and magnetisation scaling (using quantum rescaling) agree very well with experiment. As we lack the same quality of exchange interaction values for maghemite, it seems that the best starting values are those of isostructural magnetite. This is of course an approximation; however it is necessary due to the current lack of well-founded values available. As such, we will have to adjust these starting values to replicate the Curie temperature of maghemite, 950K, by multiplying each exchange value by a constant factor. By doing this, we preserve the relative values of each exchange, and therefore the scaling of magnetic properties and exponents, but maintain the Curie temperature expected.

5.4 Simulating Maghemite

As we have now compiled a suitable set of parameters for modelling maghemite, we can now investigate its temperature scaling properties. As with magnetite, we begin with a small periodic boundary conditions system to approximate the bulk properties of the system. To recap the parameters:

- The system is cubic with a lattice constant of $a = 8.347$Å
- There are three unique materials:
  - Tetrahedral site iron 3+ ions with spin moment $5\mu_B$
  - Octahedral site iron 3+ ions with spin moment $5\mu_B$
  - Non-magnetic oxygen 2- ions
- Iron vacancies (11%) occur in the octahedral sublattice

- The anisotropy direction is $\langle \bar{1}\bar{1}\bar{1} \rangle$
- The exchange interaction values (in meV) are $J^{AA} = -0.12$, $J^{BB} = 0.68$ and $J^{AB} = -3.15$. These values correspond to the values in Table 5.2 multiplied by approximately 1.08.

As with magnetite, the simulations are checked to ensure all final data points are converged. The magnetisation reaches convergence very quickly as it equilibrates after only 50k Monte Carlo time steps. The susceptibility and specific heat values take longer to converge, relaxing over the first 100k time steps and reaching equilibrium almost asymptotically. To ensure convergence for all temperatures and properties, most simulations are run until at least 1 million time steps. The convergence for a 6 nm system around room temperature is shown in Figure 5.4. While the magnetisation looks like it is still erratic, this is simply a symptom of scaling all data sets between 0-1 as the magnitudes of the magnetisation, susceptibility and specific heat are at different scales. The initial max value of the magnetisation is $0.2288m$ and the lowest is $0.2291m$ therefore the magnetisation is essentially a flat line and immediately converged. The susceptibility and specific heat take much longer to converge properly and therefore require more time steps.

Rather than plotting the magnetisation, it is worth using the raw susceptibility to find the value of T_{C} for this system. For these initial simulations, we cannot use any rescaling parameters as magnetisation scaling and the β parameter is required first, however the susceptibility will be mostly unaffected by the classical model as the most relevant data points occur around T_{C} where quantum effects no longer persist. With a precise point for T_{C} we can fit the magnetisation curve more easily for the exponent, β. According to Figure 5.5 the Curie temperature occurs around 960K, with PBC finite size effects increasing the Curie temperature moderately due to increased spin correlation through the periodic boundaries.

The sublattices also peak around 960 K ($\pm 0.5K$), with the width of the peak of each plot spanning around 100K, indicating the Curie temperature occurs in the middle of a more gradual transition from ferrimagnetic to paramagnetic. As it is a ferrimagnet, we also see the difference in magnitudes of the sublattice susceptibilities and the overall susceptibility indicating the intra and inter-sublattice modes (Figure 3.26). We now use this to more accurately fit the magnetisation scaling versus temperature, still using only the classical model.

Using Gnuplot [45], we fit the magnetisation according to the classical Curie-Bloch equation (3.9) and constrain the Curie temperature to 960K, from the

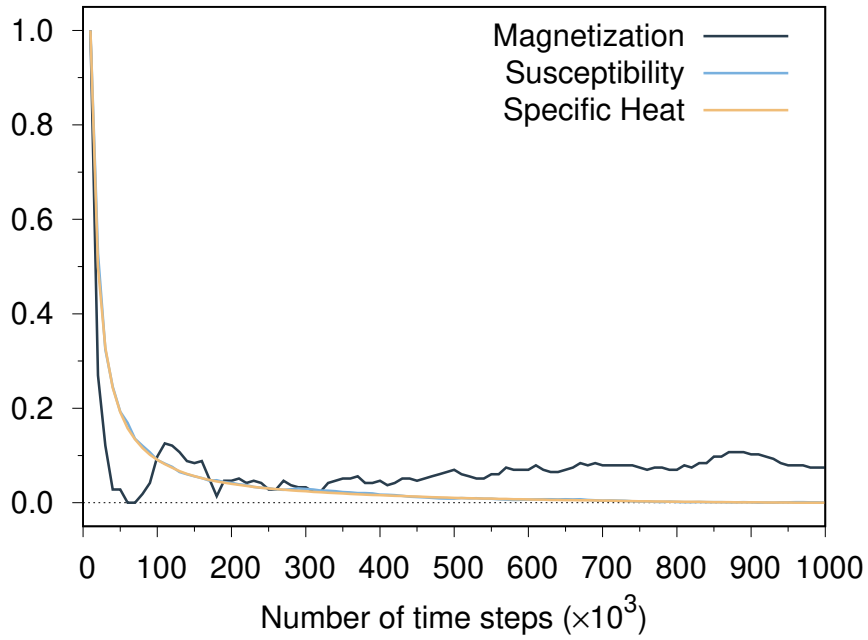

Figure 5.4: **Convergence of magnetic properties for maghemite.** Convergence of the magnetisation, susceptibility and specific heat for a 6 nm PBC system of maghemite at 300 K using 1 million Monte Carlo time steps. All properties have been scaled to lie between a value of 0-1 for visual clarity. The magnetisation is fully converged very quickly, with the changes in value shown only representing $0.0001m$, while the susceptibility and specific heat take several hundred time steps to reach a converged value.

susceptibility. The fit performs very well, with asymptotic standard errors in the derived β of less than 2%, for the fit of the overall system as well as the sublattices. This data is shown in Figure 5.6.

As we have seen in the finite size scaling analysis of PBC systems, β is expected to be moderately higher in a 6 nm system then in bulk however this only by a small amount. The calculated β for the overall system is 0.505, lower than that of magnetite and again far from the ideal version predicted for the 3D Heisenberg Hamiltonian of 1/3. As we are using exchange values based on those from magnetite, and these values have the largest impact on the magnetic properties of the system, it is not surprising that the value does not change completely. It is the changes in anisotropy, the Fe^{3+} octahedral sublattice and iron vacancies, that are the main causes of deviation from the results of magnetite.

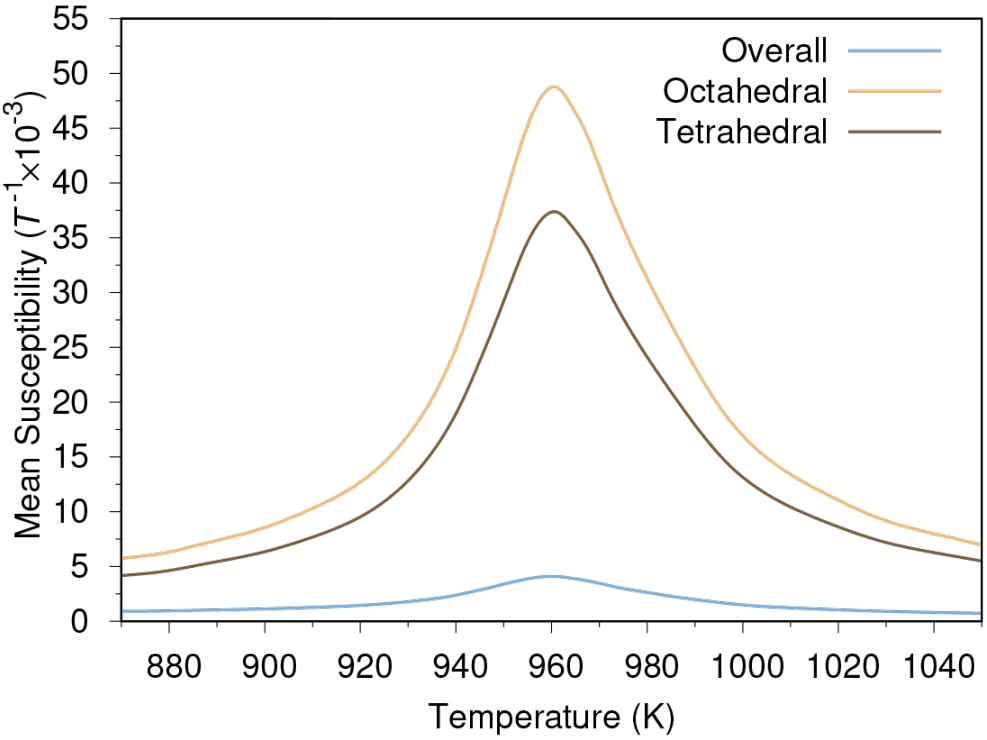

Figure 5.5: **Susceptibility versus temperature scaling of 6 nm PBC maghemite around the critical point.** The peak of the susceptibility for the overall system, as well as the sublattices, occur around 960K, moderately higher than the bulk 950 K as expected from the small system size.

5.4.1 Rescaling Parameter

To improve our magnetisation scaling, it would be ideal to find the appropriate rescaling parameter, α, for maghemite. Using this, we will be able to apply the rescaling method to achieve more realistic low temperature behaviour. Unfortunately, this is not an easy task as experimental magnetisation scaling versus temperature behaviour for bulk maghemite is essentially non-existent. A review of the literature on maghemite reveals many papers on the formation of nanoparticles using different methods [126, 134–138] and none on bulk properties. This is in part due to its stability and its formation process as well as the difficulty in forming high purity maghemite grains. α itself will likely be slightly different for nanoparticles compared to bulk due to the change in vacancy distribution described in section 5.2. In addition, most of the experimental data does not cover the whole temperature range from 0 K to T_C, but starts at 0°C, omitting the low temperature behaviour which is crucial for fitting α.

We have already come across one example of the magnetisation scaling of maghemite earlier, by Liu *et al.* [125]. For this work, fine grains of magnetite,

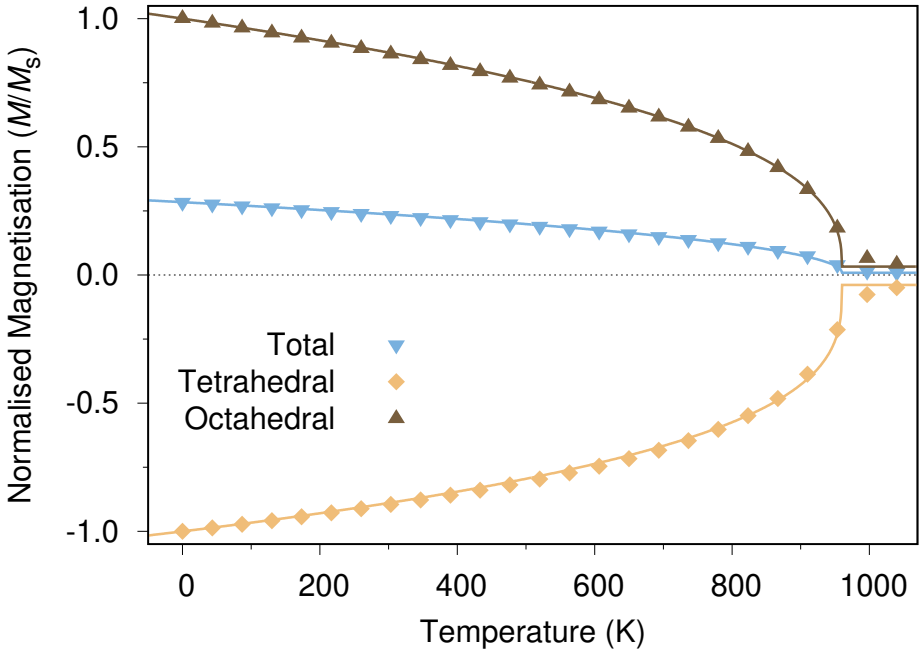

Figure 5.6: **Magnetisation versus temperature scaling of 6 nm maghemite with periodic boundary conditions.** The fits are made using the classical Curie-Bloch equation, with the Curie temperature constrained to 960 K. Calculated β for the overall system is 0.505, for the tetrahedral sublattice 0.326 and for the octahedral sublattice 0.392.

either single domain or small multi domain particles (up to $\approx 50\mu m$), were heated to 975 K and maintained at this temperature for 10 minutes. The resulting powder was found to be mostly made of of maghemite using Mössbauer spectroscopy, however some impurities remained in the sample, likely magnetite or hematite, which showed a reduced Curie temperature, around 910 K. It is therefore likely that the magnetisation scaling is a result of the largely maghemite system competing with other iron oxide impurities. Much like the work from Liu, we also find studies on the high temperature magnetisation scaling of maghemite by Özdemir *et al.* [126] and van Oorschot *et al.* [135], as well as low temperature scaling by Lee [137].

Figure 5.7 combines these works to give an idea of the different scaling behaviours found. As the systems measured are of subtly different shapes and sizes for each work, the magnetisation values and Curie temperatures have been normalised. For some of the data which have already been normalised to a value of 1.0 at 0°C, all plots have been adjusted to lie along the same magnetisation vs temperature curve. This constitutes a very rough fitting of experimental data however the critical exponents should not change drastically from one system to another. From our work on magnetite, β should be slightly reduced in nanoparticles but

still close to the bulk value.

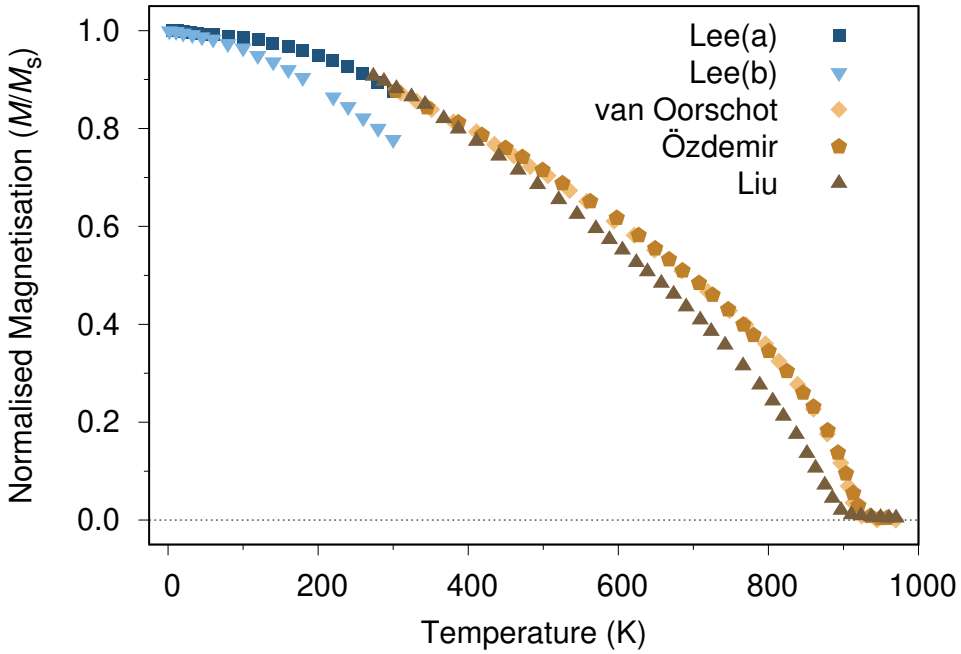

Figure 5.7: **Experimental data for the magnetisation scaling of maghemite nanoparticles.** Data from Lee *et al.* [137] in dark(a) and light(b) blue, Liu *et al.* [125] in dark brown, Özdemir *et al.* [126] in light brown, and van Oorschot *et al.* [135] in gold.

The low temperature scaling data for maghemite is from Lee *et al.* who used two different methods to form maghemite. The (a) data set was made using a pipette drop method, forming particles between 5-8 nm, while the (b) data set used a piezoelectric nozzle method which formed smaller 3-5 nm particles. These particles show a magnetisation scaling not in line with any other data set and are likely affected by strong finite size effects as well as strain due to the incomplete surface structure. Focusing on the (a) data set, we can form a smooth transition between this data and the high temperature scaling plots.

The data from Özdemir and van Oorschot agree very well with each other showing very similar scaling however the plots for each data set is distinct, with slightly different saturation values. It is worth mentioning that the work done by van Oorschot was reviewed by Özdemir, making it possible for experimental methods to be improved through collaboration from each group. The maghemite samples for these works were reported to be more than 95% pure maghemite, a notable improvement over the samples used by Liu. This is apparent due to the moderate change in scaling from each data set. To extract values for the critical exponent β and rescaling parameter α, we use a combination of the low and high

temperature data sets. While this is not ideal, it is currently the only way to get a rough estimate for the α exponent of the system.

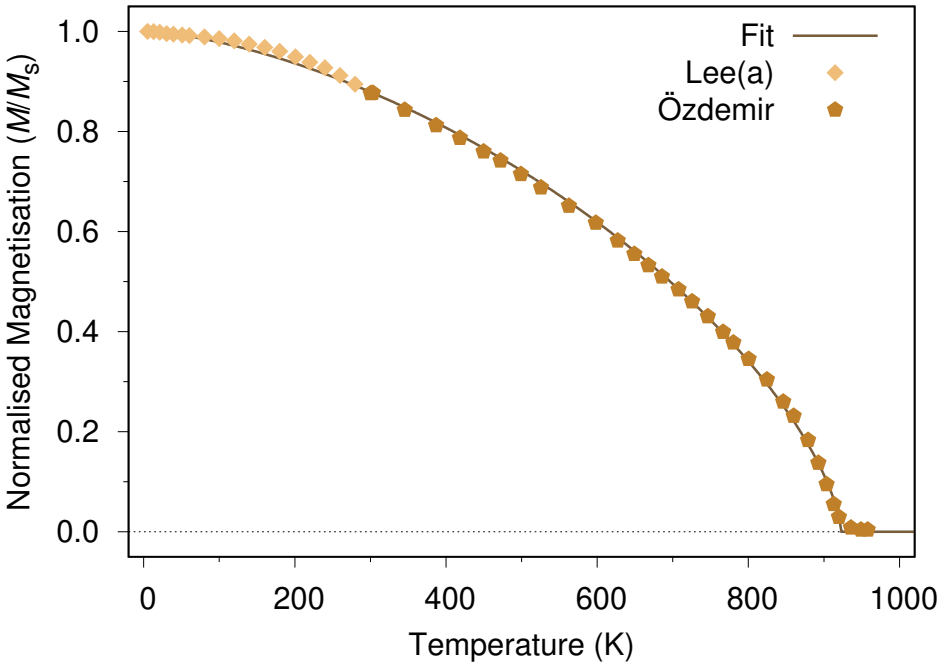

Figure 5.8: **Fitting exponents for maghemite.** Fitting the low temperature data set of Lee (a) and the mid to high temperature data set of Özdemir using the Curie-Bloch equation (2.39). The Curie temperature is around 920K, with $\beta = 0.66$ and $\alpha = 1.54$.

As the Lee(a) and Özdemir (or van Oorschot) data sets seem to agree well with each other, we can attempt to fit the data using the Curie-Bloch equation. This fit is shown in Figure 5.8, with $\beta = 0.66$ and $\alpha = 1.54$. Considering each value individually, the fit β is relatively close to that from magnetite. As the materials are similar in nature this is not unrealistic and is not necessarily an indication of high magnetite content. α is somewhat lower than the predicted value of magnetite however from communications with Jung Wei Lao (2011 PRD), there is a high possibility that the α exponent is not the same for all sublattices of maghemite. We have already explored the diverging values of β in magnetite and so this phenomenon is not new. While the tetrahedral sublattice of maghemite is fully ordered and therefore likely has an α exponent close to 2 [40], the octahedral sublattice is disordered due to the iron site vacancies and can therefore have a much lower exponent closer to 1. So far this is our best guess at the value of the critical exponent of maghemite, mostly coming from the aforementioned communication with Jung Wei Lao.

Maghemite still presents many difficulties in experiment and theoretical

modelling. The exchange interaction values as well as the critical exponents are very difficult to use accurately as there is very little high-quality information to be found. Still, we shall use the information gathered so far to study, as well as possible, the predicted properties of both bulk maghemite and nanoparticles.

5.5 FSS Properties of Maghemite

As maghemite is inherently unstable, it is not used as a bulk material but instead as nanoparticles or needle shaped particles previously used in recording media. Research into the properties of maghemite particles is therefore crucial to their application. While in nanoparticle form, maghemite will exhibit finite size effects, and these are very likely to be affecting many of the previous works discussed in this chapter. Many experimental papers suggest Curie temperatures for maghemite below the commonly referred to value of 950K, which is likely due to the lowering of T_{C} from FSS or other iron oxide impurities.

5.5.1 Periodic Boundary Conditions

In the case of maghemite, periodic boundary conditions do not offer a method of comparing simulated bulk properties of maghemite to those found in experiment as these values do not exist. In stead it offers an idea of how a bulk maghemite system could behave. Like magnetite, PBCs remove the surface element of the system and instead overestimate the magnetic properties due to an increase of spin coordination throughout the material.

Figure 5.9 shows the non-rescaled MvsT of maghemite. The system with the largest repeating cell approaches the properties of bulk with a Curie temperature around 950 K. If the Curie temperatures are normalised, we can compare the curves of maghemite to the same data set for magnetite. The data is very similar however for all temperatures maghemite maintains a higher normalised magnetisation and falls more steeply at the critical point due to a higher β. This is only comparing the classical behaviour of the magnetisation however. When rescaled, magnetite is predicted to have a scaling exponent $\alpha = 1.951$, while our estimate of that in maghemite is $\alpha = 1.54$. Higher values of alpha cause the low temperature range of the magnetisation to remain high, forming a more box-like curve, hence we expect that in experiment, magnetite nanoparticles will lose their magnetisation more slowly with increasing temperature.

The sublattices of maghemite, shown in Figure 5.10, show distinct scaling

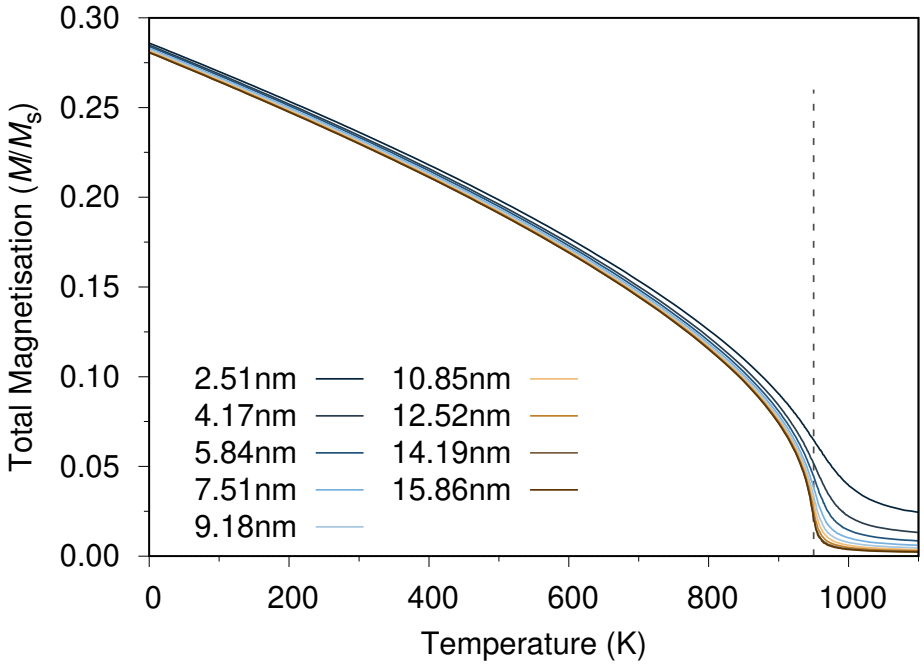

Figure 5.9: **Temperature versus magnetisation scaling for PBC maghemite.** The data has not been rescaled. As the system is periodic, smaller unit cells cause T_C to increase however the larger systems tend towards the properties of bulk maghemite with a Curie temperature of 950 K.

behaviours, both more curved than the overall plot. No rescaling has been applied as the α values for each sublattice is likely significantly different to the value found for the total. As explained earlier however, the tetrahedral lattice likely has an α exponent close to 2 as it is fully occupied.

5.5.2 Nanoparticles

Nanoparticles of maghemite have been studied extensively however the purity of the material is often in question when the experimental results show reduced Curie temperatures and Mössbauer spectroscopy suggests the presence of other iron oxides. Finite size scaling effects in nanoparticles compound these issues as small nanoparticles have their Curie temperature further reduced. From Figure 5.11 we see that all spherical nanoparticles of maghemite have a reduced Curie temperature, down to 930 K for the largest system at 16 nm. This is in agreement with the results seen in the literature by Özdemir and van Oorschot who studied high purity nanoparticles of maghemite and found Curie temperature values below the ideal 950 K [126, 135].

This reduction in the Curie temperature occurs uniformly in various nanopar-

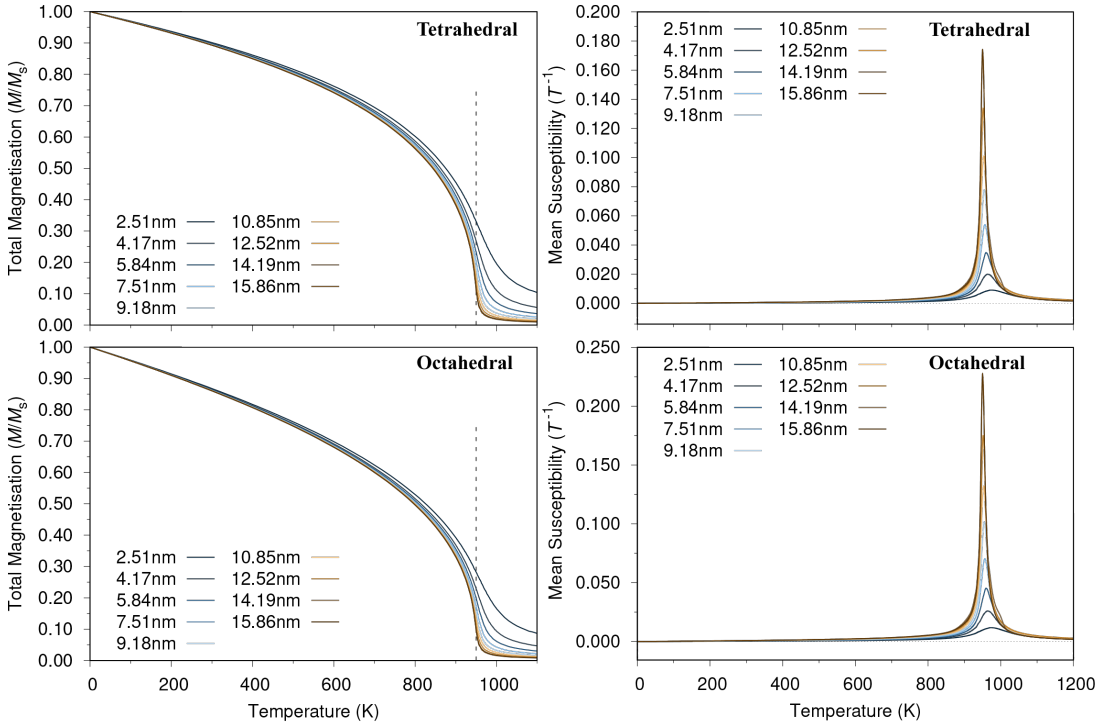

Figure 5.10: **Magnetisation and susceptibility scaling of the sublattices of maghemite.** The sublattices behave differently to each other, with the octahedral magnetisation lowering more quickly, and will therefore have differing β exponents. Despite this, the susceptibility plots show that each lattice has a closely aligned T_C.

ticle shapes including spherical and faceted systems. The scaling is also roughly proportional to the number of atoms in the system (for symmetric particles), causing spherical systems to exhibit the lowest overall Curie temperature due to having the lowest surface area to volume ratio.

5.6 Beta Scaling

So far we have only used the β parameter to describe and compare the magnetisation scaling of finite size systems for both magnetite and maghemite. The parameter itself is not set in any way but is a result of the interactions of the particular system. For bulk systems, the value of β is often used as a constant and defined as a critical exponent however this carries several implications on the value of the parameter.

In general, critical exponents describe the behaviour of a material around a continuous phase transition. It is dependent on the size of the system, the interaction range and the spin dimension (such as a 2D Ising model or 3D Heisenberg).

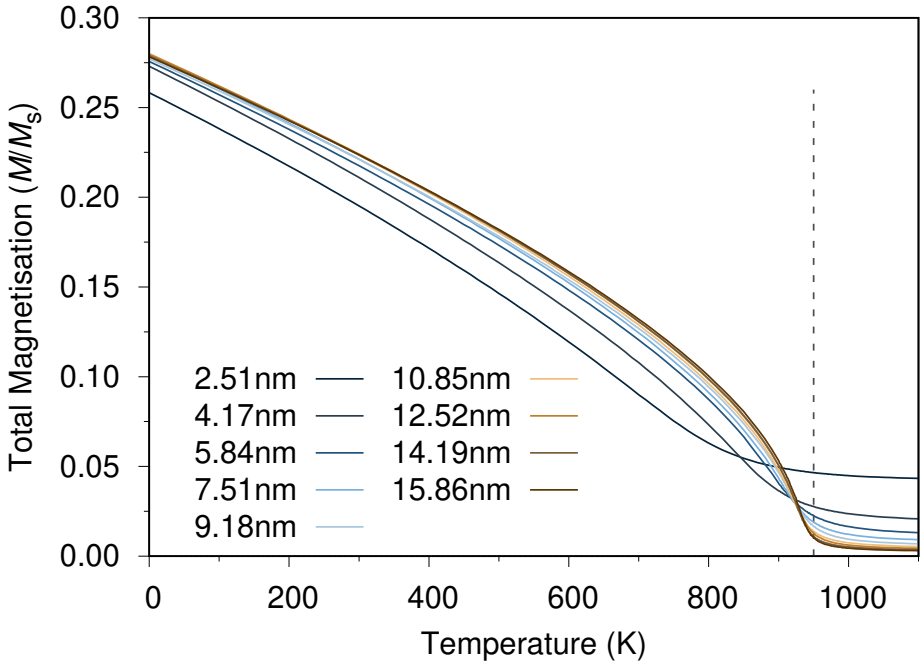

Figure 5.11: **Magnetisation scaling of spherical nanoparticles of maghemite.** All particles exhibit reduced Curie temperatures, with bulk T_C (960 K) denoted by the dotted line, including the largest sample of 16 nm which has a T_C around 930 K.

β is one such exponent, however α, which we have used to describe the classical to quantum rescaling properties of the system, is not related to another critical exponent typically denoted by the same symbol.

These constants can be derived using various and approximations such as mean field theory (which approximates a stochastic model), in conjunction with a model such as 2D Ising. The model and dimensionality of the system has a significant effect on the value of the critical exponents which are then grouped together into so called universality classes. Universality classes group together critical exponents for systems of an ideal size. For example, we have already seen that the β exponent varies according to system size and tends towards a constant value. Bulk systems represent the ideal state where the critical exponent reaches a constant value.

Focusing on β, this exponent is related to the magnetisation strength of a system below the critical point, the Curie temperature, hence it is defined for the ordered phase of the system where $\tau < 0$ and $\tau = (T - T_C)/T_C$. Further, β has a well-defined value for the classical 3D Heisenberg model, typically around 0.34 [42]. This value can vary significantly for other models, for example using the

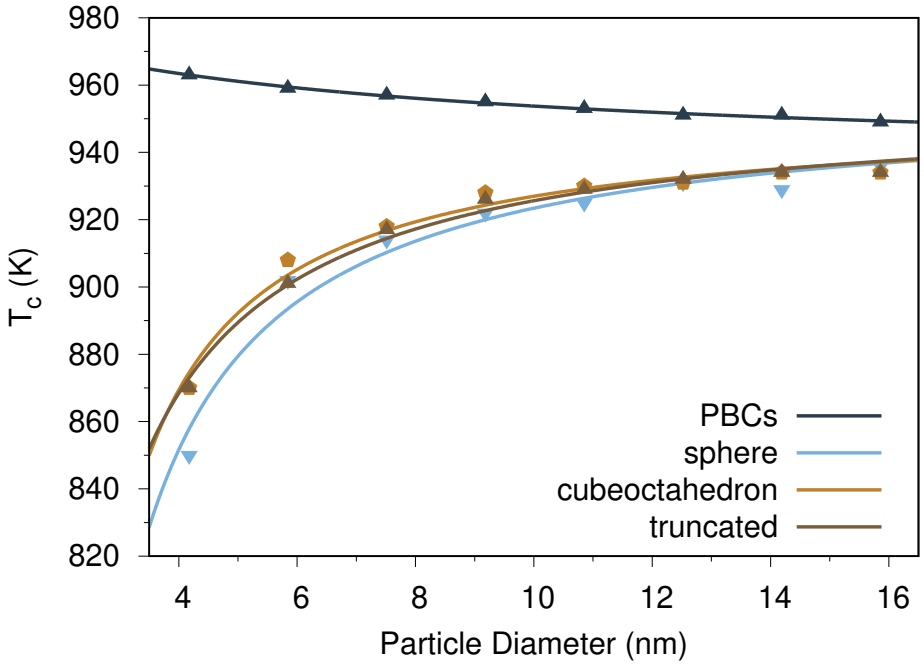

Figure 5.12: **Comparison of the Curie temperature scaling for periodic boundary condition systems and various nanoparticle shapes.** Both system types tend towards bulk properties however the nanoparticles have considerably reduced T_C for all particle diameters.

mean field approximation it is 0.5. We can calculate β using the magnetisation plots and Curie-Bloch equation to find the appropriate constant for our systems. This has already been applied to spherical nanoparticles of magnetite in Figure 4.6 and here for periodic systems which more closely approximate ideal bulk conditions in Figure 5.13.

So far, we have studied two materials which do not neatly fit into the typical university class of classical 3D Heisenberg materials as they have β values dependent on the component of the system under study. For both magnetite and now maghemite, the β exponent does not tend to 0.37 for the overall material or any of the sublattices. In stead it is significantly higher at 0.47 and 0.53 for maghemite and magnetite respectively.

From communications with Ondrej Hovorka of the University of Southampton in 2019, it is also possible that the universality classes are not only unique to the model being used but instead also a symptom of the material under study. Hovorka suggests that different materials can lead to drastically different critical exponent and are not necessarily similar to materials which share the same properties. Here we have found that the β exponent is roughly similar for all components

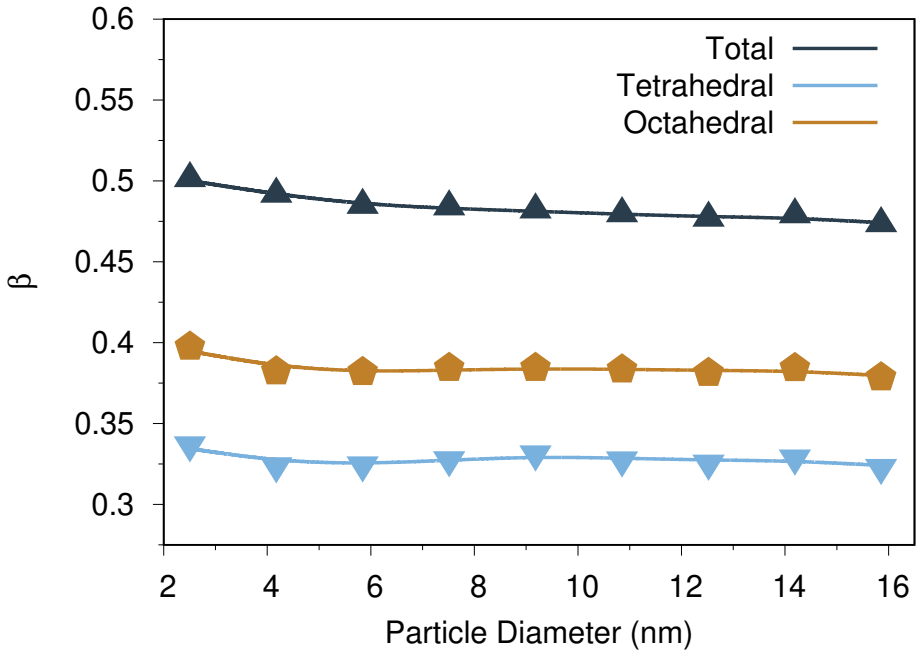

Figure 5.13: ***β* scaling for all components of maghemite.** The overall value of β tends to a value of 0.47, while the tetrahedral and octahedral sublattices tend to 0.32 and 0.38 respectively.

of magnetite and maghemite however this need not be the case. Unfortunately, it is difficult to find other materials which share the β values we have seen so far in the literature and these materials and possibly other iron oxides form a universality class of their own. At the same time, this does not fully explain the phenomenon as the values we have calculated are close to convergence and do not seem to be tending closer to each other.

5.7 Conclusion

Building from the model used on magnetite, we can make changes to the structure and material parameters to model maghemite. Many of the nanoparticle properties of maghemite are difficult to study due to its instability while at the same time we have no reference for the bulk properties either. In this Chapter we have used exchange constant and anisotropy values which are not as rigorously defined as in magnetite, however we are still able to form a mostly complete model to study the temperature dependant magnetic properties of the system in a simulated bulk, as well as nanoparticle form. As maghemite has been used in biomedical applications, as well as been found to form as rust on pure magnetite particles, it is important to have a clear picture of the effect maghemite has on

the magnetic properties of nanoparticles at the nanometer scale.

Maghemite has also shown consistency in our results compared to those of magnetite. The critical exponent β of maghemite shows values close to those found in magnetite for all components, the overall system and sublattices. This is a curious result as it is in stark contrast to most of the literature on the *3D* Heisenberg predicted value. This is possibly due to the materials belonging to a separate universality class of their own, as suggested by Hovorka, or due to separate parameters from size or shape which may be affecting the converged value of the exponent.

CHAPTER 6

COBALT FERRITE

6.1 Introduction

The surface of iron oxides such as magnetite is widely studied due to its complexity and variation. In addition to understanding the nature of surface structure, much work has gone into understanding the adsorption properties of the material. Adsorption, specifically adsorption on solid surfaces, is the adhesion of atoms, ions or molecules due to surface energy differences between the original material, and the compound. Iron oxides are able to integrate a significant number of materials into their surfaces: hydrogen [139], water [140] and organic compounds [141, 142] are of interest due to the catalytic reactions iron oxides take part in. The water-gas shift reaction for example uses an iron-oxide based catalyst to convert water and carbon monoxide to hydrogen gas and carbon dioxide [143].

Metal adsorption on Fe_3O_4 has also been intensely studied due to the use of iron oxides as a support material in catalysis, however this interaction can go a step further as some metals integrate themselves into the sub-layers or bulk of the iron oxide, forming new materials. This does not occur for all metals, and the process can be divided into two groups: non-ferrite-forming metals, such as Au, Ag, Pd and Pt [144–146], and ferrite-forming metals such as Co, Ni, Cu, Mn, Ti and more [147–149]. For this chapter we shall focus on one such metal ferrite, formed by doping magnetite with cobalt.

Cobalt ferrite, in particular nanoparticles of cobalt ferrite, have seen interest due to their many uses such as for permanent magnets [151], as high-performance

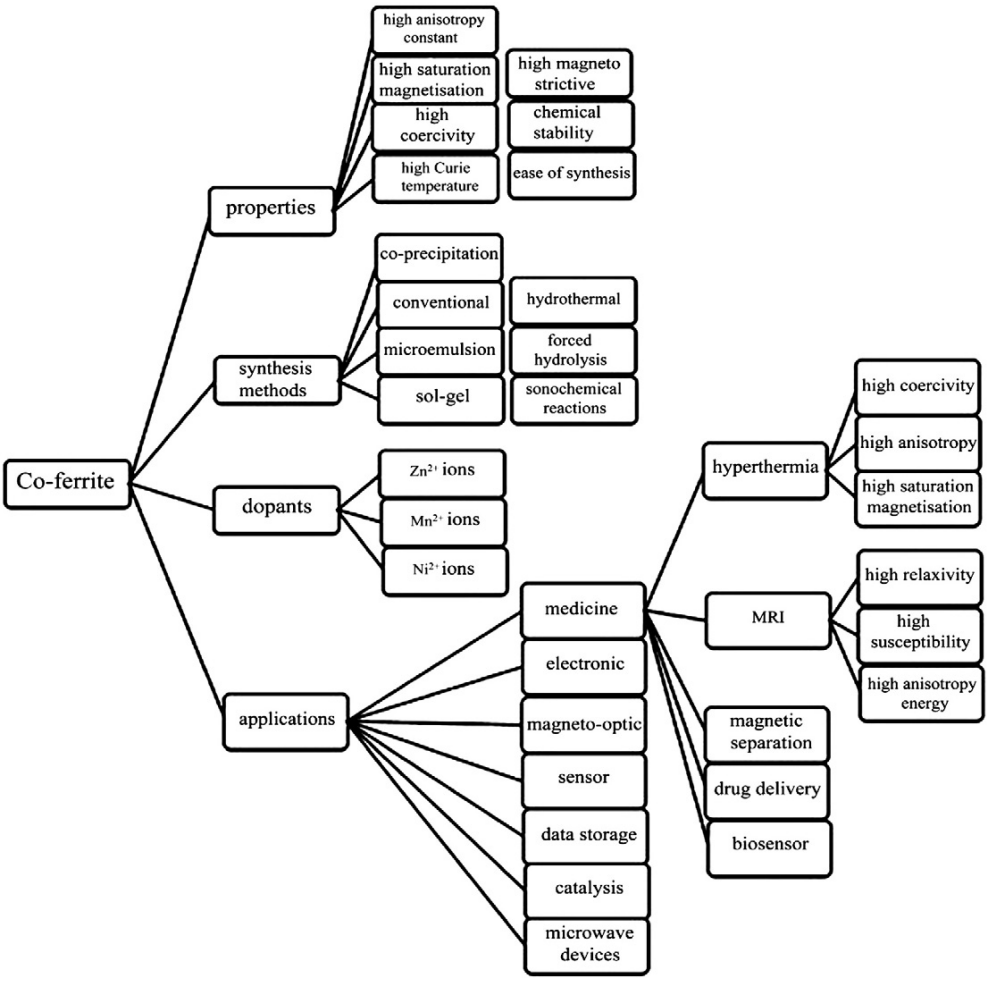

Figure 6.1: **Properties, synthesis methods and applications of cobalt ferrite.** Figure adapted from Ref. [150]

anodes in lithium batteries [152] or as spin filters for spintronics applications [153]. Like magnetite and maghemite, they have also been used in biomedical applications due to their high magneto-crystalline anisotropy which originates from the spin-orbit coupling at crystal lattice sites [14, 154, 155]. The heating characteristics and magnetisation adaptability is of critical importance and can be examined closely by atomistic simulation.

6.2 Structure

Cobalt ferrite grains are usually prepared from magnetite, in thin films [156] or nanoparticles. Cobalt ions can be introduced to magnetite and readily incorporate themselves into the surface. This behaviour is characterised best with the $(\sqrt{2} \times \sqrt{2})$R45° [100] magnetite surface reconstruction which is different to the regular bulk structure of magnetite and is the lowest energy [100] termination. Iron

vacancies form one level below the surface, separated by interstitial iron atoms as shown in Figure 6.2(a). Cobalt adatoms bind to oxygen-bridging sites initially but can also integrate themselves into the structure by filling one of the iron vacancies. In this case, the interstitial iron ion is then moved into the remaining vacancy [147] and the inverse spinel cation distribution is locally recovered. The cobalt ions are also able to penetrate further into the system replacing iron ions at sites (ii)-(v) in Figure 6.2(b).

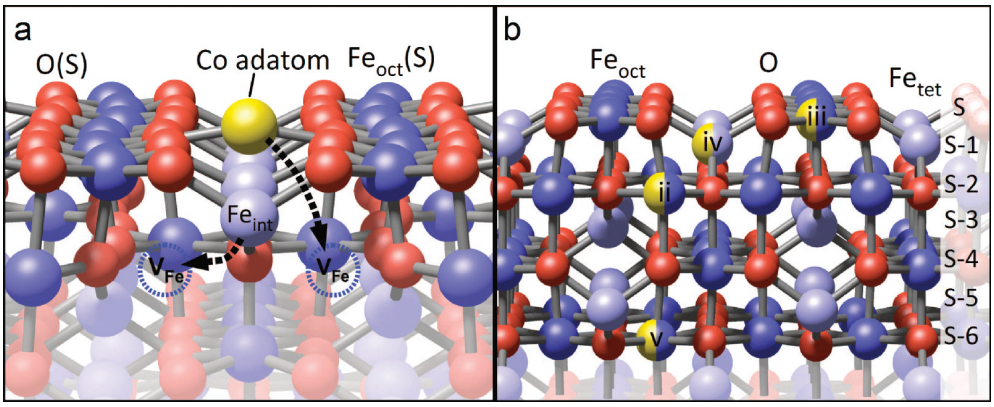

Figure 6.2: **Cobalt integration into magnetite surface.** In the $(\sqrt{2} \times \sqrt{2})$R45° [100] magnetite surface reconstruction, iron vacancies form under the surface, separated by interstitial iron atoms, Fe_{int}. Cobalt ions adsorbed onto the surface can bind to oxygen-bridging sites initially (a) and then incorporate themselves into the bulk by filling one vacancy site as the Fe_{int} fills the other (b). Figure from Ref. [156].

Configuration	Energy (eV)
Co adatom	-5.46
Co_{oct} S	-5.41
Co_{tet} S-1	-5.27
Co_{oct} S-2	-5.59
Co_{oct} S-6	-5.75

Table 6.1: **Energy differences for binding sites of Cobalt ions in the magnetite surface.** Cobalt adatoms and surface sub-level 6 have the highest energy differences and are the preferred sites for the Cobalt ions. Adapted from Ref. [156]

The associated energies for the cobalt substitutions was calculated by Gargallo-Caballero *et al.* and these results are shown in Table 6.1. The cobalt adatoms are more energetically favourable to iron replacements in the first few sub-surface layers leading to some cobalt ions being left on the surface in experiment [147]. The lowest energy configuration is a cobalt substitution in the octahedral S-6 layer (shown in Figure 6.2(b)) which shows how cobalt ions are able to penetrate into the material. The binding energies are higher for all octahedral sites than for

the tetrahedral sites, which suggests that the cobalt ferrite structure involves an iron only tetrahedral lattice and a mixed cobalt and iron octahedral lattice.

Instead of looking at nanoscale systems we can ask what a bulk cobalt ferrite system would look like. The system should be very similar to other iron oxides and form a spinel structure. The first question is whether they form a normal spinel structure with divalent atoms on the tetrahedral A sites and trivalent atoms on the octahedral B sites. Early studies on cobalt ferrite done by O'Neill *et al.* [63] looked at the oxygen positional parameter in cobalt ferrite and compared the formulas of four different proposed structures which would correspond to the general formula $CoFe_2O_4$. These are listed along with calculated lattice and oxygen positional parameters in Table 6.2.

		a(Å)	u
1	$(Co^{2+})[Fe_2^{3+}]O_4$	8.4091	0.2596
2	$(Fe^{3+})[Co^{2+}\ Fe^{3+}\ ]O_4$	8.3702	0.2536
3	$(Co^{3+})[Fe^{2+}\ Fe^{3+}\ ]O_4$	8.3439	0.2516
4	$(Fe^{2+})[Co^{3+}Fe^{3+}\ ]O_4$	8.3004	0.2638

Table 6.2: **$CoFe_2O_4$ lattice parameters.** $CoFe_2O_4$ structures with different A and B site occupancies, and their respective calculated lattice parameters and oxygen positional parameters. Table adapted from Ref. [63].

The accepted values for the cobalt ferrite lattice parameter vary slightly between sources, most likely due to slight differences in the studied samples. A lattice constant of $a = 8.38$Å is listed in textbooks such as Cullity [58] and Roiter and Paladino determined it to be 8.382 ± 0.001Å [157]. This should indicate that the $(Fe^{3+})[Co^{2+}\ Fe^{3+}\ ]O_4$ structure is the most likely candidate, leading to the overall structure of cobalt ferrite being inverse spinel, remaining isostructural to magnetite. This is still an oversimplification of the structure of cobalt ferrite as it is only the "ideal" structure for the system, where cobalt ions are randomly distributed only in the octahedral sublattice and do not replace any of the A site iron ions. Cobalt ions have been found to occupy tetrahedral coordination sites in low quantities leading to the general formula $(Co_xFe_{1-x})[Co_{1-x}Fe_{1+x}]O_4$[150]. The exact value of x is heavily dependent on temperature and method used to form the cobalt ferrite. In some cases it can also lead to iron or cobalt deficient systems of the formula $Co_{1\pm x}Fe_{2\mp x}O_4$[63].

Bulk cobalt ferrite should form more readily with the ideal configuration of cobalt ions only distributed within the octahedral lattice while within nanosystems there is a higher degree of tetrahedral occupation. This can be difficult to

model and is not necessarily useful data as the deviations from ideal structure causes the overall magnetic properties to diverge. Hence for this study we shall be using the ideal structure of $CoFe_2O_4$ nanoparticles as our base. The particles will be inverse spinel, Fd-3m, and the magnetic properties presented shall be a benchmark for cobalt ferrite behaviour.

6.3 Parameters

The Curie temperature of cobalt ferrite can be difficult to quantify much like the lattice parameter. It does not have a constant value for all system sizes which is most likely linked to the structural defects of the $(Co_xFe_{1-x})[Co_{1-x}Fe_{1+x}]O_4$ system. As smaller nanoparticles are more likely to be mixed ferrites with $x > 0$, the magnetic properties of the system such as the saturation magnetisation and the Curie temperature can change. In a study by Franco *et al.* [158], the saturation magnetisation of cobalt ferrite nanoparticles is 82% lower than in bulk, 351emu/cm^3 and 425emu/cm^3 for nanoparticles and bulk respectively.

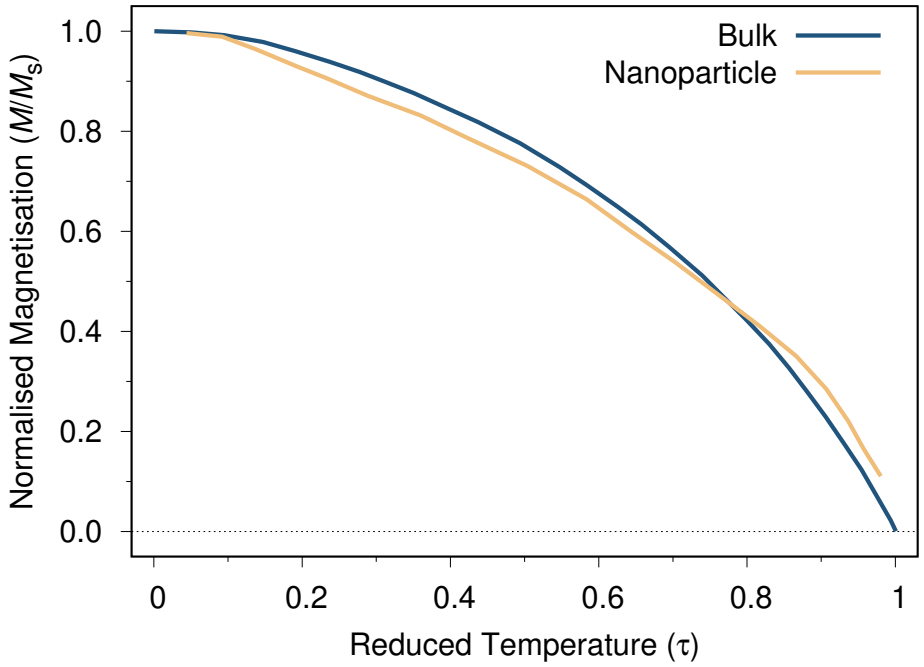

Figure 6.3: **Magnetisation vs. temperature of bulk and nanoparticle cobalt ferrite.** Both axes have been normalised as the saturation magnetisation and T_C of nanoparticle and bulk cobalt ferrite is different; however the scaling behaviour is not too dissimilar for each system indicating only a small change in the exchange values. Bulk data from Ref. [29], nanoparticle data from Ref. [158].

Cobalt ferrite nanoparticles exhibit a Curie temperature higher than bulk

and the temperature scaling behaviour changes due to structural changes, with small amounts of cobalt ferrite in the tetrahedral lattice affecting the overall system properties. A comparison of the scaling in nanoparticles and bulk is shown in Figure 6.3. In nanoparticles the Curie temperature is predicted to be around 820-830 K using magnetisation and susceptibility data, while in bulk is it reported as 795 K [29, 58], similarly the saturation magnetisation is 82% lower. In spite of this, Figure 6.3 shows that the scaling for each system deviates only slightly and the exchange values should still be heavily related.

As we are modelling cobalt ferrite as a perfect inverse spinel with no cobalt ions in the tetrahedral lattice, bulk behaviour is expected and therefore to keep our parameters consistent we shall use a Curie temperature of 795 K.

6.3.1 Anisotropy

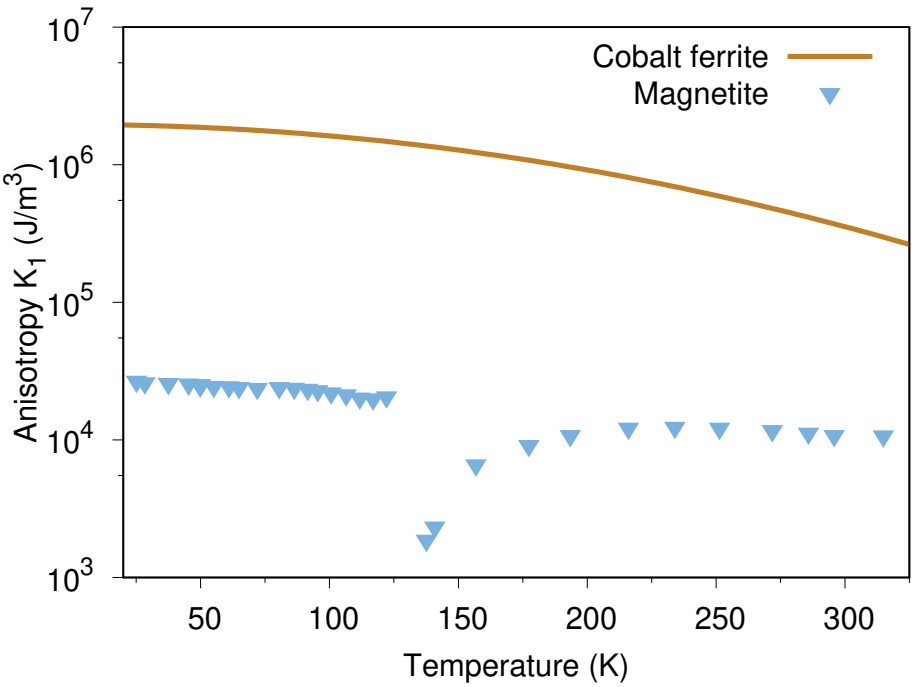

Figure 6.4: **The temperature dependence of anisotropy K_1 for cobalt ferrite.** Calculated using Eqn. 6.1 and compared to magnetite. The plot uses a log scale y-axis to show the difference in magnitude of the material anisotropies. Magnetite data from Ref. [76]

The anisotropy of cobalt ferrite is well studied compared to that in other iron oxides such as maghemite, mainly due to the effect of cobalt ions on the system and the considerable number of uses for this material. Unlike magnetite, maghemite and most other spinel forming metal ferrites, cobalt ferrite has a cubic anisotropy with an easy axis in the [100] direction, with a relatively high

magnitude. When looking at ferrites, in 1957, Shenker [159] determined the value of the K_1 constant in cobalt ferrite to vary with temperature according to the following equation between 20-350 K.

$$K_1 = 19.6 \times 10^5 \exp(-1.90 \times 10^{-5} T^2) \text{ J/m}^3 \tag{6.1}$$

Figure 6.4 shows the difference in anisotropy for magnetite and cobalt ferrite. The cobalt causes a huge change in the material anisotropy, changing both the direction and magnitude. Note that the anisotropy for magnetite at low temperatures is constrained by the Verwey phase transition and magnetite has a negative anisotropy below this point. Cobalt ferrite was speculated to have a similar phase transition below 90 K however most papers studying the anisotropy show no such behaviour [159–161]. The anisotropy of cobalt ferrite remains strong around room temperature, $K_1 \approx 4 \times 10^5 \text{J/m}^3$, however it is highest close to zero Kelvin, at $K_1 \approx 2 \times 10^6 \text{J/m}^3$.

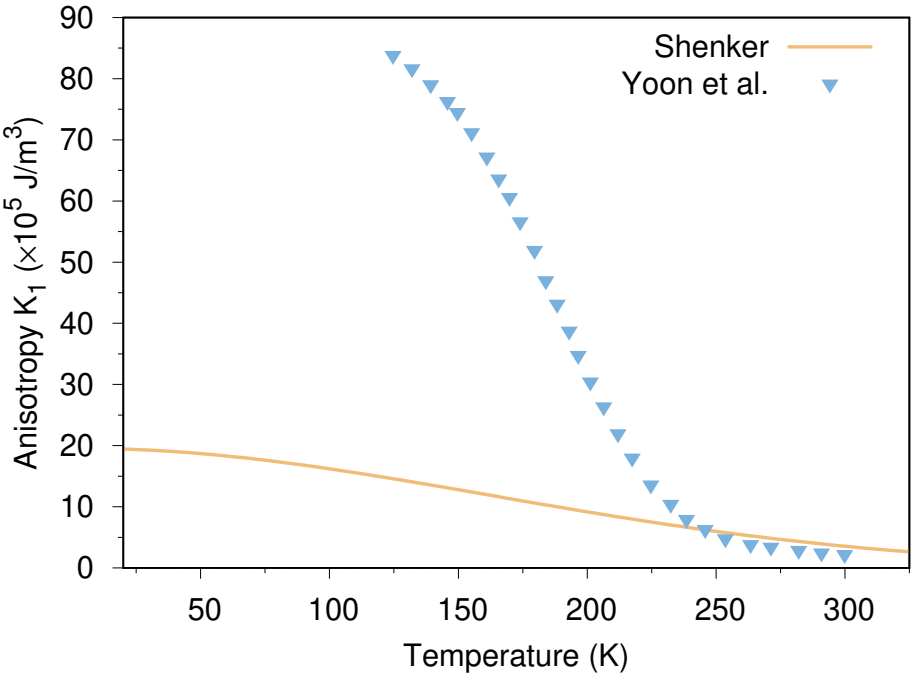

Figure 6.5: **$CoFe_2O_4$ anisotropy scaling comparison.** A comparison of the anisotropy scaling with respect to temperature of cobalt ferrite from the studies of Shenker [159] and Yoon [161]. The high temperature anisotropy is very similar however at low temperatures the measured anisotropies diverge.

A more recent study by Yoon *et al.* [161] looked at the anisotropy scaling of ultrafine cobalt ferrite nanoparticles of high purity (low tetrahedral cobalt and complete inverse spinel structure) and found that the low temperature anisotropy

was several times higher than previously reported, reaching $8 \times 10^6 J/m^3$. Both studies are shown in Figure 6.5. The anisotropy is very high close to zero Kelvin in the case of Yoon, and lowers greatly towards room temperature. Surface anisotropy is likely the largest factor causing the discrepancy between the two data sets, and is often several times larger in magnitude to the intrinsic magnetocrystalline anisotropy of the material [162].

This discrepancy makes choosing an appropriate value for the anisotropy constant of cobalt ferrite very difficult as it will affect low temperature magnetic properties more heavily. For most scaling behaviour where the magnetic properties around the Curie temperature are in focus, the room temperature value can be used as the anisotropy will have little effect. When studying the low temperature magnetic properties, the higher anisotropy strength will also be considered due to the effects on spin-switching.

6.3.2 Exchange

The exchange interaction values for cobalt ferrite are less well reviewed in the literature. Some papers list exchange interaction values for cobalt ferrite in a 2-lattice model [163] however this is a less than ideal approach to understanding cobalt ferrite. In the 2-lattice model, the spinels are assumed to have the overall formula AB_2O, with two lattices each containing a divalent species, A, and trivalent species B. Following this there are three possible exchange values, J^{AA}, J^{AB} and J^{BB}. Maghemite is a good example for this model as although both A and B species are Fe^{3+}, the superexchange distances between tetrahedral and octahedral iron ions are different and therefore the two can be treated differently. The exchange interactions for the system can therefore be fully explained using three parameters. This is the same system that was initially applied to magnetite by Néel [6] who understood that two different ionic species existed in the octahedral lattice but hoped that it could be approximated by one exchange value. This assumption would turn out to be fruitful as (omitting more recent explanations covered in Chapter 3) the Fe^{2+} and Fe^{3+} ions in magnetite form a mixed valence state of $Fe_{2.5+}$ above the Verwey transition and are mostly indistinguishable [74, 164]. This allows the 2-lattice model to work well for magnetite.

In cobalt ferrite there are three distinct ionic species: tetrahedral Fe^{3+}, octahedral Fe^{3+} and octahedral Co^{2+}, which in equal amounts make up all magnetic atoms in the unit cell. In $CoFe_2O_4$ the octahedral ions do not form a mixed state and are therefore represented as (A)[BB']O. Hence there are six total interactions:

J^{AA}, J^{AB}, $J^{AB'}$, J^{BB}, $J^{B'B'}$ and $J^{BB'}$, where B is octahedral Fe^{3+} and B' is Co^{2+}. This approach is known as the 3-sublattice model and was approached by Srivastava *et al.* [29] who calculated these values from molecular-field approximations by using M_s vs. T and χ^{-1} vs. T data. Their results are shown in Table 6.3.

		J^{AA}	J^{AB}	$J^{AB'}$	J^{BB}	$J^{B'B'}$	$J^{BB'}$
$CoFe_2O_4$	meV	-1.29	-2.24	-1.96	-0.65	4.04	-1.59
	K	-15	-26	-22.7	-7.5	46.9	-18.5

Table 6.3: **3-lattice exchange interaction values for cobalt ferrite.** The strongest interaction comes from the Co^{2+}-Co^{2+} interaction while the J^{AA} and J^{BB} are relatively weak.

According to his paper Srivastava shows that these values have good agreement with experimental results, which is somewhat expected due to the initial source for the exchange values. As the model used by Srivastava is different to previous exchange values used here, it is likely that these values will require some adjustment and fine tuning, without changing their relative strengths.

We should also assess the validity of the exchange constants against the Goodenough-Kanomori rules [78]. The tetrahedral to octahedral interactions, J^{AB} and $J^{AB'}$ fit well into the model. They are the strong antiferromagnetic interactions, negative in sign, which occur over bond angles of 120-180°. As with magnetite, this interaction is usually predicted to be the strongest. The octahedral to octahedral interactions, J^{BB}, $J^{B'B'}$ and $J^{BB'}$, are more complicated as the sign and strength of the interactions are different. The iron to iron and iron to cobalt interactions are negative while the cobalt to cobalt interactions is very strong and positive. In the case of magnetite, this interaction is predicted to be ferromagnetic and weak due to being a 90° angle. We know that cobalt has a large effect on the anisotropy of the system and these exchange values suggest that it also has a significant effect on the octahedral sublattice exchange too. A rough averaging of these three exchange parameters would lead to a similar overall value of exchange to magnetite or maghemite. Finally, the tetrahedral to tetrahedral interaction is the most problematic as it should be closest to the values we have seen in magnetite and maghemite which are much lower. The J^{AA} interaction is somewhat ambiguous as it occurs over an acute angle over large distances. The sign is usually negative however the magnitude is usually low. It is not uncommon however for the J^{AA} in other iron oxides to be listed as the second largest interaction and we can find several references to in the works of Uhl and Siberchicot as well as for other metal ferrites studied by Srivastava [28, 29].

As a comparison, we have also made an educated guess at the exchange constants for cobalt ferrite starting again from the values used in magnetite. This has the unfortunate side effect that the cobalt and iron contributions to the exchange in the octahedral lattice are averaged out however we preserve a separation in these lattices to correctly model the strong spin moment on cobalt ions as well as their contribution to the overall system anisotropy. While cobalt ferrite is a widely studied material and without the instability drawbacks of maghemite, it has been difficult to find a suitable set of exchange parameters that is clearly a good representation of experiment, as we have found with magnetite. The extra set of exchange constants is another way to try out different initial parameters, specifically those with the highest contribution to the system Hamiltonian.

6.4 Simulating Cobalt Ferrite

With the current set of parameters we have compiled for cobalt ferrite, we can start to simulate the material using the same methods used in magnetite and maghemite. Due to the uncertainty in the exchange parameters however, we shall be using two sets of data, referred to as CFA, using the exchange parameters of Srivastava *et al.*, and CFB which uses exchange parameters based on magnetite. To recap the parameters:

- The system is cubic with a lattice constant of $a = 8.382$Å
- There are four unique materials:
  - Tetrahedral site iron 3+ ions with spin moment $5\mu_B$
  - Octahedral site iron 3+ ions with spin moment $5\mu_B$
  - Octahedral site cobalt 2+ ions with spin moment $4.6\mu_B$
  - Non-magnetic oxygen 2- ions
- The anisotropy direction is $\langle 100 \rangle$
- Two sets of exchange parameters, CFA and CFB, with 6 constants each, shown below in Table 6.4.

As with previous materials we first plot for the convergence of each data set. The susceptibility and specific heat require a large amount of Monte Carlo time steps to fully relax. Figure 6.6 shows the convergence, with each plot normalised between 0 and 1 as each set varies significantly in magnitude. We are modelling

	J^{AA}	J^{AB}	$J^{AB'}$	J^{BB}	$J^{B'B'}$	$J^{BB'}$
CFA	-1.02	-1.76	-1.54	-0.51	3.18	-1.25
CFB	-0.08	-2.16	-2.16	0.47	0.47	0.47

Table 6.4: **Exchange values for CFA and CFB.** CFA values are modelled on the work of Srivastava *et al.* [29] multiplied by 0.787 to reproduce T_C, while CFB values are modelled on those of magnetite from Uhl and Siberchicot [28], also multiplied by 0.741.

systems between 2-16 nm, with the largest particles containing around 1 million atoms each. The largest systems tend to require more relaxation time and here we have shown that our largest system of 16 nm converges fully within 1 million time steps. As before while the magnetisation data is not as smooth as the susceptibility or specific heat, this is mainly due to the small difference between the initial max magnetisation at the start of the simulation and the final value. The magnetisation varies by a small amount overall and typically produces smooth data after only 300-500k time-steps.

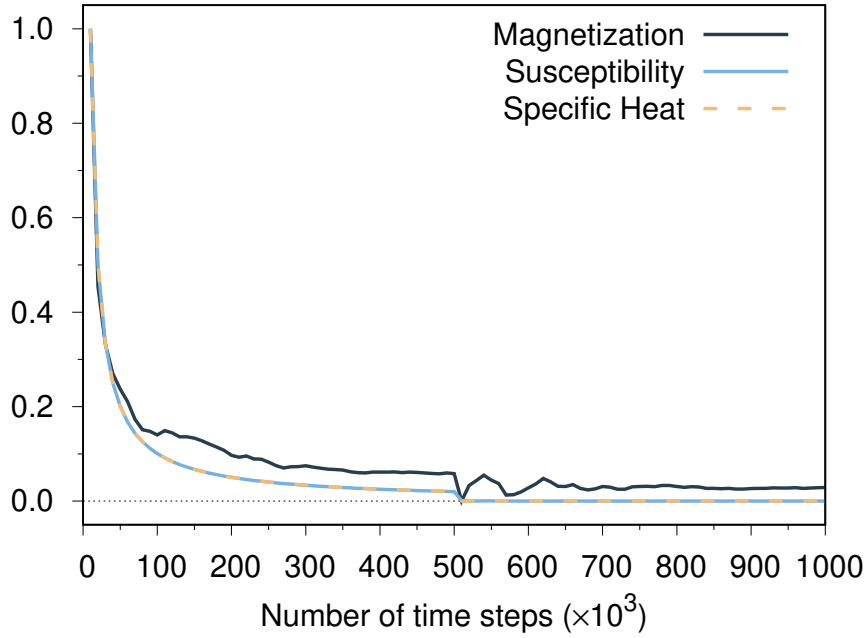

Figure 6.6: **Convergence test for $CoFe_2O_4$.** Testing the convergence of the magnetisation, specific heat and susceptibility for a 16 nm PBC system of cobalt ferrite at 1000 K. A total of 1 million Monte Carlo time steps are used for convergence.

Before we closely examine any of the magnetic properties of the system, the two sets of exchange parameters must be adjusted to keep the Curie temperature of the system close to the predicted value of 795 K. The sets of exchange values must

be multiplied by a constant to have the phase transition occur at the right position in our simulations. The exchange constants used in CFA must be increased significantly, by about 20%. This can be due to several factors, however the differences in the models used is likely a contributing factor. Meanwhile, the exchange parameters for CFB would end up with a Curie point around 850K, as in magnetite, however they must be lowered by around 7% to correctly reflect the lower critical point of cobalt ferrite.

The data sets do not agree perfectly, there is an approximately 5 K difference in the peaks, with the exchange values of CFA being slightly too high, however they both peak around 800 K, close to ideal value of 795 K. We can already see some of the difference between the sets of exchange here as in the set derived from magnetite the octahedral sublattices, including cobalt, behave very similarly, both sharing the same exchange values and lying roughly between the cobalt and octahedral plots from (a). The overall and tetrahedral components to the susceptibility agree well with each other which is promising as these are a result of completely separate exchange values.

Using the Curie temperature point predicted by the susceptibility we can fit the magnetisation scaling according to the Curie-Bloch equation. This will improve the fitting for small nanoparticles where finite size effects cause the phase transition to occur more gradually and obscure the Curie temperature. In Figure 6.8 we can compare the magnetisation scaling with temperature for both sets of exchange, as well as the fit β values.

The magnetisation curves demonstrate similar properties to the susceptibility, CFB behaves as if it is a 2-lattice model, with the cobalt and octahedral lattice behaving exactly the same and having the same β exponent. Meanwhile Figure 6.8a shows varying β exponents for the octahedral sublattices. In addition, both sets have varying β exponents for each component of the system. These are listed for comparison in Table 6.5.

The β exponents for the tetrahedral sublattice agree well with each other. Referring back the exchange constants, the J^{AA} interactions are quite different in each set, with the values from Ref [29] being the same in sign but an order of magnitude larger, making the similarity in the scaling of the tetrahedral lattice surprising. The overall β exponents are different due to the large difference in the octahedral sublattice for each system. $\beta = 0.45$ is relatively high for an octahedral β exponent compared to the values we have seen from magnetite and maghemite.

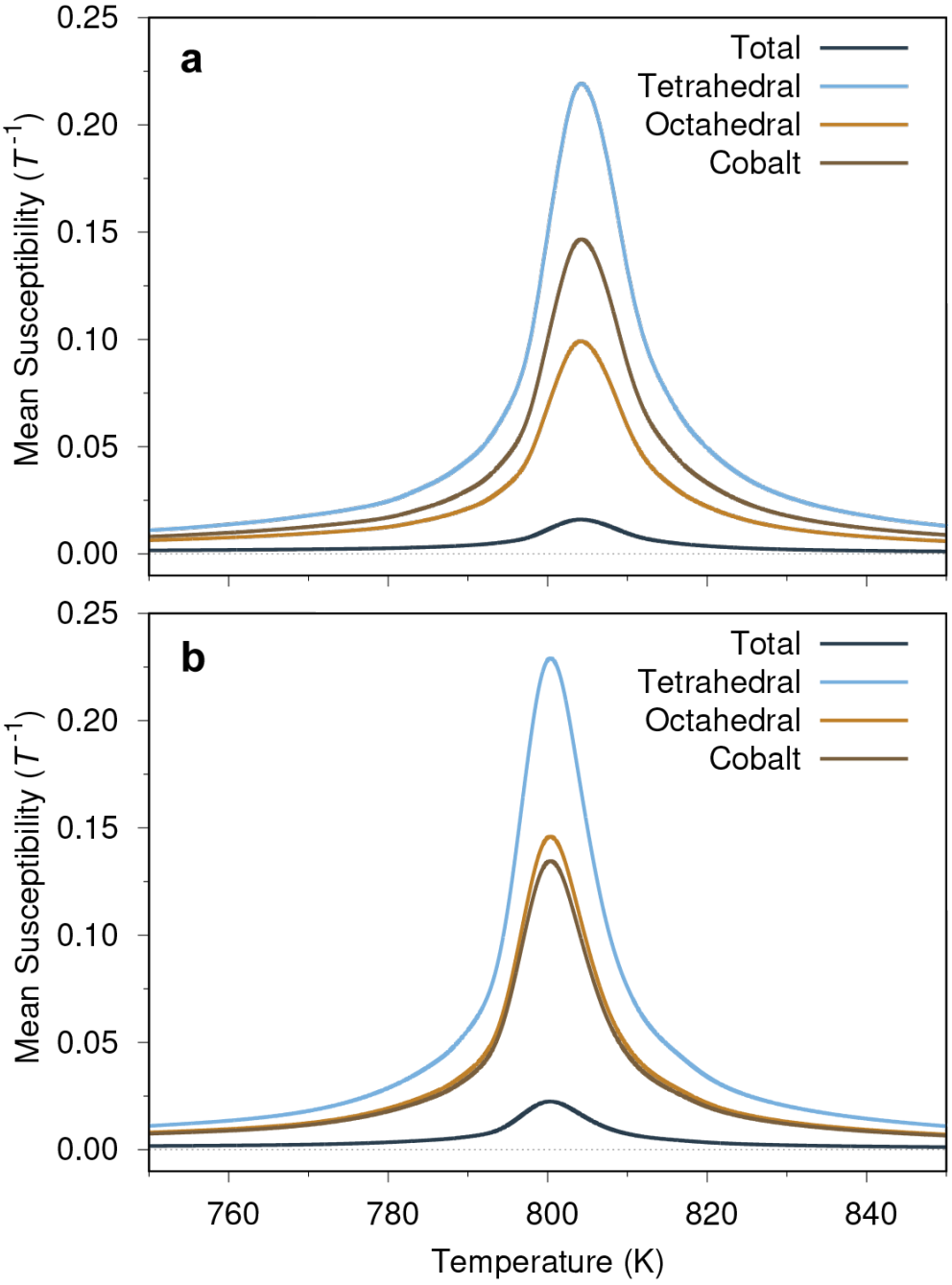

Figure 6.7: **Susceptibility for a 16 nm system of cobalt ferrite under PBCs.** Plot (a) shows the susceptibility of CFA, while plot (b) does the same for CFB.

Due to the shared exchange constants, the first column of Table 6.5 is very similar to our results from magnetite.

6.4.1 Anisotropy

Cobalt ferrite has cubic anisotropy scaling, much like magnetite, however the strength of the magnetocrystalline anisotropy is much stronger. Figure 6.9a shows

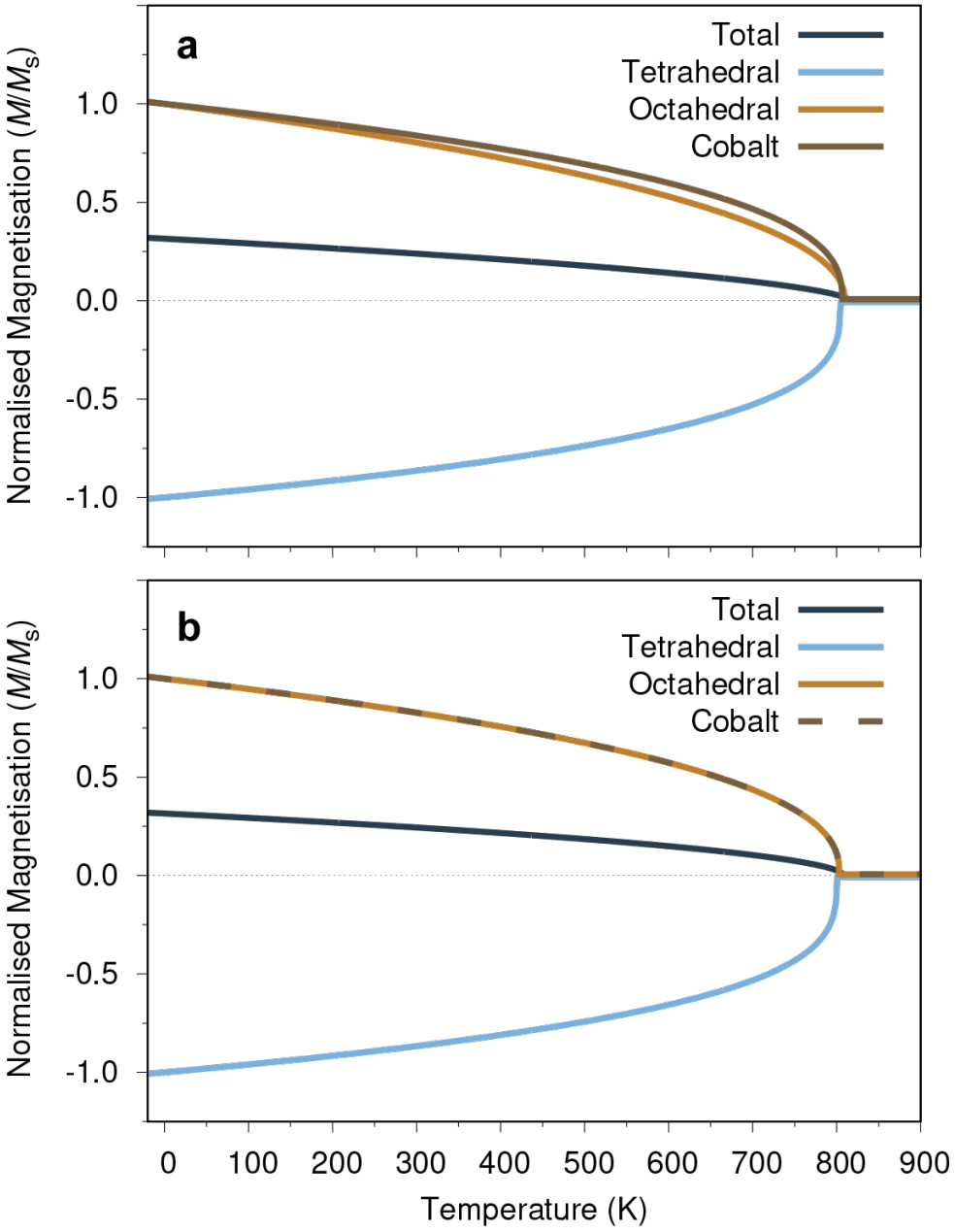

Figure 6.8: **Magnetisation scaling for a 16 nm system of cobalt ferrite under PBCs.** Plot (a) shows the magnetisation of CFA, while plot (b) shows the data from CFB.

that the torque curves for cobalt ferrite behave in the same manner as that of magnetite; a sinusoidal shape for the torque, with the peak occurring at 22.5°.

The temperature scaling of the anisotropy is notably different as can be seen in Figure 6.9b. At low temperatures, the torque is an order of magnitude higher than in magnetite, and the shape of the curve is more linear. This is likely due to the source of the increased anisotropy being restricted to the cobalt ions in the

	CFA	CFB
Total	0.57	0.53
Tetrahedral	0.32	0.31
Octahedral	0.45	0.40
Cobalt	0.37	0.40

Table 6.5: ***β* exponents for 16 nm cobalt ferrite under PBCs.** While the tetrahedral exponents are similar, the octahedral sublattices in each system vary significantly leading to the difference in the overall values.

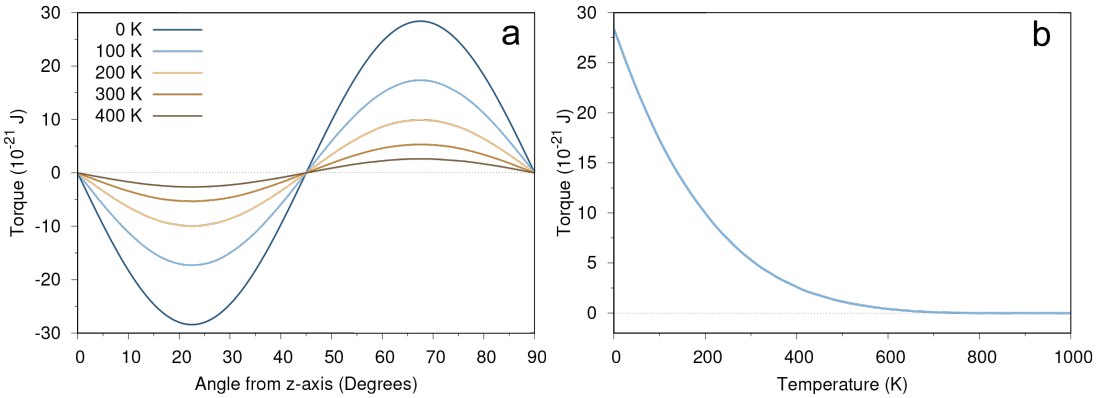

Figure 6.9: **Restoring torque and anisotropy scaling of $CoFe_2O_4$.** (a) Plot of the restoring torque for different temperatures as a function of angle from the z-axis. (b) Plot of the restoring torque as a function of temperature.

octahedral sublattice, rather than the material as a whole. The anisotropy scaling is very similar, also with a linear decrease in magnitude from 0 to around 450 K, however the strength of the anisotropy remains around ten times larger than in magnetite, even at high temperatures, as expected from Figure 6.4.

6.4.2 Particle Elongation

We can compare the superparamagnetic behaviour of cobalt ferrite to that of magnetite seen in Chapter 4.2. Cobalt ferrite has a much larger cubic anisotropy contribution which will therefore maintain the superparamagnetic state at higher temperatures than that of magnetite. We found that in magnetite, around room temperature, particle elongations caused a partially blocked state. To replicate the same behaviour in cobalt ferrite, we can increase the temperature as well as lower the particle size, reducing the number of spins and combined strength of the anisotropy. Figure 6.10 shows the magnetisation components of elongated truncated octahedral nanoparticles of 11 nm diameter at 550 K.

As the easy axis for the anisotropy of cobalt ferrite lies along the ⟨100⟩ direc-

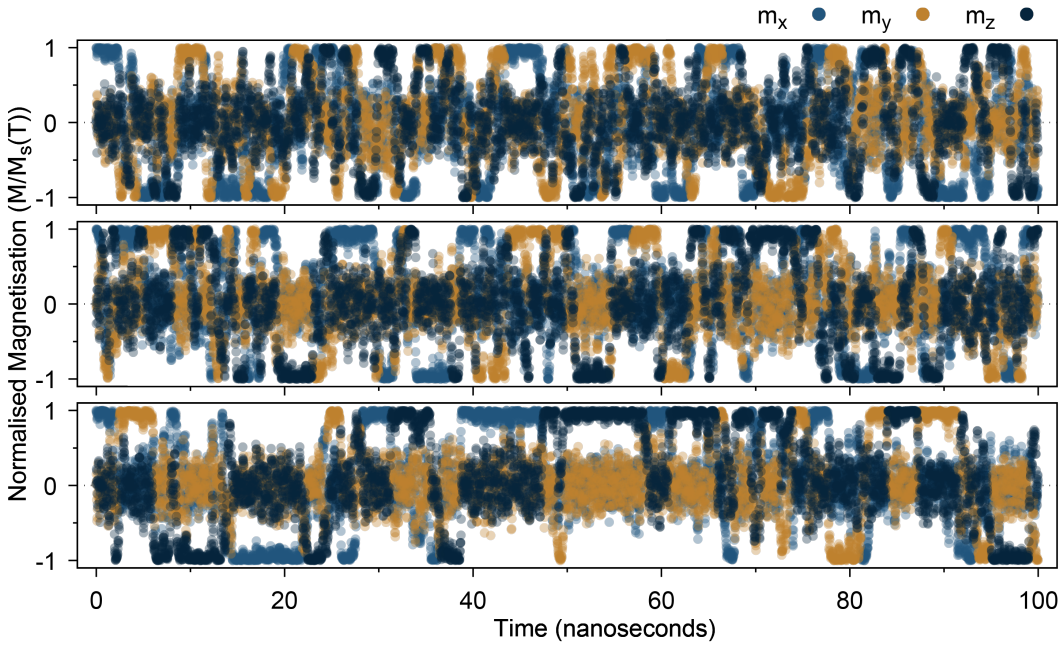

Figure 6.10: **Magnetisation components of elongated $CoFe_2O_4$ nanoparticles.** Plot of the time dependence of the magnetisation components for an 11 nm diameter octahedral nanoparticle for 0%, 10% and 20% elongation at T=550 K. The transition from a fully superparamagnetic regime to a partially blocked regime is shown by the stretched of constant spin orientation in all axes.

tions, this plot shows some change in behaviour to the magnetisation components of magnetite. Two components of the spin oscillate around 0 while the remaining component is 1. At 0% elongation we clearly see the movement of the system between the 6 possible orientations with no bias to any direction. By looking at the edge of the plots we can determine how long the spins remain aligned to one direction, with the average time being approximately 2 ns for a uniform particle. As the elongation is increased, we see a change in the spin behaviour as the system spends more time in each state, 4-5 ns in the case of 10% elongation and 6-8 ns at 20%. We note that in this case there all axes are affected equally, with the spins becoming partially blocked along the x, y and z orientations, unlike in magnetite where an elongation of the system along the z-axis caused a partial blocking of the z-component of the magnetisation.

Much like in magnetite, the shape anisotropy contribution caused by the elongation, even at 20%, is not enough to lock the system into one particular orientation and the system remains in a mostly superparamagnetic state, with a longer relaxation time.

6.4.3 Rescaling Parameter

While cobalt ferrite is widely studied for its biomedical applications, experimental data for the saturation magnetisation of bulk cobalt ferrite is somewhat rare. Along with high quality experimental data on the saturation magnetisation scaling of magnetite, the work done by Pauthenet [82] also offers similar data for cobalt ferrite. We have already shown that the experimental data of Pauthenet agrees well with our simulations therefore the data for cobalt ferrite should be of similar quality. In addition, the work done by Srivastava *et al.* on the exchange constants of spinel ferrites shows several experimental results for the magnetisation and susceptibility scaling of the studied materials, without referencing the original source. We shall use these two sets of experimental data to fit for the rescaling parameter α of cobalt ferrite.

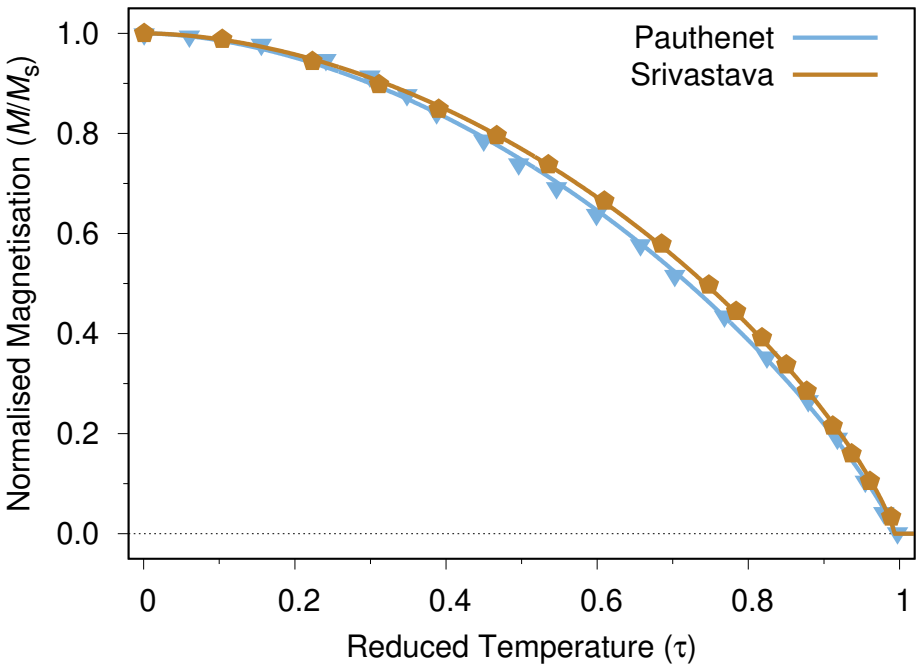

Figure 6.11: **Experimental saturation magnetisation of cobalt ferrite, from Pauthenet [82] and Srivastava [29].** Both plots are fit according to the Curie-Bloch equation, and give $\alpha \approx 1.8$.

Figure 6.11 shows the fits for each data set to the Curie-Bloch equation. Both data sets are close to linear when approaching T_C which leads to high values of β. The α fits are mostly tied to the initial drop in magnetisation at low temperatures and are roughly equal to 1.8. This is close to the rescaling constant found for magnetite, which is in line with previous discussions on the value of α for stable, fully ordered systems, compared to lower values of α found in maghemite likely due to iron vacancies.

6.5 FSS Properties of Cobalt Ferrite

Much like magnetite and maghemite, cobalt ferrite is susceptible to changes in magnetic properties due to finite size effects. Here we present a full set of FSS analysis for our models of cobalt ferrite, CFA and CFB. First we demonstrate the classic magnetisation scaling properties of both models, shown in Figure 6.12. The models differ in magnetisation scaling mainly due to the difference in exchange parameters. CFA also shows a different β exponent as the gradient of the plots is more linear than those in CFB. This is linked to a higher overall β. While β is expected to be higher than in bulk when the nanoparticle size is small, cobalt ferrite also retains a higher overall value of β in bulk. This causes the Curie temperature phase transition to occur more gradually as the magnetisation does not drop as quickly at the critical point.

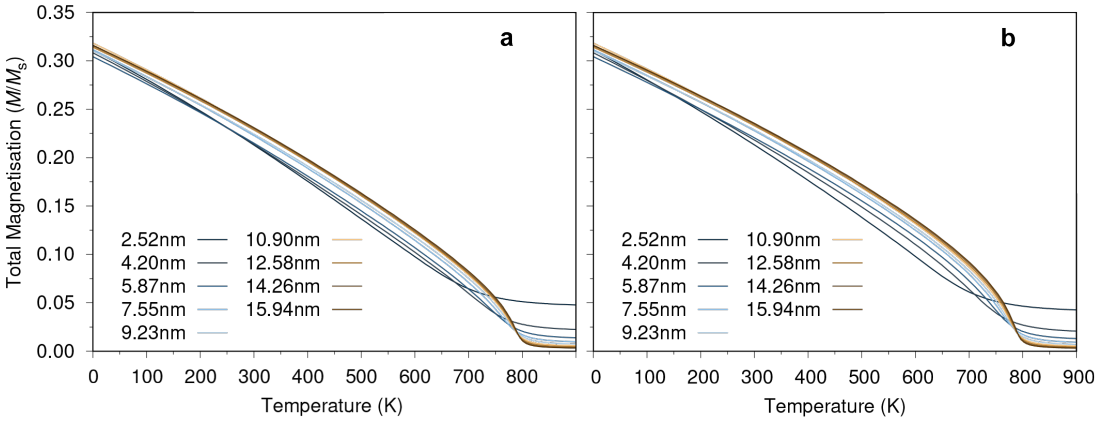

Figure 6.12: **Classical magnetisation scaling of CFA(a) and CFB(b).** The finite size effects reduce the magnetisation as the particle size decreases.

The sublattice magnetisation can be split into three components, the tetrahedral iron, octahedral iron and octahedral cobalt. Each lattice has distinct scaling however the tetrahedral lattices of both CFA and CFB behave similarly due to their like properties, while the octahedral sublattices vary, with the octahedral lattice of CFA being much lower in normalised magnetisation overall. As the octahedral sublattice makes up two thirds of the cobalt ferrite unit cell, this division of the cobalt and iron components of the octahedral sublattice also spins the system neatly into three equally sized components which are contributing to the overall magnetic properties of cobalt ferrite.

We can apply quantum mechanical rescaling to our simulated data, in particular the CFA data set as it should be comparable to the work done by Pauthenet and Srivastava (Figure 6.3). Figure 6.14a shows the rescaled magnetisation of

spherical nanoparticles. While the 16 nm system shows a sharp turning point at the Curie temperature, the smaller systems which are more strongly affected by finite size effects show good agreement with the data from Srivastava (Figure 6.14b). In both works, the source of the experimental data is not disclosed, and it is therefore possible that the samples studied were fine cobalt ferrite powders which would also be subject to finite size effects. This would also explain the very high values of β fit from the experimental plots which are very high compared to any other value of β seen in magnetite or maghemite, or indeed the 'ideal' value of $\beta = 0.34$ linked to the 3D Heisenberg Hamiltonian [42].

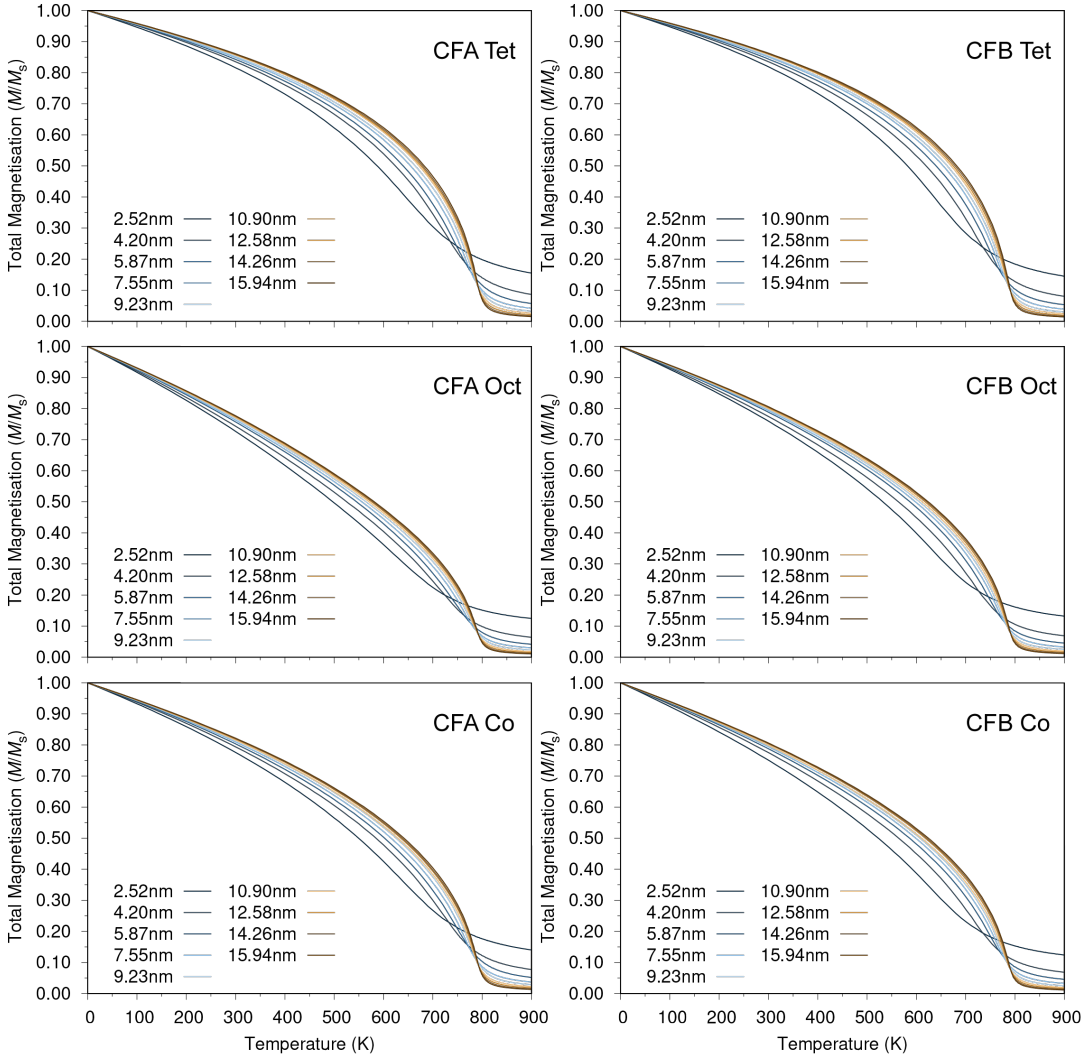

Figure 6.13: **MvsT of cobalt ferrite sublattices.** Classical magnetisation scaling of the sublattices of CFA (left column) and CFB (right column) including the distinction between the iron and cobalt components for both systems.

Fitting the magnetisation we can also extract values for β for the overall

and sublattice components of CFA, shown in Figure 6.15. As suggested by the magnetisation scaling, the β exponent is distinct for all components of the system, lowering as the particle size increases.

From the magnetisation scaling alone it is quite difficult to see how the β exponent varies between CFA and CFB. This is shown more clearly in Figure 6.16, where the β scaling for CFA and CFB under periodic boundary conditions is shown. This highlights the problems with using the exchange constants from magnetite as a basis for the exchange of cobalt ferrite. While the tetrahedral sublattice may be well behaved, the octahedral sublattice, which is made up of distinct components, collapses onto the same curve for CFB. Overall, the β values are also slightly higher in CFA, for all particle sizes.

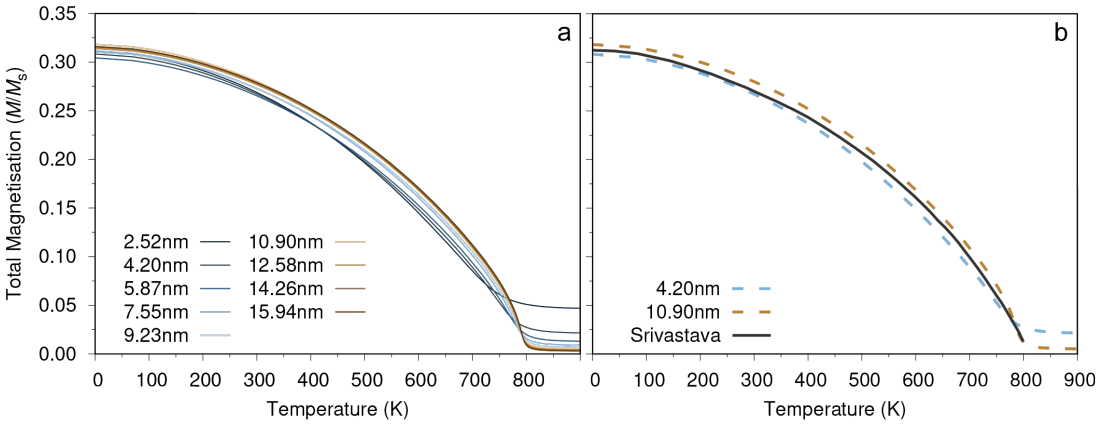

Figure 6.14: **Comparison of rescaled data and experiment.** (a) Rescaled magnetisation scaling of the CFA data set using $\alpha = 1.8$. Due to the rescaling the reduction in magnetisation with temperature increase occurs more gradually at low temperatures. (b) The experimental data from Srivastava *et al.* [29] fits well with the low diameter nanoparticle scaling.

The Curie temperature scaling for both systems is similar, with a reduction in T_C of about 18% for the smallest, 2.5 nm particles. With 1 K sampling in the data output of our simulations, the Curie temperature fit using the Curie-Bloch equation is almost always the same for the octahedral sublattice and the overall material. The tetrahedral sublattice shows very minor deviations at low particle diameters. Comparing the T_C scaling with spherical nanoparticle of magnetite and maghemite, the reduction in T_C is consistent for all three ferrites. The finite size effects on the Curie temperature are not strongly tied to the material type, instead being more heavily affected by nanoparticle shape and size.

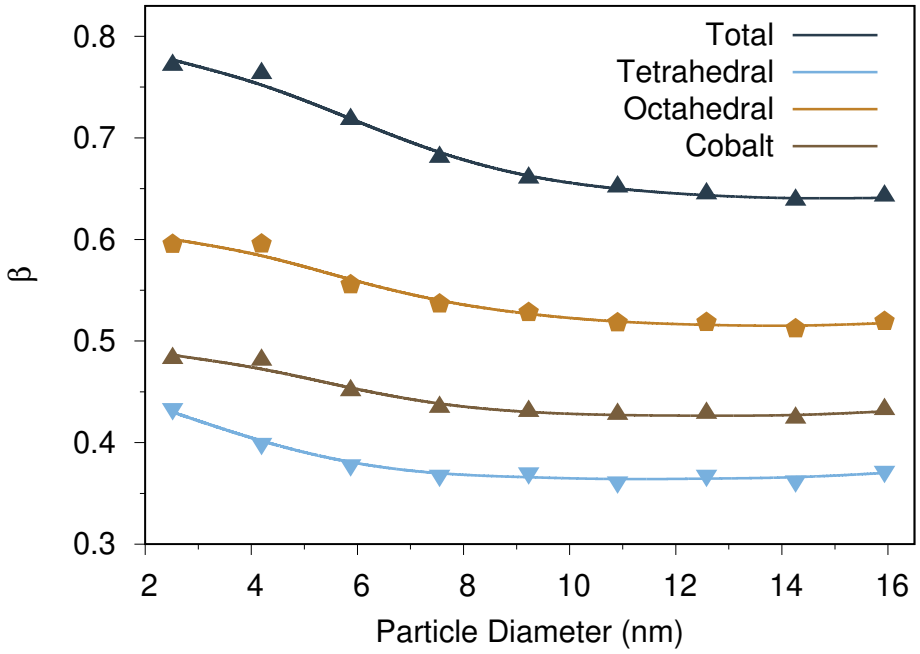

Figure 6.15: ***β* scaling of all components of CFA.** The octahedral sublattices have the lowest β values contrary to the behaviour seen in magnetite and maghemite.

6.6 Conclusion

Cobalt ferrite, both in bulk and powder form, has been studied widely due to its stability and strong magnetic anisotropy, making it suitable for many applications. The nanoscale parameters however are relatively unexplored as the exchange constants, which are crucial to forming an atomistic model of cobalt ferrite, have not been refined to the same extent as those seen in magnetite. In this Chapter we have covered two typed of cobalt ferrite, CFA and CFB, built using the same structure but differing in exchange parameters to better understand the differences in a 2 and 3-lattice model, as well as highlight the changes in the sublattice behaviour.

In comparing the two models we find that the overall magnetisation and susceptibility scaling remains similar while the octahedral sublattice shows significant changes, with a separation in the critical exponents for the iron and cobalt components, when using the 3-lattice exchange constants.

Due to the strong anisotropy arising from the cobalt ions in the system, the material shows different low temperature spin behaviour to magnetite, with the superparamagnetic phase being maintained well above room temperature.

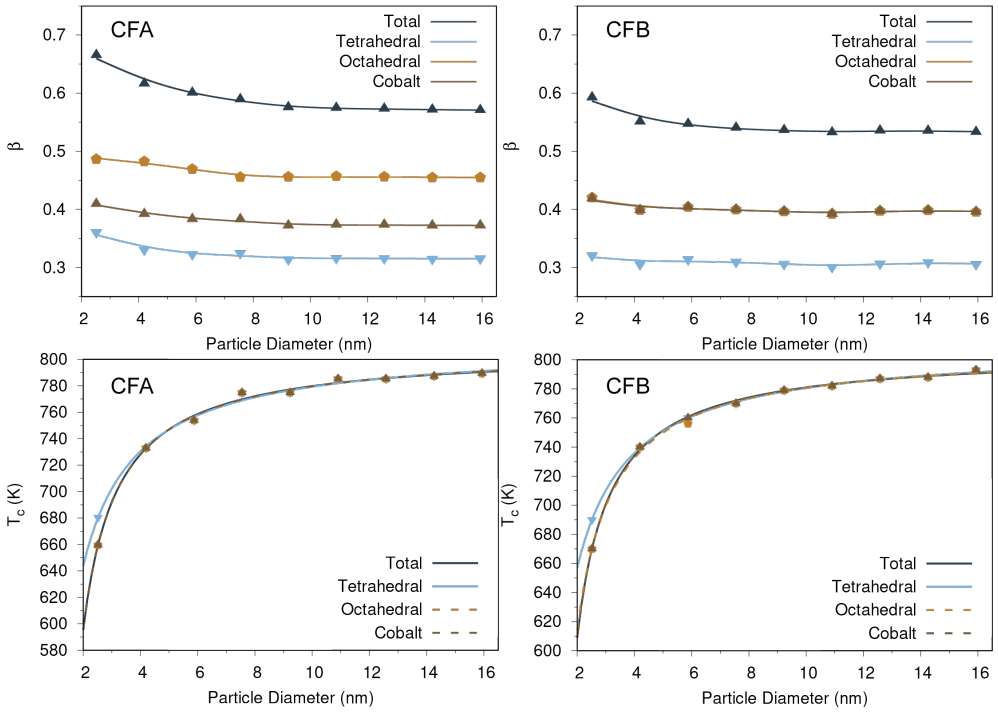

Figure 6.16: **β and T_C scaling of cobalt ferrite.** β scaling of CFA and CFB under periodic boundary conditions, and T_C scaling for spherical nanoparticles.

Elongated nanoparticles of cobalt ferrite showed a partial blocking of the spin orientation at around 500 K with particle elongations of 20%.

CHAPTER 7

CORE-SHELL NANOPARTICLES

7.1 Introduction

In hyperthermia, the heat output of the nanoparticles roughly scales with the saturation magnetisation of the magnetic material. While iron oxide nanoparticles tend to be favoured for their biocompatibility and biodegradability, most materials suffer from lower magnetocrystalline anisotropies leading to lower heat outputs. Cobalt ferrite helps to alleviate this issue as it exhibits a very high saturation magnetisation, with the cobalt ions lending a much higher anisotropy to the system. While nanoparticle properties are typically defined by the size, shape, surface and material content, one further way in which it is possible to gain further control over the magnetic properties of a sample is to form core-shell nanoparticles made up of different materials.

A core-shell nanoparticle is typically composed of two or more materials, one forming the core at the centre of the nanoparticle, and further materials forming shells on top of the core. The materials used to form core-shell nanoparticles can be substantially different in type and use case. In many biomedical applications, nanoparticles can be coated in organic or silicon based materials either to shield the magnetic particle from the surrounding environment or to perform additional functions by attaching hydrophilic/phobic molecules to the particle surface [100, 165].

In addition to shielding, core-shell particles can be used to combine the properties of similar materials, achieving an intermediate effect between the properties

of either system. The core diameter then acts as an additional parameter in fine tuning the relative strengths of the magnetic properties of each material [19]. This applies to the materials we have studied so far. As magnetite, maghemite and cobalt ferrite share similar structures, all Fd-3m materials with a tetrahedral-octahedral sublattice composition and similar lattice parameters, these materials can be mixed to form core-shell nanoparticles with overall properties defined by the relative amount of materials in each particle.

In addition, maghemite is of particular interest and the shell component of a core-shell nanoparticle as this material forms naturally over time as a product of oxidation in small magnetite nanoparticles typically used for their superparamagnetic behaviour in hyperthermia applications [166]. When around 10 nm in diameter, magnetite nanoparticles tend to form thin layers of maghemite which are typically referred to as magnetic dead layers, heavily reducing the effectiveness of the nanoparticles by decreasing their saturation magnetisation and anisotropy, as well as slightly modifying the effective size of the nanoparticles [167, 168]. Due to the similarity in material composition for these particles, it is also more difficult to identify the core-shell diameters in experiment.

Here we study two different core-shell systems: magnetite-maghemite and magnetite-cobalt ferrite, to get a better understanding of the change in magnetic properties of the particles, in particular the magnetisation scaling and the change to the Curie temperature as a result of the mixing of the materials.

7.2 Structure

The generation of core-shell nanoparticles is done natively in VAMPIRE by specifying the core-shell diameters of the contained materials. While core-shell particles can be created in various different forms, we shall be simulating the most basic system with an inner core at the centre of the particle composed of one material, surrounded by a continuous shell of the second. Figure 7.1 shows a typical spherical core-shell nanoparticle with a core diameter roughly half that of the whole particle. As we are dealing with spherical systems, the diameter of the core and shell is not related linearly to the amount of each material contained in the system. A core with a diameter of half the particle makes up less than 15% of the material content of the system. As such, particles shall be created based on the percentage content of each of the materials.

To form epitaxial particles with a single crystal approximation, the lattice

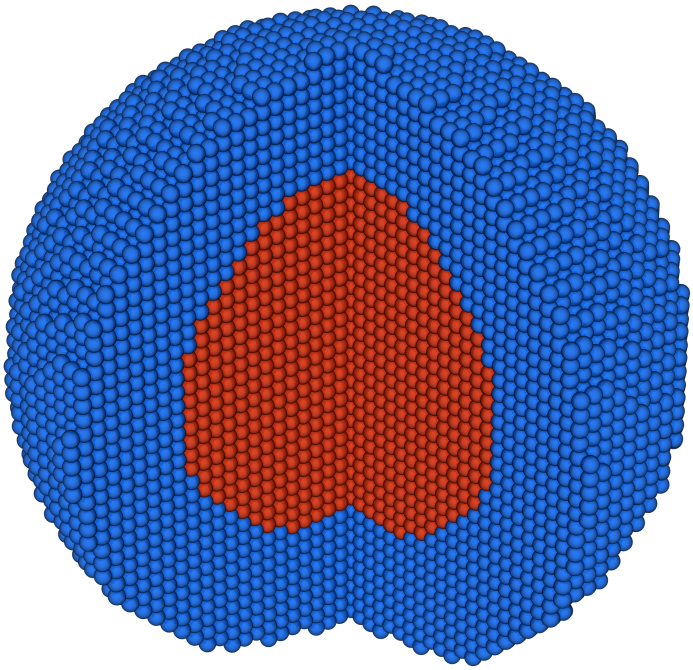

Figure 7.1: **Core-shell nanoparticle.** A spherical core-shell nanoparticle, with a corner removed to show the inner structure. The red core size is defined by a fraction of the overall system diameter, with the blue shell taking up the rest of the system.

parameters of the core and shell are averaged so that the materials have fully saturated bonds at the intersection. Core-shell systems created in experiment will likely have similar behaviour to this when formed using layers. Due to the similarity in structure between the iron oxides studied here, with lattice constants varying by at most 0.05Å, a small relaxation in the lattice parameters can occur to accommodate the formation of bonds between the surfaces of both materials. While this relaxation will not occur throughout each material, the particle sizes are small enough that this will have little knock-on effect to the rest of the particle.

The core and shell cannot be treated as non-interacting parts of the system and therefore we also require several new exchange parameters to define the interactions between each material. In the case of magnetite and maghemite which share the same number of exchange interactions individually, we find the average of similar interaction types to form the unknown exchange values. For example, to find the strength of the $J^{A_{\text{magn}}A_{\text{magh}}}$ interaction, we take a simple average of the J^{AA} interaction of magnetite and the J^{AA} interaction of maghemite.

$$J^{A_{\text{magn}}A_{\text{magh}}} = 0.5\left(J^{A_{\text{magn}}A_{\text{magn}}} + J^{A_{\text{magh}}A_{\text{magh}}}\right) \tag{7.1}$$

In the case of cobalt ferrite which includes a third sublattice due to the presence of cobalt, we calculate similar averages for the interactions by using the most appropriate exchange constants in each material. As we have two sets of exchange constants for cobalt ferrite, we shall be exclusively using the values modified from Srivastava *et al.* [29] which correctly separates out the cobalt and iron components of the octahedral sublattice.

As we have already covered the finite-size scaling properties of each material by changing the overall particle size, the core-shell particles will not vary in overall diameter. The diameter is set to 10 nm, which is typical for most biomedical applications which can take advantage of core-shell systems, or which can be affected by the formation of the magnetic dead layer on magnetite systems [167]. At this size, the particles are still affected by the same finite-size effects seen previously, which moderately lower the magnetisation and Curie temperature of the particle by ≈5%. As we are mixing different materials, we shall not be able to calculate the quantum mechanical rescaling parameter α by fitting experimental data. As a rule of thumb, the value is above 1.5 for all three materials, and seems to be close to 2.0 for magnetite and cobalt ferrite. If the β exponent were to stay constant for the core-shell particles, it would be justified to approximate the value of α and plot the rescaled magnetisation, however β is more likely to change, and this would also be another approximation which can muddy our data. Hence, we instead focus on the high temperature magnetic properties where the quantum mechanical effects are minimal.

By modelling the core-shell particles we can study the changes in the sublattice behaviour of the materials. The Curie temperature, magnetisation and susceptibility scaling need not be the same as in pure systems. In addition, the magnetic properties may remain separate to the individual materials in spite of their interaction and diverge in the overall data. As small shell thicknesses are more prominent in experiment, it is also important to find any possible limit in the effects of the shell below a thickness threshold.

7.3 Magnetite-Maghemite

In the case of magnetite-maghemite core-shell particles, we are not seeking to optimise the magnetic properties of the particle but instead understand how much

the maghemite shell affects the whole system. The maghemite layer on the surface is measured to be roughly 1 nm after formation of magnetite particles, depending on the preparation method [166]. In addition, the lifetime of the nanoparticles is also related to the slow increase in size of the maghemite shell [167]. Here we present the magnetic properties of core-shell particles as a function of core size, starting from a pure shell particle, in this case maghemite, and gradually increasing the size of the core to a pure core particle (magnetite).

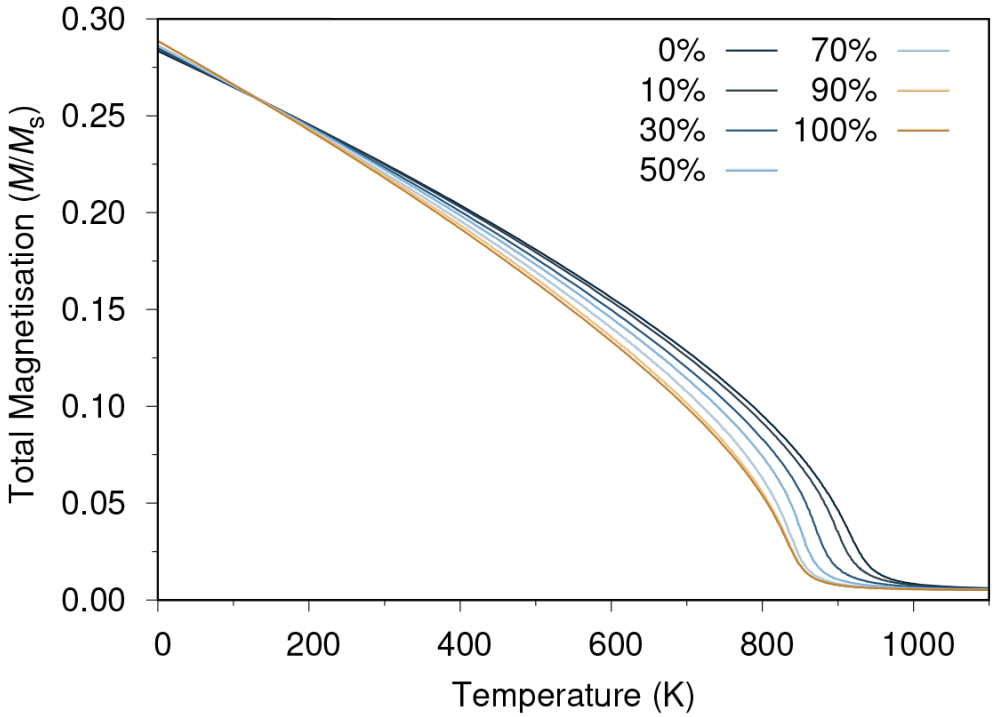

Figure 7.2: **Magnetisation scaling of 10 nm magnetite-maghemite core-shell particles.** The plots show increasing magnetite content in the particle from pure maghemite to pure magnetite.

Figure 7.2 shows the overall variation of magnetisation with particle size. We can see a clear change in the Curie temperature of the system as the turning point moves down with increasing magnetite content. The pure maghemite nanoparticle (0%) has a T_C of around 950 K which lowers towards 850K, the Curie temperature of magnetite. In addition to the change in T_C, the shape of the turning point also shifts with increasing core size. This is tied to a change in the β exponent. The pure magnetite and maghemite seem to have roughly the same gradient around T_C however the core-shell particles fall more steeply towards a value of zero magnetisation. Hence the topological change from pure to core-shell particle alone has affected the value of the exponent β.

The magnetic properties of the nanoparticles are now a result of four sublat-

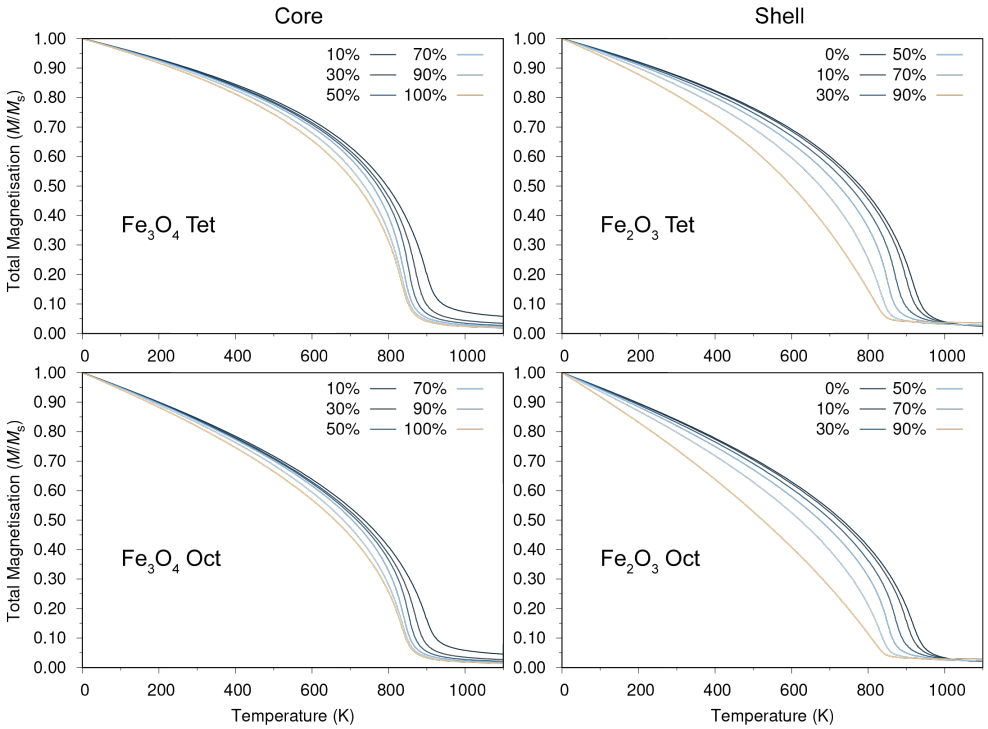

Figure 7.3: **Sublattice magnetisation temperature dependence of magnetite-maghemite core-shell nanoparticles.**

tices interacting and competing with each other. While the sublattices interact close to the intersection of the core and shell, they also retain the behaviour unique to each material. From Figure 7.3, the magnetite and maghemite sublattices have notably different magnetisation scaling. The magnetite sublattices are not heavily affected by the amount of maghemite in the system as the slope of each plot is almost constant. The main effect is the increase in the Curie temperature as the amount of maghemite increases. This also happens inversely in the maghemite sublattices however there is also a strong change in the slope of the plots. The shell of the particle has missing exchange bonds which are contributing to the change in magnetisation with size. This is a surface effect which appears more drastically in the core-shell sublattices than in pure particles. When the shell makes up less than 10% of the overall system, the maghemite sublattices have an almost linear magnetisation scaling.

Curiously, the sublattices also exhibit a finite size effect we have already seen in pure nanoparticles and PBC systems. In the core sublattices, the magnetisation does not level off at the same point for different core sizes. The core shows similar statistical effects to a pure nanoparticle where a smaller number of spins cause a non-zero magnetisation value after the Curie point due to the random distribution of spins orientations. With an increase in core size, this value lowers as the

increased number of spins can be more evenly distributed. This behaviour is muted in the shell sublattices which do level off at the same magnetisation value irrespective of the thickness of the shell and therefore the amount of maghemite in the system. This is likely a topological effect. Where the core behaves akin to a pure nanoparticle, the shell is instead more closely related to an infinite plane of spins, effectively periodic in θ and ϕ in spherical coordinates, but not in r.

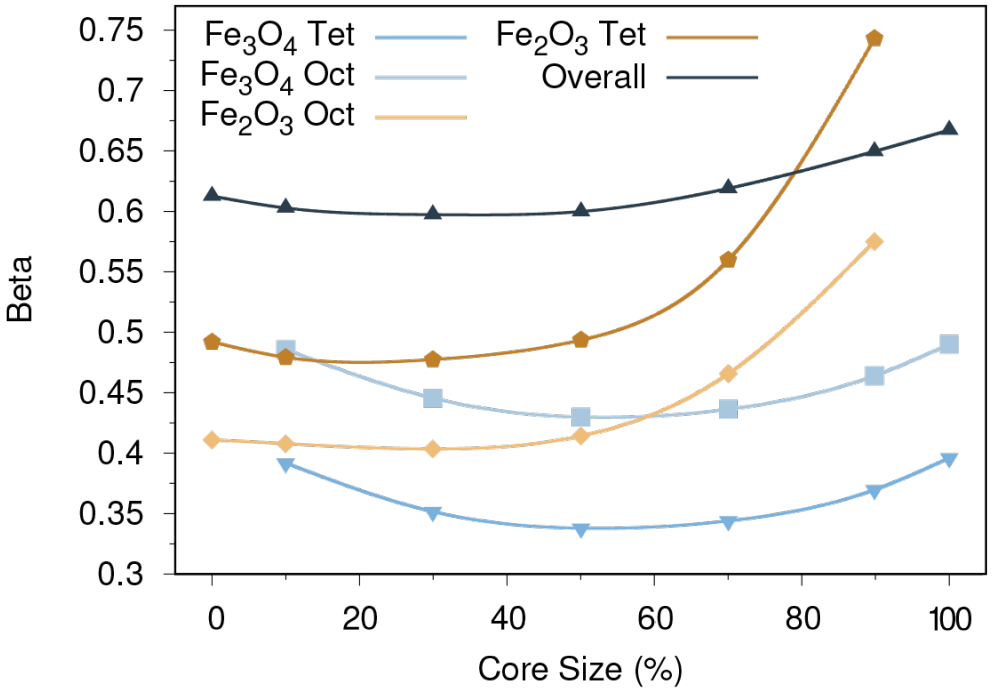

Figure 7.4: ***β* scaling of magnetite-maghemite nanoparticles**. When comparing the scaling for all sublattices of the system, we see a steep increase in the value of β as the size of the shell decreases.

We can fit the magnetisation scaling of the nanoparticles to the Curie-Bloch equation to find how the value of β changes as the relative sizes of the core and shell are swapped. Figure 7.4 shows the fit values of β for all components of the particle. Maghemite typically exhibits lower values of β for nanoparticles of any shape. Physically this corresponds to a slower reduction in the magnetisation of the system as the temperature increases. Very high values of β lead to a rapid decrease in the particle magnetisation and a more gradual phase transition. When the magnetite core is small or not present, the core-shell particle maintains a value of β around 0.6, but this value increases to 0.65 as the amount of magnetite in the system increases. Comparing this result with Figure 4.6, this agrees well with the value of β fit for spherical nanoparticle of magnetite around the same size.

The sublattices present different behaviours for each material. In the case

of maghemite in the shell, the β scaling is expected as it follows similar trends to spherical maghemite particles. When the shell thickness is low, β is high, but the value lowers smoothly as the shell thickness increases and tends towards a constant value as maghemite dominates the system. This is analogous to pure maghemite nanoparticles which have high β when the particle is very small, below 6 nm, but tend asymptotically towards a constant value which is reflected in the PBC plots of maghemite in Figure 5.13. The magnetite sublattices do not replicate this behaviour and scale differently to spherical nanoparticles. β is at the same value when there is very little magnetite in the system (around 10%) and when the system is fully magnetite. Instead β lowers to a minimum when there is a 50/50 mix of maghemite and magnetite in the system. The overall β scaling retains the features of both sets of sublattices, with a moderate increase for low shell thicknesses and a dip when the system is made up of equal proportions of each material.

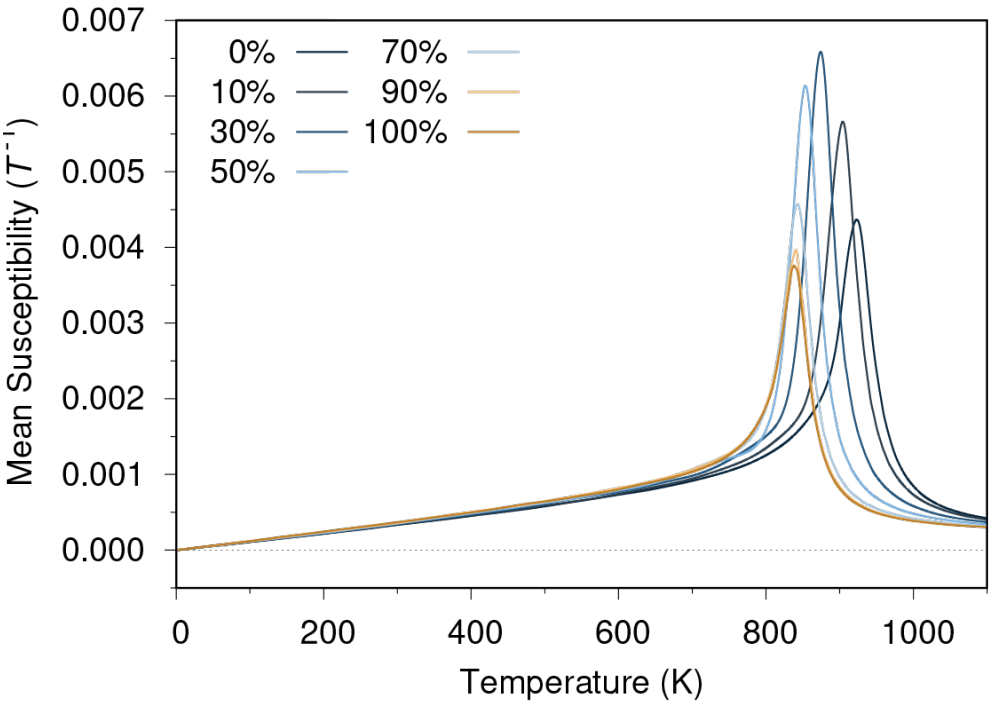

Figure 7.5: **Total susceptibility scaling of the magnetite-maghemite nanoparticles.** The magnitude of the susceptibility increases when there is a mix of both materials in the system and reaches a minimum for pure maghemite and magnetite.

The susceptibility of pure nanoparticles is affected by finite size effects where the magnitude increases with particle size. In these core-shell nanoparticle the overall size remains constant however from Figure 7.5, the magnitude of the susceptibility changes with the increase in core diameter. This is a measure of the

spin fluctuations occurring in the system, with equal amounts of core and shell leading to higher fluctuations. Typically, larger systems allow for more fluctuation due to spins being able to form larger regions of similar orientation, however in these particles the intersection between the materials does not seem to hinder this behaviour. The iron vacancies in maghemite may play a part in this allowing the system to experience stronger surface spin fluctuations.

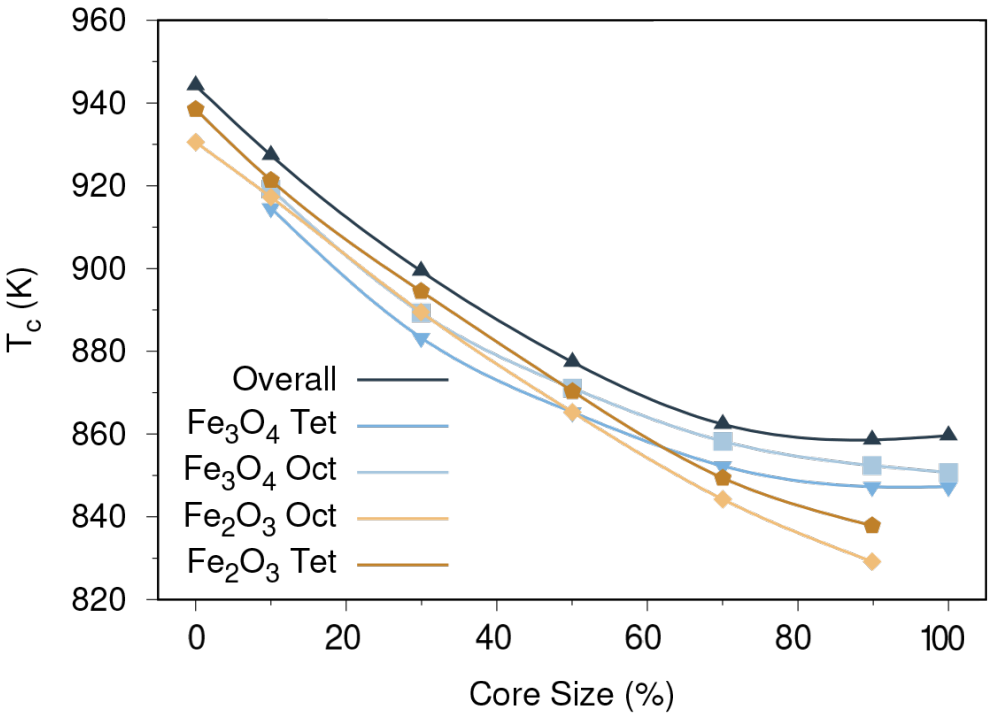

Figure 7.6: **Curie temperature of magnetite-maghemite particles and its components.** T_C moves between the bulk values for pure maghemite and magnetite as the core size increases.

By looking at the peaks in the particle susceptibility, we can also plot the Curie temperature point of the system. As the peaks remain narrow, they should be a good indication of the critical point, as in the pure nanoparticles. We can also use this with the magnetisation curves to fit for β using the Curie-Bloch equation. Figure 7.6 shows the predicted Curie temperature points for all components of the system. The Curie temperature of the overall particle is more closely linked to the magnetite sublattices in the core than the behaviour of the shell. In general, the point moves from the T_C of maghemite when the core is very small and increases to the T_C of magnetite when the core dominates the system, however this does not occur in a linear fashion. In the case of magnetite-maghemite particles the Curie temperature levels off when the core is more than 70% of the system. This suggests that an important property of the system would remain unaffected after

the formation of a thin maghemite shell. The overall magnetisation would still be reduced however due to the lower saturation magnetisation of maghemite.

7.4 Magnetite-Cobalt Ferrite

Magnetite-cobalt ferrite nanoparticles are constructed to negate the formation of an oxidised maghemite layer as well as to amplify the overall system anisotropy, and hence heating ability during Néel relaxation. Cobalt ferrite differs in several ways to maghemite, with a fully ordered octahedral sublattice, made up of both iron and cobalt. We separate these into 5 sublattices which all have distinct scaling properties. In addition, the anisotropy of the system is now mixed with the magnetite core experiencing a weaker anisotropy along the ⟨111⟩ axis, while the cobalt ferrite shell has a much stronger anisotropy along ⟨100⟩. The Curie temperatures of both systems are very close, with a difference of 50 K in bulk phases.

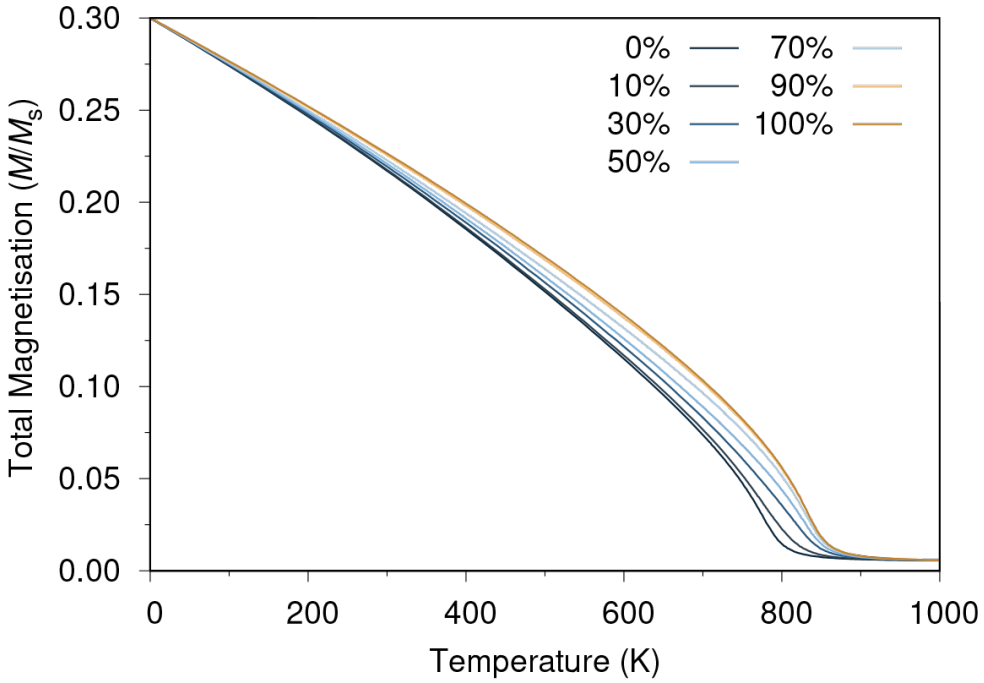

Figure 7.7: **Magnetisation scaling of 10 nm magnetite-cobalt ferrite core-shell nanoparticles.** As the core size increases, the Curie point moves from a lower value of 795 K for cobalt ferrite, to the Curie temperature of magnetite at 856 K.

Figure 7.7 shows the magnetisation scaling of magnetite-cobalt ferrite particles. As the Curie temperatures of the individual materials are close, around 50 K difference, the magnetisation curves of pure magnetite and cobalt-ferrite are close

together. To emphasise the change in the shape of the plots, the curves have been adjusted to start at a magnetisation of 0.3 at 0 K, similar to the magnetisation curves of bulk magnetite. The raw data is spread out at 0K due to the difference in structure and magnetic moments between the two materials, making it difficult to compare the plots. This resembles Figure 4.9, where the magnetisation plots are spread due to the change in surface composition of the faceted magnetite nanoparticles. We see that the core-shell particles, which lie in between the pure cobalt-ferrite and pure magnetite plots, approach the critical point more directly, making the transition broader. This is linked with an increase in the β scaling for these systems, which is the opposite behaviour to what was seen in the magnetite-maghemite particles where all mixed systems had an overall lower value of β and approached the Curie point more steeply.

The sublattice magnetisation scaling follows similar trends, with the magnetite sublattices showing very small deviations from pure magnetite for all core sizes, while the cobalt ferrite sublattices are more strongly affected by the increasing core. In these sublattices the magnetisation lowers by as much as 10% at room temperature and up to 20% at higher temperatures when the amount of cobalt ferrite in the system is decreased and it only forms a thin shell at the surface.

The susceptibility scaling of these nanoparticles (Figure 7.8) shows inverse behaviour to that in the magnetite-maghemite particles. Here the magnitude of the susceptibility is lowest when there is an equal proportion of both materials in the system. Individually, the sublattices have the highest magnitude when their material content in the particle is highest, which explains the minimum in the overall plot. Due to the very low values of susceptibility, particularly in the cobalt ferrite sublattices, it is very difficult to find a value for the Curie temperature point, as the peak is not easy to isolate. Despite this we can observe general trends in the scaling of the Curie temperature. From the overall susceptibility, the Curie temperature moves from around 800K, T_{C} of cobalt-ferrite, to 850K, T_{C} of magnetite. The Curie temperature is very close to 850 K when there is more than 70% magnetite in the particle. This follows the same behaviour as the magnetite-maghemite particles where there was also very little change in T_{C} at large core sizes. When the core size is small (0-30% particle content), the Curie temperature changes significantly. It is therefore likely that when using other magnetic materials, Curie temperature scaling in core-shell nanoparticles follows the same path regardless of the specific materials. The magnetite sublattices are not heavily affected by the amount of cobalt ferrite in the system as they do not peak below 825 K. Conversely the cobalt ferrite is heavily affected by the core as

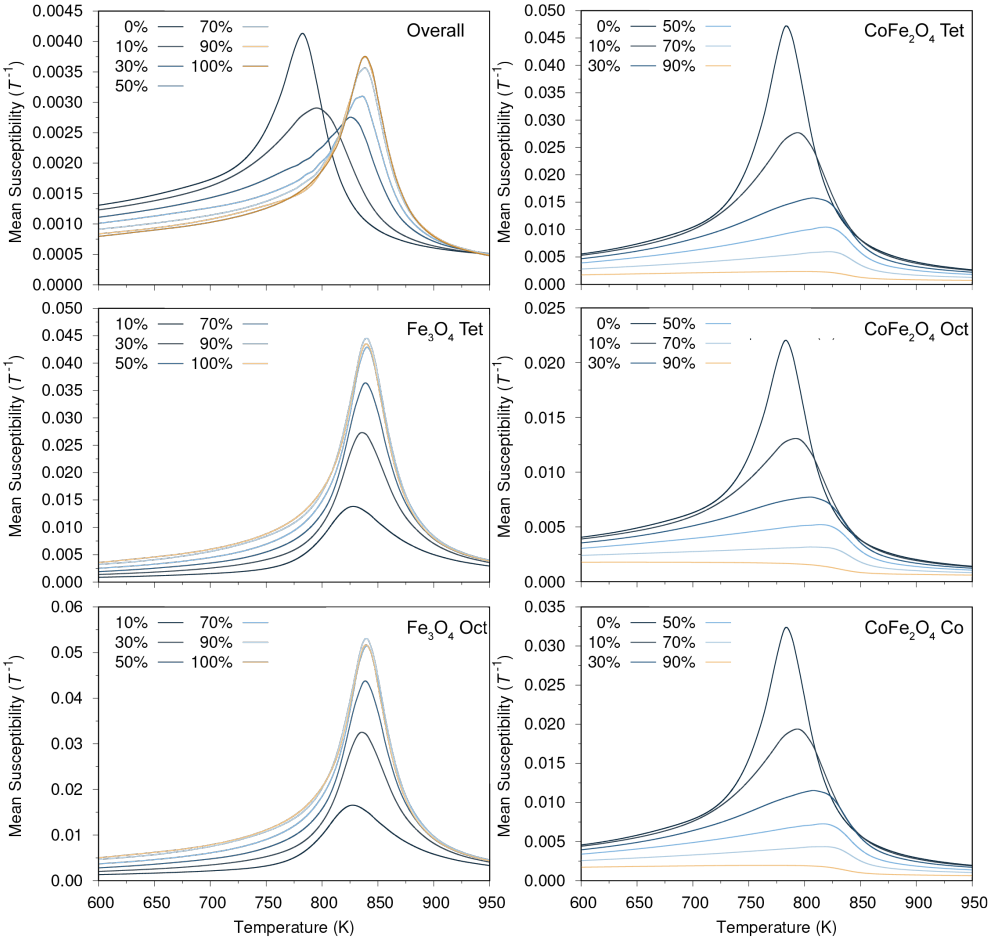

Figure 7.8: **Susceptibility scaling of all components of the magnetite-cobalt ferrite core-shell particles.** The magnitude of the susceptibility is highest when the particle is dominated by either of the materials. The cobalt ferrite shell is heavily affected by the core size of the particle, with large changes in the susceptibility and spin correlation.

the peak in susceptibility moves all the way between the two materials T_cs.

The β scaling for magnetite-cobalt ferrite nanoparticles is shown in Figure 7.9. The curves can be grouped according to the material they correspond to. For the sublattices we see similar behaviour as in magnetite-maghemite, where the core β scaling is relatively linear, with β being about 0.45 at very high and low amounts of magnetite in the system. The shell β exponents are roughly linear, showing a steady reduction in β as the shell thickness increases. As this behaviour is the same for both sets of core-shell particles studied, it is likely that this holds for other combinations of materials. The β exponent remains constant for the core component of the system while the shells behave much like pure nanoparticles where β steadily decreases towards a constant value. Hence β may not be strongly affected by the topological properties of the shell.

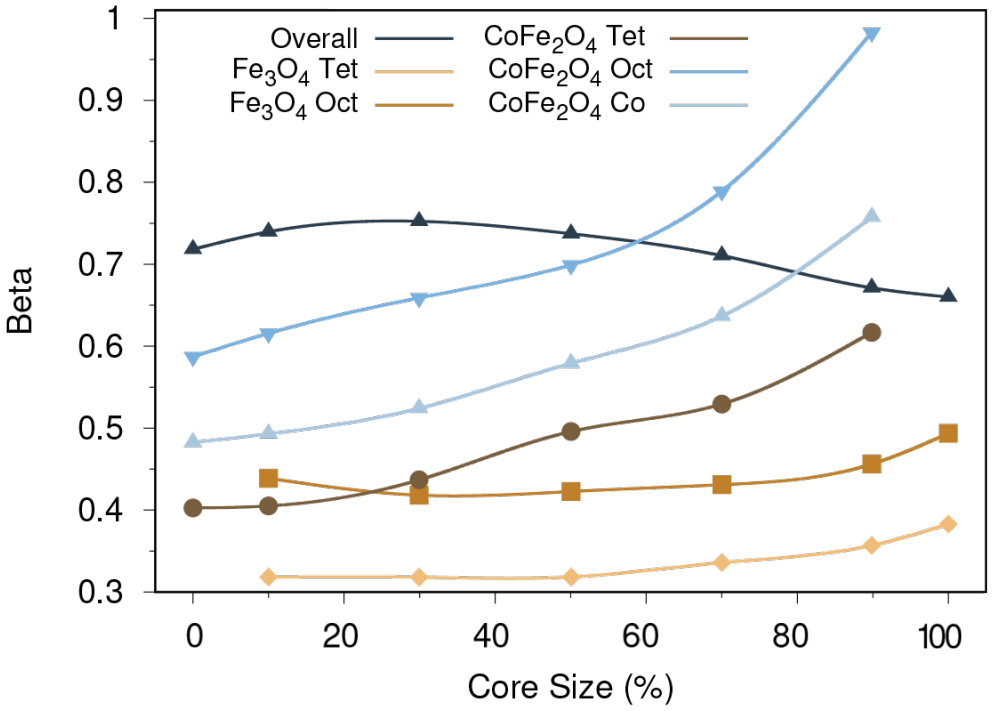

Figure 7.9: ***β* scaling of all components of the magnetite-cobalt ferrite core-shell particles.** The scaling is similar for sublattices of each material however the overall β scaling is somewhat independent.

7.5 Conclusion

In this chapter we have simulated core-shell nanoparticles by using the models developed for iron oxides as well as the material parameters gathered in previous chapters. The nanoparticles show the transition of magnetic properties from those of the core to the shell as the ratio of each component is changed.

We show how layers of maghemite formed on the surface of magnetite nanoparticles affect the temperature scaling properties of the particles by changing the Curie point of the system as well as changing the magnetisation strength depending on the thickness of the shell. The susceptibility scaling was found to be at a maximum when the system was a mix of equal parts magnetite to maghemite.

Magnetite-cobalt ferrite nanoparticles are promising for hyperthermia applications due to the oxidation resistant properties and high anisotropy of the cobalt ferrite surface. In our simulations we find that the susceptibility scaling shows competition between the materials when they are in equal proportion, suggesting that thin layers of cobalt ferrite are preferable.

From our simulations we also find clear evidence of topological effects on the

temperature scaling of the magnetic properties of the nanoparticles. The strength of the magnetic properties of the core were roughly equal at 70% material content to 100% leaving room for optimisation in the structure of core-shell systems.

CHAPTER 8

CONCLUSIONS

The magnetic properties of iron oxides are affected by topology and scale and require a better understanding to be used optimally in biomedical and industrial applications. While these materials share similar traits, small changes in composition as well as shape and size can be useful in designing nanoparticles fit for individual uses. In this chapter we summarise the key points of this work which has explored three such materials: magnetite, maghemite and cobalt ferrite.

In Chapter 3 the foundation for this work is made. A 3D Heisenberg Hamiltonian was formulated for spinel iron oxides such as magnetite, which is made up of the interactions of the tetrahedral and octahedral sublattice interactions of a ferrimagnetic material. Due to the body of research into the magnetic properties of magnetite, we can form a precise atomistic model for the material by using several parameters including the oxygen positional parameter, cubic anisotropy and exchange constants. By analysing the data produced by our simulations, we have devised different methods to extract the critical exponents of the system which are difficult to fit solely from the magnetisation, but much more clearly shown in the susceptibility. To remedy the discrepancy between our classical spin model and the real quantum mechanical effects of spin, we have also used a correcting factor to rescale our simulations and reintroduce these quantum mechanical effects into our final data. We find that the temperature dependent magnetisation of our simulations agrees very well with experiment. In our simulations we find that the sublattices of magnetite show a noticeable deviation in their fitted magnetic properties such as β and T_{C} from that of the overall material. While T_{C} remains close, β and hence the magnetisation scaling, is markedly different for

all components of the system. With increasing temperature, these components lose their magnetisation at different rates. We distinguish the modes over which the sublattices interact, with the interaction between closely aligned spins within their own sublattices, as well as the competition between antiparallel spins in different sublattices, which shows up in the comparison between the sublattice susceptibilities compared to those of the overall system.

Chapter 4 shows how the magnetic properties change when a material is in bulk and nanoparticle form. While we cannot correctly model the strains and full effects of the surface of nanoparticles, we show that finite size effects in nanoparticles around 8 nm can lower the system magnetisation by as much as 15% at room temperature, which is crucial for biomedical applications such as hyperthermia which require a consistent amount of energy output from the particles. Ideally, samples of magnetite intended for medicinal use should be about 10 nm in diameter, as this significantly reduces the finite size effects. As there is often a spread of radii produced in experimental samples, this suggests that the average diameter should be closer to 15 nm, to minimise the number of smaller particles. The Curie temperature of nanoparticles tends toward the value of bulk as the system size is increased, starting at a much lower value, reduced by more than 100K, when the particle is less than 4 nm. The strength of these effects is also tied to the surface to volume ratio of the particle which is determined by shape. Faceted nanoparticles are hence more susceptible to these effects for the same number of atoms than spherical particles. As the type of faceting, the particle shape and surface termination, is strongly dependant on the experimental methods used to form the particle, this is also crucial in tuning the properties of the system. At room temperature, elongated particles can also cause deviation in the expected superparamagnetic behaviour of the system due to an increased overall anisotropy of the system. The elongation of the particle causes a shape anisotropy which, while not as strong as surface anisotropy, can cause the system to become partially blocked for particles with a elongation of 20%.

We then apply the model and methods used to analyse magnetite on the less well understood maghemite in Chapter 5. With a closely related structure, the details of the exact structure of maghemite are dependent on several factors and their study is made more difficult due to the unstable nature of the material and the ease of contamination with other iron oxides. Due to these gaps in understanding, some of the parameters for this material are disputed. The nature of the iron vacancies is found to be regular when it is in nanoparticle form, leading to a pure Fd-3m spinel structure. To model the exchange between the

iron ions in maghemite, we must use exchange constants derived from magnetite as these have not been derived from first principles for maghemite, partially due to the uncertainty in the exact structure of the system. We show that it is very likely that many experimental measurements taken for maghemite are heavily affected by finite size effects which reduces the magnetisation scaling of the system, with some samples showing markedly different behaviour possibly due to sample contamination. The critical exponent β shows much similarity with that of magnetite, which is expected due to the similarity in structure of these materials, however in comparison to the ideal value proposed for β in a general 3D Heisenberg model, there is significant deviation. Ferromagnets modelled using the Heisenberg Hamiltonian are expected to have a β scaling of around 0.34 however our materials show much higher values, at 0.55 and 0.47 for magnetite and maghemite respectively suggesting that these materials may belong to a different universality class or that commonly assumed ideal value does not hold for all materials.

In Chapter 6 we study another related material, cobalt ferrite, which shares the same structure to magnetite but is often used for its much higher material anisotropy caused by the cobalt ions in the system. Cobalt ferrite can be difficult to study due to the variation in magnetic properties dependant on the exact amount of cobalt in the system. In fact, the structure of cobalt ferrite is dependant also on its location within each sublattice. The room temperature properties of cobalt ferrite are well understood with many studies covering the change in anisotropy strength with temperature. For our modelling however, some components are less well understood. The strength of interaction between the sublattices of the material which now contains an additional component due to the inclusion of cobalt is still being refined. We therefore model two similar systems, one using a simple 2-lattice model, which approximates the octahedral lattice by combining the effects of the iron and cobalt contributions, as well as a 3-lattice model which uses relatively untested exchange constants found in the literature. We find that the 2-lattice model cannot correctly replicate the magnetic behaviour of the octahedral sublattices which have significantly different scaling. In comparing the magnetisation scaling of our simulations with those of experiment we also find that the experimental data likely does not come from bulk like cobalt ferrite as it more closely matches the magnetisation scaling of nanoparticles under finite size effects.

The materials studied so far have been used together in different applications, sometimes without intent. Magnetite nanoparticles can suffer from the formation

of a maghemite surface which creates a magnetic dead layer and changes the overall magnetic properties, lowering the overall magnetisation. In Chapter 7 we study core-shell nanoparticles, combinations of magnetite-maghemite and magnetite-cobalt ferrite to understand how the relative sizes of the core and shell as well as contained materials affects the overall properties of the system. We find the topological effects create differences in the magnetisation of the core and shell, with the magnetisation strength of the cores reaching a maximum at around 70% core size. Depending on the combination of materials, the susceptibility is at a maximum for a mixing of the materials, in the case of magnetite-maghemite, but at a minimum at the same point in maghemite-cobalt ferrite, showing a change in the spin behaviour of each particle.

In conclusion, this is the first comprehensive atomistic investigation into several iron oxides, simulated with details which are not possible using micromagnetic or current *ab-initio* approaches. The model gives results which match experimental measurements, and from this more complex structures such as finite size systems and different core-shell combinations can be studied.

8.1 Further Work

The materials covered in this work have been studied extensively for many years, however gaps in the current knowledge of their structure and properties at the nanoscale remain. We have created models using the most up to date information for each material, in many cases choosing the parameters which best suited our use cases, however in the case of maghemite and cobalt ferrite, many of the atomistic parameters have not yet been fully refined. Much of the experimental data shows symptoms of finite size scaling effects and sample impurities, which leads to uncertainty in the reference bulk parameters such as the predicted Curie temperature and exchange parameters.

The exchange parameters in particular are the most important component of our simulations, forming the majority of the energy contributions to the system. While we find that the suggested exchange values for magnetite are promising, work is required to find a more suitable set of parameters for maghemite and cobalt ferrite, depending on their exact compositions. Density functional theory, or DFT, is a promising avenue for calculating these parameters however due to the *ab initio* nature of the simulations, many more details must be fleshed out to form a competent model. In addition, DFT does not necessarily lend itself immediately to magnetic materials and additional approximations and computation is needed

to model ferrimagnetic materials which do not have a simple spin structure.

The properties of nanoparticles are strongly tied to the effects of the particle surface, both in spherical and faceted particles, however we have been unable to model changes in the surface structure or to choose specific surface configurations for our study. This is another vast area of study, particularly in the case of magnetite, which presents several possible surface configurations depending on the orientation of the surface. An important continuation of this work would be to study various low energy configurations to better understand their effects. This is also strongly tied to the magnetocrystalline anisotropy which should also have a significant contribution from the surface. The superparamagnetic properties of low temperature iron oxides are strongly bound by the surface anisotropy which we have been unable to model here.

With the constant improvements to computer hardware, the possible system sizes which can be studied continues to increase. While today systems of 100 nm are feasible using the highest end super computers available, many magnetic phenomena such as spin vortices are only observed at or above this scale [2] and will become easier to study in the coming years. The detail and accuracy of atomistic models will be crucial to understanding the complex spin behaviours occurring in these systems.

BIBLIOGRAPHY

[1] SD Oberdick, A Abdelgawad, C Moya, S Mesbahi-Vasey, D Kepaptsoglou, VK Lazarov, RFL Evans, D Meilak, E Skoropata, J van Lierop, et al. Spin canting across core/shell $Fe_3O_4/Mn_xFe_{3-x}O_4$ nanoparticles. *Scientific reports*, 8(1):1–12, 2018.

[2] D Meilak, S Jenkins, R Pond, and RFL Evans. Massively parallel atomistic simulation of ultrafast thermal spin dynamics of a permalloy vortex. *arXiv preprint arXiv:1908.08885*, 2019.

[3] R Moreno, S Poyser, D Meilak, A Meo, S Jenkins, VK Lazarov, G Vallejo-Fernandez, S Majetich, and RFL Evans. The role of faceting and elongation on the magnetic anisotropy of magnetite Fe_3O_4 nanocrystals. *Scientific reports*, 10(1):1–14, 2020.

[4] W Gilbert. *De magnete*. Courier Corporation, 1958.

[5] W Heisenberg. Zur theorie des ferromagnetismus. *Z. Phys*, 49:619, 1928.

[6] L Néel. Propriétés magnétiques des ferrites; ferrimagnétisme et antiferromagnétisme. In *Annales de physique*, volume 12, pages 137–198, 1948.

[7] JL Kirschvink, A Kobayashi-Kirschvink, and BJ Woodford. Magnetite biomineralization in the human brain. *Proceedings of the National Academy of Sciences*, 89(16):7683–7687, 1992.

[8] F Ahmad and Y Zhou. Pitfalls and challenges in nanotoxicology: a case of cobalt ferrite nanocomposites. *Chemical research in toxicology*, 30(2):492–507, 2017.

[9] RM Cornell and U Schwertmann. *The iron oxides: structure, properties, reactions, occurrences and uses*. John Wiley & Sons, 2003.

[10] S Guo, D Li, L Zhang, J Li, and E Wang. Monodisperse mesoporous superparamagnetic single-crystal magnetite nanoparticles for drug delivery. *Biomaterials*, 30(10):1881–1889, 2009.

[11] S Chandra, S Mehta, S Nigam, and D Bahadur. Dendritic magnetite nanocarriers for drug delivery applications. *New Journal of Chemistry*, 34(4):648–655, 2010.

[12] B Perlstein, Z Ram, D Daniels, A Ocherashvilli, Y Roth, S Margel, and Y Mardor. Convection-enhanced delivery of maghemite nanoparticles: increased efficacy and MRI monitoring. *Neuro-oncology*, 10(2):153–161, 2008.

[13] EM Múzquiz-Ramos, V Guerrero-Chávez, BI Macías-Martínez, CM López-Badillo, and LA García-Cerda. Synthesis and characterization of maghemite nanoparticles for hyperthermia applications. *Ceramics International*, 41(1):397–402, 2015.

[14] SW Lee, S Bae, Y Takemura, IB Shim, TM Kim, J Kim, HJ Lee, S Zurn, and CS Kim. Self-heating characteristics of cobalt ferrite nanoparticles for hyperthermia application. *Journal of Magnetism and Magnetic Materials*, 310(2):2868–2870, 2007.

[15] RK Gilchrist, R Medal, WD Shorey, RC Hanselman, JC Parrott, and CB Taylor. Selective inductive heating of lymph nodes. *Annals of surgery*, 146(4):596, 1957.

[16] J Hu, G Chen, and IMC Lo. Selective removal of heavy metals from industrial wastewater using maghemite nanoparticle: performance and mechanisms. *Journal of environmental engineering*, 132(7):709–715, 2006.

[17] GS Parkinson. Iron oxide surfaces. *Surface Science Reports*, 71(1):272–365, 2016.

[18] AV Ramos, JB Moussy, MJ Guittet, AM Bataille, M Gautier-Soyer, M Viret, C Gatel, P Bayle-Guillemaud, and E Snoeck. Magnetotransport properties of Fe_3O_4 epitaxial thin films: thickness effects driven by antiphase boundaries. *Journal of applied physics*, 100(10):103902, 2006.

[19] AH Habib, CL Ondeck, P Chaudhary, MR Bockstaller, and ME McHenry. Evaluation of iron-cobalt/ferrite core-shell nanoparticles for cancer thermotherapy. *Journal of Applied Physics*, 103(7):07A307, 2008.

[20] J Mazo-Zuluaga and J Restrepo. Magnetite thin films: A simulational approach. *Physica B: Condensed Matter*, 384(1-2):224–226, 2006.

[21] J Mazo-Zuluaga, J Restrepo, and J Mejía-López. Influence of non-stoichiometry on the magnetic properties of magnetite nanoparticles. *Journal of Physics: Condensed Matter*, 20(19):195213, 2008.

[22] E Ising. Beitrag zur theorie des ferromagnetismus. *Zeitschrift für Physik*, 31(1):253–258, 1925.

[23] MJ Donahue, DG Porter, J Lau, RD McMichael, and MJ Donahue. Interagency report NISTIR 6376. national institute of standards and technology, gaithersburg. *NIST Journal of Research*, 114:57–67, 1999.

[24] W Scholz, J Fidler, T Schrefl, D Suess, H Forster, V Tsiantos, et al. Scalable parallel micromagnetic solvers for magnetic nanostructures. *Computational Materials Science*, 28(2):366–383, 2003.

[25] D Jiles. *Introduction to magnetism and magnetic materials*. CRC press, 2015.

[26] NW Ashcroft, ND Mermin, et al. *Solid state physics*. New York: Holt, Rinehart and Winston„ 1976.

[27] D Thouless. Magnetism in condensed matter. *American Journal of Physics*, 71(1):94–94, 2003.

[28] M Uhl and B Siberchicot. A first-principles study of exchange integrals in magnetite. *Journal of Physics: Condensed Matter*, 7(22):4227, 1995.

[29] CM Srivastava, G Srinivasan, and NG Nanadikar. Exchange constants in spinel ferrites. *Physical Review B*, 19(1):499, 1979.

[30] RFL Evans, WJ Fan, P Chureemart, TA Ostler, MOA Ellis, and RW Chantrell. Atomistic spin model simulations of magnetic nanomaterials. *Journal of Physics: Condensed Matter*, 26(10):103202, 2014.

[31] LD Landau and EM Lifshitz. To the theory of magnetic permeability dispersion in ferromagnetic solids. *Sov. Phys*, 8:153–166, 1935.

[32] TL Gilbert. A lagrangian formulation of the gyromagnetic equation of the magnetization field. *Phys. Rev.*, 100:1243, 1955.

[33] MOA Ellis, RFL Evans, TA Ostler, J Barker, U Atxitia, O Chubykalo-Fesenko, and RW Chantrell. The Landau–Lifshitz equation in atomistic models. *Low Temperature Physics*, 41(9):705–712, 2015.

[34] W Brown. Thermal fluctuation of fine ferromagnetic particles. *IEEE Transactions on Magnetics*, 15(5):1196–1208, 1979.

[35] DV Berkov and NL Gorn. Thermally activated processes in magnetic systems consisting of rigid dipoles: equivalence of the Ito and Stratonovich stochastic calculus. *Journal of Physics: Condensed Matter*, 14(13):L281, 2002.

[36] E Süli and DF Mayers. *An introduction to numerical analysis*. Cambridge university press, 2003.

[37] JL García-Palacios and FJ Lázaro. Langevin-dynamics study of the dynamical properties of small magnetic particles. *Physical Review B*, 58(22):14937, 1998.

[38] N Metropolis, AW Rosenbluth, MN Rosenbluth, AH Teller, and E Teller. Equation of state calculations by fast computing machines. *The journal of chemical physics*, 21(6):1087–1092, 1953.

[39] D Hinzke and U Nowak. Monte Carlo simulation of magnetization switching in a Heisenberg model for small ferromagnetic particles. *Computer physics communications*, 121:334–337, 1999.

[40] RFL Evans, U Atxitia, and RW Chantrell. Quantitative simulation of temperature-dependent magnetization dynamics and equilibrium properties of elemental ferromagnets. *Physical Review B*, 91(14):144425, 2015.

[41] RM White. *Quantum theory of magnetism*, volume 1. Springer, 1983.

[42] M Campostrini, M Hasenbusch, A Pelissetto, P Rossi, and E Vicari. Critical exponents and equation of state of the three-dimensional Heisenberg universality class. *Physical Review B*, 65(14):144520, 2002.

[43] J Crangle. Lix. the magnetic moments of cobalt-copper alloys. *The London, Edinburgh, and Dublin Philosophical Magazine and Journal of Science*, 46(376):499–513, 1955.

[44] J Crangle and GM Goodman. The magnetization of pure iron and nickel. *Proceedings of the Royal Society of London. A. Mathematical and Physical Sciences*, 321(1547):477–491, 1971.

[45] T Williams, C Kelley, et al. Gnuplot 4.6: an interactive plotting program. `http://gnuplot.sourceforge.net/`, April 2013.

[46] A Herraez. Biomolecules in the computer: Jmol to the rescue. *Biochemistry and Molecular Biology Education*, 34(4):255–261, 2006.

[47] RA Sayle and EJ Milner-White. RASMOL: biomolecular graphics for all. *Trends in biochemical sciences*, 20(9):374–376, 1995.

[48] T Plachetka. POV Ray: persistence of vision parallel raytracer. In *Proc. of Spring Conf. on Computer Graphics, Budmerice, Slovakia*, volume 123, 1998.

[49] S Süsstrunk, R Buckley, and S Swen. Standard RGB color spaces. In *Color and Imaging Conference*, pages 127–134. Society for Imaging Science and Technology, 1999.

[50] P Lennie and M D'Zmura. Mechanisms of color vision. *Critical reviews in neurobiology*, 3(4):333–400, 1988.

[51] CA Brewer. Color use guidelines for mapping. *Visualization in modern cartography*, 1994:123–148, 1994.

[52] CA Brewer. Spectral schemes: Controversial color use on maps. *Cartography and Geographic Information Systems*, 24(4):203–220, 1997.

[53] P Kovesi. Good colour maps: How to design them. *arXiv preprint arXiv:1509.03700*, 2015.

[54] P Kovesi. Perceptually uniform colourmaps, 2015.

[55] T Shinjo, T Okuno, R Hassdorf, K Shigeto, and T Ono. Magnetic vortex core observation in circular dots of permalloy. *Science*, 289(5481):930–932, 2000.

[56] MATLAB. *version 7.10.0 (R2010a)*. The MathWorks Inc., Natick, Massachusetts, 2010.

[57] JF Keithley. *The story of electrical and magnetic measurements: from 500 BC to the 1940s*. John Wiley & Sons, 1999.

[58] BD Cullity and CD Graham. *Introduction to magnetic materials*. John Wiley & Sons, 2011.

[59] J Katriel and R Pauncz. Theoretical interpretation of Hund's rule. *Advances in Quantum Chemistry*, 10:143–185, 1977.

[60] WH Bragg. The structure of magnetite and the spinels. *Nature*, 95(2386):561–561, 1915.

[61] EJW Verwey and JH de Boer. Cation arrangement in a few oxides with crystal structures of the spinel type. *Recueil des Travaux Chimiques des Pays-Bas*, 55(6):531–540, 1936.

[62] ME Fleet. The structure of magnetite. *Acta Crystallographica Section B: Structural Crystallography and Crystal Chemistry*, 37(4):917–920, 1981.

[63] HSC O'Neill and A Navrotsky. Simple spinels; crystallographic parameters, cation radii, lattice energies, and cation distribution. *American Mineralogist*, 68(1-2):181–194, 1983.

[64] RD Shannon and CT Prewitt. Effective ionic radii in oxides and fluorides. *Acta Crystallographica Section B: Structural Crystallography and Crystal Chemistry*, 25(5):925–946, 1969.

[65] RD Shannon. Revised effective ionic radii and systematic studies of interatomic distances in halides and chalcogenides. *Acta crystallographica section A: crystal physics, diffraction, theoretical and general crystallography*, 32(5):751–767, 1976.

[66] EJW Verwey. Electronic conduction of magnetite (Fe_3O_4) and its transition point at low temperatures. *Nature*, 144(3642):327–328, 1939.

[67] F Walz. The Verwey transition-a topical review. *Journal of Physics: Condensed Matter*, 14(12):R285, 2002.

[68] K Jordan, A Cazacu, G Manai, SF Ceballos, S Murphy, and IV Shvets. Scanning tunneling spectroscopy study of the electronic structure of Fe_3O_4 surfaces. *Physical Review B*, 74(8):085416, 2006.

[69] D Ihle and B Lorenz. Small-polaron band versus hopping conduction in Fe_3O_4. *Journal of Physics C: Solid State Physics*, 18(21):L647, 1985.

[70] D Ihle and B Lorenz. Small-polaron conduction and short-range order in Fe_3O_4. *Journal of Physics C: Solid State Physics*, 19(26):5239, 1986.

[71] A Yanase and K Siratori. Band structure in the high temperature phase of Fe_3O_4. *Journal of the Physical Society of Japan*, 53(1):312–317, 1984.

[72] A Yanase and N Hamada. Electronic structure in high temperature phase of Fe_3O_4. *Journal of the Physical Society of Japan*, 68(5):1607–1613, 1999.

[73] HT Jeng, GY Guo, and DJ Huang. Charge-orbital ordering in low-temperature structures of magnetite: GGA+U investigations. *Physical Review B*, 74(19):195115, 2006.

[74] J García and G Subías. The Verwey transition-a new perspective. *Journal of Physics: Condensed Matter*, 16(7):R145, 2004.

[75] MS Senn, I Loa, JP Wright, and JP Attfield. Electronic orders in the Verwey structure of magnetite. *Physical Review B*, 85(12):125119, 2012.

[76] K Abe, Y Miyamoto, and S Chikazumi. Magnetocrystalline anisotropy of low temperature phase of magnetite. *Journal of the Physical Society of Japan*, 41(6):1894–1902, 1976.

[77] Z Kakol and JM Honig. Influence of deviations from ideal stoichiometry on the anisotropy parameters of magnetite $Fe_{3(1-\delta)}O_4$. *Physical Review B*, 40(13):9090, 1989.

[78] JB Goodenough. Goodenough-kanamori rule. *Scholarpedia*, 3(10):7382, 2008.

[79] L Néel. Magnetism and local molecular field. *Science*, 174(4013):985–992, 1971.

[80] ML Glasser and FJ Milford. Spin wave spectra of magnetite. *Physical Review*, 130(5):1783, 1963.

[81] KT Moglestue. Exchange integrals in magnetite. *Neutron inelastic scattering*, 2:117–122, 1968.

[82] R Pauthenet and L Bochirol. Aimantation spontanée des ferrites. *Journal de Physique et le Radium*, 12(3):249–251, 1951.

[83] F Bloch. Zur theorie des ferromagnetismus. *Zeitschrift für Physik*, 61(3-4):206–219, 1930.

[84] S Chikazumi and CD Graham. *Physics of Ferromagnetism 2e*. Oxford University Press on Demand, 2009.

[85] RM Suter and C Hohenemser. Review of measurements of critical exponent beta in simple magnetic systems. *Journal of Applied Physics*, 50(B3):1814–1816, 1979.

[86] AW Sandvik. Critical temperature and the transition from quantum to classical order parameter fluctuations in the three-dimensional Heisenberg antiferromagnet. *Physical review letters*, 80(23):5196, 1998.

[87] MD Kuz'min. Shape of temperature dependence of spontaneous magnetization of ferromagnets: quantitative analysis. *Physical review letters*, 94(10):107204, 2005.

[88] L Greg. Temperature enthaply relationship of 1 mol of water through its phase changes under constant pressure, 2006.

[89] AR Muxworthy and E McClelland. Review of the low-temperature magnetic properties of magnetite from a rock magnetic perspective. *Geophysical Journal International*, 140(1):101–114, 2000.

[90] KP Belov. Ferrimagnets with a weak magnetic sublattice. *Physics-Uspekhi*, 39(6):623, 1996.

[91] P Asselin, RFL Evans, J Barker, RW Chantrell, R Yanes, O Chubykalo-Fesenko, D Hinzke, and U Nowak. Constrained monte carlo method and calculation of the temperature dependence of magnetic anisotropy. *Physical Review B*, 82(5):054415, 2010.

[92] N Akulov. Zur quantentheorie der temperaturabhängigkeit der magnetisierungskurve. *Zeitschrift für Physik*, 100(3-4):197–202, 1936.

[93] HB Callen and E Callen. The present status of the temperature dependence of magnetocrystalline anisotropy, and the l (l+ 1) 2 power law. *Journal of Physics and Chemistry of Solids*, 27(8):1271–1285, 1966.

[94] DP Landau, HH Lee, and W Kao. Critical behavior of a *3D* ising model in a random field. *Journal of Applied Physics*, 49(3):1356–1358, 1978.

[95] K Binder. Applications of monte Carlo methods to statistical physics. *Reports on Progress in Physics*, 60(5):487, 1997.

[96] J Wang, F Zhao, W Wu, and G Zhao. Finite-size scaling relation of the curie temperature in barium hexaferrite platelets. *Journal of Applied Physics*, 110(12):123909, 2011.

[97] O Hovorka, S Devos, Q Coopman, WJ Fan, CJ Aas, RFL Evans, Xi Chen, G Ju, and RW Chantrell. The Curie temperature distribution of FePt granular magnetic recording media. *Applied Physics Letters*, 101(5):052406, 2012.

[98] J Wang, W Wu, F Zhao, and G Zhao. Curie temperature reduction in SiO_2-coated ultrafine Fe_3O_4 nanoparticles: quantitative agreement with a finite-size scaling law. *Applied physics letters*, 98(8):083107, 2011.

[99] L Zhao, H Zhang, Y Xing, S Song, S Yu, W Shi, X Guo, J Yang, Y Lei, and F Cao. Morphology-controlled synthesis of magnetites with nanoporous

structures and excellent magnetic properties. *Chemistry of Materials*, 20(1):198–204, 2008.

[100] QA Pankhurst, J Connolly, SK Jones, and J Dobson. Applications of magnetic nanoparticles in biomedicine. *Journal of physics D: Applied physics*, 36(13):R167, 2003.

[101] R Řezníček, V Chlan, H Štěpánková, P Novák, and M Maryško. Magnetocrystalline anisotropy of magnetite. *Journal of Physics: Condensed Matter*, 24(5):055501, 2012.

[102] DA Garanin and H Kachkachi. Surface contribution to the anisotropy of magnetic nanoparticles. *Physical review letters*, 90(6):065504, 2003.

[103] P Allia, G Barrera, P Tiberto, T Nardi, Y Leterrier, and M Sangermano. Fe_3O_4 nanoparticles and nanocomposites with potential application in biomedicine and in communication technologies: Nanoparticle aggregation, interaction, and effective magnetic anisotropy. *Journal of Applied Physics*, 116(11):113903, 2014.

[104] JMD Coey, IV Shvets, R Wiesendanger, and HJ Güntherodt. Charge freezing and surface anisotropy on magnetite (100). *Journal of applied physics*, 73(10):6742–6744, 1993.

[105] G Vallejo-Fernandez and K O'Grady. Effect of the distribution of anisotropy constants on hysteresis losses for magnetic hyperthermia applications. *Applied Physics Letters*, 103(14):142417, 2013.

[106] AG Roca, L Gutiérrez, H Gavilán, MEF Brollo, S Veintemillas-Verdaguer, and M del Puerto Morales. Design strategies for shape-controlled magnetic iron oxide nanoparticles. *Advanced drug delivery reviews*, 138:68–104, 2019.

[107] SK Piotrowski, MF Matty, and SA Majetich. Magnetic fluctuations in individual superparamagnetic particles. *IEEE Transactions on Magnetics*, 50(11):1–4, 2014.

[108] EL Schubarth. *Lehrbuch der theoretischen Chemie*, volume 1. Springer, 1837.

[109] O Baudisch and LA Welo. Hysteresis-messungen als werkzeug zur ermittlung der feinstruktur ferromagnetischer verbindungen. *Naturwissenschaften*, 14(46):1005–1011, 1926.

[110] H Sachse and R Haase. Die magnetischen umwandlungen des regulären ferrioxyds. *Z. physik. Chem., Abt. A*, 148:401–412, 1930.

[111] C Marvin. Magnetic impulse record member, magnetic material, and method of making magnetic material, 1947. US Patent 2694656A.

[112] S Mornet, F Grasset, J Portier, and E Duguet. Maghemite silica nanoparticles for biological applications, 2002.

[113] M Hua, S Zhang, B Pan, W Zhang, L Lv, and Q Zhang. Heavy metal removal from water/wastewater by nanosized metal oxides: a review. *Journal of hazardous materials*, 211:317–331, 2012.

[114] AF Wells. *Structural inorganic chemistry*. Oxford university press, 2012.

[115] L Pauling and SB Hendricks. The crystal structures of hematite and corundum. *Journal of the American Chemical Society*, 47(3):781–790, 1925.

[116] C Dejoie, P Sciau, W Li, L Noé, A Mehta, K Chen, H Luo, M Kunz, N Tamura, and Z Liu. Learning from the past: Rare ϵ-Fe_2O_3 in the ancient black-glazed Jian (Tenmoku) wares. *Scientific Reports*, 4:4941, 2014.

[117] TJ Bastow, A Trinchi, MR Hill, R Harris, and TH Muster. Vacancy ordering in γ-Fe_2O_3 nanocrystals observed by 57Fe NMR. *Journal of Magnetism and Magnetic Materials*, 321(17):2677–2681, 2009.

[118] R Grau-Crespo, AY Al-Baitai, I Saadoune, and NH De Leeuw. Vacancy ordering and electronic structure of γ-Fe_2O_3 (maghemite): a theoretical investigation. *Journal of Physics: Condensed Matter*, 22(25):255401, 2010.

[119] PB Braun. A superstructure in spinels. *Nature*, 170(4339):1123–1123, 1952.

[120] JE Jørgensen, L Mosegaard, LE Thomsen, TR Jensen, and JC Hanson. Formation of γ-Fe_2O_3 nanoparticles and vacancy ordering: An *in situ* X-ray powder diffraction study. *Journal of Solid State Chemistry*, 180(1):180–185, 2007.

[121] R Haul and T Schoon. Zur struktur des ferromagnetischen eisen (III)-oxyds γ-Fe_2O_3. *Zeitschrift für physikalische Chemie*, 44(1):216–226, 1939.

[122] H Takei and S Chiba. Vacancy ordering in epitaxially-grown single crystals of γ-Fe_2O_3. *Journal of the Physical Society of Japan*, 21(7):1255–1263, 1966.

[123] K Haneda and AH Morrish. Vacancy ordering in γ-Fe_2O_3 small particles. *Solid State Communications*, 22(12):779–782, 1977.

[124] AU Gehring, H Fischer, M Louvel, K Kunze, and PG Weidler. High temperature stability of natural maghemite: a magnetic and spectroscopic study. *Geophysical Journal International*, 179(3):1361–1371, 2009.

[125] XM Liu, J Shaw, JZ Jiang, J Bloemendal, P Hesse, T Rolph, and XG Mao. Analysis on variety and characteristics of maghemite. *Science China Earth Sciences*, 53(8):1153–1162, 2010.

[126] Ö Özdemir. High-temperature hysteresis and thermoremanence of single-domain maghemite. *Physics of the Earth and planetary interiors*, 65(1-2):125–136, 1990.

[127] J Gee and M Nakanishi. Magnetic petrology and magnetic properties of western pacific guyots: implications for seamount paleopoles. In *Proceedings of the Ocean Drilling Program. Scientific results*, volume 144, pages 615–630, 1995.

[128] V Chevrier, PE Mathé, P Rochette, and HP Gunnlaugsson. Magnetic study of an antarctic weathering profile on basalt: Implications for recent weathering on mars. *Earth and Planetary Science Letters*, 244(3-4):501–514, 2006.

[129] S Krupicka and K Zaveta. Anisotropy, induced anisotropy and related phenomena, edited by DJ Craik. *Magnetic Oxides*, pages 235–287, 1975.

[130] J Restrepo, Y Labaye, and JM Greneche. Surface anisotropy in maghemite nanoparticles. *Physica B: Condensed Matter*, 384(1-2):221–223, 2006.

[131] H Kachkachi, A Ezzir, M Nogues, and E Tronc. Surface effects in nanoparticles: application to maghemite γ-Fe_2O_3. *The European Physical Journal B*, 14(4):681–689, 2000.

[132] RH Kodama, AE Berkowitz, EJ McNiff Jr, and S Foner. Surface spin disorder in $NiFe_2O_4$ nanoparticles. *Physical Review Letters*, 77(2):394, 1996.

[133] MA Gilleo. Superexchange interaction energy for Fe^{3+}-O^{2-}-Fe^{3+} linkages. *Physical Review*, 109(3):777, 1958.

[134] W Wu, XH Xiao, SF Zhang, TC Peng, J Zhou, F Ren, and CZ Jiang. Synthesis and magnetic properties of maghemite (γ-Fe_2O_3) short-nanotubes. *Nanoscale research letters*, 5(9):1474–1479, 2010.

[135] IHM Van Oorschot and MJ Dekkers. Dissolution behaviour of fine-grained magnetite and maghemite in the citrate–bicarbonate–dithionite extraction method. *Earth and Planetary Science Letters*, 167(3-4):283–295, 1999.

[136] S Mo, F Bo, PV Hendriksen, S Linderoth, et al. Spin-glass-like ordering of the magnetic moments of interacting nanosized maghemite particles. *Physical Review B*, 52(1):287, 1995.

[137] SJ Lee, JR Jeong, SC Shin, JC Kim, and JD Kim. Synthesis and characterization of superparamagnetic maghemite nanoparticles prepared by coprecipitation technique. *Journal of Magnetism and Magnetic Materials*, 282:147–150, 2004.

[138] VN Nikiforov, AE Goldt, EA Gudilin, VG Sredin, and V Yu Irhin. Magnetic properties of maghemite nanoparticles. *Bulletin of the Russian Academy of Sciences: Physics*, 78(10):1075–1080, 2014.

[139] N Mulakaluri and R Pentcheva. Hydrogen adsorption and site-selective reduction of the Fe_3O_4 (001) surface: Insights from first principles. *The Journal of Physical Chemistry C*, 116(31):16447–16453, 2012.

[140] CHF Peden, GS Herman, IZ Ismagilov, BD Kay, MA Henderson, YJ Kim, and SA Chambers. Model catalyst studies with single crystals and epitaxial thin oxide films. *Catalysis today*, 51(3-4):513–519, 1999.

[141] O Gamba, H Noei, J Pavelec, R Bliem, M Schmid, U Diebold, A Stierle, and GS Parkinson. Adsorption of formic acid on the Fe_3O_4 (001) surface. *The Journal of Physical Chemistry C*, 119(35):20459–20465, 2015.

[142] Z Li, DV Potapenko, KT Rim, M Flytzani-Stephanopoulos, GW Flynn, RM Osgood, XD Wen, and ER Batista. Reactions of deuterated methanol (cd_3od) on Fe_3O_4 (111). *The Journal of Physical Chemistry C*, 119(2):1113–1120, 2015.

[143] C Ratnasamy and JP Wagner. Water gas shift catalysis. *Catalysis Reviews*, 51(3):325–440, 2009.

[144] R Bliem, J van der Hoeven, A Zavodny, O Gamba, J Pavelec, PE de Jongh, M Schmid, U Diebold, and GS Parkinson. An atomic-scale view of CO

and H_2 oxidation on a Pt/Fe_3O_4 model catalyst. *Angewandte Chemie*, 127(47):14205–14208, 2015.

[145] GS Parkinson, Z Novotny, G Argentero, M Schmid, J Pavelec, R Kosak, P Blaha, and U Diebold. Carbon monoxide-induced adatom sintering in a $Pd–Fe_3O_4$ model catalyst. *Nature materials*, 12(8):724–728, 2013.

[146] DH Zhang, HB Li, GD Li, and JS Chen. Magnetically recyclable ag-ferrite catalysts: general synthesis and support effects in the epoxidation of styrene. *Dalton Transactions*, pages 10527–10533, 2009.

[147] R Bliem, J Pavelec, O Gamba, E McDermott, Z Wang, S Gerhold, M Wagner, J Osiecki, K Schulte, M Schmid, et al. Adsorption and incorporation of transition metals at the magnetite Fe_3O_4 (001) surface. *Physical Review B*, 92(7):075440, 2015.

[148] P Xue, Z Fu, and Z Yang. The density functional theory studies on the promoting effect of the Cu-modified Fe_3O_4 catalysts. *Physics Letters A*, 379(6):607–612, 2015.

[149] CC Winterbourn. Toxicity of iron and hydrogen peroxide: the Fenton reaction. *Toxicology letters*, 82:969–974, 1995.

[150] S Amiri and H Shokrollahi. The role of cobalt ferrite magnetic nanoparticles in medical science. *Materials Science and Engineering: C*, 33(1):1–8, 2013.

[151] A López-Ortega, E Lottini, CJ Fernandez, and C Sangregorio. Exploring the magnetic properties of cobalt-ferrite nanoparticles for the development of a rare-earth-free permanent magnet. *Chemistry of Materials*, 27(11):4048–4056, 2015.

[152] P Lavela, GF Ortiz, JL Tirado, E Zhecheva, R Stoyanova, and Sv Ivanova. High-performance transition metal mixed oxides in conversion electrodes: a combined spectroscopic and electrochemical study. *The Journal of Physical Chemistry C*, 111(38):14238–14246, 2007.

[153] F Rigato, S Piano, M Foerster, F Giubileo, AM Cucolo, and J Fontcuberta. Andreev reflection in ferrimagnetic $CoFe_2O_4$ spin filters. *Physical Review B*, 81(17):174415, 2010.

[154] DH Kim, DE Nikles, DT Johnson, and CS Brazel. Heat generation of aqueously dispersed $CoFe_2O_4$ nanoparticles as heating agents for magnetically activated drug delivery and hyperthermia. *Journal of Magnetism and Magnetic Materials*, 320(19):2390–2396, 2008.

[155] M Pita, JM Abad, C Vaz-Dominguez, C Briones, E Mateo-Martí, JA Martín-Gago, M del Puerto Morales, and VM Fernández. Synthesis of cobalt ferrite core/metallic shell nanoparticles for the development of a specific PNA/DNA biosensor. *Journal of colloid and interface science*, 321(2):484–492, 2008.

[156] R Gargallo-Caballero, L Martín-García, A Quesada, C Granados-Miralles, M Foerster, L Aballe, R Bliem, GS Parkinson, P Blaha, JF Marco, et al. Co on Fe_3O_4 (001): Towards precise control of surface properties. *The Journal of Chemical Physics*, 144(9):094704, 2016.

[157] BD Roiter and AE Paladino. Phase equilibria in the ferrite region of the system FeCoO. *Journal of the American Ceramic Society*, 45(3):128–133, 1962.

[158] A Franco Jr and FC e Silva. High temperature magnetic properties of cobalt ferrite nanoparticles. *Applied Physics Letters*, 96(17):172505, 2010.

[159] H Shenker. Magnetic anisotropy of cobalt ferrite ($Co_{1.01}Fe_{2.00}O_{3.62}$) and nickel cobalt ferrite ($Ni_{0.72}Fe_{0.20}Co_{0.08}Fe_2O_4$). *Physical Review*, 107(5):1246, 1957.

[160] M Tachiki. Origin of the magnetic anisotropy energy of cobalt ferrite. *Progress of Theoretical Physics*, 23(6):1055–1072, 1960.

[161] S Yoon. Temperature dependence of magnetic anisotropy constant in $CoFe_2O_4$ nanoparticles examined by Mössbauer spectroscopy. *Hyperfine Interactions*, 231(1-3):21–28, 2015.

[162] D Peddis, F Orru, A Ardu, C Cannas, A Musinu, and G Piccaluga. Interparticle interactions and magnetic anisotropy in cobalt ferrite nanoparticles: influence of molecular coating. *Chemistry of Materials*, 24(6):1062–1071, 2012.

[163] SJ Kim, SW Lee, and CS Kim. Mössbauer studies on exchange interactions in $CoFe_2O_4$. *Japanese Journal of Applied Physics*, 40(8R):4897, 2001.

[164] R Bliem, E McDermott, P Ferstl, M Setvin, O Gamba, J Pavelec, MA Schneider, M Schmid, U Diebold, P Blaha, et al. Subsurface cation vacancy stabilization of the magnetite (001) surface. *Science*, 346(6214):1215–1218, 2014.

[165] R Ghosh Chaudhuri and S Paria. Core/shell nanoparticles: classes, properties, synthesis mechanisms, characterization, and applications. *Chemical reviews*, 112(4):2373–2433, 2012.

[166] R Frison, G Cernuto, A Cervellino, O Zaharko, GM Colonna, A Guagliardi, and N Masciocchi. Magnetite–maghemite nanoparticles in the 5–15 nm range: Correlating the core–shell composition and the surface structure to the magnetic properties. a total scattering study. *Chemistry of Materials*, 25(23):4820–4827, 2013.

[167] SJ Iyengar, M Joy, CK Ghosh, S Dey, RK Kotnala, and S Ghosh. Magnetic, X-ray and Mössbauer studies on magnetite/maghemite core–shell nanostructures fabricated through an aqueous route. *RSC advances*, 4(110):64919–64929, 2014.

[168] L Signorini, L Pasquini, L Savini, R Carboni, F Boscherini, E Bonetti, A Giglia, M Pedio, N Mahne, and S Nannarone. Size-dependent oxidation in iron/iron oxide core-shell nanoparticles. *Physical Review B*, 68(19):195423, 2003.